ENABLING CONCEPTUAL DESIGN AND ANALYSIS OF CRYOGENIC IN-SPACE VEHICLES THROUGH THE DEVELOPMENT OF AN EXTENSIBLE BOIL-OFF MODEL

A Dissertation
Presented to
The Academic Faculty

By

Eugina D. Mendez Ramos

In Partial Fulfillment
of the Requirements for the Degree
Doctor of Philosophy in the
School of Aerospace Engineering

Georgia Institute of Technology

May 2021

Copyright © Eugina D. Mendez Ramos 2021

ENABLING CONCEPTUAL DESIGN AND ANALYSIS OF CRYOGENIC IN-SPACE VEHICLES THROUGH THE DEVELOPMENT OF AN EXTENSIBLE BOIL-OFF MODEL

Approved by:

Dr. Dimitri Mavris, Advisor
School of Aerospace Engineering
Georgia Institute of Technology

Dr. Daniel Schrage
School of Aerospace Engineering
Georgia Institute of Technology

Dr. Bradford Robertson
School of Aerospace Engineering
Georgia Institute of Technology

Dr. Jechiel Jagoda
School of Aerospace Engineering
Georgia Institute of Technology

Dr. Thomas Percy
Human Lander System Program
NASA Space Marshall Flight Center

Date Approved: April 22, 2021

"One of the great challenges in this world is knowing enough about a subject to think you're right, but not enough about the subject to know you're wrong... A proper skeptic questions what they're unsure of, but recognizes when valid evidence is presented to change their mind."

– Neil deGrasse Tyson

To my younger self – No regrets in life. Just lessons learned.

ACKNOWLEDGEMENTS

I would like to take this opportunity to acknowledge those that have made my journey through graduate school possible through their support and encouragement. I would first like to thank my advisor, Dr. Dimitri Mavris for providing me the opportunity to be a part of the Aerospace Systems Design Laboratory. You taught me that the goal of the Ph.D. was not in obtaining the degree itself, but in acquiring the capacity to think critically though a problem. I would also like to thank the committee formed by Dr. Dimitri Mavris, Dr. Daniel Schrage, Dr. Jechiel Jagoda, Dr. Bradford Robertson, and Dr. Thomas Percy. I appreciate the time you took from your busy schedules to provide feedback and guidance on this research. This work is made stronger because of your participation.

I would like to express great appreciation for my Research Engineer, Dr. Bradford Robertson. Thank you for meeting with me on a weekly, and often daily, basis during the critical phases of this dissertation. Thank you to my fellow ASDL-ers: Nicole Robertson, Alicia Sudol, Kevin Reilley, and Manual Diaz. I appreciate the both technical and emotional support you have provided throughout this process.

Last, but not least, I would like to thank my husband, Miguel Mendez-Ramos, and my brother, Jake Olivas, for their unwavering support. I could not have done this without you.

TABLE OF CONTENTS

LIST OF TABLES

LIST OF FIGURES

NOMENCLATURE

A	=	Area (m^2)
a	=	Local acceleration (m/s^2)
c_p	=	Specific heat at constant pressure (J/kg-K)
c_v	=	Specific heat at constant volume (J/kg-K)
F	=	Thrust (kN)
FL	=	Fill level by percent volume ($\%$)
g_o	=	Gravity (m/s^2)
Gr	=	Grashof number
h	=	Specific enthalpy (J/kg)
h_c	=	Heat transfer coefficient (W/m^2-K)
h_{vap}	=	Enthalpy of vaporization (J/kg)
k	=	Thermal conductivity (W/m-K)
L_s	=	Characteristic length (m)
M	=	Molecular weight (kg/mol)
m	=	Mass (kg)
$\dot{m}$	=	Mass transfer rate (kg/s)
P	=	Pressure (Pa) or perimeter (m)
$\mathcal{P}$	=	Percentage of boil-off mass vented ($\%$)
Pr	=	Prandtl number
$\dot{Q}$	=	Rate of heat transfer (W)
R_u	=	Universal gas constant (J/mol-K)
T	=	Temperature (K)
T_{crit}	=	Critical temperature (K)
T_{nbp}	=	Normal boiling point (K)
t	=	Time (s)

U = Internal energy (J)

V = Volume (m^3)

$\dot{W}$ = Rate of work (J)

Z = Compressibility factor

β = Coefficient of thermal expansion (1/K)

ρ = Density (kg/m^3)

μ = Dynamic viscosity (kg/m-s)

Subscripts

bo = Boil-off

cv = Control volume

e = External surroundings or environment

v = Evaporation

f = Final

g = Ullage gas

g, sat = Saturated ullage gas

o = Initial

s = Interface

l = Bulk liquid propellant

sat = Saturation, or saturated

w = Tank wall

SUMMARY

This work is motivated by the high degree of uncertainty surrounding early estimates of the propellant losses due to boil-off and the resulting impact to the vehicle design space. Typically, the heat entering the propellant tank is assumed to be directly responsible for boil-off of the liquid propellant. This is equivalent to the worst-case scenario, since in an actual tank only a portion of the incoming heat contributes to the boil-off process. This approach has the potential to significantly overestimate boil-off, and therefore the propellant losses, due to the simplicity and corresponding low fidelity that is used when representing the boil-off phenomenon. This uncertainty in the propellant losses is then propagated throughout the vehicle during the sizing process through the propellant mass requirements, resulting in oversized vehicles and an artificial reduction in the design space.

In addition, the above approach ascribes a constant value for the rate at which the propellant losses occur. In reality, boil-off is influenced by a number of factors and changes throughout the mission. Recent studies have shown that cryogenic in-space vehicles have the potential to not only be sensitive to small changes in the boil-off rate, but also to the form of the rate used in the sizing process (a constant rate versus one that changes with time). This has important design consequences to not just to the vehicle mass, but also to the mission duration (via propellant lifetime) as well as the selection of the thermal management approach and pressure control method utilized.

To increase the fidelity in the boil-off rate, the heat transfer responsible for the boil-off of the liquid propellant must be determined. This requires modeling of the physical processes that occur within the tank. Modeling and analysis of the propellant tank is generally incorporated once the design has been matured or narrowed down to a handful of designs, since these models are detailed and require long evaluation times. This presents a gap with respect to the boil-off prediction capability that is available to designers within the space community.

The objective of this research is to address this gap by developing a simplified cryogenic propellant tank model capable of simulating the physical processes in the tank, so as to improve the fidelity in boil-off. This task presents a unique set of challenges, since the vast majority of cryogenic propellant tank models available in literature focus primarily on predicting the fluid conditions in the tank, rather than boil-off. Therefore, validation becomes an issue. However, for low thermal loads the pressure change in the tank is directly related to the evaporation process that occurs at the interface, otherwise known as boil-off. This suggests that a model capable of predicting the pressure change with certain fidelity will predict boil-off with a similar degree of fidelity.

For the model developed here, it is assumed that during pressurization there is no boiling of liquid propellant or condensation of the propellant vapor; pressure control is achieved with direct venting, which affects the ullage region alone. The ability of the model to predict the conditions in the tank during pressurization is validated using several LH_2 self-pressurization experiments from literature. Once the fidelity in the pressurization rate, and thus boil-off, is established, the approach used to represent the venting process is then examined. Once the model evaluation is complete, the propellant losses due to boil-off and subsequent venting are compared with those obtained using the standard approach. The results of the comparison support other observations in literature – that the traditional method utilized during the conceptual design process has the tendency to overestimate boil-off.

To demonstrate the benefits of the higher-fidelity boil-off model, the model is implemented in the sizing process of a relevant system – the descent stage of the Human Landing system. Approximately 23,000 candidate designs were evaluated. The higher-fidelity model predicted boil-off losses that were significantly lower than the losses predicted by the theoretical model, thus resulting in smaller vehicles and with increased payload and loiter capabilities. These results demonstrate the severity of the impact to the vehicle and the design space when assuming the worst-case scenario with respect to boil-off.

CHAPTER 1
INTRODUCTION

Historically, storage durations for cryogenic propellants used in crewed missions have been measured in hours. Future missions will require storage periods on the order of weeks or months, and are thus considered extended, or long-term storage durations. This chapter introduces the primary issue associated with long-term storage of cryogenic propellants – boil-off – and its effect on the vehicle. Investigations are currently underway in order to better understand this impact, as the benefits can outweigh the disadvantages, depending on the design and the mission. To support these efforts, a higher-fidelity boil-off model is introduced as a key enabler for improving the conceptual design and analysis of cryogenic in-space vehicles.

1.1 Challenges of Long-Term Storage of Cryogenic Propellants

1.1.1 Cryogenic Propellant Boil-Off

While the utilization of cryogenic propellants in crewed space exploration has been successful in the past, they have one major disadvantage – they are particularly susceptible to heat. In their naturally occurring state, these fluids exist as gases. In their cold liquefied state, they are stored at or near their boiling points, around 100 K (-270 °F) or less, depending on the propellant [39]. Given the low temperature requirements, providing adequate thermal insulation is a challenge for both ground-based [88, 99, 157] and space-bound tanks [32, 113]. It is inevitable that heat will penetrate the tank, causing the temperature of the propellant to rise and eventually reach the boiling point. As such, cryogenic propellants are notorious for their ability to evaporate, or *boil-off*. This is especially true in the case of liquid hydrogen (LH_2), which requires a storage temperature of approximately 20 K.

Boil-off becomes problematic because as the propellant evaporates, the pressure in the

tank increases. Once the maximum operating pressure of the tank is reached, the excess pressure must be released by venting. The vented gas represents a loss, as it can no longer be used for propulsion [62, 70, 126]. The severity of this issue is exemplified by the Shuttle External Tank (ET), which required a constant supply of liquid oxygen (LOX) and LH_2 at a rate of 475 liters and 380 liters per minute, respectively, to replace the propellant lost to boil-off while sitting on the launch pad [122]. The Saturn V S-IVB upper stage used in the Apollo lunar missions lost approximately 1,200 kg of LH_2, or 8% of the propellant remaining in the tank after orbit insertion, over the course of the short 3-hour coast in Low Earth Orbit (LEO) before performing the second burn for Trans-Lunar Injection (TLI)[1]. The Centaur upper stage on the Titan IIIE launch vehicle (LV), utilized by NASA to launch several interplanetary spacecraft during the 1970s, lost LH_2 at a rate of approximately 73 kg per day during extended coast[2].

Storage of supercritical LOX and LH_2 with limited boil-off was successfully demonstrated during the Apollo and Space Shuttle missions via the Power Reactant Storage and Distribution (PRSD) tanks [45, 61, 110]. The boil-off gases from the tanks were used as reactants for the fuel cells to generate power for the spacecraft, as well as water and oxygen for the crew. The tanks produced boil-off rates that were below the flow rates required by the fuel cells; in-tank heaters were included in order to generate the necessary flow rates on demand [61, 110]. Unfortunately, storage of supercritical fluids is limited to small amounts, as high storage pressures are required, which results in correspondingly heavy tanks [62, 126]. For example, the LH_2 PRSD tank weighed approximately 2.4 times more than the propellant it carried [114], whereas the LH_2 tank on the S-IVB weighed approximately 0.8 times as much as the propellant [20].

Table 1.1 lists the LH_2 boil-off rate and the demonstrated maximum time on orbit for the aforementioned space systems. Currently, the longest in-space storage duration of LOX and LH_2 propellants is held by the Centaur upper stage [1]. Given the relatively high values

[1]Based on the numbers for the Apollo 17 mission reported in [120]

[2]Based on values for the Titan-Centaur 5 (TC-5) Helios B mission reported in [1] and [31]

Table 1.1: Boil-off rates for several flown cryogenic space systems used in crewed missions. Rates for upper stages are based on the propellant remaining in the tank after orbit insertion. Rates for the Shuttle ET and PRSD tank are based on total tank capacity.

System	LH_2 Boil-Off Rate	Total LH_2 Mass	Time on Orbit
Shuttle ET[a]	11 %/hour on launch pad	101.8 mt	–
S-IVB[b]	2.7 %/hour during coast	19,845 kg	3 hours
Centaur D-1T[c]	$\sim$1 %/hour during coast	2,227 kg	9 hours
PRSD[d]	2.03 %/day not operating	41.7 kg	17 days

[a]Boil-off rate [122] and propellant mass [119]

[b]Boil-off rate, propellant mass, and (nominal) time on orbit [120]

[c]Boil-off rate [1, 32] and time on orbit [32]; propellant mass [103]

[d]Boil-off rate [32] and propellant mass [114]; time on orbit [115]

for the boil-off rate, the use of cryogenic propellants has been limited to LVs and upper stages [84]. In order to manage the losses, the Shuttle utilized a "top off and go" approach, whereas upper stages have and continue to operate within a short window – a few hours or less – in which losses are not negligible, but are tolerable [40, 113]. However, if these boil-off rates were to be applied to the scale and storage durations expected in future missions, the losses become prohibitive [25, 126]. This remains true even if propellant tanks can achieve the lower rate of 2.03 %/day provided by the PRSD LH_2 tank. In order to achieve large-scale long-term storage of cryogenic propellants, boil-off must be addressed.

1.1.2 Cryogenic Fluid Management

Cryogenic Fluid Management (CFM) refers to the technologies related to the storage and transfer of cryogenic fluids in space [44, 62]. The primary issues associated with storage include reducing the thermal load on the tank (thermal management) and controlling the subsequent pressure build-up due to boil-off (pressure control). The issues associated with cryogenic fluid transfer focus on the withdrawl of vapor-free liquid from the tank (liquid acquisition), bringing the tank and feedlines down to the appropriate temperature (chill-down), and filling the tank with the desired fluid (fill) [62]. Here, the storage aspect of

CFM is discussed.

The area of thermal management aims to reduce boil-off by reducing the amount of heat that penetrates the tank. Approaches fall into two primary categories: passive and active. Passive approaches make use of, but are not limited to, insulation, paints, surface finishes, and sunshades [59, 156], and include methods such as placing the vehicle in a thermally optimal orientation or location [18, 111, 112, 124]. Active approaches reduce the heat transfer to the tank by incorporating a refrigeration system, or cryocooler, which can significantly reduce or even eliminate boil-off [125, 137]. However, cryocoolers are more complex than passive approaches, and require power [45, 67]. When compared to traditional passive systems, the additional mass from the cryocooler is not anticipated to offset propellant losses until several months into the storage duration [129].

In the past two decades, considerable progress has been made towards advancing thermal management technologies. In 2001, ground-based testing of variable density multilayer insulation (VDMLI) combined with spray-on foam insulation (SOFI) successfully demonstrated a reduced boil-off rate of 3 %/month in a large-scale LH_2 tank during simulated on-orbit conditions [104]. Development and testing of cryocoolers for the purposes of providing reduced boil-off (RBO) or zero boil-off (ZBO) in large-scale tanks anticipated in future missions has been ongoing since the late 1990s. Initial tests using readily available components and flight-rated cryocoolers demonstrated either high inefficiencies or cooling capacities that were too low [76, 126–128]. Current state of the art 20 K cryocoolers still require an order of magnitude improvement in cooling capacity order to achieve ZBO in LH_2 [30, 126].

Recently, a novel concept developed at NASA's Glenn Research Center utilizing a 90 K cryocooler in combination with multilayer insulation (MLI) and distributed cooling has successfully demonstrated ZBO in LOX and RBO in LH_2. A cold working fluid is circulated through tubing attached directly to the external tank wall in the case of LOX, or to an aluminum shield (Broad Area Cooling, or BAC shield) embedded within the MLI of the

LH_2 tank [125]. The shield intercepts a significant portion of the incoming heat and provides a thermal environment of 90 K for the tank, as opposed to the warmer environment of LEO (220 K) [125]. The concept has proven to be effective in removing heat from large surface areas, and provides a substantial reduction in LH_2 boil-off ($\sim$60%) when compared to insulation alone, and with less power than if a 20 K cryocooler were used [125, 126].

In efforts to curtail boil-off, and the thermal management challenges that come along with it, liquid methane (LCH_4) is being considered as an alternative to LH_2 in the upcoming Artemis missions [35]. The temperature requirement is less stringent – approximately 111 K – which is much closer to the 90 K requirement for LOX and easier to maintain. The similar temperature requirements allow for the same or similar thermal management strategies to be employed, thereby avoiding otherwise heavier and more complex thermal management implementations for LH_2 that have been described by some as "heroic" [61, 110]. While LCH_4 offers the advantages of simpler storage and lower boil-off rates, the LOX/LCH_4 propellant combination comes at a cost of reduced performance. The Raptor engine developed by SpaceX produces an I_{sp} of 380 s [143], which is a marked improvement over other commonly used in-space propellant combinations such as MMH/N_2O_4 (330 s - 340 s), yet is considerably lower than the 450 s provided by LOX/LH_2 [35].

In addition to thermal management, the tank will need to incorporate some form of pressure control technology in order to relieve the excess pressure that builds within the tank due to boil-off of the liquid propellant. In ground-based systems, the excess pressure is relieved through direct venting. However, in the low-gravity environment of space, the exact location of the gas and liquid propellant are not well known, and it is not possible to guarantee that vapor, rather than the liquid propellant, is vented from the tank. In fact, it was the venting of LH_2 (rather than gaseous hydrogen) that caused the Atlas-Centaur 4 vehicle to tumble out of control in 1964 [62]. To avoid this issue, spacecraft currently utilize propellant settling maneuvers, where the thrust provided by auxiliary thrusters places the liquid propellant at the bottom of the tank and the gas at the top near the vent [75].

Given that the need to settle the propellants may come at inopportune times during the mission, propellant settling maneuvers can increase mission complexity. Further, depending on the number of maneuvers required, it can be undesirable to consume propellant for the purposes of venting, rather than propulsion. In response, NASA has been developing a pressure control capability that would allow venting without the need for settling the propellants [75, 151]. Ground-based testing of the concept, the thermodynamic vent system (TVS), has been successful demonstrated at NASA's Marshall Space Flight Center for several different propellant and pressurant combinations [52–54, 75]. The TVS maintains the tank pressure through a combination of mixing and venting. During mixing, the cooler liquid propellant absorbs heat from the warmer gas, causing the temperature and pressure of the gas to decrease. This acts to reduce boil-off and subsequently prolongs the time before venting is required.

1.2 Boil-Off in Conceptual Design

1.2.1 Obtaining a Preliminary Estimate

In conceptual-level design and analysis, the boil-off rate for a system can be determined from one of two approaches. In the first approach, the rate is selected based on a value provided by a subject matter expert [140], a current technology [50, 159], or a value that is anticipated to be achievable through incorporation of a future technology (e.g., LH_2 ZBO) [8, 46, 86, 138, 139]. The second approach involves calculating the boil-off rate through Equation 1.1 [7, 60, 141], where $\dot{Q}$ (W) is the heat entering the tank, and h_{vap} (J/kg) is the enthalpy of vaporization, which represents the energy required to convert a kilogram of the propellant from a liquid to a gas. The approach assumes that the tank is at a constant temperature and pressure, with the temperature of the propellant held at the boiling point [7], and that the heat entering the tank goes directly towards evaporation of the propellant (boil-off) [7, 47, 58]. Since the evaporated propellant will at some point need to be vented, it is further assumed that the propellant that is evaporated is equivalent to the propellant lost

through venting [7]. This is the standard practice used in conceptual design, analysis, and trade studies of cryogenic thermal management approaches [30, 124], cryogenic storage tanks [45, 55, 112], propulsive stages [27, 28, 138, 139], and depots [80, 123].

$$\dot{m}_{bo} = \frac{\dot{Q}}{h_{vap}} \tag{1.1}$$

$$m_{bo} = \dot{m}_{bo} t \tag{1.2}$$

Given that h_{vap} is a thermodynamic property of the propellant, boil-off is primarily a function of $\dot{Q}$. Typically, $\dot{Q}$ is assumed constant [7, 45, 113], and thus Equation 1.1 results in a fixed value for the rate at which propellant losses occur, in units of kg per second. Rates in terms of other time frames (e.g., per day or per month) can be determined by applying the appropriate conversion factor to Equation 1.1. Once the boil-off rate is known, the total propellant mass lost due to boil-off, m_{bo}, is obtained by multiplying the boil-off rate by the total storage, or mission time, t, as shown in Equation 1.2.

1.2.2 Impact on Vehicle Sizing

In the sizing process, boil-off affects the vehicle through the propellant mass requirements. The propellant mass is determined from the ideal rocket equation, as shown in Equation 1.3 [146, 156], where ΔV is total change in velocity required by the vehicle in order to reach the desired destination, g_o is the gravitational constant, $m_{initial}$ is the initial (or gross) mass of the vehicle, consisting of the propellant mass m_{prop} and the vehicle dry mass m_{dry} (Eq. 1.4), and m_{final} is the mass of the vehicle after the propellant has been expended (Eq. 1.5).

$$\Delta V = g_o I_{\text{sp}}\, ln \frac{m_{initial}}{m_{final}} \tag{1.3}$$

$$m_{initial} = m_{prop} + m_{dry} \tag{1.4}$$

$$m_{final} = m_{dry} \tag{1.5}$$

$$m_{prop} = m_{bl} + m_{bo} + m_{penalty} \tag{1.6}$$

For a mission utilizing non-cryogenic propellants, Equation 1.3 provides the propellant mass required based on the mission ΔV, vehicle I_{sp}, and an initial estimate of the vehicle dry mass [156]. If, however, the vehicle utilizes one or more cryogenic propellants, the process is not as straightforward. In order to account for the propellant that will be lost to boil-off over the course of the mission, an additional amount of propellant (m_{bo}) must be added to the propellant mass in Equation 1.4. This causes the vehicle gross mass to increase as a result of the additional propellant load and the corresponding growth in one or more vehicle subsystems (e.g., thermal control and structures) in order to accommodate it [136]. Because of the nature of the rocket equation, any additional mass that is added to the vehicle requires more propellant in order to carry it. Thus, an additional amount of propellant is required in order to (1) transport the propellant to account for boil-off, and (2) carry the additional dry mass of the vehicle [124]. This additional propellant mass can be considered the penalty associated with boil-off. The total propellant load required by the vehicle is the sum of the (baseline) propellant m_{bl} required to complete the mission (assuming no boil-off occurs), the propellant losses from boil-off, and the penalty $m_{penalty}$, as shown in Equation 1.6 [124].

Equation 1.6 emphasizes the need to mitigate boil-off, as it only further constrains an already constrained problem. For high mass missions requiring long transit times, unless boil-off can be reduced significantly, the performance benefits provided by the propellant will be outweighed by the additional mass that must be taken on by the system. For example, Perrin and Casler [124] found that for a Mars Cargo Vehicle with a 288-day transit time, the amount of propellant to compensate for boil-off was approximately twice the mass of the boil-off itself. The Mars Design Reference Architecture (DRA 5.0) proposed by NASA in 2010 was projected to double its initial mass in LEO (IMLEO) unless a marked improvement in boil-off was achieved [25].

1.3 The Need for Higher-Fidelity Modeling

The previous section introduced two primary methods – selection and calculation – utilized by designers and engineers within the space community for obtaining a preliminary estimate of the boil-off rate. This section focuses on the latter method of calculation.

Equation 1.1 stems from a theoretical analysis for evaluating the heat flow into a region based on a known value for the rate of evaporation of the liquid [7, 83]. The method is commonly used to evaluate the insulation on cryogenic tanks (via boil-off tests) [71, 150, 153]. Figure 1.1a depicts a tank consisting of liquid propellant and propellant vapor, the latter of which is located in the ullage (gas space above the liquid). The theory states that for a tank at steady state (constant temperature T and pressure P), the heat entering the tank causes evaporation at a rate of $\dot{m}_{bo}$, which is equivalent to the mass flow rate of the escaping gas at the vent [7, 83]. Measurement of $\dot{m}_{bo}$ at the vent provides the value of $\dot{Q}$ via Equation 1.1. Alternatively, knowledge of the incoming $\dot{Q}$ provides an estimate for the boil-off rate, which is the more familiar form of the theory that is currently used in conceptual design [7].

The primary drawback of using the theoretical analysis to estimate the boil-off rate is that it tends to be conservative, primarily due to the assumption regarding how the entering heat is distributed within the tank [7, 83]. Experiments conducted in a 56 cm diameter spherical tank containing LH_2 showed that the measured propellant losses were approximately one-half the losses predicted by theory [7]. Further, since propellant tanks are not typically in a state of constant venting, a more accurate representation is that of a closed tank undergoing self-pressurization, as shown in Figure 1.1b. The heat entering the tank causes the tank pressure to rise due to an increase in temperature of the ullage and the added mass from the evaporation at the interface [5, 96]. As the pressure in the tank rises, so too does the boiling point of the liquid. The body, or bulk, of the liquid does not respond as quickly as the interface; evaporation continues while the bulk temperature slowly rises with the absorption of the incoming heat [71, 150]. Given that the heat within the tank is

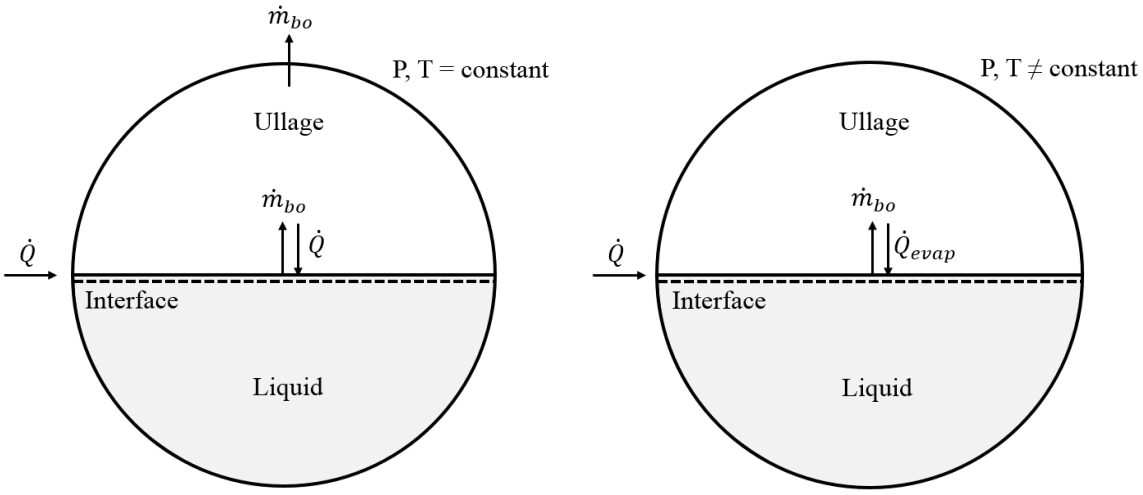

(a) Theory (b) Self-Pressurization

Figure 1.1: Heat responsible for evaporation of the liquid propellant at the interface as described by (a) the theoretical approach used by the space community, and (b) the self-pressurization process.

distributed between the ullage, liquid, and interface regions, the heat that is responsible for evaporation $\dot{Q}_{evap}$ is some value less than $\dot{Q}$ [5]. Thus, a more appropriate form of Equation 1.1 can be obtained by replacing $\dot{Q}$ with $\dot{Q}_{evap}$, as shown in Equation 1.7.

$$\dot{m}_{bo} = \frac{\dot{Q}_{evap}}{h_{vap}} \tag{1.7}$$

The boil-off rate in Equation 1.7 is affected by a variety of factors. The first, and most obvious, is the thermal environment as it determines the value of $\dot{Q}$, which in turn affects the magnitude of thermal distribution in each region within the tank [5, 112]. Another factor affecting the boil-off rate is the tank geometry; spherical tanks offer the lowest boil-off rates when compared to tanks of any other shape since they provide the lowest surface area per unit volume, thus minimizing the heat transfer to the tank [112, 141]. Boil-off rates are higher for smaller tanks than for larger tanks due to the smaller liquid "sink" available for the incoming heat [112]. For an individual tank, assuming that the heat enters the tank uniformly, the boil-off rate increases as the amount of propellant in the tank decreases [112].

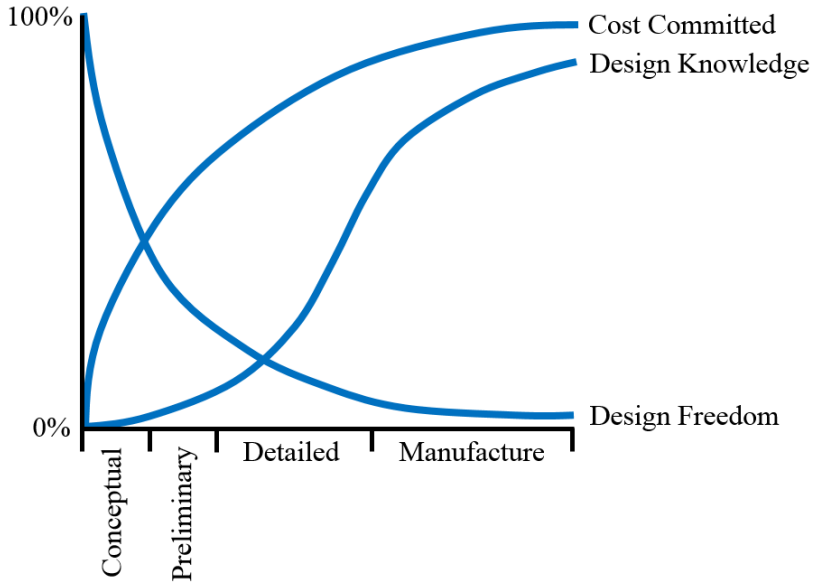

Figure 1.2: Variation in the design knowledge, design freedom, and cost committed throughout the various stages of the vehicle design process (adapted from [107]).

These dependencies mean that the boil-off rate is affected not only by the tank configuration, but also by the amount of propellant in the tank, which unless used immediately is changing throughout the mission due to boil-off and/or use in vehicle maneuvers.

The advantage of using the theoretical model in Figure 1.1a is that it provides a simple and convenient method for determining the boil-off rate (via Equation 1.1), which can easily be incorporated into the vehicle sizing process. While use of simplified models early in the design process allows for quick evaluation and greater flexibility when conducting trade studies, the fidelity of the analysis is generally very low [45, 133]. Historically, the uncertainty surrounding early estimates is reduced through higher fidelity numerical simulations and system testing as the design process proceeds. However, for complex vehicles that display a high degree of coupling between the subsystems, increasing analytical fidelity in the conceptual design phase is highly desirable, as many of these interactions are not captured by lower fidelity analyses [133].

Figure 1.2 depicts the traditional aircraft design process, but it applies equally well to in-

space vehicles. Initially, the knowledge about the design is minimal. As the design process proceeds, the design knowledge slowly increases as information from higher fidelity analyses becomes available, yet the freedom to make changes in the design decreases rapidly and the cost committed is locked in relatively early. The overall goal is to incorporate information from higher fidelity analyses earlier in the design process so that more informed decisions can be made sooner, rather than at a point where the opportunity to make major design changes is limited [107]. In this case, utilizing the lower fidelity theoretical model in the vehicle sizing process results in oversized vehicles due to the conservative nature of the model. This acts to artificially shrink the design space. The uncertainty introduced by the model can be reduced by increasing the fidelity in the boil-off rate, which will then open up the design space.

At the conceptual stage, additional fidelity in the boil-off rate is typically achieved by improving the estimate of $\dot{Q}$ in Equation 1.1. Honour et al. [80] presented a thermally optimized propellant depot concept capable of achieving extremely low boil-off rates (< 0.05 %/day) in LEO through a combination of sun shields and a strategically selected spacecraft orientation. A computer-aided design (CAD)-based thermal model of the depot was developed using Thermal Desktop. Thermal analysis included heat transfer contributions from the thermal environment – which consisted of solar radiation, albedo, Earth and deep space infrared radiation (IR) – the spacecraft orientation, and the optical properties of the sun shields and propellant tanks. The thermal loads on the LOX and LH_2 tanks, and the corresponding boil-off rates, were evaluated for several combinations of spacecraft beta[3] ($0^\circ \leq \beta \leq 30^\circ$) and theta[4] ($-10^\circ \leq \theta \leq 10^\circ$) angles. The optimal orientation for the depot was selected based on the beta and theta angles that produced the minimum total propellant boil-off per day for the system.

Trade studies conducted by Perrin and Casler [124] and Chai and Wilhite [30] investigated the number of MLI layers that would minimize the mass penalty (MLI mass plus

[3] Angle between the orbital and ecliptic planes

[4] Angle between the spacecraft minor axis and the ecliptic plane

boil-off) to the spacecraft. While it is true that the boil-off rate decreases with an increasing number of MLI layers, there is point of diminishing returns. Perrin and Casler used the Modified Lockheed Model [73] to determine the heat that penetrated the MLI and entered the propellant tank. The model calculates the heat transfer due to radiation between each layer of MLI, and the solid and gas conduction through the spacer material located in between the layers. Chai and Wilhite utilized an analytical one-dimensional model developed by NASA's Marshall Space Flight Center, which uses the same heat transfer mechanisms to determine the heat load through the MLI. In addition to the heat load through the MLI, the thermal analysis of the propellant tank also included heat transfer from the tank support structure and penetrations, as well as parasitic heat loads. In both studies, the thermal analysis was performed across a varying number of MLI layers. The resulting thermal load on the propellant tank was then used to calculate the boil-off rate, estimate the propellant losses, and determine the combined mass of the MLI and boil-off.

While there is certainly value in improving the estimate of $\dot{Q}$ entering the tank, it does very little to improve the fidelity of the boil-off rate since the model being used to represent the boil-off process (Figure 1.1a and Equation 1.1) remains unchanged. Several parametric studies by Schaffer et al. [138, 139] characterized the impact of using a varying, versus a constant boil-off rate, when sizing a crewed Mars LOX/LH_2 vehicle requiring a total storage time of 750 days (200 days in transit, 550 days in Mars orbit). The vehicle was sized across a range of propellant mass fractions (PMFs) (0.75 - 0.95) and boil-off rates (0.00 %/day to 0.05 %/day, in increments of 0.01 %/day[5]), where the boil-off rates represented the losses at the beginning of the mission when the propellant tanks were fully loaded.

In the baseline (constant) case, the boil-off rate was held constant throughout the mission. In the alternative (varying) case, the boil-off rates decreased each day as the amount of propellant in the tank decreased[6]. The authors noted that: (1) for missions with long transit times (months or years), vehicles utilizing cryogenic propellants are very sensitive

[5]Increments in [139] were 0.00 %/day, 0.001 %/day, 0.01 %/day, 0.025 %/day, and 0.05 %/day

[6]Boil-off rate measured as percentage of fully loaded tank that evaporates each day

to changes in the boil-off rate since boil-off represents a major fraction of the total vehicle mass; (2) for the baseline case, a combination of high boil-off rates and low PMFs caused the vehicle mass to quickly spiral out of control and become infeasible; (3) for the alternative case, the vehicle was less sensitive to changes in the boil-off rate, which allowed the vehicle to close for all combinations of PMF and boil-off rates considered.

The results of these studies show that not only do vehicles incorporating cryogenic propellants have the potential to be sensitive to small changes in the boil-off rate, but also that there are implications for sizing a vehicle assuming the boil-off rate is constant, when in fact it is not. Bear in mind that Schaffer et al. implemented a boil-off rate that decreased with time, whereas texts [112] and experiments on cryogenic tanks [5, 6] support the opposite. This further supports the need to increase the fidelity in the boil-off rate so as to properly identify the design space.

This has become especially important with the upcoming lunar missions. NASA has baselined cryogenic propellants for use in future architectures to support the Artemis Program [70]. Yet studies are still ongoing in order to determine which propellants – LOX/LH_2, LOX/LCH_4, or MMH/N_2O_4 – will provide the best performance while minimizing the impact to the vehicle mass [35]. The propellant selection affects the vehicle mass through the propellant mass requirements, the size of the propellant tanks, and the mass of the passive and/or active systems to mitigate boil-off. Given the different properties of the propellants, each of these factors is affected to varying degrees [35]. Without a firm grasp of the design space, a thorough evaluation of the cryogenic propellant options cannot be conducted.

To increase the fidelity in boil-off rate estimates, the current representation of the boil-off process must be transitioned from the theoretical model (Figure 1.1a) to one that includes more physical effects (Figure 1.1b). This will allow for a more accurate determination of the heat transfer responsible for boil-off of the liquid propellant – $\dot{Q}_{evap}$ in Equation 1.7. Modeling and analysis of cryogenic propellant tanks dates back as early as the Saturn V era [24, 155]. Models focus on predicting the pressure and/or temperature in the tank

based on analysis of the heat and mass transfer that occur between the various regions. Numerous models exist in the literature, and models vary widely in the approach and degree of fidelity used to analyze the tank.

The advantages and limitations of several notable models are investigated in a formal literature review, with the goal of identifying a suitable replacement for the theoretical model the is currently used in the conceptual design process. The results from the literature review will show that given the longer durations anticipated in future missions, the tank will undergo multiple cycles of pressurization and pressure release; in order properly analyze the tank, the model must have the ability to model the effects due to a pressure control device [22]. This represents a new paradigm, and relatively few models in the literature are capable of doing so. Three state-of-the-art models that include the necessary pressure control capability are considered as potential replacements for the theoretical model. However, the these models are best suited for use once the design space has been narrowed down and there is more turnaround time between design iterations. Following these observations, a technical approach is formulated regarding the development of a cryogenic propellant tank model capable of providing boil-off estimates with greater fidelity than is provided by the current model, while maintaining a quick evaluation time.

1.4 Dissertation Objective and Document Outline

The primary motivation for this research is the high degree of uncertainty surrounding early estimates of propellant losses due to boil-off and the resulting impact on the vehicle design space. The current method for estimating boil-off assumes that the heat entering the tank goes directly toward evaporation of the propellant, where the rate of the evaporation (the boil-off rate, in kilograms per unit time) is equal to the heat transfer rate to the tank divided by the enthalpy of vaporization of the propellant. This method has the tendency to significantly overestimate the boil-off rate, and thus the propellant losses, due to the simplicity and correspondingly low fidelity of the model representing the boil-off process.

The uncertainty in the propellant losses is then propagated throughout the vehicle during the sizing process via the propellant mass requirements, resulting in oversized vehicles and artificial reduction of the design space.

The objective of the work presented here is to increase the fidelity of the boil-off rate through the development of a model that includes more of the physical processes responsible for the boil-off phenomenon. Increasing the fidelity in the boil-off rate will more clearly define the vehicle design space, and thus allow for better design, analysis, and trade studies of cryogenic in-space vehicles during the conceptual phase of the design process. Efforts will focus on LH_2, since it is the most problematic of the cryogenic propellants with respect to boil-off.

Research Objective: To improve conceptual design and analysis of cryogenic in-space vehicles by providing more accurate propellant mass estimates through the development of a higher fidelity boil-off model.

The remainder of the dissertation is organized as follows:

- Chapter 2 provides a brief introduction of the fundamental concepts regarding cryogenic fluid behavior during long-term storage.
- Chapter 3 summarizes the notable cryogenic propellant tank models in literature; observations provide motivation for the research objective, as well as the identification of the requirements and technical approach for the development of the model.
- Chapter 4 details the formulation of the model, including the heat and mass transfer during the self-pressurization and pressure control phases and modifications to account for thermal stratification in the ullage and bulk liquid regions.
- Chapter 5 presents research questions, hypotheses, and proposed experiments for evaluating the ability of the model to predict boil-off during the self-pressurization and pressure control phases of the mission.
- Chapter 6 demonstrates the benefits of incorporating higher-fidelity boil-off estimates in the vehicle sizing process by comparing the results obtained using the new boil-off model with those obtained using Equation 1.1.
- Chapter 7 contains the conclusions and contributions of this research and recommendations for future work.

CHAPTER 2

CRYOGENIC FLUID BEHAVIOR DURING LONG-TERM STORAGE

This chapter provides an introduction to the fundamental concepts regarding the behavior of cryogenic propellants during periods of long-term storage in normal gravity or in settled conditions. Section 2.1 presents terms and definitions that are commonly used to describe systems consisting of a cryogenic liquid and its vapor. Section 2.2 discusses the physics of the phase-change process that occurs within a cryogenic propellant tank subject to external thermal load, with the presumption that the propellant and vapor coexist in equilibrium. Section 2.3 breaks away from the equilibrium condition and introduces several physical phenomena that occur in the tank during storage.

2.1 Terms and Definitions

Pure substance	"A substance or mixture that has a fixed chemical composition throughout; homogeneous. This extends to a mixture of two or more phases of the same substance (e.g. water and ice)." [29]
Subcooled liquid	"A liquid that exists below the boiling point." [29]
Saturated liquid	"A liquid that exists at the boiling point." [29]
Saturated vapor	"A vapor that exists at the boiling point." [29]
Superheated vapor	"A vapor that exists above the boiling point." [29]
Saturated liquid-vapor mixture ...	"A mixture of liquid and vapor that exist in equilibrium at the boiling point." [29]

Saturation temperature, T_{sat} ..... "For a specified pressure, the temperature at which a pure substance undergoes a phase change." [29]

Saturation pressure, P_{sat} ..... "For a specified temperature, the pressure at which a pure substance undergoes a phase change." [29]

Triple point ..... "The pressure and temperature at which a solid, liquid, and vapor co-exist in equilibrium." [29]

Critical point ..... "The greatest pressure and temperature at which a saturated liquid and vapor can co-exist." [29]

Vapor pressure, P_v ..... "For a system containing a cryogenic liquid, its corresponding vapor and one or more gases, this is equivalent to the partial pressure of the liquid vapor. For a system consisting of the liquid and vapor alone, the vapor pressure is equivalent to the system pressure." [131]

Liquid vapor pressure, P_l ..... For a cryogenic liquid, this is the pressure of its corresponding vapor if the two were in equilibrium [73].

2.2 Behavior of a Pure Substance in Equilibrium

Recall from Chapter 1 that the theoretical model utilized in the conceptual design process for estimating propellant losses assumes that, with the exception of the mass transfer process that occurs at the interface, the tank is at steady state. Steady state conditions require that the ullage and bulk liquid are at same temperature and that the tank pressure is con-

stant. These conditions are indicative of a system consisting of a saturated liquid and a saturated vapor in equilibrium.

How the conditions in the tank change during the boil-off process is best understood with the aid of a property diagram. The relationship between the pressure, temperature and specific volume v of a pure substance in equilibrium can be represented by a surface in three dimensions, as shown by the central diagram in Figure 2.1. All points on the surface represent equilibrium states; all states along the path of a quasi-equilibrium process lie on the PvT surface, since such a process must pass through equilibrium states [29]. The surfaces outlined in blue represent regions in which two phases – liquid-gas, solid-gas, and solid-liquid (abbreviated S-L) – coexist in equilibrium. The surfaces outside the blue regions represent areas in which a single phase – gas, liquid, or solid (abbreviated G, L, and S, respectively) – exists. The critical point for the system is represented by point C, located at the apex of the liquid-gas region. The line formed by points A and B, the "triple line", represents the conditions for which all three phases co-exist. These states are characterized by the same pressure and temperature, but have different values for the specific volume [55].

Because of the difficulty involved when visualizing and developing these surfaces, the data is typically viewed using a 2D version of the diagram, which is obtained by projecting the 3D surface onto the PT and/or Pv planes [55]. The PT diagram resulting from the projection of the surface onto the PT plane is depicted immediately to the left of the PvT surface in Figure 2.1. For a pure substance in equilibrium, the number of independent intensive variables required to specify the thermodynamic state is three minus the number of phases present in the system. For the triple line, consisting of three phases, zero intensive variables are required since the state can only exist at a single temperature and pressure. For this reason, the projection of the triple line onto the PT plane results in a single point, the triple point. For each of the two-phase regions on the PvT surface, only a single intensive variable is required, either P or T; once one of these variables is known, the other is

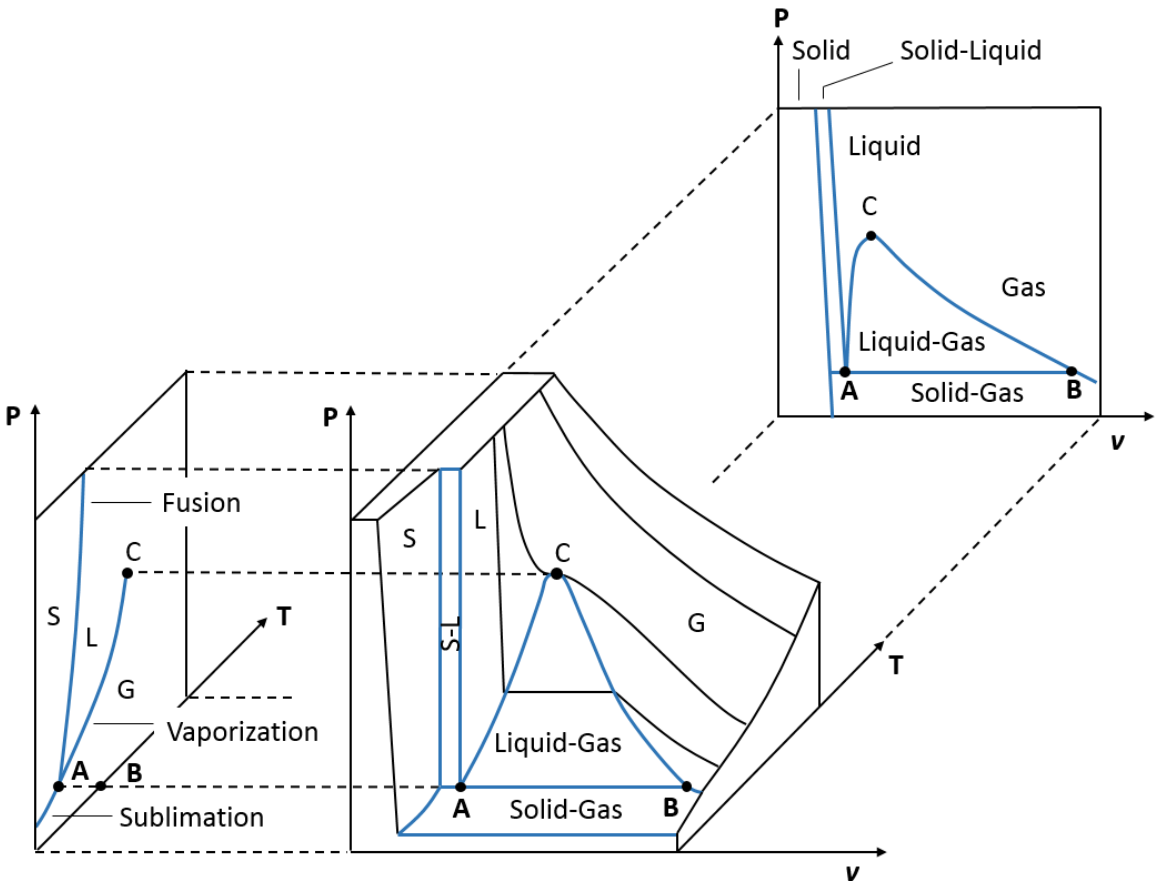

Figure 2.1: PvT surface and the projections onto the PT and Pv planes (adapted from [55]).

automatically specified. Therefore, the two-phase regions project as lines, which represent the various phase change processes – fusion (from projection of the solid-liquid region), vaporization (via the liquid-gas region), and sublimation (via the solid-gas region) – which meet at the triple point [29, 55].

The PT diagram does not provide any information regarding the scale of the system. This information is, however, given explicitly by the Pv diagram. As shown by the diagram in the upper right hand corner in Figure 2.1, all surfaces in the 3D diagram project as areas on the PV plane [55]. The liquid-gas region is presented in more detail in Figure 2.2. Line AC denotes the Pv values for which a saturated liquid exists, and similarly for line CB with respect to a saturated vapor. The area enclosed by the curve ACB represents the two-phase region where the saturated liquid and vapor co-exist at equilibrium.

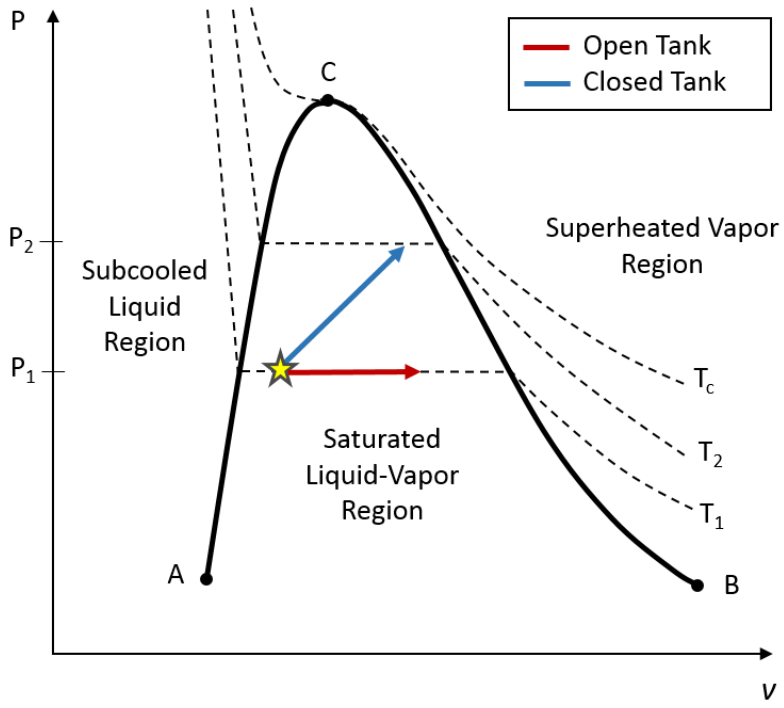

Figure 2.2: Pv diagram (adapted from [29]).

The dashed lines, denoted by T_1, T_2, and T_c, represent isotherms. Isotherms below the critical point have a distinctive horizontal segment that passes through the two-phase region, since saturated liquid-vapor mixtures exist at a constant P and T. Points along this horizontal line represent the proportions of liquid and vapor in the system, ranging from all liquid at the left to all vapor at the right. The horizontal line segments become progressively shorter as the temperature increases, until the critical point is reached.

The area to the left of line AC corresponds to the subcooled liquid region. The portions of the isotherms in this region are very steep since liquids are not very compressible. That is, a large pressure change is required in order to impart a small change in the volume of the liquid. The portions of the isotherms located to the right of line AB lie in the superheated vapor region. The isotherms in this region present slopes that are more gradual since gases are much more responsive to changes in pressure [29, 55].

Returning now to the theoretical model, depicted in Figure 1.1a, the system formed by the liquid propellant and its corresponding vapor is that of a single component, two-

phase system in equilibrium (i.e., a saturated liquid-vapor mixture) that is undergoing a phase change process. This system is represented by the star in Figure 2.2, with a notional state defined by P_1 and T_1. Initially, the tank is predominantly full and contains a small amount of vapor. As heat enters the tank and the propellant boils-off, the tank pressure is maintained through the open vent. During the evaporation process, the system works its way to the saturated vapor line along the path described by the red arrow in the figure, all the while maintaining a constant pressure P_1 and temperature T_1.

An alternative model utilized in literature assumes that the tank is closed; as the propellant evaporates, the temperature and pressure both increase, through it is presumed that the liquid and vapor continue to exist as a saturated mixture [5]. This system follows the path outlined by the blue arrow in Figure 2.2. For the same initial state, the tank pressure and temperature increase from P_1 and T_1 to P_2 and T_2, respectively.

For the alternative model, the conditions in the tank – pressure, temperature, and the relative amounts of liquid and vapor – during and at the end of the storage period are determined either through direct measurement of the contents within an actual physical tank or, if a tank is not available, through a theoretical or computational analysis of the system (this topic is covered in more detail in the next chapter). For the theoretical boil-off model, the state is always known, since the pressure and temperature remain constant during the evaporation process, and thus throughout the storage period, with the amounts of liquid and vapor provided by Equation 1.1. This further demonstrates the simplicity of the theoretical model and how it allows for a quick evaluation of the boil-off losses based on a single pressure and/or temperature value for the tank.

In reality, the heat that enters that tank produces behaviors that are determined by the fluid properties in each region, as well as a variety of other factors. The ullage and bulk liquid are no longer in equilibrium; the ullage exists as a superheated vapor, the bulk liquid is subcooled, and the two are separated by a saturated interface, with a temperature that is related to the tank pressure via $T=T_{sat}(P_g)$. The next section introduces several nonequilib-

rium fluid behaviors, with an emphasis placed on systems composed of LH_2 and its vapor (GH_2).

2.3 Fluid Behavior During Periods of Storage and Pressure Control

Numerous experimental, analytical, and numerical analyses have been conducted in order to fully understand the exact mechanisms responsible for the fluid behavior during periods of storage and pressure control [16, 69]. Given that theoretical and computational models vary in levels of sophistication in how they interpret and predict these behaviors, this section will focus on providing an overview of the processes responsible and the primary factors that influence them, where applicable.

2.3.1 Thermal Stratification

In the absence of mixing, a closed cryogenic tank subject to an external thermal load will experience thermal stratification. For in-space vehicles utilizing cryogenic propellants, thermal stratification of the liquid is problematic for several reasons. If the warmer propellant is introduced into the propellant feed system, it can lead to pump cavitation, which can adversely affect performance or, worse, result in the loss of the mission and/or vehicle [4, 147]. In addition, the temperature at the interface greatly influences the tank pressure, which is higher when thermal stratification is present than if the liquid were thoroughly mixed. In the case of liquid hydrogen, a temperature increase in 0.5 K at the interface represents an approximate 20 kPa increase in the tank pressure [34, 141]. This greatly reduces the time before venting is required and the time between successive venting events.

Thermal stratification in the ullage occurs as a result of the buoyancy force acting on the fluid. The gas in contact with the tank wall becomes heated and rises to the top of the tank, whereas the cooler denser gas falls to the bottom of the ullage region, near the interface. Thermal stratification in the bulk liquid is predominately due to the fluid motion that results at the vertical portion of the tank wall during heating. Due to convective flow along the side walls of the tank, the lighter warmer fluid moves upward along the tank wall

and to the upper portion of the liquid. From there the warmer liquid is distributed along the interface, which causes a warm thermal layer to develop and that continues to increase in thickness with time [34, 51].

For a given tank, the primary factors affecting thermal stratification are the heat transfer rate to the tank, the location at which the heat is applied, and the amount of propellant in the tank [5, 147, 150]. Thermal stratification increases with the heat transfer rate to the tank. For the bulk liquid, the temperature difference between the liquid at the interface and the liquid at the bottom of the tank is limited to a few degrees, depending on the properties of the propellant. For liquid nitrogen, hydrogen, and helium, this can be as little 1 K and as much as 15 K [51]. In the ullage region, the temperature difference can be much greater and is typically bound by the maximum operating pressure of the tank or the maximum pressure limit designated by the pressure control device employed. Figure 2.3 depicts thermal stratification in the LH_2 tank of the S-IVB upper stage during an orbital experiment to verify the engine restart capability. As can be seen from the figure, the temperature difference was approximately 3 K (5 °R) in the bulk liquid and 100 K (177 °R) in the ullage region.

Figure 2.4 depicts the effect of the amount of propellant in the tank, or propellant fill level (FL, % by volume), on thermal stratification. For the ullage region, as the fill level decreases, a larger portion of the tank wall becomes exposed. This increases the amount of gas that gets heated, and thus causes the temperature gradient across the region to increase [5, 152]. For the tank depicted in Figure 2.4, the temperature variation in the ullage region increased from 16 K, to 25 K, to 30 K when the propellant fill level was decreased from 83%, to 49%, to 29%, respectively.

The effect of propellant fill level on thermal stratification in the bulk liquid is not as straightforward. As previously discussed, thermal stratification in the liquid region is a result of convective fluid motion at the vertical tank wall during heating; the heat transfer at the bottom of the tank contributes very little to the effect. This has implications with

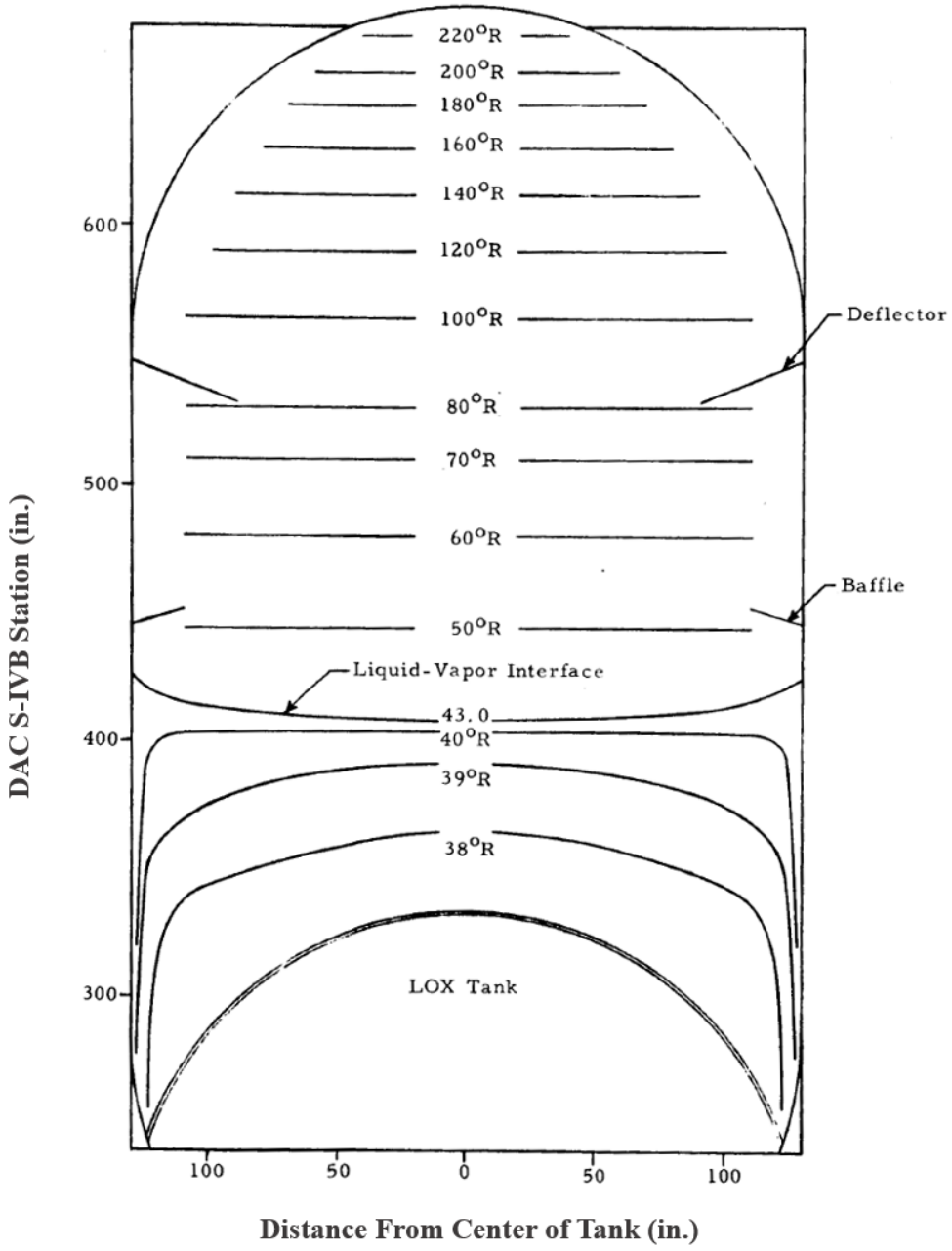

Figure 2.3: Thermal stratification in the LH_2 tank of the S-IVB upper stage during the closed tank experiment on the AS-203 flight [155].

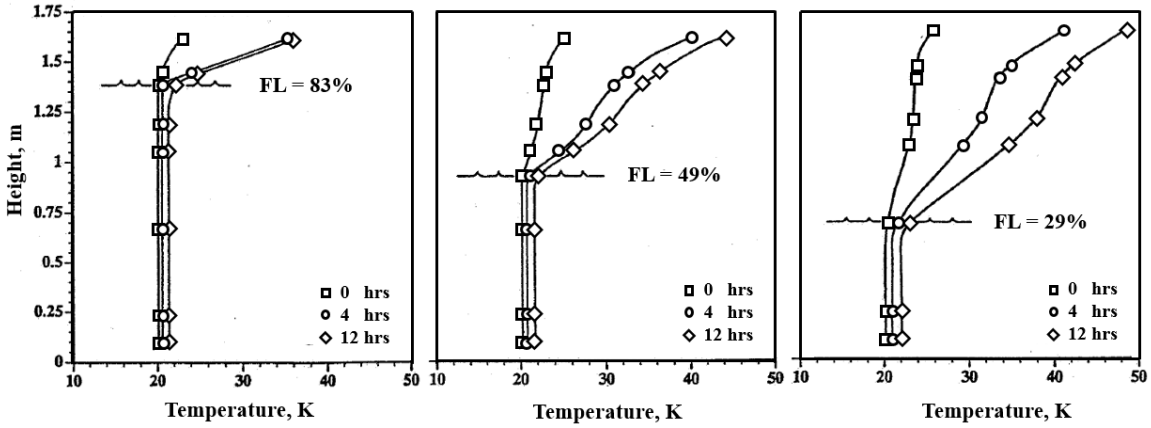

Figure 2.4: Temperature distribution measured near the vertical tank axes for different propellant fill levels in a 4.89 m^3 oblate spheroidal tank, subject to a heat flux of 2.0 W/m^2 [150].

respect to tank geometry – cylindrical tanks will display a greater amount of thermal stratification than spherical tanks [51]. In Figure 2.4, thermal stratification in the bulk liquid, or lack thereof, is due to a combination of the low heat transfer rate to the tank, the large tank volume, and the tank shape – an oblate spheroid, or Earth-shaped – though some stratification near the interface can be observed at each propellant fill level for later test times (at the 12 hour mark).

2.3.2 Self-Pressurization

Self-pressurization refers to the pressurization of a closed tank due evaporation of the liquid propellant [69]. The self-pressurization rate of cryogenic propellant tanks has been the subject of many investigations within the space community since the 1960s, as the rate has important design consequences with respect to the propellant lifetime as well as the selection of the thermal management approach and the pressure control method utilized. [13, 69, 96]. The pressurization rate is governed by the heat transfer between the ullage gas and the interface, which drives the rate of evaporation of the liquid propellant. This heat transfer process is complicated by the combined effects of thermal stratification, the propellant fill level, and the tank geometry [5, 96, 150].

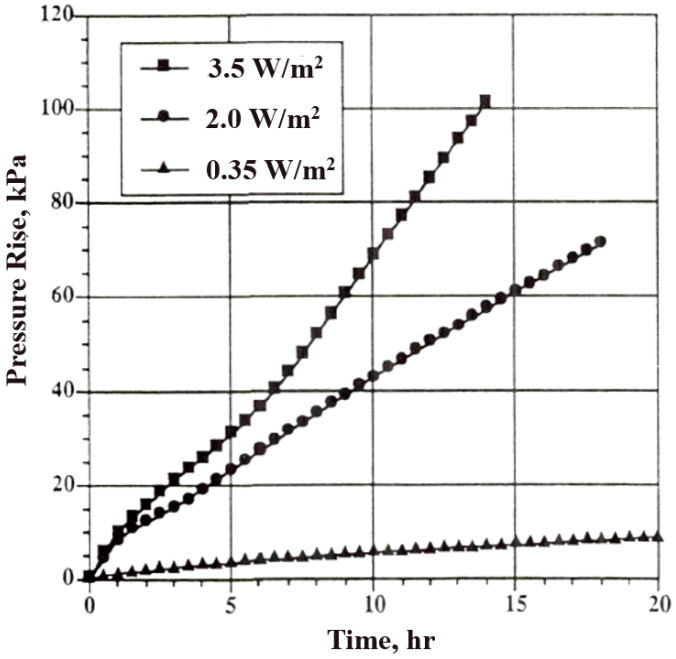

Figure 2.5: LH_2 tank pressures (measured relative to the initial tank pressure) for a propellant fill level of 83%, and heat transfer rates of 3.5 W/m^2, 2.0 W/m^2, and 0.35 W/m^2 [71].

The pressurization rate is typically characterized by an initial transient followed by a period in which the tank pressure continues to increase at a uniform rate [5, 71, 150], as shown in Figure 2.5. The transient is due the initial period of heat transfer within the tank, where the convective fluid motion causes thermal stratification to develop in each of the ullage and bulk liquid regions. Once the initial transient has passed, the flow field and temperature field in each region are fully developed, resulting in a stationary temperature field. While the temperature in each region will continue to increase with time, since the temperature gradient is now constant, the temperature at any given location within the tank will rise at the same rate. Since the pressurization rate is a result of the evaporation due to the net heat transfer from the gas-side to the liquid-side of the interface (this process is discussed in more detail in Section 2.3.4), once the temperature gradient is fully developed, the tank pressure will increase at a uniform rate [13].

While the exact mechanisms responsible for the behavior in the tank pressure during

storage are still under investigation, the individual effect of several factors has been established in literature. The effect of the heat flux rate on the pressurization rate can be seen in Figure 2.5. As the heat flux rate increases, so too does the pressurization rate; simply put, increasing the heat input to the to ullage and bulk liquid regions further increases the heat transfer at the interface, thus increasing the amount of evaporation and the tank pressure [5]. Another factor affecting the pressurization rate is the amount of propellant in the tank. For spherical and cylindrical tank geometries, the pressurization rate increases with the amount of propellant in the tank; at high propellant fill levels, the additional mass added to the small volume of the ullage space during evaporation has a much larger impact on the tank pressure than at lower fill levels with larger ullage volumes [5, 72]. Of the two effects – the heat transfer rate and the amount of propellant in the tank – the latter has a greater influence on the tank pressurization rate [5].

2.3.3 Depressurization

Design constraints regarding the tank's maximum operating pressure makes controlling the tank pressure a necessity. Depressurization of the tank has traditionally been achieved through direct venting of ullage space. While venting relieves the ullage pressure, it can cause bulk liquid boiling or result in a collapse of the ullage space (these behaviors are discussed in more detail in Sections 2.3.4 and 2.3.5). Further, this method is an inefficient means of pressure control which can result in large propellant losses [75].

Alternative methods, such as mixing, are being investigated for use in longer missions. NASA has tested two different mixing strategies, where the subcooled bulk liquid is extracted and reinserted into the tank in the form of a spray to induce mixing [74]. In the first concept, depicted in Figure 2.6a, the spray is introduced back into the bulk liquid region through an axial jet located at the bottom of the tank. The circulation from the spray causes destratification of the bulk liquid. By removing the warm thermal layer at the interface, the much cooler bulk liquid is exposed to the ullage. This removes the heat from the region,

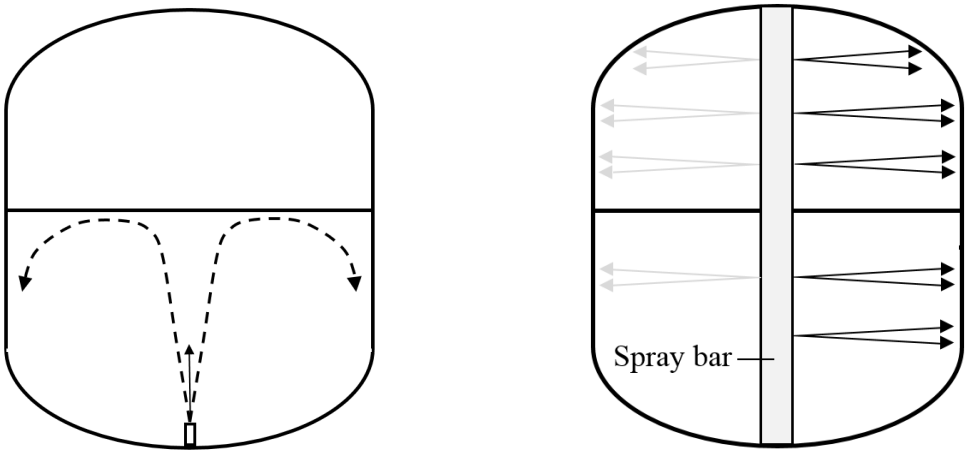

Figure 2.6: Mixing strategies for (a) axial jet [22] and (b) spray bar [72] TVS concepts.

causing the gas near the interface to condense and fall under the force of gravity into the bulk liquid. The combined removal of heat and mass from the ullage space causes the tank pressure to decrease [22].

In the second concept, shown in Figure 2.6b, the subcooled liquid is sprayed radially into both the ullage and bulk liquid regions through a vertical bar located along the longitudinal axis of the tank. A portion of the spray remains in the ullage while the remainder falls back into the bulk liquid. The spray droplets that remain in the ullage warm up to saturation conditions and evaporate. Since evaporation is an endothermic process, the energy required to evaporate the droplet is drawn from the nearby gas, which results in a temperature and pressure reduction of the ullage region [72].

With both mixing strategies, the overall result is a decrease in the tank pressure from destratification due to mixing. With a sufficient thermal management approach, mixing may be enough to maintain the tank pressure for missions ranging from a few days to weeks [75]. However, at some point the liquid will absorb an amount of heat such that the temperature of the liquid will increase enough that mixing will no longer be effective, and the tank will have to be vented [72, 75].

2.3.4 Boiling

2.3.4.1 Evaporation

Recall from Section 2.3.1 that heat transfer from the tank wall to the bulk liquid causes warm convection currents to develop along the vertical portion of the tank wall. The warmer fluid, which is slightly superheated by the heat transfer [23], rises to the surface and is distributed along the interface. Once at the surface the heated liquid evaporates, as shown in Figure 2.7. The amount of evaporation that occurs is determined by Equation 1.7, where $\dot{Q}_{evap}$ represents the heat transfer from the ullage to the bulk liquid.

The heat transfer between the two phases occurs through the saturated interface, which is warmer than the subcooled bulk liquid beneath it but cooler than the superheated gas above it. Therefore the heat transfer responsible for evaporation is the net heat transfer through interface, as depicted in Figure 2.8a, where $\dot{Q}_{gs}$ is the heat transfer from the ullage to the top side of interface, and $\dot{Q}_{ls}$ is the heat transfer that leaves through the bottom side of the interface and enters the bulk liquid.

With time, as thermal stratification develops, the warm thermal layer that accumulates at the surface increases in thickness and acts to facilitate evaporation by reducing the heat transfer through the bottom side of the interface [14]. This effect is depicted in Figure 2.8b, where the thermal layer is represented by the orange band at the interface. This layer, which is exaggerated in the figure, is on the order of a few millimeters in thickness [23]. Based on the tank pressures observed for several self-pressurization experiments in literature, the amount of time before the temperature gradient becomes constant, that is, the time for thermal stratification and hence the liquid layer to fully develop, increases with tank capacity. This occurs because large liquid volumes take longer to respond to the thermal input to the region [5, 6, 72, 150]. This demonstrates the benefits of utilizing a mixer for the purposes of depressurization, rather than direct venting, since venting can leave the thermal layer in tact while mixing destroys the layer, thus reducing the amount of evaporation that occurs.

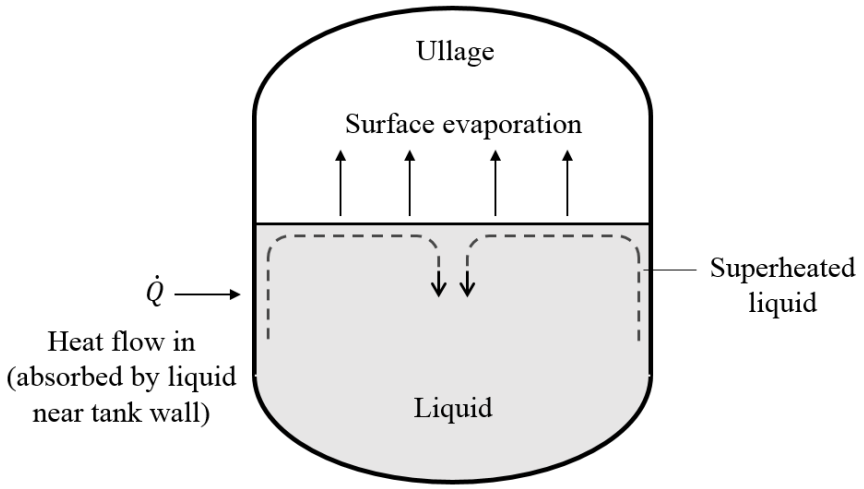

Figure 2.7: Convection current created from heating of the liquid propellant near the tank wall. The warmer fluid is carried to the surface, where it evaporates. (Adapted from [23].)

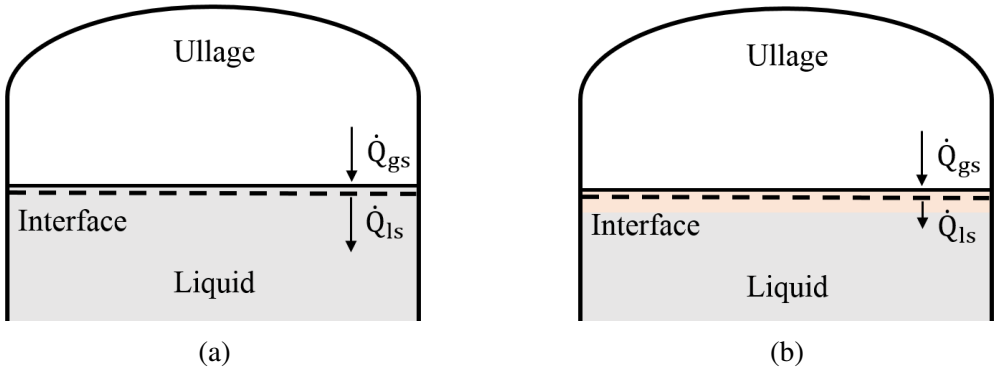

Figure 2.8: The net heat transfer across the interface (a) without and (b) with the presence of a liquid thermal layer.

2.3.4.2 Boiling at the Tank Wall

Boiling at the tank wall is the result of convective heat transfer from the warmer tank wall to the subcooled bulk liquid. If the heat transfer is large enough, the liquid reaches the saturation temperature and begins to boil. For LH_2 systems, this phenomenon has been experimentally observed for heat flux rates above 100 W/m^2 at atmospheric pressure [26]. For lower heat flux rates, boiling can occur at hot spots that develop on the tank wall due to conduction from the tank support structure [71, 113].

A detailed discussion of the mechanism responsible for this boiling process is presented by Lienhard [94]. However, the basic principles of this fluid behavior can be briefly summarized as follows: for a heated surface that is completely submerged in a saturated liquid, the type of boiling that occurs is a function of the heat flux $\dot{Q}/A$ from the surface and the temperature difference ΔT between the surface (the tank wall, at temperature T_w) and the saturated liquid (at temperature T_{sat}), as illustrated in Figure 2.9. For small temperature differences, the heat transfer results in evaporation, which was described in the previous section. As the temperature of the surface increases, small bubbles begin to form on the surface and grow as the heating process continues to add evaporated liquid to the bubble. This corresponds to the nucleate boiling regime in Figure 2.9.

Eventually, the difference in the density of the vapor bubble and the density of the surrounding liquid causes the bubble to break free from the surface, rise through the liquid, and reach the interface. If the temperature of the surrounding bulk liquid is below T_{sat} (the liquid is subcooled), the bubbles may collapse before reaching the interface, and the net vapor generation is zero [10, 78]. If the vapor bubbles reach the surface, they contribute to the pressure rise in the tank. For this reason, the support structure surrounding the tank uses a few contact points as possible, and utilizes low conductive materials in order to reduce the heat transfer to the tank [44, 113].

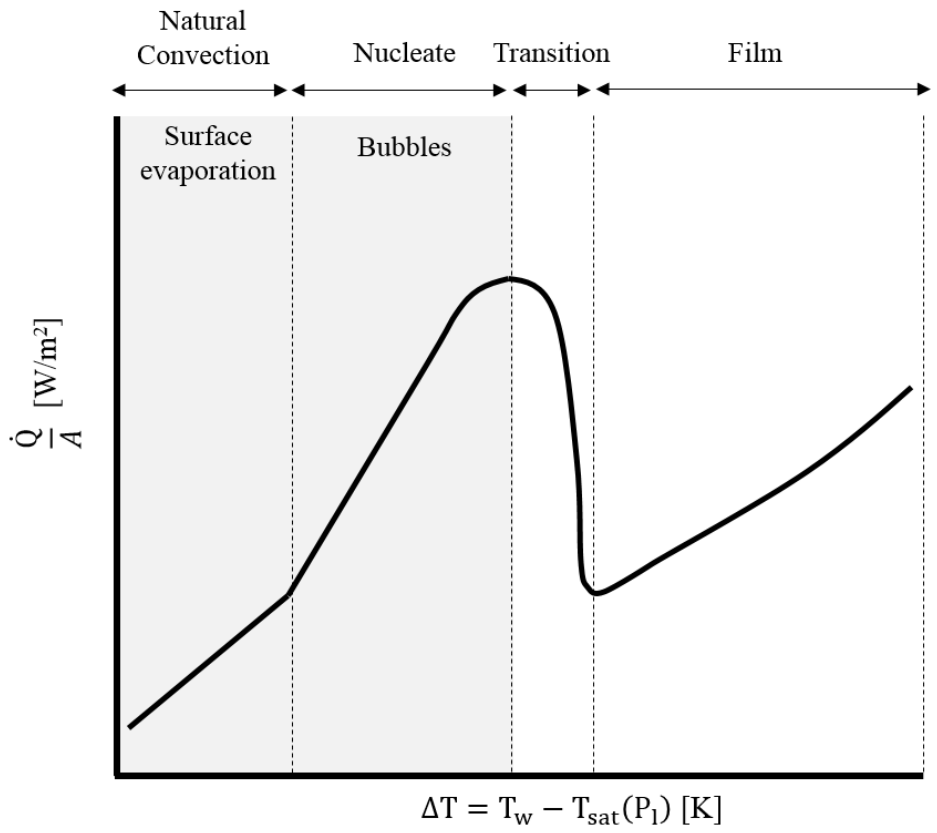

Figure 2.9: Typical boiling characteristic curve consisting of free convection evaporation, nucleate, transition, and film boiling regions (adapted from [10]). The shaded regions denote the types of boiling typically encountered in cryogenic propellant tanks during nominal operations.

2.3.4.3 Bulk Liquid Boiling

Bulk liquid boiling occurs as a result ofheat transfer to the interior or "bulk" of the liquid propellant and/or a pressure drop in the tank. In the first scenario, the temperature of the propellant rises due to a combination of (1) liquid heating at the bottom of the tank, which results in uniform heating rather than stratification, and (2) the addition of warmer fluid to the interior of the region from convection currents [23, 147], as shown in Figure 2.7. If the temperature of the propellant reaches the saturation temperature corresponding to the tank pressure $T_l = T_{sat}(P_g)$, the propellant will spontaneously boil in large volumes [36]. The same phenomena occurs during the venting process if the tank pressure drops below

the vapor pressure of the bulk liquid, $P_g < P_l$ [21]. If depressurization is slow, evaporation from the interface interface may be sufficient to maintain the ullage pressure above the liquid vapor pressure. However, if venting occurs rapidly, the tank pressure will drop below the liquid vapor pressure and cause superheating of the bulk liquid [17, 19].

The energy for this boiling process is drawn from the surrounding liquid, which causes cooling of both the ullage and the bulk liquid regions. The decrease in the temperature of the bulk liquid can then trigger boiling at the tank wall by increasing the temperature difference (and thus heat transfer) between the tank wall and liquid [22]. Information in the literature is sparse regarding how often the above conditions are met and how to mitigate the resulting effects.

2.3.5 Condensation

The last of the fluid phenomena covered in this chapter is that is of condensation. There are two types of condensation that can occur within a cryogenic propellant tank: film condensation and homogeneous condensation. The first form of condensation is the most prevalent within the tank, and occurs when the ullage gas (saturated or superheated) comes into direct contact with a surface that has a temperature that less than the saturation temperature of the gas, $T_{surface} < T_{sat,g}(P_g)$ [10]. This is the method utilized by the axial jet in Section 2.3.3 to condense the gas near the interface; before mixing, the interface is saturated, with a temperature corresponding to the tank pressure, $T_s = T_{sat}(P_g)$, where the subscript 's' denotes the the interface. Once mixing is initiated, the warmer liquid at the interface is replaced by the subcooled liquid from the interior, which is at a temperature less than the saturation temperature of the ullage and thus induces condensation.

Homogeneous condensation occurs when a rapid pressure drop – such as during engine operation when the propellant is being expelled from the tank, or during venting – causes the temperature and therefore the density of the gas to decrease. The gas within the ullage then spontaneously begins to condense, forming a fog within the region [3, 42]. If the

condensation is severe enough, it can result in ullage gas collapse, that is, there will not be enough pressure to maintain the tank structure. During engine operation, this scenario is avoided by introducing a pressurant, typically a noncondensable gas, into the tank [41, 131]. During venting operations, when gas is being expelled rather than introduced into the tank, it is unclear from the open literature which limits are applied to either the depressurization rate or the minimum pressure that must be maintained in order to prevent excessive condensation and avoid ullage collapse altogether.

CHAPTER 3
LITERATURE REVIEW

There are numerous cryogenic propellant tank models available in open literature. Models vary widely in their approach and the degree of fidelity used to analyze the heat and mass transfer that occur within the tank. Some models focus entirely on the physical processes that occur in the ullage [63, 79, 95, 101, 135], while others include both the ullage and the bulk liquid [5, 72, 98, 99], and there are the remainder that include all three regions – the ullage, the bulk liquid, and the interface – in the analysis [12, 22, 36, 102, 121, 131].

The goal of the literature review that follows is to identify a propellant tank model with an appropriate balance of complexity and accuracy such that the fidelity in boil-off estimates is improved, while maintaining a quick evaluation time. The selected model can then serve as a replacement for the one that is currently used in the conceptual design process (Equation 1.1 and Figure 1.1a). Unfortunately, the primary objective of propellant tank modeling and analysis is to predict how the pressure and/or temperature within the tank change with time; while the boil-off process is included in the modeling effort, there are relatively few research efforts in literature that publish boil-off as part of the results. This creates a bit of a dilemma, since the boil-off predicted by any potential candidate model is unavailable and thus cannot be compared with the boil-off from Equation 1.1.

This issue can be addressed by considering the relationship between the tank pressure and the boil-off that occurs at the interface. For a closed cryogenic tank subject to an external thermal load, the change in the tank pressure is most affected by the change in mass in the ullage region due to the addition of propellant vapor from evaporation, bulk liquid boiling, and boiling at the tank wall. The ability of a propellant tank model to accurately predict the tank pressure hinges on its ability to capture the aforementioned mass transfer processes [131]. For well-insulated tanks (heat flux rates < 5.0 W/m^2), such

as those anticipated for use in future missions, the tank undergoes self-pressurization. That is, the change in the tank pressure is strictly due to evaporation – or more specifically, the rate of evaporation – that occurs at the interface [150]. Therefore, for the case of self-pressurization due to a low thermal load, it stands to reason that a model capable of predicting the tank pressure with a certain fidelity must predict boil-off with a similar degree of fidelity.

The following chapter presents a review of notable cryogenic propellant tank models available in literature. In order to make use of the relationship between the tank pressure and boil-off, focus is given – though not limited – to model performance during self-pressurization. Because pressure and temperature are both indicative of how well the heat and mass transfer processes are captured within an individual model, temperature predictions are included, where applicable. The models are divided into three categories, according to the approach used to analyze the physical processes within the tank. In the sections that follow, the model categories are first introduced, followed by a discussion of the figures of merit used to evaluate model performance. A summary of the models in each category is then presented, and their predictions compared with results from ground-based and flight experiments. The chapter concludes with observations that influenced the research objective and the technical approach implemented in this dissertation.

3.1 Model Classification

Theoretical Theoretical models are the simplest models available for evaluating the pressurization in a closed cryogenic propellant tank in normal-gravity conditions. The tank is analyzed using a single control volume and basic assumptions regarding the fluid conditions and the how the incoming heat is distributed within the tank [5].

Analytical Analytical models analyze the heat and mass transfer in the tank using multiple control volumes, or nodes. The accuracy of the model increases with the

number of control volumes, as more physical effects can be included. Model capabilities extend beyond self-pressurization, and include pressurization due to bulk liquid boiling and boiling at the tank wall, as well as depressurization due to TVS operation and/or direct venting. Given the shortage of data due to the few on-orbit experiments that have been conducted, modeling efforts focus on normal-gravity conditions where the mechanisms responsible for heat and mass transfer are well known [66, 72].

Numerical The propellant tank models in this category provide the highest accuracy in solutions. Numerical methods include Network Flow Analysis (NFA) and Computational Fluid Dynamics (CFD). NFA provides a practical alternative by trading accuracy for computational expense; CFD is recommended when accuracy is critical [85].

3.2 Model Performance: Figures of Merit

Before reviewing the propellant tank models, the primary figures of merit used to assess a model's predictive capability must first be introduced. Pressure and temperature are indicative of the heat and mass transfer processes occurring in the tank, physical or simulated. Given that models differ in assumptions and accuracy, the ability to capture the effects responsible for the behavior in the tank pressure varies. For this reason, the pressurization rate (dP/dt) [5, 71, 150] and the ratio of the model-to-experimental pressurization rate (dP/dt ratio) [71, 150] serve as the primary figures of merit when comparing the results obtained from experiment and simulation, rather than the absolute pressure. The pressurization rate is defined as the average value obtained from the difference in the final and initial pressures, divided by the total experiment or simulation time [5, 71, 150]. Experimental and model pressures are typically presented together, as shown in Figure 3.1a. This allows for a qualitative comparison of the experimental and model values. Pressures are compared directly, while a visual inspection of the initial and final pressure values provides information

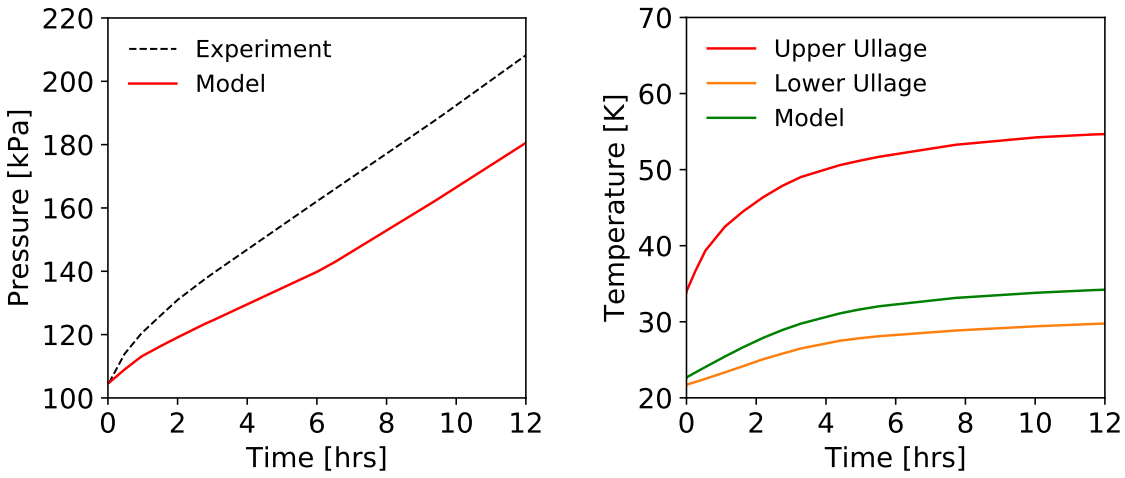

(a) Pressure

(b) Temperature

Figure 3.1: Example pressure and temperature plots used for comparing results from experiment and simulation of the conditions in a cryogenic propellant tank.

regarding the pressurization rates [11, 15, 22, 36, 105]. A quantitative comparison of the experimental and model rates is accomplished through the dP/dt ratio [71, 150].

The ullage and bulk liquid temperatures serve as secondary figures of merit. Unlike the tank pressure, which is defined by a single value, the temperatures of the ullage and bulk liquid vary with distance from the interface due to thermal stratification [5, 71, 150]. It is not uncommon in the literature to compare the temperature obtained from the model with experimental temperatures obtained from multiple locations. In the sections that follow, the ability of the propellant tank models in each model category to capture the heat and mass transfer in the tank will be reviewed using the aforementioned figures of merit, where available.

3.3 Theoretical Models

The theoretical homogeneous and surface evaporation models seek to predict the pressurization rate of a closed cryogenic propellant tank undergoing self-pressurization. The two models presented here each apply their own assumptions regarding how the entering heat is distributed between heating of the ullage and bulk liquid regions, and the evaporation at

the interface.

3.3.1 Homogeneous Model

The homogeneous model is one of the earliest models available for predicting the pressurization rate in a closed tank containing a cryogenic liquid and its vapor [14], and has been used considerably in the literature to compare with results obtained from simulation [11, 13, 14, 96, 121, 142] and experiment [5, 71, 150]. The tank is represented by a single control volume that encloses the ullage and bulk liquid regions [96]. It is assumed that the ullage and bulk liquid form a saturated mixture that remains in thermal equilibrium at all times [5]. This is illustrated in Figure 3.2a, where the tank is at some initial temperature and pressure, denoted by T_o and P_o, respectively. At some later time after an amount of heat has entered the tank, the tank is at an elevated temperature T' and pressure P', as shown in Figure 3.2b.

A numerical expression relating the tank pressurization rate dP/dt, to the rate at which heat enters the tank $\dot{Q}$, can be obtained through application of the first law of thermodynamics and the law of conservation of mass to the control volume [130]. This relation is provided in Equation 3.1, where V is the tank volume and ϕ is energy derivative, defined in Equation 3.2. For a closed tank subject to constant heating rate, dP/dt increases with time since ϕ increases with tank pressure [96]. The total pressure change in the tank is determined from integration of Equation 3.1 and a known initial tank state. Due to the absence of a temperature gradient between the ullage and bulk liquid, evaporation in this model does not occur through the traditional means. Rather, the evaporation that occurs goes towards maintaining the saturated liquid-vapor mixture as the temperature and pressure of the system changes [29, 96].

$$\frac{dP}{dt} = \frac{\phi}{V}\dot{Q} \tag{3.1}$$

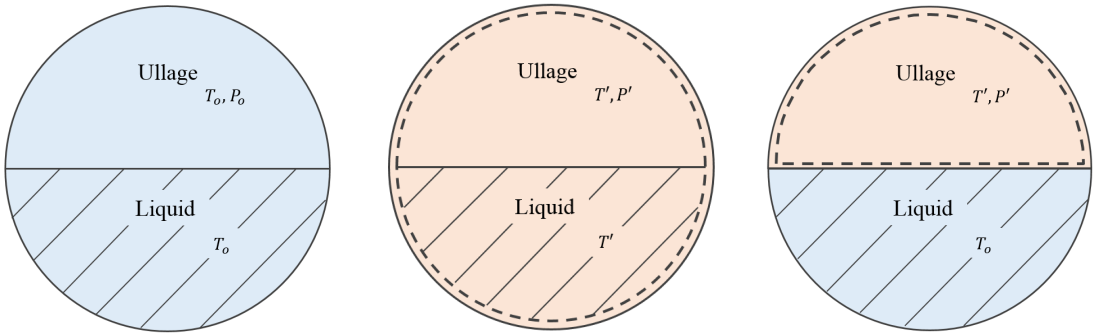

(a) (b) (c)

Figure 3.2: A closed cryogenic propellant tank (a) initially in thermal equilibrium, and some time later after heat has entered the tank as described by (b) the homogeneous model, and (c) the surface evaporation model.

$$\phi = \frac{1}{\rho}\left(\frac{\partial u}{\partial P}\right)_{\rho}^{-1} \tag{3.2}$$

3.3.2 Surface Evaporation Model

The surface evaporation model was first presented in 1967 as an alternative view regarding the distribution of heat within the tank [5]. Though informative, the model has been utilized to a much lesser degree in literature [14]. The tank begins in the same initial state as the homogeneous model (Figure 3.2a). Rather than assume thermal equilibrium, it is assumed that the heat entering the tank goes directly toward evaporation of the liquid at the interface; the temperature of the bulk liquid remains unchanged, while the ullage pressure and temperature increase due to the added mass from evaporation [5], as shown in Figure 3.2c. Given that the thermodynamic properties of the bulk liquid do not change with time, the change in the ullage pressure can be determined from analysis of the ullage space alone. Unlike the homogeneous model, a similar numerical expression relating $\dot{Q}$ to dP/dt is not readily available in the literature. However, a method exists for calculating dP/dt based on experimental measurements of $\dot{Q}$, the ullage temperature, and the propellant fill level [5].

3.3.3 Comparison with Experiment

3.3.3.1 23 cm Diameter Spherical LH_2 Tank

In 1967, Aydelott [5] conducted a series of self-pressurization experiments using a 23 cm diameter spherical LH_2 tank under normal-gravity conditions. One of the objectives was to compare the pressurization rate obtained from experiment with those obtained from the homogeneous and surface evaporation models. The ullage pressure was monitored while subjecting the tank to a heat flux rate of approximately 200 W/m^2 at fill levels of 34.9%, 48.9%, and 76.5%.

The results from the experiment are presented in Figure 3.3. The triangles, circles, and squares represent the experimental data for fill levels of 34.9%, 48.9%, and 76.5%, respectively. Predictions obtained from the homogeneous and surface evaporation models are represented by the '· -' and '- -' lines, respectively, where each line connects the initial pressure measured by experiment and the final pressure obtained from theory. Pressurization rates obtained from the homogeneous model decrease with increasing fill level, contrary to the trend in the experimental data, with experimental rates approximately 1.8, 2.0, and 2.1 times higher that homogeneous rates for fill levels of 34.9%, 48.9%, and 76.5%, respectively. Pressurization rates obtained from the surface evaporation model follow the trend in the experimental rates, however, pressurization rates diverge further away from the experimental rates with increasing fill level. Pressurization rates obtained from the surface evaporation model are approximately 1.2, 1.3, and 1.9 times higher than experimental rates for fill levels of 34.9%, 48.9%, and 76.5%, respectively.

The results demonstrate that for a self-pressurizing cryogenic propellant tank the homogeneous model underestimates the pressurization rate, while the surface evaporation model tends to overestimate the pressurization rate. Relating these observations to the model assumptions, the results further indicate that the homogeneous model is conservative regarding the amount of heat that contributes towards evaporation, whereas the surface evaporation model is aggressive in its assumption that all the incoming heat contributes

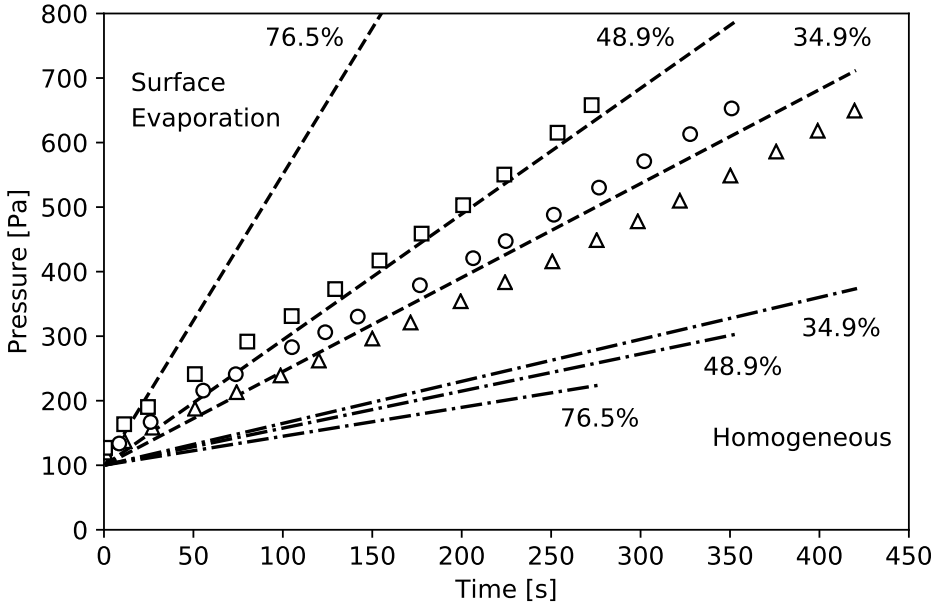

Figure 3.3: Experimental results for self-pressurization in 23 cm diameter spherical LH_2 tank versus predictions obtained from theory [5]. Experimental data is represented by triangles (FL = 34.9%), circles (FL = 49.9%), and squares (FL = 76.5%).

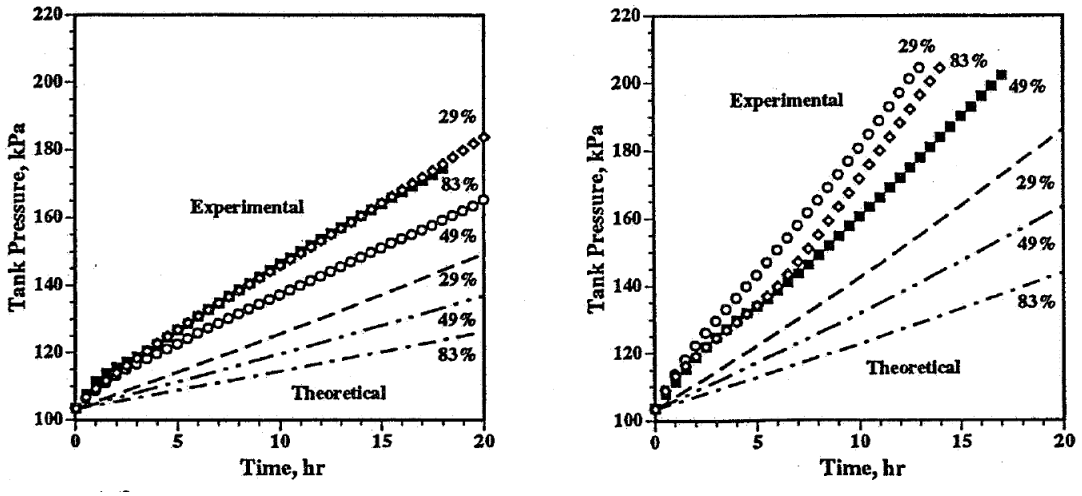

(a) 2.0 W/m^2 (b) 3.5 W/m^2

Figure 3.4: Experimental results for self-pressurization in a flightweight LH_2 tank versus predictions obtained from the theoretical homogeneous model [150].

directly towards evaporation at the interface, especially for higher propellant fill levels.

3.3.3.2 Flightweight LH_2 Tank

Similar experiments were performed by Hasan et al. in 1991 [71] and Van Dresar et al. [150] in 1992 for a 4.89 m^3 oblate spheroid tank with a diameter of 2.2 m and a height of 1.83 m. These experiments are of particular interest as they demonstrate the change in the pressurization rate due to the effects of (1) increased heat into the tank, and (2) the tank geometry. The tank is approximately the same size as propellant tanks anticipated in future spacecraft applications and represents roughly a 3.0 order of magnitude increase in volume when compared to the tank utilized in previous experiments conducted by Aydelott. Experiments were conducted using heat flux rates typically experienced by well-insulated propellant tanks in the space environment [71, 150].

The tank was subjected to heat flux rates of 2.0 W/m^2 and 3.5 W/m^2, at fill levels of 29% [150], 49% [150], and 83% [71]. Results from the experiment are presented in Figures 3.4a and 3.4b. Pressure predictions obtained from the homogeneous model are represented by the dashed lines. As before, each line connects the initial pressure measured by experiment and the final pressure obtained from theory. The effect of increasing the heat flux rate from 2.0 W/m^2 to 3.5 W/m^2 results in an increase in the pressurization rates, with the gap between experimental and predicted values increasing with the additional heat into the tank[1]. In both cases, the highest experimental pressurization rate occurs for the fill level of 29%. The authors ascribe this behavior to the shape of the tank and its effect on the heat transfer at different propellant fill levels. The heat transfer into the ullage and bulk liquid from the surrounding environment is determined by the amount of contact with the dry and wet tank wall areas, respectively; the heat transfer at the interface is dependent upon area of the interface. Both of these factors – the area of the dry and wet tank walls, and the area of the interface – are determined by the height of the liquid in the tank and the geometry of

[1]Experimental pressurization rates were between 1.4 and 2.4 times larger than homogeneous rates for the heat flux rate of 2.0 W/m^2 [150], and between 1.7 and 3.1 times larger for a heat flux of 3.5 W/m^2 [71].

the tank [150]. For this reason the experimental pressurization rates observed by Aydelott strictly increase with propellant fill level, while in this case a different trend is observed.

As can be seen from comparison of Figures 3.3 and 3.4, the influence of the tank geometry is not captured by the pressurization rates predicted by the homogeneous model. This is a direct consequence of Equation 3.1. The tank geometry enters the equation via the tank volume V, which can have the same value for a number of tank shapes. The homogeneous model also fails to capture the initial transient behavior present at the start of each experiment, which occurs as a result of the initial period of heat transfer between the ullage, bulk liquid, and interface when temperature gradients are first being established [71, 150]. Since the model assumes a uniform temperature throughout the tank, it is incapable of capturing the initial transient behavior, which in turn affects the model's ability to predict the pressure in the tank [13, 150].

3.3.4 Concluding Remarks

The theoretical surface evaporation and homogeneous models represent the upper and lower bounds, respectively, for pressurization rates observed in self-pressurization experiments conducted by Aydelott [5]. The homogeneous model continued to underestimate pressurization rates in experiments that followed [71, 150]. The prediction capability of these models is a direct result of the strict assumptions placed on the fluid conditions and how the incoming heat is distributed within the tank. The homogeneous model assumes a uniform temperature distribution within the tank, resulting in the lowest pressurization rate in most normal-gravity situations [96], whereas the surface evaporation model assumes the incoming heat contributes entirely to evaporation, resulting in the maximum pressurization rate for the same tank, subject to the same conditions. In both cases, the evaporation that occurs goes towards maintaining the fluid – the ullage for the surface evaporation model and the liquid-vapor mixture for the homogeneous model – at the saturation temperature corresponding to the tank pressure. While these models do not necessarily provide accu-

rate predictions, they have provided valuable insight over the years, particularly the homogeneous model, which has served as a baseline for other self-pressurization models in literature [13–15, 96, 121].

3.4 Analytical Models

The primary drawback of the models in the previous section was in their assumptions regarding the fluid conditions and how the heat is distributed within the tank. The models in this category resolve these issues by (1) relaxing the saturated assumption placed on the ullage and/or bulk liquid, (2) incorporating empirical relationships and correlations governing heat and mass transfer, and (3) dividing the tank into several control volumes in order to allow for the transfer of that heat and mass between the various regions in the tank.

An analytical method utilizing thermodynamics to evaluate the heat and mass transfer within the tank was developed by E. Ring in 1964 for the purposes of preliminary design and analysis of the pressurization of liquid rocket propellant tanks [131]. The analysis has been considered one of the most comprehensive treatments to date and has provided the foundation for other analytical propellant tank pressurization models in literature [49, 158], including two of the three models reviewed in this section – the model developed by Hastings et al. and the Computational Propellant and Pressurization Program (CPPPO). The third model – Tank System Integrated Model (TankSIM) – rather than implement a thermodynamic treatment, utilizes numerous detailed equations to capture the physical processes in the tank.

The above models can be considered state of the art in analysis of cryogenic propellant tanks requiring pressure control. Given the longer durations anticipated in future missions, tanks will have to incorporate some sort of pressure control device to ensure that the tank pressure remains within acceptable limits. This represents a new paradigm, and relatively few models in the literature are capable of modeling the conditions in the tank for extended storage periods where pressure control is required [36].

Since operation is no longer limited to self-pressurization in a closed tank, these models consist of several components – one for modeling the heat and mass transfer in the tank (the propellant tank model) and the remaining components for modeling the operation of the pressure control device (the TVS) [22, 72]. To remain within the scope of this research, the TVS model is not considered; discussion will focus on the propellant tank model and the additional heat and mass transfer effects due to TVS operation.

Section 3.4.1 presents the propellant tank model developed by Hastings et al. to predict the performance of a spray bar TVS. The propellant tank models utilized by CPPPO and TankSIM are presented in Sections 3.4.3 and 3.4.2, respectively. Published validation studies using ground-based and flight experiments provide an opportunity to evaluate the predictive capability of each model, and are presented in Section 3.4.4. Schematics for each of the propellant tank models and the corresponding heat and mass transfer processes included are located in Appendix B.

3.4.1 Model of Hastings et al.

Hastings et al. developed a FORTRAN-based analytical model to predict the ability of the spray bar TVS, depicted in Figure 3.5, to maintain pressure control within the Multipurpose Hydrogen Test Bed (MTHB) tank. The TVS device reduces the tank pressure through mixing and venting without the need to settle the propellant [72]. During mixing, the cold liquid propellant is withdrawn from the tank with a pump and is sent back into the tank through the vertical spray bar. Heat from the warm ullage gas is redistributed within the tank by circulation and mixing from the spray, thus reducing the temperature and pressure in the tank regardless of the locations of the ullage and liquid [72]. Depending on the heat transfer from the external environment, the bulk liquid temperature may increase to a point where mixing is no longer effective. At this point, a portion of the liquid is removed from the tank and goes through an expansion process where it undergoes a phase change. The now cooler gas is passed through the spray bar where it removes heat from the liquid before

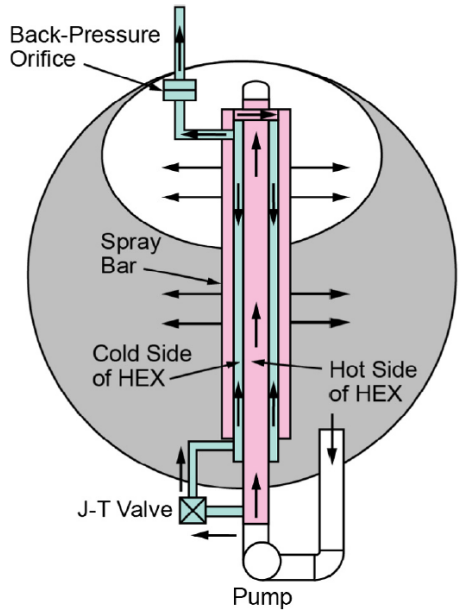

Figure 3.5: Spray bar TVS [102].

the liquid is sprayed back into the tank. The gas is then vented overboard [72, 102].

As can be seen from the propellant tank model schematic depicted in Figure B.1, a total of 19 heat and mass transfer quantities are tracked within the model, 8 of which correspond to heat transfer, and the remaining 11 corresponding to mass transfer. It is assumed that the tank contains an ideal gas and a saturated incompressible liquid [72]. The predominant form of heat transfer is still described using natural convection, with the exception of the heat transfer between the liquid spray and ullage, which is described using forced convection [108]. Because boiling of liquid film that accumulates on the dry tank wall from the spray contributes a nontrivial amount to the pressure increase in the tank, the liquid film on the tank wall in included as a control volume in the model. Mass transfer in the bulk liquid is due to the combination of bulk liquid boiling, condensation at the surface of the bulk liquid, the addition of liquid mass from the incoming spray, and the liquid mass that is removed and/or vented during TVS operation [72].

3.4.2 Tank System Integrated Model

TankSIM is a FORTRAN-based program that predicts the performance of cryogenic storage systems during in-space missions. The program is capable of simulating in-space coast, propellant transfer system chilldown, propellant tank pressurization, propellant settling, and main engine operation. A mission can be constructed using as many of these mission segments as desired and in any combination; accelerations, external heat loads, and duration can be adjusted for each segment [22]. For extended storage periods where pressure control is necessary, several pressure control options are available. Excess pressure can be relieved directly through cyclic or continuous venting of the ullage, or via a spray bar or axial TVS [22]. The program allows for various tank shapes and end cap geometries (flat, elliptical, and spherical). In the case of cylindrical tanks, the geometries of the top and bottom end caps need not be the same [22].

The heat and mass transfer in the tank are analyzed using the seven control volumes illustrated in the propellant tank model schematic provided in Figure B.2. The ullage and bulk liquid are evaluated as a function of temperature and pressure using NIST REFPROP [91]. One major difference from the previous model is inclusion of a control volume representing the gas-liquid interface, which is assumed thin and massless, and defined solely by its temperature which serves as the driving force for the heat and mass transfer with adjacent regions [22]. The interfacial heat transfer is described using conduction, as corresponding convection correlations do not exist for the finite volume representation used at the interface [22]. Evaporation of the liquid propellant is a result of the net heat transfer from the ullage to the bulk liquid through the interface.

As can be seen in Figure B.3, numerous heat and mass transfer processes are included in the model. Considerations include heat transfer from the upper and lower end caps, and in the case of cylindrical geometries, the contribution from the cylindrical (or barrel) portion of the tank wall. Natural convection is used to describe the heat transfer between the bulk liquid and any portion of the tank wall [33, 134], and the ullage and cylindrical portion

of the tank wall [33]. Due to the lack of appropriate heat transfer correlations, conduction is used to capture the heat transfer between the ullage and the upper and lower end caps of the tank [22]. Heat transfer during unsettled conditions is evaluated using the ullage and bulk liquid configurations in Figure B.4. For an unsettled tank undergoing mixing, the ullage and bulk liquid are assumed to form a homogeneous mixture (Figure B.4a). In the absence of mixing, the ullage assumed to be surrounded by the bulk liquid (Figure B.4b). The location, amount of contact with the tank wall, and the extent of the deformation of the ullage varies depending on the acceleration experienced by the tank [22]. Heat transfer is evaluated using the same approach described above for settled conditions, but with the new interface and the dry tank wall areas. An additional feature provided by the model is the ability to track the total liquid propellant lost due to evaporation, bulk liquid boiling, and boiling at the wet tank wall.

3.4.3 Computational Propellant and Pressurization Program

CPPPO (pronounced see-THREE-pee-oh) was developed during the Constellation program to enable modeling and analysis of cryogenic propellant tanks during extended periods of in-space storage [36]. The model predicts the propellant conditions in liquid rocket-based vehicles during launch, coast, or in-space maneuvers and has been considered critical to the design and maturation of the Ares V Earth Departure Stage and Altair Lunar Lander concepts [36]. CPPPO was created in Excel VBA [85], and allows for analysis of different design configurations with minimal modifications to the model. The author asserts that model predictions exhibit a reasonable level of fidelity when compared with other higher fidelity analytical models [36].

As can be seen in Figure B.5, the propellant tank model consists of the same control volumes utilized by TankSIM, less the control volumes of the spray droplet in the ullage and the liquid film on the dry tank wall. The tank is analyzed using a total of 14 heat and mass transfer processes. The heat and mass transfer due to spray and mixing during

TVS operation are not captured with the same methods utilized by TankSIM and Hastings et al. Here, the effects of TVS operation are captured by a simple removal of heat from the bulk liquid, although this quantity is not reflected in the propellant tank schematic provided by the author [36]. In order to obtain a closed-form solution, the ullage is modeled as a perfect gas; however real gas properties are used and are obtained from curve fits of thermodynamic property data from NIST REFPROP [92]. The bulk liquid is modeled as a compressible fluid, with the option of including thermal stratification through an empirical correlation derived from Saturn V data; the correlation provides the bulk liquid temperature as a function of the propellant liquid level and time [36]. The interface is considered saturated, thin and massless, with a temperature determined by the ullage pressure through the saturation condition, $T=T_{sat}(P_g)$. Evaporation is due to net heat transfer through the interface and is described using natural convection. The total propellant loss is tracked by the model as the sum of the contributions from evaporation, bulk liquid boiling, and the vented mass due to TVS operation [36].

3.4.4 Validation Against Ground-Based and Flight Experiments

3.4.4.1 Pressure Control in the Multipurpose Hydrogen Test Bed Tank

The MHTB tank is a system-level test bed developed by NASA's Marshall Space Flight Center in order to evaluate various CFM concepts. The tank is cylindrical, with a height and diameter of 3.05 m and 2:1 elliptical end caps, and is representative in size and shape of LH_2 propellant tanks utilized in space transportation vehicles [72]. The first CFM technology evaluated with the MHTB tank was a cryogenic thermal protection concept for ground-based upper stages consisting of VDMLI and SOFI [104].

Recently the MHTB tank was used to evaluate the spray bar TVS in Figure 3.5. One of the primary objectives of the experiment was to verify that the TVS can maintain pressure control defined by the upper and lower pressure limits of 137.9 kPa and 131 kPa, respectively, for storage periods lasting between 12 and 36 hours. Experiments were conducted

by using heating rates of approximately 20 W and 50 W for propellant fill levels of 25%, 50%, and 90% [72]. Upon reaching steady state (steady pressure rise in the ullage and thermal equilibrium in the bulk liquid), the tank was closed and allowed to self-pressurize until the upper pressure limit was reached. TVS operation was then initiated, causing a reduction in the pressure and temperature in the tank until the lower pressure limit was reached. The tank was then allowed to repressurize, and the TVS cycled on and off in order to maintain pressure control within the prescribed band until the end of the experiment was reached [72].

The TVS demonstration tests conducted in the MHTB tank provide an opportunity to directly compare the prediction capabilities of the model developed by Hastings et al. and TankSIM, as the results from the validations have been published. Table 3.1 lists the conditions for each test. Note that only three of the four tests were used in the TankSIM validation study [22] (Tests P263981D, P263968KT, and P263981T), and include data for the tank pressure, as well as the ullage and bulk liquid temperatures. The validation conducted by Hastings et al. [72] covers all four tests; however data for ullage and bulk liquid temperatures covering the entire duration of the test were only available for two of the tests (Tests P263981D and P263968EF). Table 3.2 lists the pressurization rates for the initial self-pressurization period that were obtained from experiment versus those obtained from simulation. Included are values for the ratio of the model-to-experimental pressurization rates (dP/dt ratio), as the ratio provides a more appropriate metric for comparison between models.

The results from the validation studies are presented in Figures 3.6 through 3.9, with each figure corresponding to a single test. Measured values obtained from experiment are represented by the dashed lines; predicted values obtained from simulation for the pressure and the ullage and bulk liquid temperatures are represented by the red, green, and blue lines, respectively. Ullage temperatures were measured at a location corresponding to a propellant fill level of 95.4%, with the exception of Test P263981T, which uses the average

of the temperatures measured at a propellant fill level of 95.4% and a location corresponding to a lower fill level that was not identifiable in the literature. Bulk liquid temperatures were measured at a fill level corresponding to 11.5% [72].

As can be seen in Table 3.2, TankSIM predicts pressurization rates that are in relatively good agreement with the experimentally observed pressurization rates. The model by Hastings et al. overestimates the tank pressurization rate in all cases, with predictions between 2 and 5 times higher than experimental rates. The effect of TVS operation on the ullage temperature is clearly visible through the oscillatory behavior in the data. The same effect is not visible in the bulk liquid temperature, except at the lowest propellant fill level of 25% (Test P263968KL in Figure 3.8d). Overall, ullage temperatures predicted by both models are in relatively good agreement with experimental values, with the exception of Test P263968EF (Figure 3.7b). At the start of the self-pressurization phase, the measured temperature rapidly increases and then drops, whereas the model temperature increases at a constant rate until the TVS is initiated. Hastings et al. attribute the rapid decrease in the ullage temperature to the addition of cold gas due to evaporation of the cooler bulk liquid at the interface, whereas the model assumed a constant rate of thermal input to the ullage without mass transfer. The authors assert that the effects of such a complex energy exchange are not capable of being captured when a single node is used to represent each of the ullage and bulk liquid regions [72]. As for the bulk liquid temperatures, experimental and predicted values are in excellent agreement for Tests P263981D, P263968KT, and P263981T, and are in good agreement for Test P263968EF.

Table 3.1: Test conditions for TVS demonstration experiments conducted in the MHTB tank.

Test No.	P (kPa)	FL ($\%$ by vol.)	$\dot{Q}$ (W)	t (s)
P263981D	111.5	90	54.1	46,790[a]
P263968EF	111.5	90	20.2	138,599[b]
P263968KL	122.0	25	18.8	200,130[a]
P263981T	111.5	50	51.0	89,231[a]

[a]Bolshinskiy [22]

[b]Hastings et al. [72]

Table 3.2: Measured and predicted pressurization rates for initial self-pressurization period obtained from TVS demonstration tests in MHTB tank.

	dP/dt (kPa/hr)			Model to Exp. dP/dt Ratio	
Test No.	Experiment	Hastings et al.[b]	TankSIM[a]	Hastings et al.	TankSIM
P263981D	4.87[a]	9.99	5.23	2.05	1.07
P263968EF	1.74[b]	3.96	N/A	2.27	N/A
P263968KL	0.87[a]	4.14	0.81	4.78	0.94
P263981T	1.91[a]	9.81	2.97	5.13	1.46

[a]Calculated from data in Ref. [22]

[b]Calculated from data in Ref. [72]

TEST P263981D

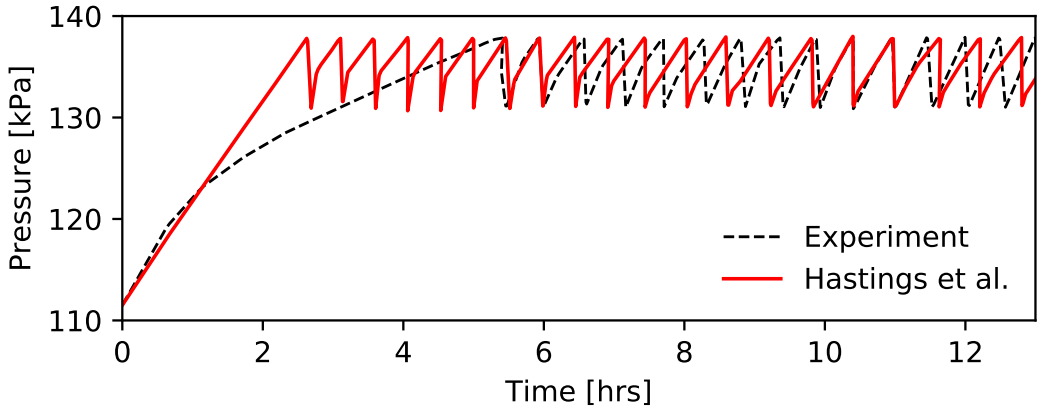

(a)

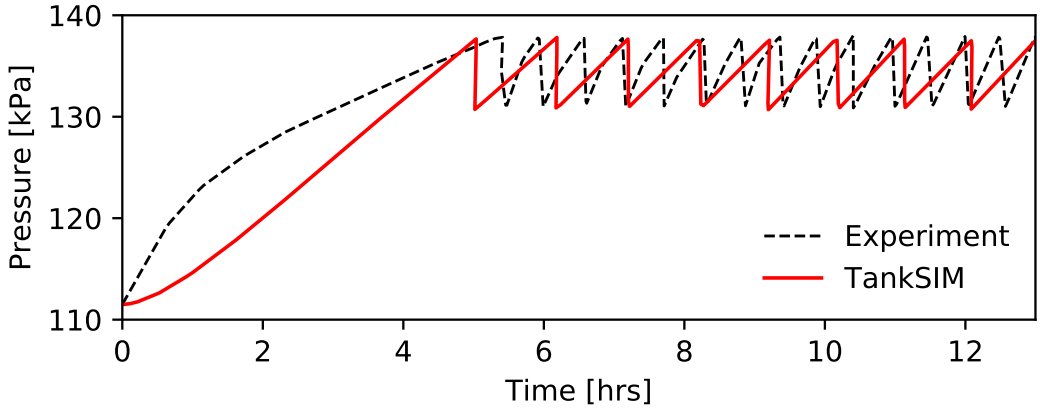

(b)

Figure 3.6: Test P263981D – Measured [22] and predicted pressure values [22, 72] for self-pressurization and TVS operation in the MHTB tank for FL = 90% and $\dot{Q}$ = 54.1 W.

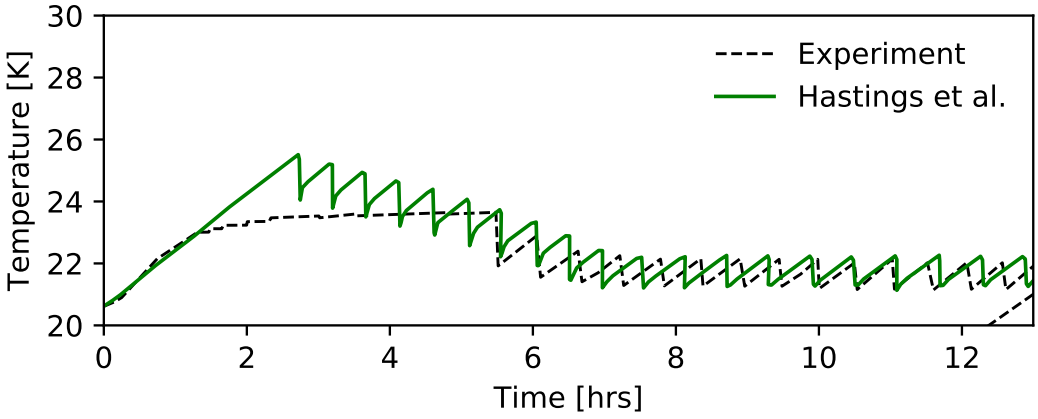

(c)

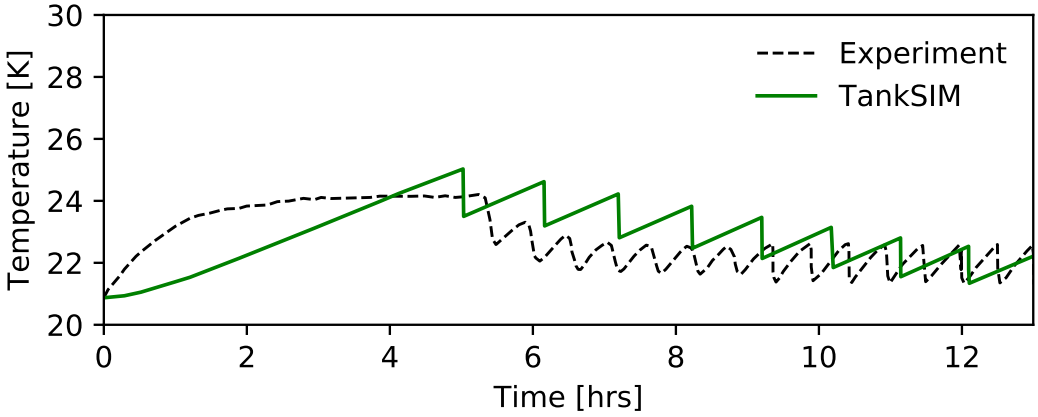

(d)

Figure 3.6: Test P263981D (continued) – Measured [22] and predicted ullage temperatures [22, 72] for self-pressurization and TVS operation in the MHTB tank for FL = 90% and $\dot{Q}$ = 54.1 W.

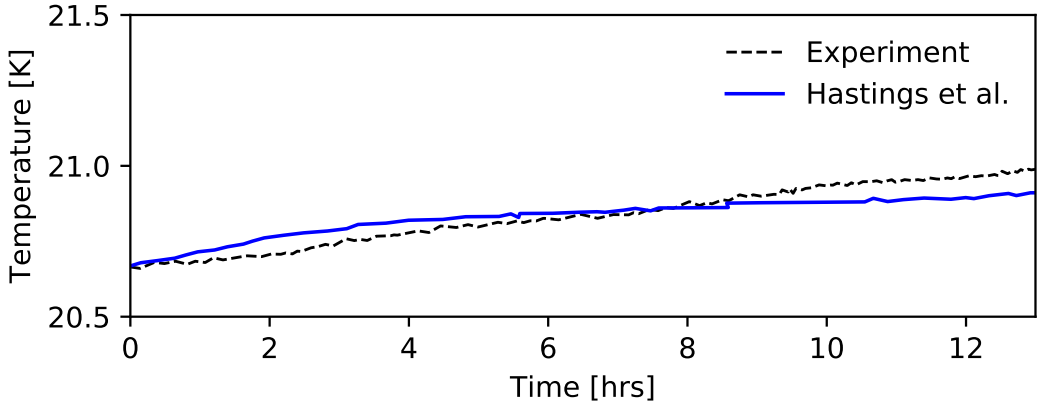

(e)

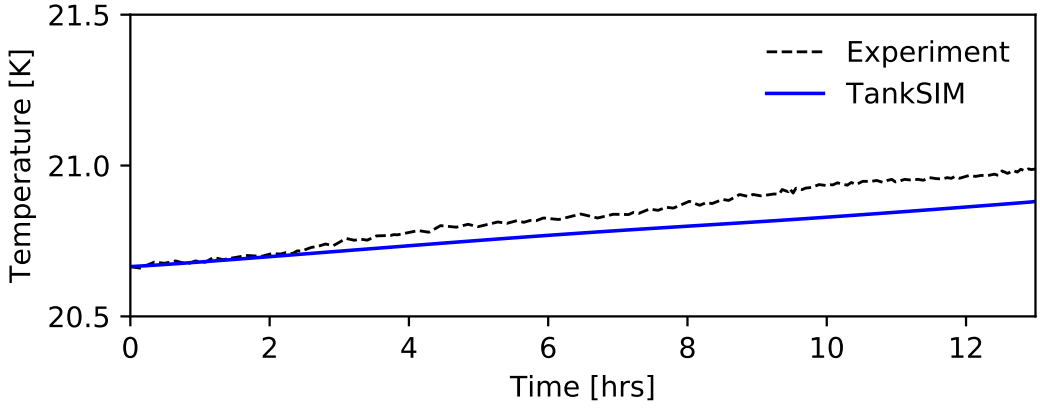

(f)

Figure 3.6: Test P263981D (continued) – Measured [22] and predicted bulk liquid temperatures [22, 72] for self-pressurization and TVS operation in the MHTB tank for FL = 90% and $\dot{Q}$ = 54.1 W [72].

TEST P263968EF

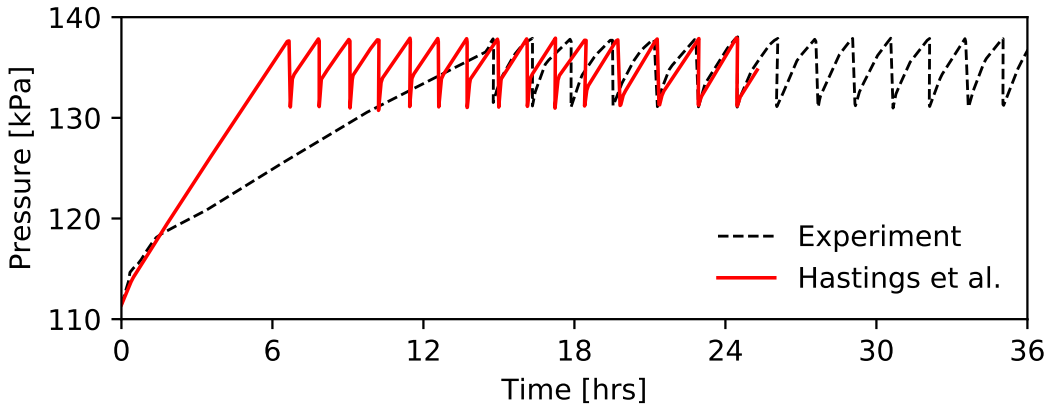

(a)

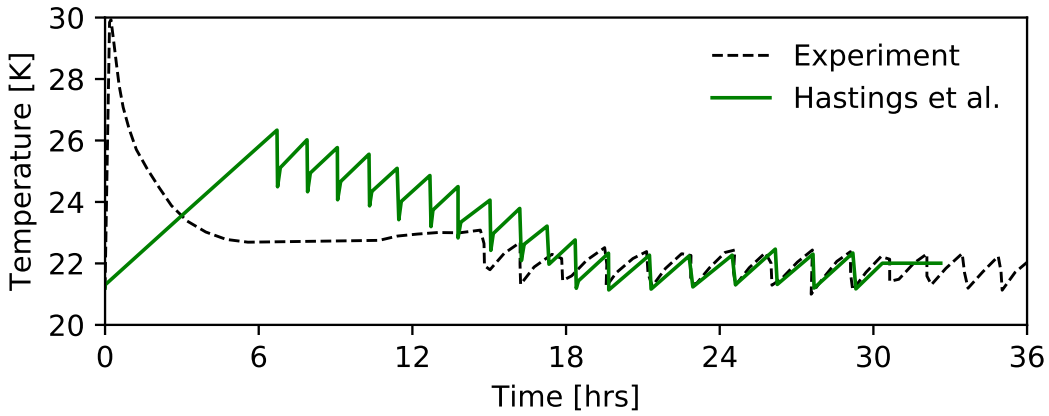

(b)

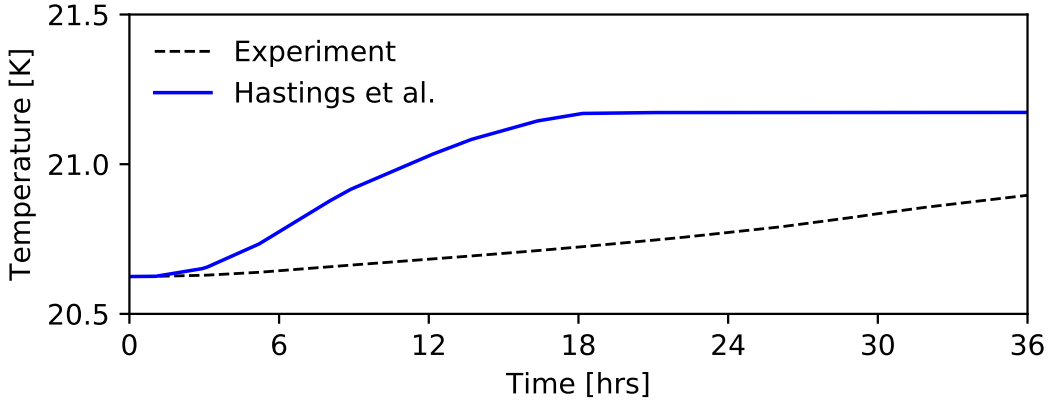

(c)

Figure 3.7: Test P263968EF – Measured and predicted values for self-pressurization and TVS operation in the MHTB tank for FL = 90% and $\dot{Q}$ = 20.2 W [72].

TEST P263968KL

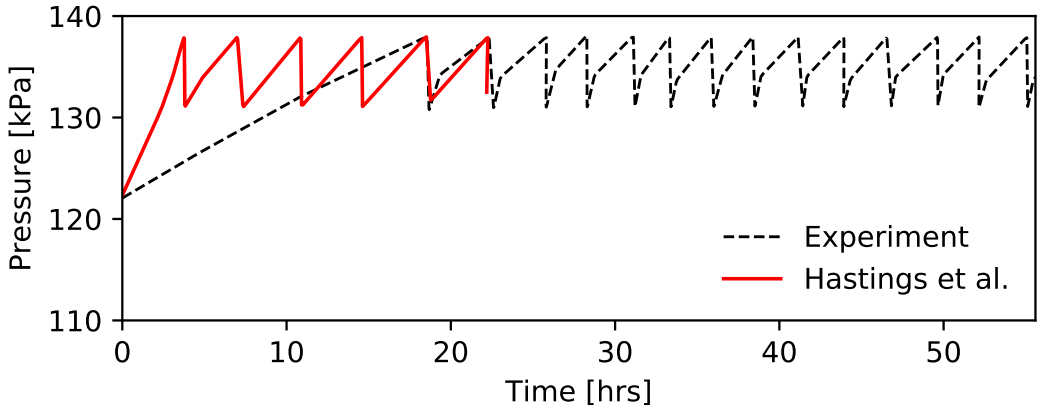

(a)

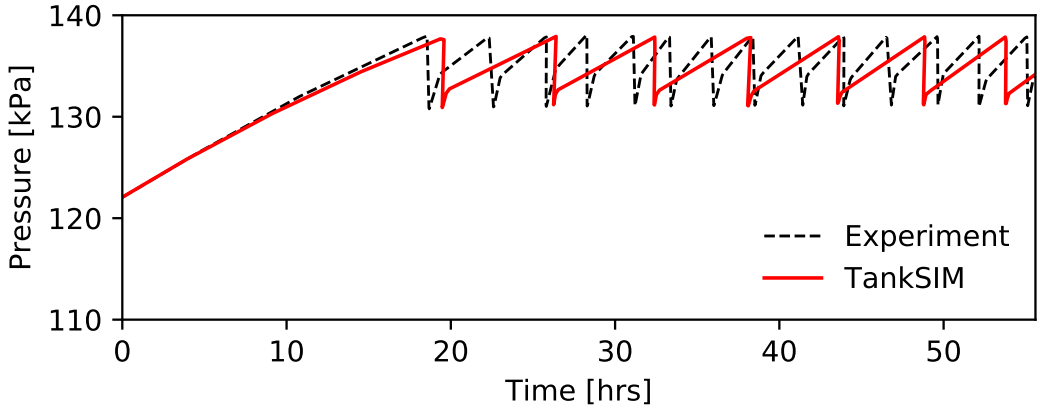

(b)

Figure 3.8: Test P263968KL – Measured [22] and predicted pressure values [22, 72] for self-pressurization and TVS operation in the MHTB tank for FL = 25% and $\dot{Q}$ = 18.8 W.

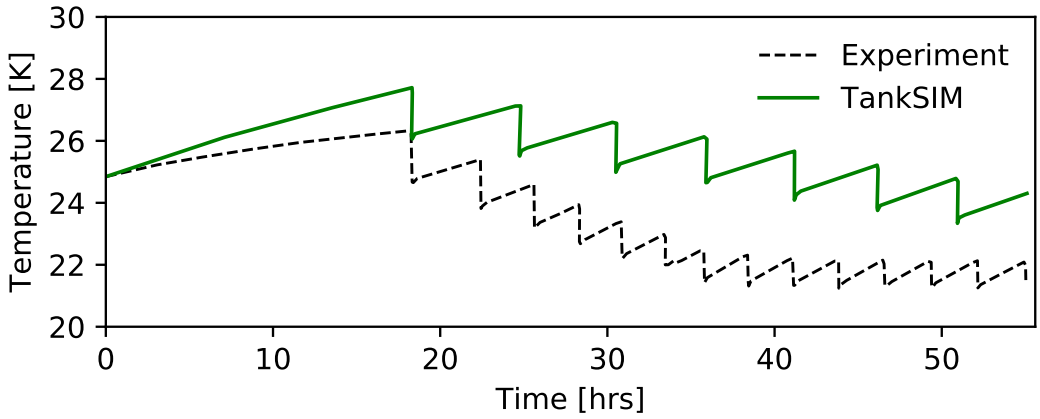

(c)

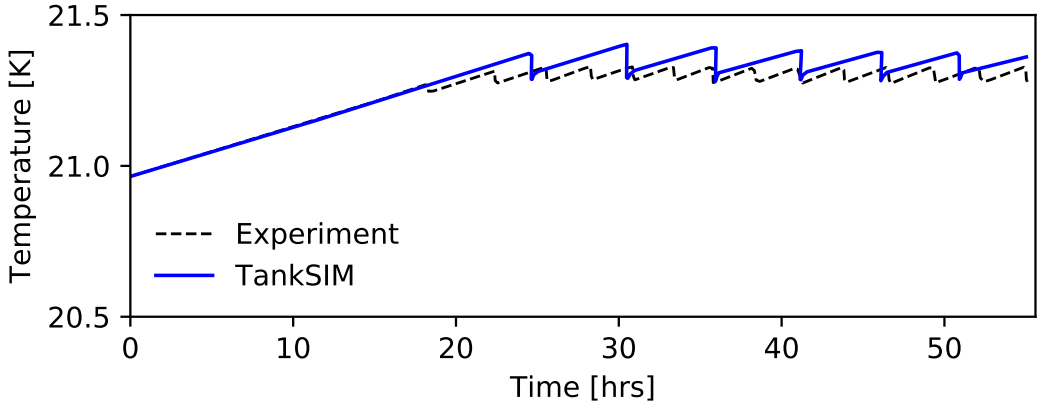

(d)

Figure 3.8: Test P263968KL (continued) – Measured and predicted temperatures for the (a) ullage and (b) bulk liquid during self-pressurization and TVS operation in the MHTB tank for FL = 25% and $\dot{Q}$ = 18.8 W [22].

TEST P263981T

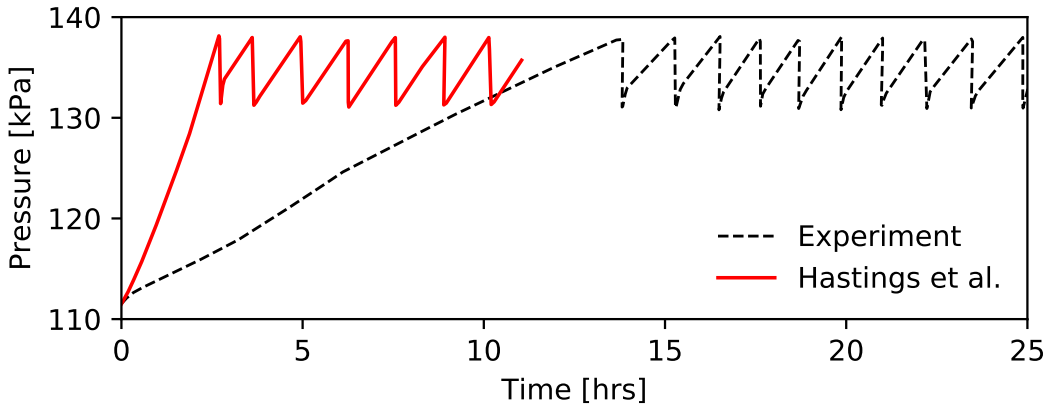

(a)

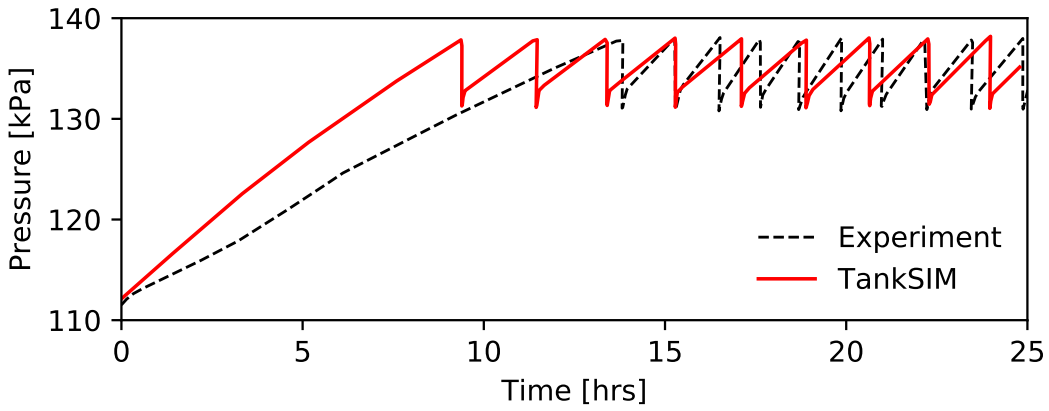

(b)

Figure 3.9: Test P263981T – Measured [22] and predicted pressure values [22, 72] for self-pressurization and TVS operation in the MHTB tank for FL = 50% and $\dot{Q}$ = 51.0 W.

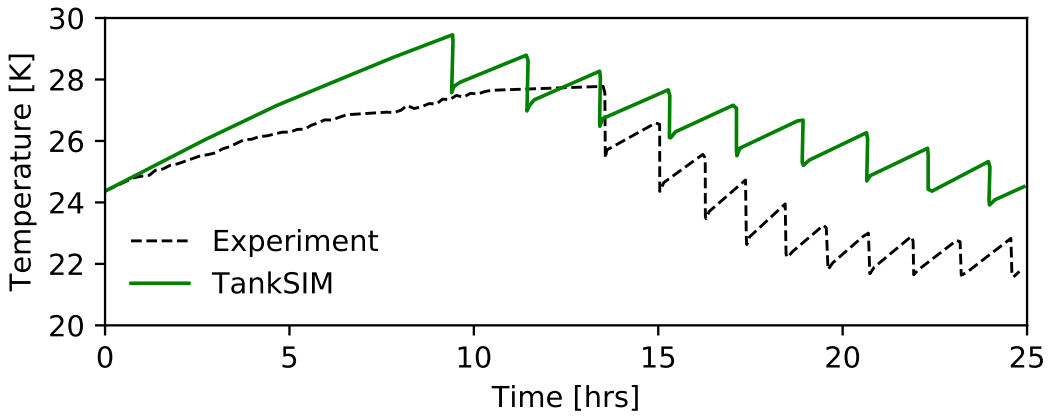

(c)

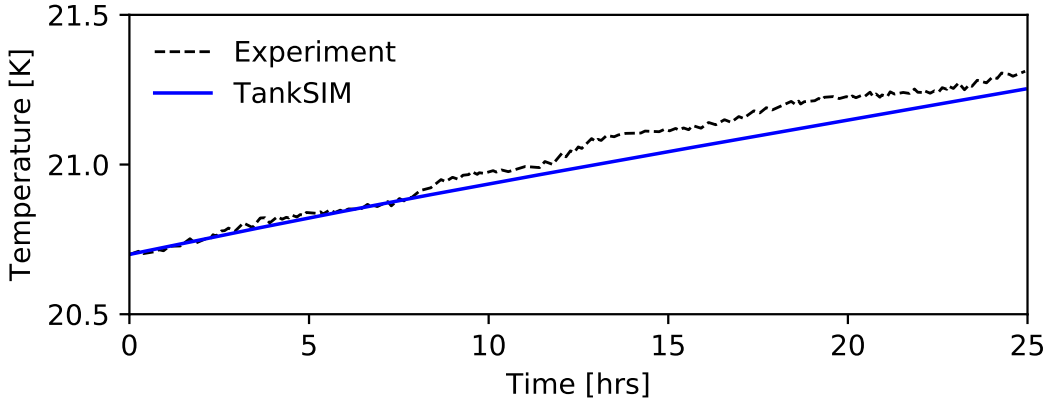

(d)

Figure 3.9: Test P263981T (continued) – Measured and predicted temperatures for the (a) ullage and (b) bulk liquid during self-pressurization and TVS operation in the MHTB tank for FL = 50% and $\dot{Q}$ = 51.0 W [22].

3.4.4.2 Flightweight LH_2 Tank

Validation of CPPPO with ground-based and flight experiments is presented by Corpening [36]. Self-pressurization experiments carried out in a flightweight LH_2 tank were described in Section 3.3.3.2. CPPPO was validated using experiments conducted at a heat flux rate of 2.0 W/m^2 and fill levels of 29% and 49%. As can be seen in Figures 3.10a and 3.10b, CPPPO underestimates the tank pressurization rate in both cases. Corpening attributes the discrepancy to inaccurate assumptions regarding the heat entering the tank. Prior to each experiment, the heat transfer into the tank was determined through boil-off tests [150]. The heat entering the tank causes evaporation, and the increased pressure in the tank is relieved through a vent valve. Measurement of the mass flow rate of the escaping gas allows for an estimate of the heat entering the tank. The heat flux rates obtained from the boil-off tests were assumed by Van Dresar et al. to enter the tank uniformly through the tank walls. Corpening asserts that this can be a poor assumption, and that the mass flow rates are indicative of evaporation due to heating of the bulk liquid [36]. Further, Corpening was able to obtain good agreement with experimental values by including an additional 20% of heat into the ullage for a fill level of 29%, and an additional 40% for the fill level of 49%, as shown in Figure 3.11. Other studies have reported similar findings when validating their models against the same experiments [11, 15].

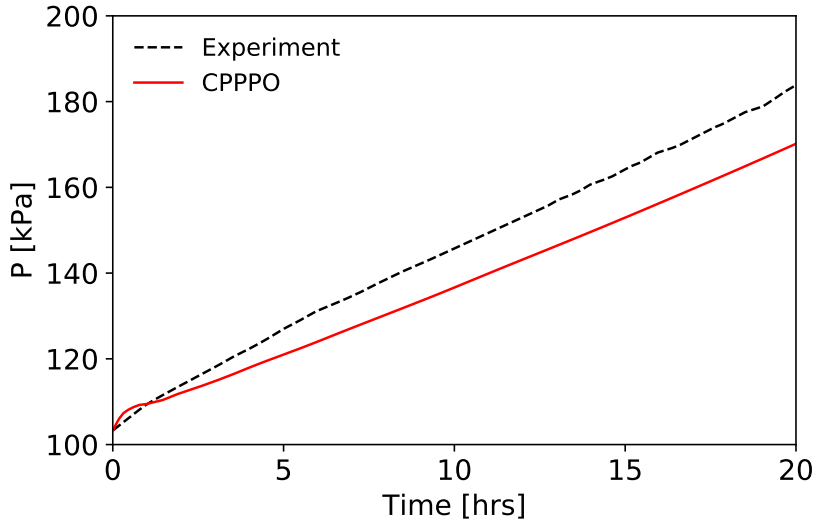

(a) FL = 29%

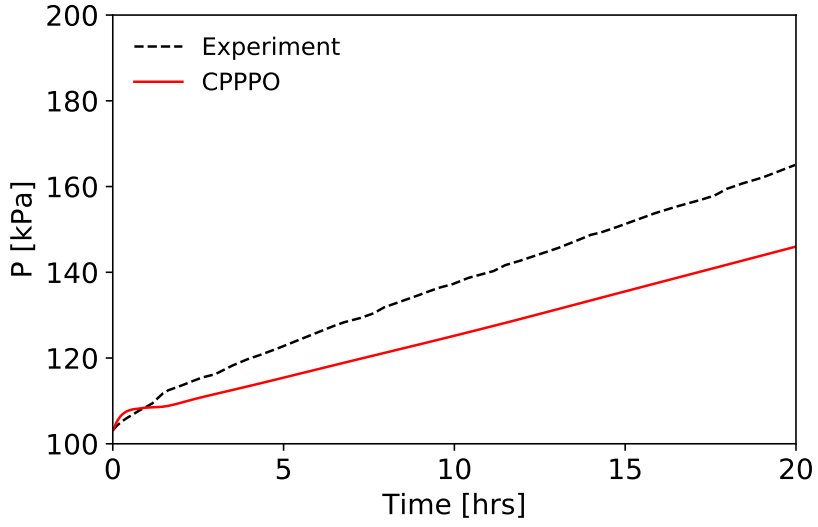

(b) FL = 49%

Figure 3.10: CPPPO validation against self-pressurization experiments conducted in a flightweight LH_2 tank subject to heat flux rate of 2.0 W/m^2 [36].

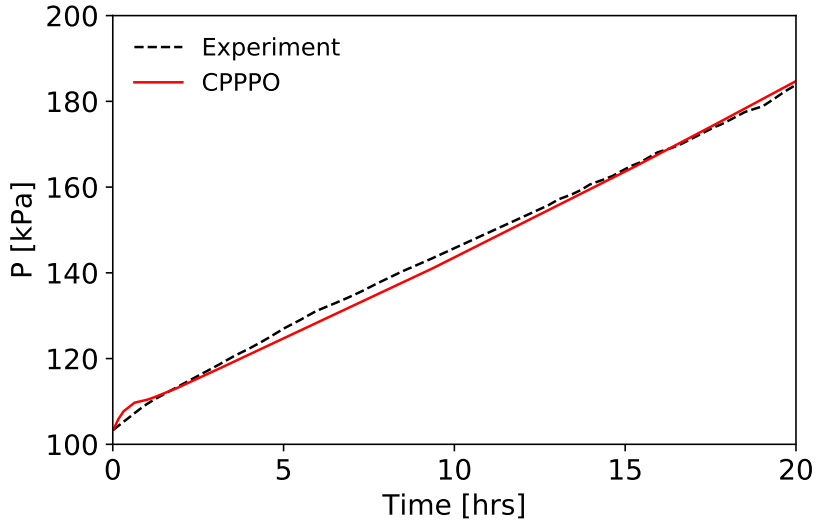

(a) FL = 29%

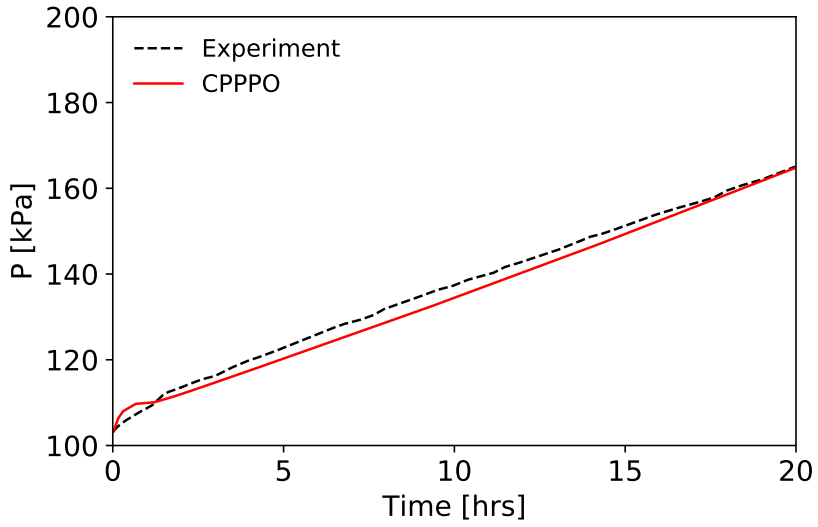

(b) FL = 49%

Figure 3.11: CPPPO validation against self-pressurization experiments conducted in a flightweight LH_2 tank subject to heat flux rate of 2.0 W/m^2 with an additional (a) 20% and (b) 40% heat input to the ullage [36].

3.4.4.3 AS-203 LH_2 Closed Tank Experiment

In preparation for the Apollo lunar missions NASA conducted an orbital experiment, the AS-203, to verify propellant control and the engine restart capability of the S-IVB upper stage after several hours of coast [155]. The primary objective of the closed tank experiment was to determine the pressurization rate of the LH_2 tank. The vent valve on the tank was closed and allowed to self-pressurize, with settling of the liquid propellant maintained throughout the experiment by the LOX ullage thruster system. During the approximate 1.5 hour coast, the pressure in the tank increased roughly 174 kPa, corresponding to a pressurization rate of 117 kPa/hr.

A report published in 1967 [155] estimated the heat transfer to the ullage and bulk liquid regions based on pressure and temperature measurements recorded during the experiment. Two methods were used in order to determine the heat transfer. The first method involved determining the amount of heat required to cause the changes observed in the ullage and bulk liquid fluid properties. The second method estimated the heat entering the tank based on tank wall temperatures measured at 40 locations. Results from validation of the pressurization rates obtained from the AS-203 experiment and CPPPO are provided in Figure 3.12a. Initially the predicted values obtained using the heat transfer estimated from the change in fluid properties is in good agreement with the experimental rate. However, the predicted values diverge approximately halfway through the experiment. The heat transfer rate obtained using the tank wall temperature results in predictions that are too high. An updated report published in 1970 [24] revised the heat transfer to the ullage region by including the absorptivity (α) of the forward dome on the tank. Validation with the updated heat transfer rates using two potential values for the absorptivity showed much better agreement, as shown in Figure 3.12b.

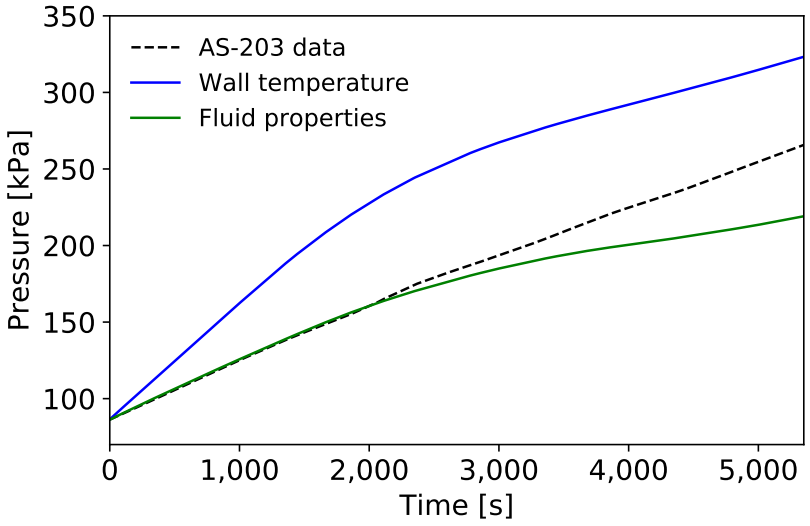

(a)

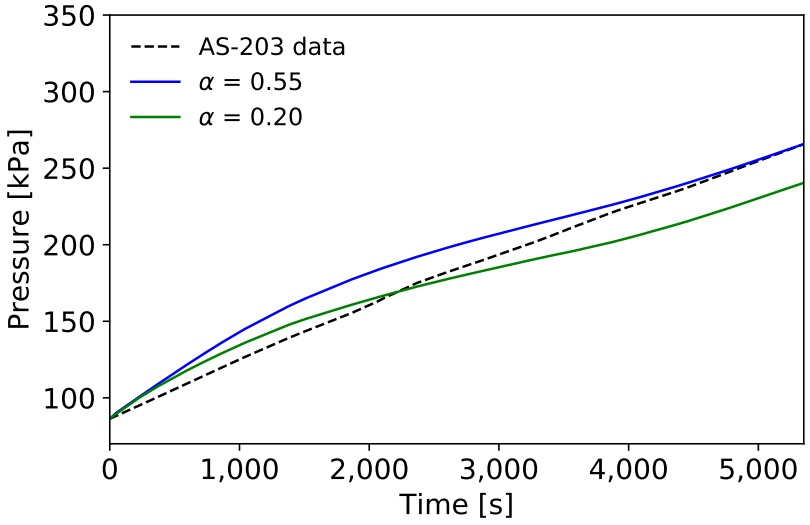

(b)

Figure 3.12: CPPPO validation against AS-203 LH_2 closed tank experiment using heat transfer rates published in (1) a 1967 report, and (b) a 1970 report [36].

3.4.5 Concluding Remarks

The propellant tank models reviewed in this section vary in complexity from simple (CPPPO), to intermediate (Hastings et al.), to detailed (TankSIM). The effects on the heat and mass transfer in the tank due to TVS operation are captured in greater detail by TankSIM and Hastings et al., whereas CPPPO invokes a high-level approach. Due to limitations in the validation studies available in literature, it is not possible to directly compare the prediction capability of all three models. However, pressure control experiments conducted in the MHTB tank allowed for a direct comparison between two of the three models – TankSIM and Hastings et al. The results of the validation showed that the two models are capable of predicting the conditions in the tank with good agreement (TankSIM) or within a conservative margin (Hastings et al.). Validation studies for CPPPO were limited to ground-based and flight experiments of settled tanks undergoing self-pressurization. The validation exercises were successful, but do not provide a means for comparison with the other models.

3.5 Numerical Models

There are a number of numerical models in the literature for analyzing the fluid conditions in cryogenic propellant tanks during active [9, 79, 97, 101, 154] and self-pressurization [65, 77, 121, 144, 145]. The intent of this portion of the literature review is not be exhaustive, but rather, to illustrate the benefits and limitations provided by the NFA and CFD analysis methods and to compare the accuracy in the results with those of the analytical models in the previous section. Section 3.5.1 introduces a pressure control model of the MHTB tank developed using a finite volume-based NFA program known as Generalized Fluid System Simulation Program (GFSSP). Sections 3.5.2 and 3.5.3 present CFD models for predicting self-pressurization in the MHTB tank and the S-IVB upper stage LH_2 tank, respectively.

3.5.1 Pressure Control in the MHTB Tank

GFSSP was developed by NASA's Marshall Space Flight Center for analyzing fluid dynamics and heat transfer in complex systems, such as liquid propulsion systems and cryogenic

propellant tanks [100, 102]. Systems are modeled as fluid networks consisting of boundary and internal nodes connected by branches. The objective is to solve for the temperature and pressure of the internal nodes and the mass flow rates in each branch based on known temperatures and pressures of the boundary nodes [100, 102]. The program is capable of analyzing a range of problems, from simple systems that can be modeled using a few nodes and branches, to intricate systems requiring multiple complex networks [100]. Since its initial development in 1994, GFSSP has been used to investigate the pressurization in cryogenic propellant tanks utilizing helium as the pressurant during engine firing [79, 101], and conduct insulation studies in the LH_2 storage tanks at Launch Complex 39 at Kennedy Space Center [99].

Recently, a system-level model for simulating pressure control in the MHTB tank was developed by Majumdar et al. [102]. The self-pressurization and TVS capabilities were developed and tested separately before being fully integrated into the system model depicted in Figure 3.13. The TVS model estimates the temperature and mass flow rate of the liquid spray. The flow through various parts of the TVS is represented using a total of seven branches; heat transfer within the spray bar is modeled using eight nodes. The self-pressurization model estimates the fluid conditions in the tank based on the heat and mass transfer between the ullage and bulk liquid, and the ullage and tank wall [102]. The model consists of five ullage nodes, a single bulk liquid node, and two layers of nodes for the tank wall. A pseudo-boundary node is used to represent the interface and maintain separation between the ullage and bulk liquid. During periods of self-pressurization, heat transfer from the ullage to the bulk liquid via the interface causes evaporation and increases the tank pressure. When the maximum pressure limit in the tank is reached, the fluid conditions are sent to the TVS model. The temperature and mass flow rate of the spray are introduced back into the self-pressurization model as mass and energy sources and sinks, respectively, thus reducing the temperature and pressure in the tank [102].

The system-level model was validated using TVS demonstration Test P263981T. A

simulation time of approximately 8 hours was required with a PC laptop (Intel, 2.6 GHz). A time step of 0.1 seconds was used to simulate self-pressurization, and a time step of 0.01 seconds during TVS operation. Experimental and model pressures are presented in Figure 3.14a. With the exception of a small offset due to an overestimate in the increase in the tank pressure at the beginning of the experiment, the values obtained from the model for both the tank pressure and the pressurization rate are in good agreement with experimental values for the initial self-pressurization period. During the period of TVS operation, the model takes longer to repressurize, resulting in fewer predicted TVS cycles. Table 3.3 lists the pressurization rate for the initial self-pressurization period and the corresponding dP/dt ratio obtained from the numerical model, as well the analytical models in the previous section. As expected, the numerical model provides the most accurate prediction for the pressurization rate in the tank.

An additional benefit of the model is the ability to predict the variation in the ullage temperature due to thermal stratification, as shown in Figure 3.14b. The orange and green curves represent temperatures predicted by the model for nodes located at fill levels of 80% and 65%, respectively. The experimental temperature corresponds to measurements taken at an intermediate fill level of 70%. Model predictions are more accurate during the initial self-pressurization period, and underestimates the temperature reduction during TVS operation. Majumdar et al. attribute the discrepancy in the results to the uncertainty in the heat transfer coefficient at the interface, and the assumption that the liquid spray is uniformly distributed among the ullage nodes during TVS operation.

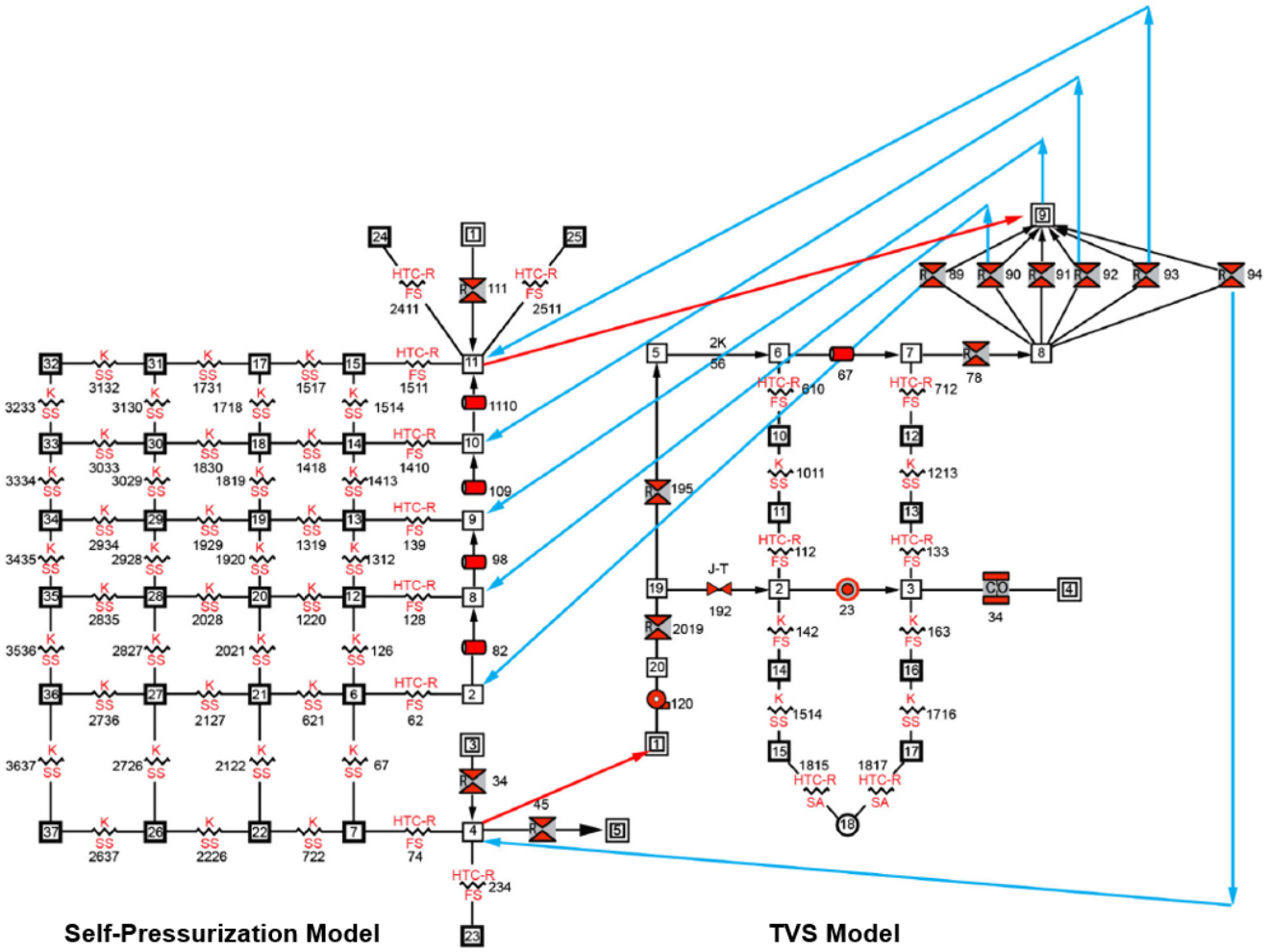

Figure 3.13: System-level model of pressurization in the MHTB tank composed from self-pressurization and TVS models developed using GFSSP [102]. Information passed from the self-pressurization model to the TVS model and vice versa are represented by the red and blue arrows, respectively.

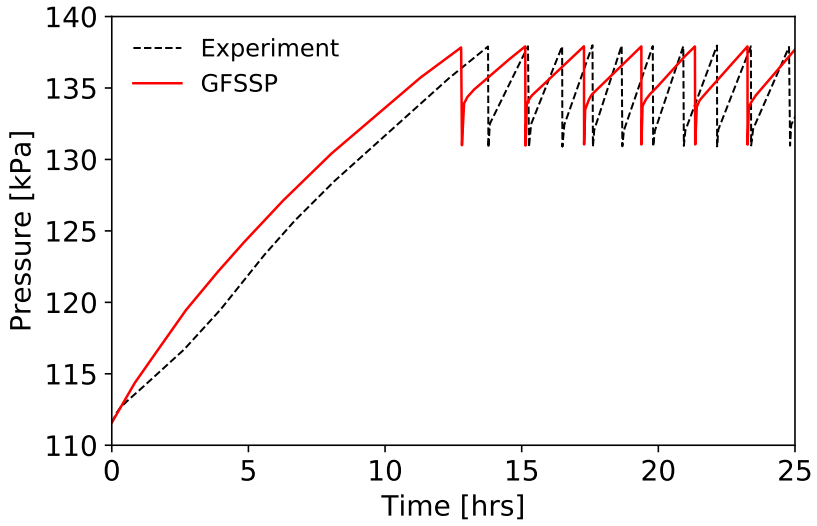

(a) Pressure

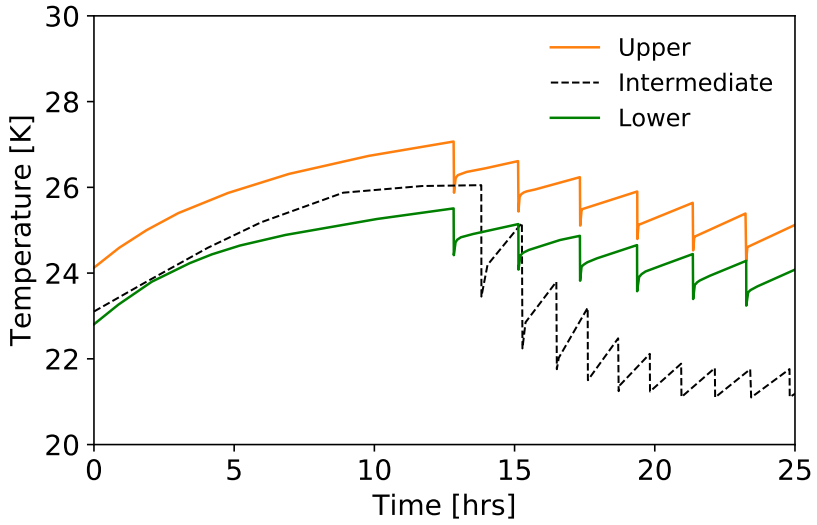

(b) Ullage Temperature

Figure 3.14: Measured and predicted values obtained from validation of system-level cryogenic propellant tank pressurization model developed using GFSSP against TVS demonstration Test P263981T conducted in the MHTB tank [102].

Table 3.3: Measured and predicted pressurization rates and dP/dt ratios obtained from analytical and numerical models for the initial self-pressurization segment of TVS demonstration Test P263981T conducted in the MHTB tank.

Source	dP/dt (kPa/hr)	Model to Exp. dP/dt Ratio
Test P263981T	1.91[a]	–
Hastings et al.	9.81[b]	5.13
TankSIM	2.79[a]	1.46
GFSSP	2.05[c]	1.07

[a]Calculated from data in Ref. [22]

[b]Calculated from data in Ref. [72]

[c]Calculated from data in Ref. [102]

3.5.2 Self-Pressurization in the MHTB Tank

A two-phase CFD model for simulating self-pressurization in the MHTB tank was developed and validated by Kartuzova et al. using the self-pressurization segment of Test P263981T. The tank is analyzed using a 2D axisymmetric grid consisting of 9,246 cells. The ullage is modeled as a compressible ideal gas. The bulk liquid is assumed incompressible with variable temperature-dependent properties, with the exception of the density which is assumed constant. The heat and mass transfer at the interface are captured using the Volume-of-Fluid (VOF) method, with evaporation and condensation described using a kinetics-based mass transfer model and assuming natural convection within the laminar regime.

Simulation of the 5,000 second self-pressurization experiment required approximately 9.6 hours of computational time using 8 AMD Opteron^{TM} 6100 Series processors. A uniform heat flux of 0.89873 W/m^2 and 2.0841 W/m^2 were applied to the wet and dry tank walls, respectively, with these values determined from previous analysis with multinodal simulations. An experimental profile of the tank taken from experiment was input as the starting temperature for the simulation. As shown in Figure 3.15a, both the tank pressure and pressurization rate obtained from the model are in excellent agreement with the experimental values. Figure 3.15b shows the temperature measured near the tank centerline at the end of the experiment, with the green and blue curves corresponding to the ullage and bulk liquid temperatures predicted by the model, respectively. Comparison of the experimental and model data shows that the model is accurate in predicting the bulk liquid temperature, and while the model predicts a warmer ullage, the overall trend in the thermal stratification within the region is captured.

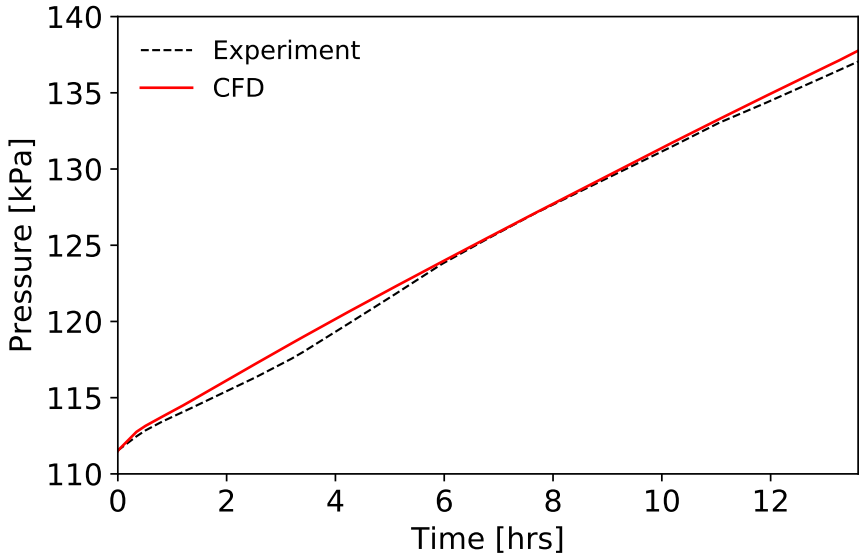

(a) Pressure

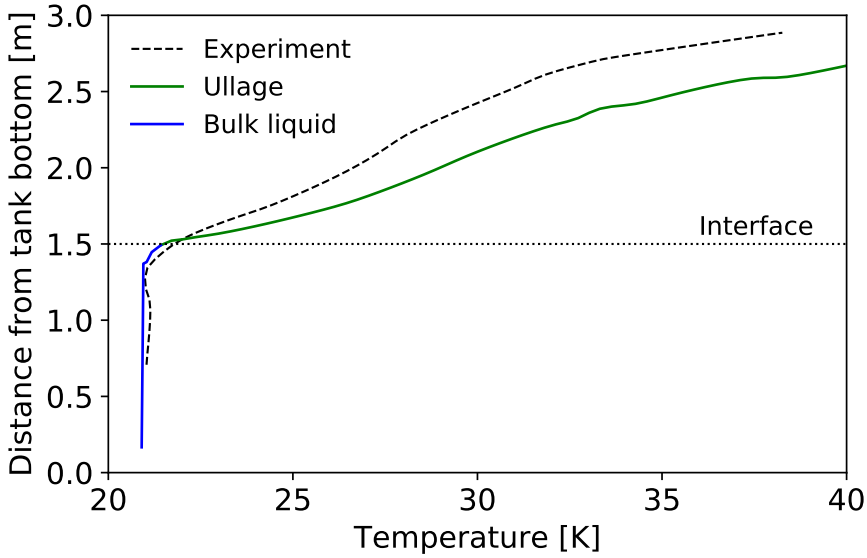

(b) Temperature profile

Figure 3.15: Pressure and temperatures obtained from CFD analysis versus experimental values for self-pressurization in the MHTB tank during Test P263981T [87]. The temperature profile corresponds to the temperature distribution in the tank at the end of the experiment.

3.5.3 Self-Pressurization in Orbital Flight

Mattick et al. [105] present a multi-element unstructured CFD model as part of a suite of analysis tools used for analyzing different types of cryogenic propellant tank pressurization problems. The CFD model leverages previous work for solving problems relating to cryogenic cavitation in feed systems [2] and turbomachinery equipment [81, 82]. In order to adjust from cavitation to tank applications, a broader operational envelope on the fluid properties is included to allow for compressibility effects in the bulk liquid to be captured [2, 105]. An arbitrary number of gases and liquids can exist within the tank, with the amounts of the ullage, bulk liquid, and pressurant tracked by individual species transport equations. Phase change is modeled using finite rate source terms based on the difference between the local pressure and the saturation pressure [2, 105]. The analysis method works well for shorter investigations (on the order of minutes) where the time-step is small relative to the grid size. Longer investigations force the use of longer times steps relative to the grid size in order to solve the problem in a reasonable time frame, resulting in dissipation, or diffusion, of the interface and thus affecting the heat and mass transfer in the tank [105].

The model was validated against the AS-203 LH_2 closed tank experiment [155]. Due to limitations of the model, only the first 500 seconds of the experiment were evaluated. The tank wall was divided into several sections, with the acceleration and heat transfer for each section defined as a function of time [155]. Figure 3.16 illustrates the tank wall sections, which consist of (A) the upper dome and (B) cylindrical portion of the dry tank wall, (C) the cylindrical portion and (D) the bottom curved portion of the wet tank wall, and (E) the common bulkhead. The experimental and model pressures obtained from the validation are depicted in Figure 3.17. Included is the tank pressurization rate reported for the full duration of the orbital experiment (117 kPa/hr), as the experimental values in the figure are limited to the first three data points from the experiment. Model values are in excellent agreement with the experimental pressurization rate, with the exception of the small deviation near the end of the 500 second simulation.

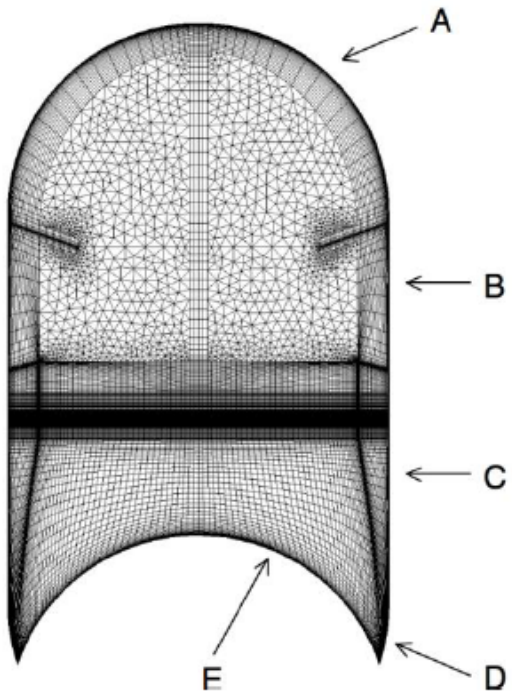

Figure 3.16: Division of the tank wall into a several sections, with each subject to an individual acceleration and heat transfer rate [105].

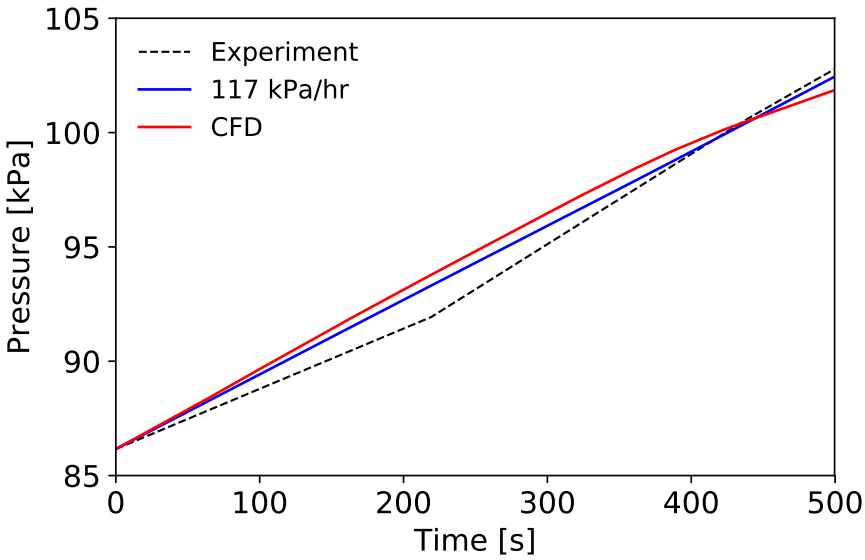

Figure 3.17: Pressure obtained from CFD analysis of the first 500 seconds of the AS-203 LH_2 closed tank experiment versus the experimentally observed pressure and the pressurization rate for full duration of the experiment [105].

3.5.4 Concluding Remarks

Analysis with NFA and CFD methods provides accurate prediction of the conditions in the tank. Pressure predictions are no longer limited to the pressurization rate as these models are capable of capturing how the behavior in the tank pressure changes with time. GFSSP and CFD models of the MHTB tank provide the temperature distribution in the ullage, whereas the analytical models in Section 3.4 are only capable of providing a single value for the temperature due to the single nodal representation of the region. Of the two methods, CFD provides the highest accuracy but is limited to analysis of short time frames due to the high computational expense. GFSSP provides slightly less accurate solutions but permits analysis of the tank for several hours. Given the combination of model complexity and evaluation time, numerical modeling is more suitable for system analysis beyond the conceptual design stage.

3.6 Summary of Observations and Technical Approach

The purpose of this chapter was to provide a summary of the notable cryogenic propellant tank models in literature, in order to identify a model with a suitable balance of complexity and accuracy, so that the model can serve as a replacement for the one that is currently utilized in the conceptual design process. Given that the boil-off prediction capability is typically not available in open literature, the pressurization prediction capability served as a surrogate in the identification process.

Based on the literature review, it was found that theoretical models – while simple and easy to integrate into the vehicle sizing process – provide poor estimates of the pressurization rate due to their strict assumptions regarding the fluid conditions and how the incoming heat is distributed within the tank. Numerical models, as expected, provide the most accurate values for the pressurization rate. However, given the computational expense, these models are not practical during the conceptual design phase where multiple vehicle alternatives must be evaluated. Analytical models, when compared to their theoretical counter-

parts, display a modest to significant increase in the number of physical processes used to analyze the tank and thus demonstrate better accuracy in predictions.

Of the three analytical models reviewed, CPPPO would be the easiest to implement. In addition, the high-level approach used to capture the effects due to TVS operation makes the model a desirable candidate. Unfortunately, information regarding the operational parameters of the TVS is not included in the original study. Determination of these parameters would require modeling and analysis of an additional system which is better left for a separate investigation. Further, due to the lack of a baseline validation case, the prediction capability of the model cannot be compared with that of TankSIM and the model of Hastings et al. The above issues preclude CPPPO from being a suitable replacement.

Of the two models that remain, the results from the baseline validation case showed that they are capable of predicting the conditions in the tank with good agreement (TankSIM) or within a conservative margin (Hastings et al.). Note, however, that caution should be used when implementing a model that was developed to predict the conditions within a specific tank, such as the model of Hastings et al. Typically, the model will contain modifications in order to account for fluid behaviors exhibited by the tank in question. These modifications are not always clear and can negatively impact the model's predictive capability when applied to other tanks. TankSIM presents no such issue since the model allows for simulation using various tank geometries. This point aside, the critical issue exhibited by both models is the large number of equations used to analyze the tank. Unfortunately, this level of detail makes the two models more suitable for use once the design space has been narrowed down and there is more turnaround time between design iterations.

In summary, the results from the literature review show that analytical models exhibit the desired fidelity, but either do not provide enough information or are so detailed that the computational time involved becomes prohibitive. These findings necessitate the development of a cryogenic propellant tank model that can predict the tank pressurization rate, and thus boil-off, with a similar fidelity provided by the above analytical models but with

a simpler approach for modeling the heat and mass transfer in the tank. Any model that is developed must be capable of analyzing tanks of multiple shapes and sizes. That is, it must be *extensible*. For reasons that have been previously discussed, it is imperative that the propellant tank model include a pressure control capability. Such a model will act as an enabler for the research objective, and thereby provide more accurate boil-off estimates than the current method provided by Equation 1.1. The research objective and the model requirements are restated below.

Research Objective: To improve conceptual design and analysis of cryogenic in-space vehicles by providing more accurate propellant mass estimates through the development of a higher fidelity boil-off model.

The newly developed model must meet the following requirements:

1. Rapid evaluation time: allows for evaluation of multiple alternative designs
2. Extensible: allows for analysis of tanks of various geometries
3. Pressure control capability: enables simulation of long-term missions

The chief difficulty in developing this new cryogenic propellant tank model is in capturing the primary fluid behaviors in the tank without incurring the penalty of the additional complexity. This motivates the following research question:

Research Question 1: How can a simplified cryogenic propellant tank model with pressure control capability be developed?

Consider for the moment that the propellant tanks utilized in future missions will be well-insulated (heat flux rates < 5.0 W/m^2) [71, 72, 150]. While the tank may encounter higher thermal loads during certain phases of the mission, for the purposes of conceptual design it is not unreasonable to assume nominal operation during the storage period. Therefore, it can be assumed that the conditions in the tank are maintained such that there is no boiling of the liquid propellant (within the bulk or at the tank walls) or condensation of

the propellant vapor. That is, pressurization is due to evaporation of the propellant at the interface (i.e. self-pressurization).

Regarding the pressure control portion of the storage period, given the complexity of the TVS and that the information on the high-level implementation is not readily available in literature, the model will utilize direct venting as the form of pressure control. This is the current method used by cryogenic upper stages [75, 113]. While the heat and mass transfer in the tank will differ depending on the pressure control method utilized, the overall behavior in the tank pressure is the same as that shown in the pressure plots in Figures 3.6 through 3.9 due to TVS operation. That is, once the maximum pressure limit in the tank is reached the pressure cycles between depressurization and repressurization, until the propellant is needed. From the pressure plots it can also be seen that the time over which depressurization occurs is much shorter, on the order of minutes, than the time required for repressurization of the tank. Therefore it would not be unreasonable to assume that depressurization occurs instantaneously. This would obviate the need to capture the heat and/or mass transfer that occur during depressurization.

From the above discussion, the number of heat and mass transfer processes that must be included in the analysis can be greatly reduced if it is assumed that (1) the tank is subjected to low thermal loads during storage, and (2) depressurization is instantaneous. This mode of operation will be referred to as "ideal operation" and provides the desired simplicity. This idea is presented formally in the following hypothesis:

Hypothesis 1: *If ideal operation within the tank is assumed, then pressurization can be attributed strictly to evaporation of the liquid propellant at the interface, followed by an instantaneous reduction in the tank pressure due to venting of the ullage gas. This will greatly reduce the number of physical processes necessary to analyze the tank.*

The next chapter presents the formulation of the pressurization and venting capabilities for the cryogenic propellant tank model and the subsequent implementation of the two capabilities to form the boil-off model identified in the research objective.

CHAPTER 4
MODEL FORMULATION

Any additional improvement in boil-off estimates must be obtained through modeling of the physical processes in the tank. The literature review showed that relatively few cryogenic propellant tank models are capable of predicting the conditions in the tank during longer missions where pressure control is required. Further, these models are not suitable for conceptual-level studies requiring evaluation of multiple alternative designs. An alternative model was proposed based on the concept of ideal operation, which reduces the number heat and mass transfer processes that must be included in analysis. This proposed model is divided into two separate components – one for tank pressurization and the other strictly for pressure control. Section 4.1 presents the formulation of the self-pressurization component of the model, which leverages the work of E. Ring for pressurization of liquid propellant tanks. Section 4.2 presents the formulation of the venting component, which utilizes thermodynamics to determine mass released during venting. Section 4.3 presents the implementation of both model components to form an extensible boil-off model. The boil-off that occurs within the tank is linked to the propellant loss during venting of the excess pressure, which ultimately provides the desired capability for this dissertation – a higher fidelity estimate of the propellant losses due to boil-off.

4.1 Self-Pressurization

Like the analytical propellant tank models reviewed in the previous chapter, the model developed here will implement the analysis method developed by Ring to evaluate the heat and mass transfer in the tank. The method was developed for the purposes of analyzing the pressure in liquid rocket propellant tanks during all phases of flight. The tank is analyzed using five control volumes – the ullage, bulk liquid, interface, and the dry and wet tank

walls – and includes a total of twelve heat and mass transfer processes, as shown in the propellant tank schematic in Figure B.6. The propellant can be storable, volatile, or cryogenic; pressurization can occur as result of evaporation of the liquid propellant, bulk liquid boiling, and/or from the introduction of a pressurant gas other than the propellant vapor [131]. Since the analysis does not subscribe to a particular tank size or shape, it provides the necessary extensibility listed as the second model requirement that was developed on behalf of the research objective.

A model representing a cryogenic propellant tank undergoing self-pressurization was obtained by making the appropriate modifications to Ring's model in Figure B.6. This included the removal of the bulk liquid boiling ($\dot{m}_{bb}$), the mass flow rates entering ($\dot{m}_{pg}$) and leaving ($\dot{m}_{prop}$) the tank, and the condensation of the propellant vapor on the tank wall ($\dot{m}_{gvw}$) and the interface ($\dot{m}_{gcs}$). The resulting self-pressurizing propellant tank model is illustrated in Figure 4.1. The model allows for different thermal inputs from the surrounding environment to the dry ($\dot{Q}_{ewg}$) and wet tank walls ($\dot{Q}_{ewl}$). The heat entering the ullage and bulk liquid is determined by the heat transfer from the dry and wet tank walls to their corresponding regions ($\dot{Q}_{gw}$ and $\dot{Q}_{lw}$, respectively). Evaporation of the liquid propellant ($\dot{m}_v$) is a result of the net heat transfer from the ullage to the bulk liquid through the interface ($\dot{Q}_{gs}$ - $\dot{Q}_{ls}$).

One of the major disadvantages of utilizing a single node to represent the primary regions in the tank is the inability to capture complex fluid behaviors that influence the physical processes at the interface. Ring's method is no exception. In efforts to capture these complex fluid behaviors, and to further reduce the complexity of the analysis, several adjustments were made to model in Figure 4.1. These modifications are briefly introduced below.

- Removal of the dry and wet tank walls from the analysis: this further simplifies the analysis by reducing the number of control volumes, and therefore the number of equations that need to be evaluated

- The inclusion of the effects of thermal stratification on the heat transfer at the interface:
  - Use of saturated properties, rather than the real gas properties, when evaluating the heat transfer between the ullage and the interface
  - Presumption that a warm thermal layer exists just beneath the interface; this acts to facilitate the evaporation at the interface by impeding the heat transfer to the bulk liquid
- Evaluation of thermodynamic properties:
  - The ullage is modeled as an ideal gas, but real gas properties are implemented in the analysis
  - The bulk liquid is modeled as an incompressible fluid
  - The above fluid properties are evaluated using equations developed from thermodynamic property data

The final form of the self-pressurizing propellant tank model is illustrated in Figure 4.2. The various aspects of the model and the modifications used in its formulation are described in the sections that follow.

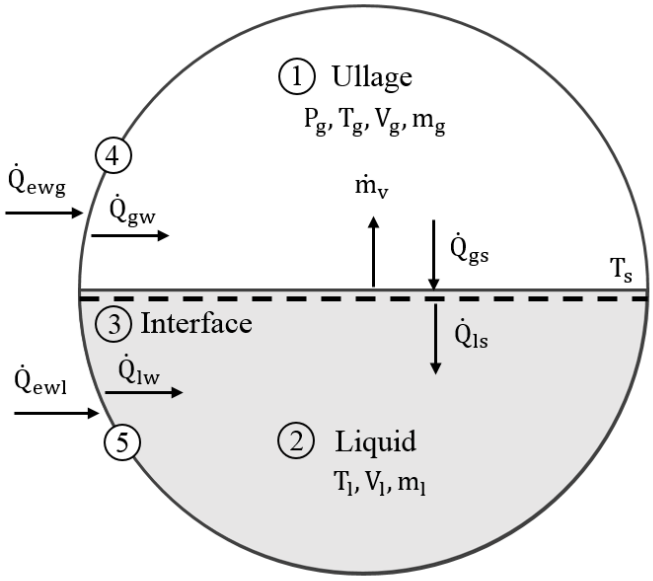

Figure 4.1: Self-pressurizing propellant tank model obtained from modification of the liquid rocket propellant tank model developed by Ring.

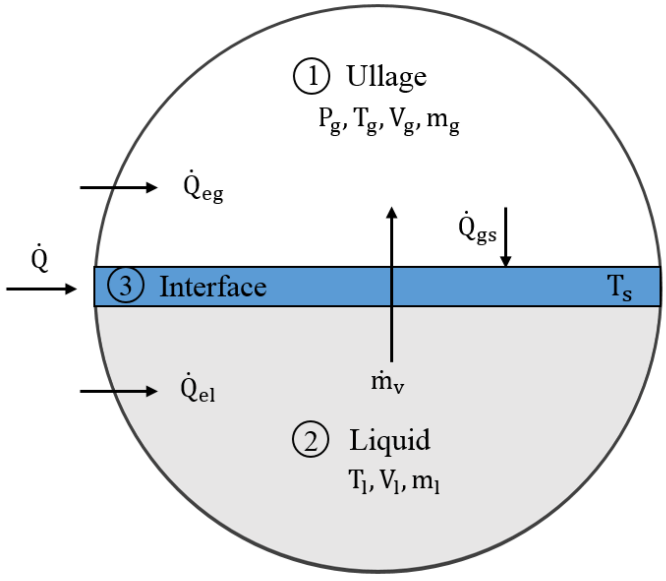

Figure 4.2: Final form of the self-pressurizing propellant tank model.

4.1.1 Analysis Method

The analysis method presented here follows the theory developed by Ring [131], and the implementation of that theory as presented by Estey [49]. A liquid propellant tank consisting of an ideal gas composed entirely of the propellant vapor and an incompressible liquid can be analyzed using the principles of conservation of mass and energy. Realistically, the regions within a self-pressurizing cryogenic tank are subject to heat and mass transfer, and cannot be considered in equilibrium. However, it can be assumed that deviations from equilibrium are small, or that the heat and mass transfer processes occur slowly enough such that the system can be considered to be in quasi-equilibrium. The system can then be evaluated using standard thermodynamic equations [158].

The number of thermodynamic state variables required to specify the (macroscopic) thermodynamic state of a system depends on the number and type of subsystems it possesses [29]. For the subsystem consisting of an ideal gas (the ullage) consisting entirely of the propellant vapor, three of four state variables – pressure, temperature, volume, and mass – must be specified. For the subsystem consisting of a saturated incompressible fluid (the bulk liquid), only two are required if one of the variables is either temperature or pressure, since they are linked through the saturation condition $T_l=T_{sat}(P_l)$ [29]. Similarly, the subsystem consisting of an infinitely thin, saturated interface has a temperature and pressure that are linked through the saturation condition $T_s=T_{sat}(P_g)$. However, the thermodynamic state of the interface can be specified only if the ullage pressure is known. Thus, for all regions comprising the propellant tank system in Figure 4.2, a total of five state variables are required to fully define the thermodynamic state of the tank, with three state variables originating from the ullage, and two state variables originating from the bulk liquid.

If the initial state of the tank is known, the value of each state variable at any time t can be determined when solved as an initial value problem, as in Equation 4.1, where y is the thermodynamic state variable of interest, y_o is the initial value of the state variable, and $\dot{y}$ is the derivative in the state variable [131].

$$y = y_o + \int \dot{y} dt \tag{4.1}$$

The derivatives of the temperature, mass, and volume state variables can be obtained through application of the first law of thermodynamics to the ullage and bulk liquid regions, resulting in a set of ordinary differential equations (ODEs), presented in Equations 4.2 - 4.5 [49]. These equations are not yet fully defined, as denoted by the trailing "..." in each equation. To fully close the problem, the heat and mass transfer rates and the thermodynamic properties of all fluids involved must be determined. Once the heat and mass transfer rates are known, the system of equations can be solved at each time step to provide the new conditions in the tank [49, 131].

$$\dot{m}_g = f_1(m_g, V_g, T_g, m_l, T_g, t, ...) \tag{4.2}$$

$$\dot{V}_g = f_2(m_g, V_g, T_g, m_l, T_g, t, ...) \tag{4.3}$$

$$\dot{T}_g = f_3(m_g, V_g, T_g, m_l, T_g, t, ...) \tag{4.4}$$

$$\dot{T}_l = f_4(m_g, V_g, T_g, m_l, T_l, t, ...) \tag{4.5}$$

Note that while five state variables are required to fully define the system, only four equations appear in the set of ODEs. This is due to the fact that in the self-pressurization process the change in mass in the ullage and bulk liquid regions are equal and opposite of one another, $\dot{m}_g = -\dot{m}_l$. Thus, the equation for the derivative of the bulk liquid mass is redundant and is not included in the final set of ODEs.

The preliminary form of Equations 4.2 through 4.5 are developed in Section 4.1.2. The heat and mass transfer processes within the tank are analyzed in Sections 4.1.3 and 4.1.4, respectively. The method for determining the thermodynamic properties of the gas and bulk liquid is presented in Section 4.1.5. Section 4.1.6 concludes the self-pressurization portion of the analysis, and presents the final form of Equations 4.2 through 4.5.

4.1.2 Governing Equations

Each region in the tank can be modeled as a control volume enclosing an open, unsteady flow process [158]. A mass balance of the control volume provides for the rate of change in the mass and volume state variables. Determination of the rate of change in the temperature state variable is less straightforward and requires manipulation of the equation obtained from conducting an energy balance of the control volume. The general form of the conservation of energy applied to a control volume enclosing an open unsteady process, assuming that changes in the kinetic and potential energies are negligible, can be written as shown in Equation 4.6 [29, 158]. $\dot{Q}_{net}$ represents the net rate of heat transfer into the control volume, $\dot{W}$ is the net rate of work output from the control volume, and $\frac{dE_{cv}}{dt}$ is the rate of change of energy within the control volume. The third and fourth terms in Equation 4.6 represent the energy associated with any incoming and outgoing masses from the control volume. The rate of change in the temperature state variable is obtained through manipulation of $\frac{dE_{cv}}{dt}$ [131].

$$\dot{Q}_{net} + \dot{W} + \sum_{in} \dot{m}h - \sum_{out} \dot{m}h = \frac{dE_{cv}}{dt} \tag{4.6}$$

In the sections that follow, mass and energy balances are applied to each of the control volumes enclosing the ullage, bulk liquid, and interface regions. The heat and mass transfer quantities that appear in the analysis ($\dot{Q}_{eg}$, $\dot{Q}_{el}$, $\dot{Q}_{gs}$, $\dot{m}_v$) are further developed in Sections 4.1.3 and 4.1.4, respectively.

4.1.2.1 Ullage

Application of the conservation of mass to a control volume surrounding the ullage space depicted in Figure 4.2 yields Equations 4.7 and 4.8 for the rate of change in the ullage mass $\dot{m}_g$, and volume $\dot{V}_g$, respectively. The single source of mass transfer in the ullage is due to evaporation at the gas-liquid interface, $\dot{m}_v$. As a consequence of the conservation of

mass, the change in volume of the ullage is equal and opposite the change in the bulk liquid volume $\dot{V}_l$ [131, 158].

$$\dot{m}_g = \sum \dot{m}_{in} - \sum \dot{m}_{out} = \dot{m}_v \tag{4.7}$$

$$\dot{V}_g = -\dot{V}_l \tag{4.8}$$

Application of the conservation of energy to the control volume yields Equations 4.9 - 4.13. The net rate of heat transfer into the ullage space is due to the incoming heat from the external environment, $\dot{Q}_{eg}$, and the outgoing heat to the top surface of the interface, $\dot{Q}_{gs}$. The only work considered is due to the compression or expansion of the ullage gas, where work done by the gas is assigned $-P\dot{V}$ [131]. The evaporated bulk liquid enters the ullage space with an energy $\dot{m}_v h_v$, where h_v is the enthalpy of the mass entering the ullage [49].

$$\dot{Q}_{net} = \dot{Q}_{eg} - \dot{Q}_{gs} \tag{4.9}$$

$$\dot{W} = -\frac{d}{dt}(PV) = -P_g \dot{V}_g \tag{4.10}$$

$$\sum_{in} \dot{m}h = \dot{m}_v h_v \tag{4.11}$$

$$\sum_{out} \dot{m}h = 0 \tag{4.12}$$

$$\frac{dE_{cv}}{dt} = \frac{dU}{dt} = \frac{d}{dt}(m_g u_g) \tag{4.13}$$

The change in energy within the ullage is due to the change the in internal energy of the ullage as a result of (1) the change in mass within the control volume and (2) the change in the temperature within the control volume [131]. These two contributions to $\frac{dU}{dt}$ are represented by the first and second terms in Equation 4.14, respectively. For an ideal gas, the internal energy is directly related to the temperature via $u = mc_vT$, and Equation 4.14 can be rewritten as Equation 4.15 [131]. Substitution of Equations 4.9 - 4.12 and Equation 4.15

into Equation 4.6 yields Equation 4.16. Finally, rearrangement of Equation 4.16 provides an expression for the change in temperature in the ullage, as shown in Equation 4.17.

$$\frac{d}{dt}(m_g u_g) = \dot{m}_g u_g + m_g \dot{u}_g \tag{4.14}$$

$$= \dot{m}_g u_g + m_g c_{v,g} \dot{T}_g \tag{4.15}$$

$$\dot{Q}_{eg} - \dot{Q}_{gs} - P_g \dot{V}_g + \dot{m}_v h_v = \dot{m}_g u_g + m_g c_{v,g} \dot{T}_g \tag{4.16}$$

$$\dot{T}_g = \frac{\dot{Q}_{eg} - \dot{Q}_{gs} - P_g \dot{V}_g + \dot{m}_v h_v - \dot{m}_g u_g}{m_g c_{v,g}} \tag{4.17}$$

4.1.2.2 Bulk Liquid

Application of the conservation of mass to a control volume enclosing the bulk liquid region yields Equations 4.18 and 4.19 for the rate of change in the bulk liquid mass $\dot{m}_l$, and volume $\dot{V}_l$, respectively. The single source of mass transfer is due to the mass leaving the bulk liquid through the bottom side of the interface, $\dot{m}_v$. The change in volume of the bulk liquid is due to the change in mass of the bulk liquid [131].

$$\dot{m}_l = \sum \dot{m}_{in} - \sum \dot{m}_{out} = -\dot{m}_v \tag{4.18}$$

$$\dot{V}_l = \frac{\dot{m}_l}{\rho_l} \tag{4.19}$$

Application of the conservation of energy to the bulk liquid control volume yields Equations 4.20 - 4.24. The net rate of heat transfer into the bulk liquid volume is due solely to the incoming heat from the surrounding thermal environment, $\dot{Q}_{el}$. As with the ullage, only work due to compression or expansion is considered [131]. For the bulk liquid, this is $P_l \dot{V}_l$. The mass leaving the control volumes leaves with an energy of $\dot{m}_v h_l$, where h_l is the enthalpy of the mass leaving the bulk liquid [49]. The rate of change of energy within the control volume is due to the change in internal energy as a result of the change in the mass

and the change in temperature within the control volume, represented by $\dot{m}_l u_l$ and $m_l c_{p,l} \dot{T}_l$, respectively [131]. Substitution of Equations 4.20 through 4.24 into Equation 4.6, followed by rearrangement for $\dot{T}_l$ provides the final expression for the rate of change of temperature of the bulk liquid region, as shown in Equation 4.25

$$\dot{Q}_{net} = \dot{Q}_{el} \tag{4.20}$$

$$\dot{W} = \frac{d}{dt}(PV) = P_l \dot{V}_l \tag{4.21}$$

$$\sum_{in} \dot{m} h = 0 \tag{4.22}$$

$$\sum_{out} \dot{m} h = \dot{m}_v h_l \tag{4.23}$$

$$\frac{dE_{cv}}{dt} = \dot{m}_l u_l + m_l c_{p,l} \dot{T}_l \tag{4.24}$$

$$\dot{T}_l = \frac{\dot{Q}_{el} + P_l \dot{V}_l - \dot{m}_v h_l - \dot{m}_l u_l}{m_l c_{p,l}} \tag{4.25}$$

4.1.2.3 Interface

The approach commonly used in literature is to model the interface as an infinitely thin layer of saturated propellant located at the top surface of the bulk liquid [22, 36, 49, 131, 158]. This allows for the exchange of mass and energy between the ullage and bulk liquid regions; any work done by the ullage is assumed to be transmitted directly to the bulk liquid [49]. Because the interface contains no mass, its temperature cannot be obtained through the same process that was used for the ullage and bulk liquid [49]. For cryogenic propellants, the interface is assumed to be saturated with a temperature T_s, corresponding to the partial pressure of the liquid vapor in the ullage space. For a system comprised solely of a propellant and its vapor, as in this case, the temperature is determined by the ullage pressure, as shown in Equation 4.26 [34, 131].

$$T_s = T_{sat}(P_g) \tag{4.26}$$

4.1.3 Heat Transfer

The primary form of heat transfer within the tank occurs via natural convection [131]. The rate of heat transfer is a function of the heat transfer coefficient h_c, the contact area A through which the heat transfer occurs, and the temperature difference ΔT between the fluid and surface exchanging heat, as shown in Equation 4.27. The heat transfer coefficient is determined using the correlation in Equation 4.28 [10]. The values of the constants C and n are typically obtained with the aid of an empirical relationship developed from experimental data of the heat flux rate versus X for the system in question [55, 131], or a similar system [36]. Typically, the values of C and n for heat transfer between a fluid and a vertical or horizontal surface are used [10, 131]. The Prandtl-Grashof product X, presented in Equation 4.29, is a function of the local acceleration a, the characteristic length L_s, and the fluid properties, where β is the coefficient of thermal expansion, c_p is the specifc heat at constant pressure, μ is the dynamic viscosity, ρ is the density, and κ is the thermal conductivity [10].

$$\dot{Q} = h_c A \Delta T \tag{4.27}$$

$$h_c = C \frac{k}{L_s} X^n \tag{4.28}$$

$$X = \left(\frac{L_s^3 \rho^2 a \beta \left| \Delta T \right|}{\mu^2} \right) \left(\frac{c_p \mu}{k} \right) \tag{4.29}$$

4.1.3.1 Tank Walls

The tank wall affects the heat transfer from the surrounding thermal environment to the interior of the tank [131, 150]; a portion of the incoming heat goes towards heating of the

tank material, thus reducing the heat transfer to the ullage and bulk liquid regions. Per the analysis method of Ring [131], evaluating the net heat transfer from the surrounding environment, through the tank wall, and to the interior of the tank requires a total of fifteen equations. The appropriate form of Equations 4.27 through 4.29 are required to evaluate the heat transfer on either side of the dry and wet tank walls ($\dot{Q}_{ewg}$, $\dot{Q}_{gw}$, $\dot{Q}_{ewl}$, and $\dot{Q}_{lw}$ in Figure 4.1). In order to determine these heat transfer quantities, the temperatures of the dry and wet tank walls must also be determined through Equations 4.30 through 4.32 below [131].

$$T_{wg} = T_{wg,i} + \int_{t_1}^{t_2} \frac{\dot{Q}_{ewg} - \dot{Q}_{gw} + c_{p,wl}(T_{wl} - T_{wg})\dot{m}_{wg}}{m_{wg}c_{p,wg}} dt \tag{4.30}$$

$$m_{wg} = m_{wg,i} + \int_{t1}^{t_2} \dot{m}_{wg} dt \tag{4.31}$$

$$T_{wl} = T_{wl,i} + \int_{t_1}^{t_2} \frac{\dot{Q}_{ewl} - \dot{Q}_{lw}}{m_{wl}c_{p,wg}} dt \tag{4.32}$$

The subscripts "wg" and "lg" represent quantities corresponding to the dry (the wall adjacent to the ullage gas) and wet (the wall adjacent to the liquid) tank walls, respectively. The temperature of the dry tank wall T_{wg} at any time is calculated using Equation 4.30. Within the integral, the first and second terms represent the net heat transfer through the tank wall; the third term in the integral represents the heat required to increase the temperature of the newly exposed tank wall (from propellant evaporation due to boil-off or propellant outflow during engine firing), where T_{wg} and T_{wl} take the values from the previous time step [131]. The mass of the dry tank wall which appears in the denominator is determined from Equation 4.31, where the change in mass due to the newly exposed tank wall $\dot{m}_{wg}$ is found by relating the change in volume in the ullage to region to the change in the liquid height of the propellant. The temperature of the wet tank wall is determined in a

similar manner via Equation 4.32 [131].

From the above discussion, a considerable portion of the analysis is dedicated to evaluating the heat transfer at the tank wall. However, under certain conditions, it may not be necessary to include the tank wall in the analysis. For a series of LH_2 self-pressurization experiments conducted by Van Dresar et al.[1] [150], the authors reported that due to the low temperature of the liquid propellant, the portion of the tank wall that was in contact with the liquid was at the same or a similar temperature as the propellant; the heat transfer from the environment had a little to no effect on the tank wall. The authors also reported that approximately 3% to 7% of the total heat entering the tank contributed to heating of the dry tank wall, with the higher percentages corresponding to low propellant fill levels [150].

For the case of self-pressurization due to a low thermal load, the tank walls add a degree of complexity to the analysis when the benefits of doing so appear minimal. Based on the observations made by Van Dresar et al. [150], the incoming heat can be considered to penetrate the wet tank wall and enter the bulk liquid directly; and while the heat that is intercepted by the dry tank wall is not negligible, it is small compared to the heat that enters the tank. Therefore, the model developed here omits the dry and wet tank walls from the analysis. This reduces the the number of control volumes from the five illustrated in Figure 4.1, to the three in Figure 4.2.

The heat transfer from the surrounding environment to the interior of the tank can now be evaluated as follows: the thermal load on the tank $\dot{Q}$ is assumed constant and uniformly distributed around the tank. For a tank with surface area A_{tank}, this corresponds to a heat flux rate of $\dot{Q}/A_{tank}$. The amount of heat entering the ullage and bulk liquid regions is determined by their respective contact areas with the tank wall, denoted by A_{gw} and A_{lw} in Equations 4.33 and 4.34, respectively.

$$\dot{Q}_{eg} = \frac{\dot{Q}}{A_{tank}} A_{gw} \tag{4.33}$$

[1] These experiments were introduced in Section 3.3.3.2 of the literature review.

$$\dot{Q}_{el} = \frac{\dot{Q}}{A_{tank}} A_{lw} \tag{4.34}$$

This analysis reduces the number of equations required to evaluate the heat transfer from the environment to the interior of the tank from fifteen (per Ring's analysis) to two. This excludes the equations for determining the surface area of the dry and wet tank walls, which are necessary in either case. These surface areas are calculated using standard mathematical formulas for spherical, elliptical, and cylindrical geometries, and are re-evaluated as the liquid level in the tank changes with time. These equations are provided in Appendix C.

4.1.3.2 Interface

One of the major disadvantages of utilizing a single node to represent any individual region is the inability to capture complex fluid behaviors [102, 105]. One such behavior is the heat transfer at the interface, which is intimately associated with the thermal stratification that develops within the tank [34]. In order to accurately model thermal stratification and capture the heat transfer at the interface, experimental data of the tank in question is greatly desired [36]. For the conceptual design process, where numerous vehicle configurations are evaluated, this is just not feasible. Alternatively, thermal stratification can be captured by increasing the number of control volumes used to analyze the ullage and bulk liquid regions, but this would significantly increase the complexity of the analysis [102]. Another option is to implement a few modifications, based on logical assumptions.

Recall from Chapter 2 that the heat entering the tank causes a temperature gradient to develop on either side of the interface [23, 34, 51]. Located immediately below the interface is a warm thermal layer, which increases in thickness with time. The thermal layer acts to facilitate evaporation by reducing the heat transfer from interface to the bulk liquid [14] (Figure 2.8b). The time required for the thermal layer to develop (i.e. for the thermal gradient within the bulk liquid to become time invariant) increases with the propellant fill

level and the tank capacity. For the experiments performed by Van Dresar et al. [150] in a 4.89 m^3 tank using heat fluxes of 2.0 W/m^2 and 3.5 W/m^2, the thermal gradient was established within first five hours of the experiment (this period corresponds to the initial transient in the pressure curves in Figure 2.5).

The results from these experiments suggest that for storage periods greater than a few hours, the thermal layer at the interface can be considered developed (or at the very least, the effect due to the presence of the thermal layer can be considered active). Further, given that the thermal layer increases in thickness with time, it is reasonable to assume that the heat transfer from the ullage to the interface is much greater than the heat transfer from the interface to the bulk liquid, $\dot{Q}_{gs} >> \dot{Q}_{ls}$.

For the model developed here, it is assumed that due to thermal stratification the heat transfer at the interface occurs as a result of the heat transfer from the ullage region alone. This heat transfer process is described by Equation 4.35 [10], where h_{gs} is the heat transfer coefficient, A_s is the area of the interface, and T_g and T_s are the temperatures of the ullage and the interface, respectively. The heating configuration presented by the ullage gas and the interface is that of a warmer fluid above a cooler surface. For this configuration, the correlation constants in Equation 4.28 take the values of C = 0.27 and n = 1/4 [10, 108].

For heat transfer between a fluid (ullage gas) and a surface (interface) with an appreciable temperature difference, a condition which occurs in self-pressurizing tanks with extended storage periods, the standard approach in literature is to evaluate the heat transfer coefficient using the fluid properties at the mean film temperature T_m (the average of the ullage and interface temperatures) [10]. However, experiments have shown that due to thermal stratification in the ullage region, the propellant vapor near the interface exhibits a temperature similar to that of the interface [150] (Figures 2.3 and 2.4). Given that the interface exists at a temperature and pressure of $T = T_{sat}(P_g)$, if the ullage gas which is at the same pressure P_g also exists at the same temperature T, then the ullage must also be saturated. The heat transfer coefficient in Equation 4.36 is evaluated using the saturated

properties, denoted by the subscript "g,sat", rather than the real gas properties of the ullage gas. Note that this approach remains valid as long as the mean film temperature is below the critical temperature.

$$\dot{Q}_{gs} = h_{gs} A_s (T_g - T_s) \tag{4.35}$$

$$h_{gs} = 0.27 \frac{k_{g,sat}}{L_s} X_{g,sat}^{1/4} \Big|_{T_m} \tag{4.36}$$

4.1.4 Mass Transfer at the Interface

The mass transfer that occurs at the interface is best described using the model presented by Estey [49]. Recall that the interface is thin and massless, and is the means by which heat and mass are exchanged between the ullage and bulk liquid regions. These physical processes are depicted in more detail in Figure 4.3. Evaluation of the mass transfer requires application of the conservation of energy to the control volume enclosing the interface, resulting in Equation 4.37 [49]. Since the interface is massless, it contains no energy ($\frac{dE}{dt} = 0$) and performs no work ($\dot{W} = 0$). The liquid mass enters the control volume at a rate $\dot{m}_v$, and with energy $\dot{m}_v h_l$. This mass is evaporated due to the incoming heat from the ullage $\dot{Q}_{gs}$, and leaves the interface with energy $\dot{m}_v h_v$. Recognizing that the enthalpy associated with the mass leaving the interface h_v is equivalent to the enthalpy of the ullage gas h_g, Equation 4.37 can be rearranged to provide an expression for the liquid propellant evaporation that occurs at the interface, as shown in Equation 4.38 [49].

$$\dot{Q}_{gs} + \dot{m}_v h_l - \dot{m}_v h_v = 0 \tag{4.37}$$

$$\dot{m}_v = \frac{\dot{Q}_{gs}}{h_g - h_l} \tag{4.38}$$

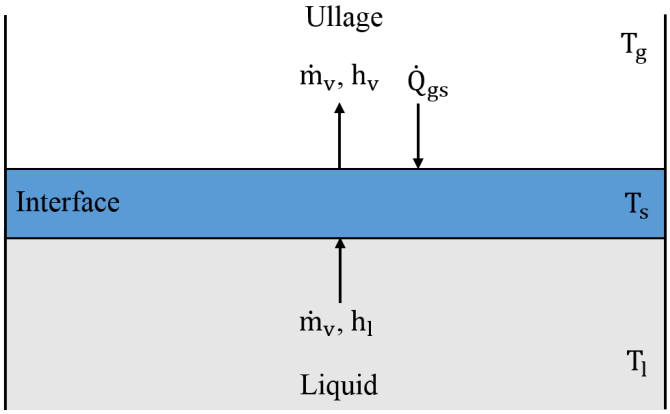

Figure 4.3: Evaporation model (adapted from [49]).

In order to better illustrate the physical processes occurring during evaporation of the bulk liquid, the term $h_g - h_l$ can be expanded, as shown in Equations 4.39 and 4.40 [49]. For evaporation of the bulk liquid to occur, the temperature of the liquid must first be raised from T_l, to the interface temperature T_s. The energy required for this temperature change is represented by the first term in Equation 4.40. The second term in Equation 4.40 represents the energy required for the phase change. Once the phase change has concluded, the temperature of the newly evaporated propellant (still at temperature T_s) must be raised to that of the ullage temperature T_g, in order for the propellant vapor to join the ullage space. The energy required for this temperature change is represented by the third term in Equation 4.40. Thus, the quantity $\dot{Q}_{gs} - \dot{Q}_{ls}$ contributes to three processes at the interface: heating of the bulk liquid, evaporation, and heating of newly evaporated propellant. By combining Equations 4.38 and 4.40, the relation for the bulk liquid evaporation can be written as shown in Equation 4.41 [49].

$$h_g - h_l = \Delta h_{l\to ls} + \Delta h_{ls\to gs} + \Delta h_{gs\to g} \tag{4.39}$$

$$= c_{p,l}(T_s - T_l) + h_{vap} + (c_{v,g} + R_u)(T_g - T_s) \tag{4.40}$$

$$\dot{m}_v = \frac{\dot{Q}_{gs}}{c_{p,l}(T_s - T_l) + h_{vap} + (c_{v,g} + R_u)(T_g - T_s)} \tag{4.41}$$

Equation 4.41 is the desired higher-fidelity representation of the boil-off rate equation used in conceptual design (Equation 1.1), where the heat entering the tank $\dot{Q}$ has been replaced with the heat transfer at the interface $\dot{Q}_{gs}$. Given that the heat transfer at the interface is a function of the area of the interface (Equation 4.35), $\dot{Q}_{gs}$ inherently captures the effects of the tank geometry and the amount of propellant in the tank on the rate at which the propellant boils-off.

4.1.5 Thermodynamic Properties

Thermodynamic properties can be determined from a variety of methods. Techniques range from use of data tables of measured quantities to utilization of sophisticated equation-of-state based software programs. The technique should be selected based on the number of chemical components and phases involved, the pressure and temperature ranges required, the availability of the data, and the desired accuracy [158].

For the single component two-phase system consisting of GH_2/LH_2, data was readily available. The thermodynamic properties of hydrogen were obtained from the NIST Chemistry WebBook for Thermophysical Properties of Fluid Systems [92]. Saturated data was collected for the temperature range of approximately 18 K - 30 K, in increments of 0.03 K. Data for the real gas properties (c_v, u, and h) was collected for the pressure range of 0.10 MPa to 0.75 MPa, in pressure increments of 0.01 MPa, for the temperature range of approximately 20 K to 150 K.

Results from preliminary investigations showed that using methods that either extracted or interpolated data from property tables were prohibitive, requiring evaluation times on the order of minutes. In order to reduce the computational time, equations for the thermodynamic properties were developed using JMP statistical analysis software. Curve fits for the saturated thermodynamic properties were obtained using a total of 472 data points for each property. Saturated property equations are listed in Appendix E.6. Equations for the real gas properties of hydrogen were obtained using artificial neural networks (NN). Each NN

was trained using 9,874 points, with 2,469 points used for model validation. The resulting R^2 values for the validations were R^2 = 0.999 for c_v, and R^2 = 1 for u and h. The error and predictive accuracy for each of the NN fits is available in Appendix D. The equations obtained from the NN fits are listed in Appendix E.7.

4.1.6 Final System of Equations

Analysis of the ullage and bulk liquid control volumes in Section 4.1.2 provided the governing equations for the derivatives of the mass, temperature, and volume state variables presented in Equations 4.2 through 4.5. Subsequent analysis of the heat and mass transfer processes within the tank provided the remaining quantities in order to fully define these equations, resulting in the set of first order ODEs presented in Equations 4.42 through 4.45. The heat transfer quantities $\dot{Q}_{eg}$, $\dot{Q}_{el}$, and $\dot{Q}_{gs}$ are defined by Equations 4.33, 4.34, and 4.35, respectively. The quantities h_g and $h_{g,sat}$ correspond to the enthalpies of the ullage gas at the ullage temperature T_g, and the saturated gas near the interface with a temperature T_s, respectively. The equations can be further simplified through substitution of $\dot{m}_v = \dot{m}_g$ and $\dot{m}_v = -\dot{m}_l$. However, it is beneficial to be able to differentiate which processes are due to the exchange between regions ($\dot{m}_v$) versus those occurring within region itself ($\dot{m}_g$ and $\dot{m}_l$).

$$\dot{m}_g = \frac{\dot{Q}_{gs}}{c_{p,l}(T_s - T_l) + h_{vap} + (h_g - h_{g,sat})} \tag{4.42}$$

$$\dot{T}_g = \frac{\dot{Q}_{eg} - \dot{Q}_{gs} + \dot{m}_v h_g - P_g \dot{V}_g - \dot{m}_g u_g}{m_g c_{v,g}} \tag{4.43}$$

$$\dot{T}_l = \frac{\dot{Q}_{el} - \dot{m}_v h_l + P_l \dot{V}_l + \dot{m}_l u_l}{\rho_l V_l c_{p,l}} \tag{4.44}$$

$$\dot{V}_g = \frac{\dot{m}_v}{\rho_l} = -\dot{V}_l \tag{4.45}$$

4.2 Venting

Venting of cryogenic propellant tanks is accomplished by first settling the tank to ensure that the liquid propellant is located away from the vent [87, 105]. The ullage gas is then released until the desired pressure is reached [66]. The conditions in the tank when the maximum pressure is reached is provided by the self-pressurization component of the model. The information now required in order to complete the venting component is the mass released during venting, and the conditions in the tank once venting has concluded. This leads to the following research question:

Research Question 2: How can the mass released during venting, and the subsequent conditions in the tank be determined?

Section 4.2.1 examines the traditional approach utilized in literature for estimating propellant losses due to venting. This approach was initially introduced in Chapter 1. Here, the underlying assumptions behind the method are presented, and the corresponding estimates compared with observations from venting experiments in literature. Section 4.2.2 presents an alternative approach for modeling the venting process by representing the ullage as an insulated thermodynamic system, which provides the information required in order to complete the pressure control component of the model.

4.2.1 Traditional Approach in Literature

The familiar theoretical expression for estimating the propellant losses due to boil-off is presented in Equation 4.46. As discussed in Chapter 1, this expression assumes that the heat entering the tank goes directly towards evaporation of the bulk liquid propellant, and further, that the rate of evaporation is equal to the mass flow rate of the escaping gas at the vent [83]. The lesser-known assumptions associated with Equation 4.46, are that the ullage and bulk liquid are both saturated, with a temperature corresponding to the tank pressure. During venting, the tank is in steady state, with the exception of the evaporation that occurs at the interface. The gas that leaves the tank is saturated, and the specific volume of the

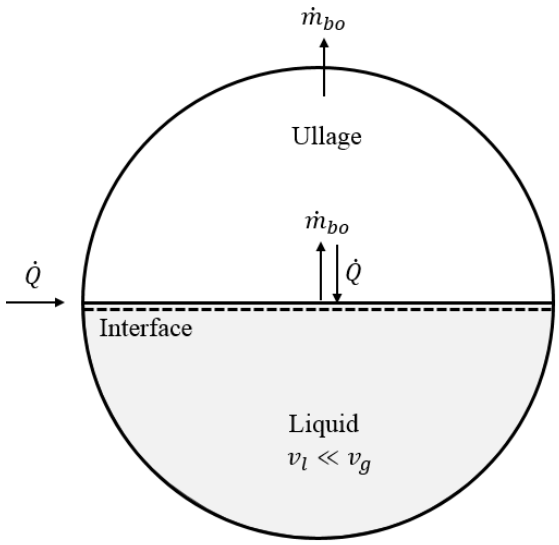

Figure 4.4: Standard scenario for estimating the propellant loss due to venting. The heat $\dot{Q}$ entering the tank contributes directly towards evaporation of the liquid propellant, where the rate of the evaporation is assumed to be equivalent to the rate at which the tank is vented.

bulk liquid is much, much smaller than the specific volume of the gas, $v_l << v_g$ [7, 83]. This scenario is depicted in Figure 4.4.

$$\dot{m}_{bo} = \frac{\dot{Q}}{h_{vap}} \tag{4.46}$$

Several experiments carried out by Aydelott and Spuckler [7] in a 56 cm diameter spherical LH_2 tank examined the validity of these assumptions, and compared the venting rate predicted by Equation 4.46 with the rate obtained from experiment. Experiments were conducted using heat flux rates of 74.1 W/m^2 and 275.7 W/m^2, at a propellant fill level of 65%. The tank was closed and allowed self-pressurize. When the pressure reached 345 kPa, the valve was opened and the tank allowed to vent until the pressure decreased to approximately 310 kPa. Venting cycles were repeated until the end of experiment was reached.

Results from the venting experiments demonstrated that the theoretical method largely overestimates the mass flow rates during venting, by as much two times the values observed

during experiment. The primary cause is attributed to venting of superheated, rather than saturated gas [7, 93, 118]. In reality, the gas that occupies the ullage space is not saturated and experiences thermal stratification [71, 72, 150]. For the case of a settled tank, venting releases not only superheated gas, but also releases the warmer gas located at or near the vent. An additional cause for the difference between the theoretical and experimental values is the departure from steady-state conditions. During the experiment, there was significant variation in the ullage temperature, by as much 100 K. The bulk liquid temperature also increased for the duration of the experiment, although to a lesser extent. Lastly, for the case of hydrogen, the assumption that $v_l << v_g$ is valid at atmospheric pressure, where v_l is approximately 1% of v_g. However, the assumption becomes less valid as the tank pressure increases, since the specific volume of the gas decreases, whereas the specific volume of the liquid remains relatively constant. For the maximum pressure of 345 kPa observed during experiment, v_l was approximately 6.5% of v_g [7].

While the theoretical model provides a simple and convenient method for estimating the mass flow rate during venting, the actual conditions in the tank are not representative of the conditions assumed by the model, particularly the state of the vented gas, which results in poor estimates for the propellant mass released during venting. Further, due to the steady-state assumption, the venting process releases gas at a constant pressure, rather than releasing gas until the desired pressure reduction is achieved. Additionally, the key assumption of the model – that the heat entering the tank is directly responsible for evaporation of the liquid propellant – is not listed by Aydelott and Spuckler as one of the assumptions responsible for the poor correlation between experimental and model values. Yet, several models surveyed in the literature review [22, 36, 102], as well as numerous propellant tank models in literature [9, 12, 101, 105, 121, 131, 158] have shown that the evaporation of the liquid propellant is due to a portion of the heat that enters the tank, and not the entire quantity. Thus, the standard method is not suitable for estimating the propellant mass released during venting, or for providing the conditions in the tank after

venting has concluded.

4.2.2 Venting Using an Analogous Thermodynamic System

Recall from Chapter 3 that for extended storage durations, the tank goes through an initial period of self-pressurization, followed by cycling between depressurization and repressurization due to the pressure control device, as shown in Figure 4.5. The conditions in the tank for the initial period of self-pressurization, including the instant when P_{max} is reached, is provided by the self-pressurization component of the model that was developed in Section 4.1. The information now required is the mass released during venting of the tank pressure from P_{max} to P_{min}, and the conditions in the tank at P_{min} once venting has concluded.

Consider the following assumptions:

1. The venting processes releases gas only
2. Venting is immediate and does not affect the bulk liquid temperature
3. The gas is in thermodynamic equilibrium just prior to, and immediately after venting
4. Immediately after venting, the ullage is saturated with pressure P_{min} and temperature $T = T_{sat}(P_{min})$

Because venting is immediate, the heat transfer between the ullage, the surrounding environment, and the interface can be excluded from the analysis. By assuming that venting releases gas only and that the bulk liquid is undisturbed, the bulk liquid can also be excluded. Thus, the first and second assumptions act to restrict the analysis to the ullage space alone. The third assumption is reasonable given that tank is presumed to be in quasi-equilibrium for the duration of the analysis [36, 72, 131], and allows for the determination of the mass released during venting without the need to examine the venting process itself. In other words, if the thermodynamic state of the ullage at the beginning and end of the venting process is known, then the mass removed from the system in order to cause the observed change can be determined [68]. The final thermodynamic state of the ullage is

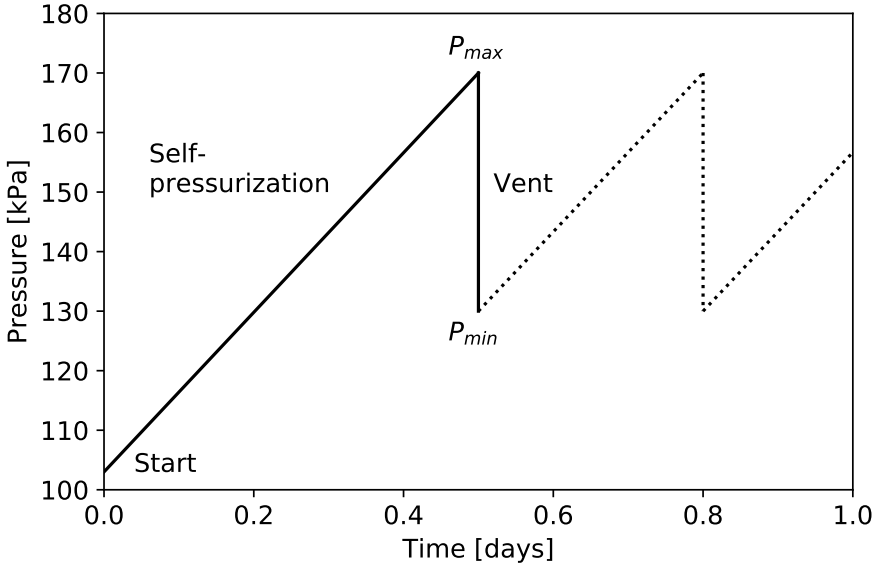

Figure 4.5: Pressure changes experienced by a cryogenic propellant tank over the course of a notional mission.

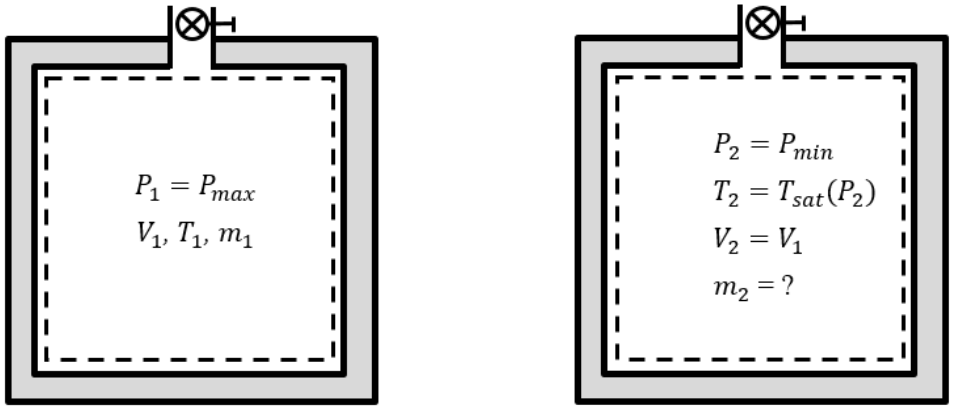

(a) State 1

(b) State 2

Figure 4.6: A thermodynamic system consisting of an insulated container and an ideal gas, representing the conditions in the ullage (a) immediately prior to, and (b) immediately after venting.

provided by the fourth assumption which states that immediately after venting the ullage consists of a saturated gas. This assumption has been used in theoretical analysis of mixing [96], TVS operation [96], and direct venting [7, 96]. These assumptions allow for the formulation of the venting capability, which is presented in the following hypothesis:

Hypothesis 2: *If the ullage is modeled as a thermodynamic system consisting of an ideal gas in an insulated container in thermodynamic equilibrium just prior to, and immediately after venting, and further, if the state of the gas after venting is assumed saturated, then the final conditions in the tank and the mass released during venting can be determined.*

Figure 4.6 depicts the thermodynamic system representing the change in the ullage due to the venting process. State 1 represents the conditions in the ullage when the maximum pressure limit is reached, denoted by P_1, T_1, V_1, and m_1. State 2 represents the conditions in the ullage just after venting has concluded, denoted by P_2, T_2, V_2, and m_2. While the final thermodynamic state of the system has been defined by Hypothesis 2, the final system mass must still be determined. The mass can be determined by applying the ideal gas equation to states 1 and 2, as shown in Equations 4.47 and 4.48, respectively, where R_u is the universal gas constant, and M is the molecular weight of the propellant. Equations 4.47 and 4.48 can be rearranged to provide expressions for V_1 and V_2, as shown in Equations 4.49 and 4.50, respectively. Since the volume for states 1 and 2 are equivalent, the expression for the system mass at state 2 can be obtained by setting the right-hand side of Equations 4.49 and 4.50 equal to one another, and subsequently solving for m_2, as shown in Equation 4.51. Finally, the mass released during the venting process, m_{vent}, can be determined by subtracting the mass of the system at state 1 (before venting has occurred), from state 2 (after venting has occurred). This expression is provided in Equation 4.52.

$$P_1 V_1 = \frac{m_1 R_u T_1}{M_1} \tag{4.47}$$

$$P_2 V_2 = \frac{m_2 R_u T_2}{M_2} \tag{4.48}$$

$$V_1 = \frac{m_1 R_u T_1}{P_1 M_1} \tag{4.49}$$

$$V_2 = \frac{m_2 R_u T_2}{P_2 M_2} \tag{4.50}$$

$$m_2 = \frac{P_2 T_1 m_1}{P_1 T_2} \tag{4.51}$$

$$m_{vent} = m_1 - m_2 \tag{4.52}$$

4.3 Implementation

A high-level overview of the extensible boil-off model is presented in Figure 4.7. The model consists of two primary components: a self-pressurization component and a venting component. The crux of the model is formed by the self-pressurization component, represented by the inner loop (denoted by ①) in Figure 4.7. For each time step, a set of tank conditions is received, the thermodynamic processes within the tank are evaluated, and the tank conditions are subsequently updated. Self-pressurization continues as long as the tank pressure is less than the maximum pressure limit. If the maximum pressure limit is reached, venting is initiated, and the model follows path ② along the outer loop. The conditions in the ullage are then updated and passed on to the next iteration, and self-pressurization is resumed. For each venting event, the mass vented is tracked, with the total at the end of the simulation representing the boil-off losses for the mission.

The code for the boil-off model is listed in Appendix E. The model is written in Python and utilizes the solve_ivp module from SciPy's integrate subpackage to numerically integrate the system of ODEs formed by Equations 4.42 through 4.45. The default integration method (LSODA) is used. The solver is robust and provides accuracy in solutions to the fourth decimal place for time steps as small as 0.1 seconds and as large as 60 minutes if venting does not occur. For standard simulations consisting of self-pressurization and

venting, a time step of 10 seconds is used.

A detailed description of the model is as follows: The model requires a total of 11 input variables. Two variables are provided by the vehicle mission – the storage or flight time t, and the heat flux rate $\dot{Q}$ on the tank based on the thermal environment encountered by the vehicle. Three variables are required to specify the tank geometry: shape, diameter, and height. The tank shape can be spherical or cylindrical, where the end caps on cylindrical tanks can be hemispherical or 2:1 elliptical. Another three variables are required to specify the initial conditions in the tank: pressure P_o, temperature T_o, and propellant fill level FL_o. Because the tank is initially assumed to be in thermal equilibrium ($T_g = T_l = T_o$), only the initial temperature or pressure needs to be specified. The value of the remaining variables is determined from the saturation condition, $T = T_{\text{sat}}(P_{\text{g}})$. The final two input variables P_{max} and P_{min} govern the venting process. Together, P_{max} and P_{min} form the operational pressure band for the venting process. Once the pressure in the tank reaches P_{max}, the venting process is initiated. An amount of gas is released such that the final pressure in the tank at the end of the process is equal to P_{min}.

The tank geometry and initial conditions in the tank are sent to the self-pressurization component of the model where the thermodynamic processes within the tank are evaluated. Based on the pressure and temperature in the tank, the thermodynamic properties in each of the ullage, bulk liquid, and interface regions are determined. The propellant fill level allows for the determination of the liquid height in the tank, which provides the location of the interface. From this information, the area of the interface (A_s) and the characteristic length (L_s) are determined, as well as the surface areas of the dry (A_{gw}) and wet (A_{lw}) tank walls. With the thermodynamic properties and the area of the interface now known, the heat transfer coefficient (h_{gs}) can be evaluated, and the heat transfer rates into the ullage ($\dot{Q}_{eg}$), bulk liquid ($\dot{Q}_{el}$), and across the interface can be determined ($\dot{Q}_{gs}$). Next, the system of ODEs is solved, the state variables in the tank are updated (m_g, V_g, T_g, and m_l), and the next iteration begins with the updated conditions serving as the initial tank state. Self-

pressurization continues until P_{max} is reached, or the mission time has elapsed. In the case of venting, the venting process occurs as described in Section 4.2.2. The mass released for each venting event is tracked, with the value at the end of the simulation representing the propellant mass lost due to boil-off over the course of the mission.

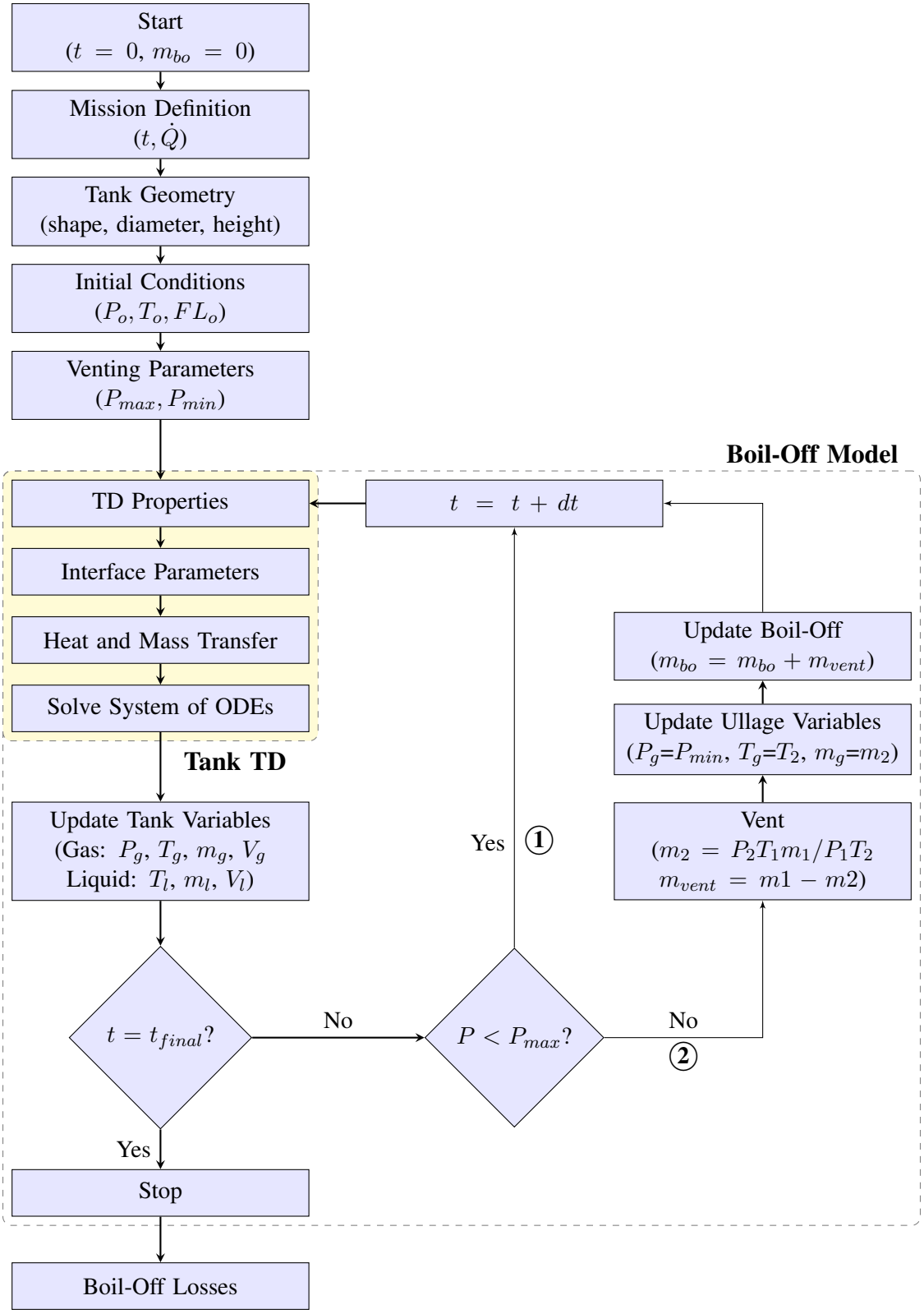

Figure 4.7: High-level overview of the boil-off model, including the logic for the self-pressurization and venting processes, represented by loops 1 and 2, respectively.

4.4 Summary

This chapter presented the formulation of a physics-based model capable of providing higher fidelity estimates of the propellant mass lost due to boil-off. The first portion of the chapter focused on the development of the self-pressurization component of the model. For a tank with a specified geometry, the model takes in an input value for the heat transfer from the surrounding environment $\dot{Q}$, and predicts the increase in the tank pressure due to heating of the ullage and boil-off of the liquid propellant, where boil-off occurs as a result of the heat transfer from the warmer ullage to the cooler interface. The second portion of the chapter focused on the development of the venting component. Research Question 2 was posed regarding how the venting process should be modeled so that the mass released during venting and the subsequent conditions in the tank could be determined. It was found that the standard theoretical approach utilized in literature for modeling the venting process provides poor estimates of the mass loss during venting due to strict assumptions regarding the internal state of the tank. An alternative approach was developed based on the hypothesis that the venting process can be captured by modeling the ullage as an ideal gas in an insulated container. The conditions in the tank once venting has concluded serve as the input conditions for the next self-pressurization cycle; the total mass released during venting is equal to the propellant mass loss due to boil-off, which is utilized in the vehicle sizing process – m_{bo} in Equation 1.6. Integration of the two model components allows for the prediction of the propellant losses incurred due to boil-off over the course of the mission, where for a particular tank boil-off is a function of the heat transfer rate $\dot{Q}$, propellant fill level FL, and the mission time, t.

CHAPTER 5
MODEL EVALUATION

The previous chapter presented the formulation of a simplified cryogenic propellant tank model capable of predicting the conditions in the tank during longer missions where pressure control is required. The model was formulated based on the hypothesis that the physical processes in the tank can be greatly simplified if it is assumed that during operation the conditions in the tank are maintained such that there is no boiling of the liquid propellant or condensation of the propellant vapor, and that the time over which depressurization occurs is much shorter than the time required for repressurization of the tank. As a result, pressurization can be attributed strictly to evaporation of the liquid propellant at the interface, followed by an instantaneous reduction in the tank pressure due to venting of the ullage gas (Hypothesis 1). The total mass released during venting is equal to the propellant mass loss due to boil-off over the course of the mission. The next step in the research focuses on the evaluation of the newly developed model, which motivates the following research question:

Research Question 3: What is the boil-off prediction capability of the model?

To answer the above research question, the prediction capability of the individual model components must be evaluated. The self-pressurization component of the model is evaluated in Sections 5.1 and 5.2. Section 5.1 examines the ability of the component to predict the fluid conditions (T, P, dP/dt) in the tank during the self-pressurization process by simulating several self-pressurization experiments obtained from literature. Section 5.2 evaluates the fidelity of the dP/dt predictions obtained from the model by comparing with the pressurization rates obtained from other cryogenic propellant tank models in literature. Given that during self-pressurization, the change in the tank pressure is directly related to the mass transfer that occurs at the interface, the fidelity in the dP/dt is directly related to

the fidelity with which the boil-off process is captured by the model. Lastly, Section 5.3 evaluates the ability of the venting component to predict the effects of the venting process on the ullage pressure, temperature, and mass during the period of pressure control by simulating a storage period where venting is required. The total propellant losses due to venting over the course of the storage period are then compared the losses predicted by the theoretical model in literature. This final evaluation provides the boil-off prediction capability of the model, which is a direct result of the model formulation that was identified by Research Questions 1 and 2, and their corresponding hypotheses. These research questions and hypotheses are restated below. The findings from the model evaluation are then used to address the validity of these hypotheses.

Research Question 1: How can a simplified cryogenic propellant tank model with pressure control capability be developed?

Hypothesis 1: *If ideal operation within the tank is assumed, then pressurization can be attributed strictly to evaporation of the liquid propellant at the interface, followed by an instantaneous reduction in the tank pressure due to venting of the ullage gas. This will greatly reduce the number of physical processes necessary to analyze the tank.*

Research Question 2: How can the mass released during venting, and the subsequent conditions in the tank be determined?

Hypothesis 2: *If the ullage is modeled as a thermodynamic system consisting of an ideal gas in an insulated container in thermodynamic equilibrium just prior to, and immediately after venting, and further, if the state of the gas after venting is assumed saturated, then the final conditions in the tank and the mass released during venting can be determined.*

5.1 Experiment 1a - Validation of Self-Pressurization Capability

The cryogenic propellant tank model that was developed as part of this research is depicted in Figure 4.2. During self-pressurization, the change in the tank pressure is attributed to heating of the ullage and boil-off of the liquid propellant at the interface. In order to account for the effects of thermal stratification, it was assumed that (1) the ullage gas near the interface is saturated, and (2) a warm thermal layer exists just beneath the interface which impedes the heat transfer to the bulk liquid. The former provides a more accurate representation of the fluid properties involved in the heat transfer between the ullage gas and the interface; the latter affects the mass transfer process by ascribing all of the incoming heat from the ullage to evaporation of the liquid propellant. In efforts to further reduce the complexity of the model, it was assumed that the dry and wet tank walls can be omitted from the analysis. The next logical step in the research process is to test the validity of the above assumptions by evaluating the self-pressurization capability of the model:

Research Question 3.1: What is the ability of the model to simulate the self-pressurization process?

In reality, the tank wall intercepts a portion of the incoming heat from the surrounding environment. By removing the tank wall from the analysis, the model inputs a greater amount of heat into the tank, particularly to the ullage region at lower propellant fill levels. The assumption that the heat transfer from the ullage to the interface – rather than net heat transfer through the interface – results in evaporation is valid in situations where the thermal stratification in the tank has reached a quasi-steady state. The assumption becomes less valid at higher propellant fill levels where it takes longer for the temperature gradients to develop and become time invariant. In this scenario, the model would yield an artificially high rate of evaporation.

Thus, for the duration of the storage period, the model is inputting a greater amount of heat into the tank (by omitting the tank wall) and is ascribing the maximum possible rate of evaporation (by including a modification to account for thermal stratification). Both of

these effects – increasing the thermal load tank and increasing the vapor mass in the ullage region – will result in higher tank pressures, especially at higher propellant fill levels. This idea is restated in the following hypothesis:

Hypothesis 3.1: *Due to the assumptions regarding heat transfer at the tank wall and at the interface, the model will predict higher pressurization rates than observed in literature, especially at higher propellant fill levels.*

Chapter 3 introduced several LH_2 pressurization experiments that are utilized frequently in literature for the purposes of model validation (theoretical and numerical). (To avoid confusion with this experiment and others conducted within this chapter, the self-pressurization experiments from literature will be referred to as self-pressurization "tests".) In a similar fashion, Experiment 1a uses a subset of these tests to validate the model response (P, T, and dP/dt), and test the above hypothesis. These include the self-pressurization tests presented by Aydelott [5] for a small spherical tank and Hastings et al. [72] for the cylindrical flight-scale MHTB tank.

The subset consists of a total of nine self-pressurization tests, carried out across a range of conditions. Additionally, the tanks differ not only in shape but also in scale, with the MHTB tank roughly three orders of magnitude larger in volume than the spherical tank. For each test, data for the tank pressure, and the ullage and bulk liquid temperatures is available. This provides an opportunity to examine whether the model assumptions, and thus the prediction capability of the model, are affected by the tank geometry. For simplicity, the small spherical tank will be referred to as the "Aydelott" tank.

A summary of the experimental objectives is provided in Section 5.1.1. Section 5.1.2 discusses the process for recreating the self-pressurization tests within the model and the procedure for analyzing the outputs from the simulation. Section 5.1.3 presents the results from simulation of self-pressurization in the Aydelott and MHTB tanks. A summary of the experimental findings is provided in Section 5.1.4

5.1.1 Purpose of Experiment

The primary objectives of the numerical experiment are as follows:

1. Explore the differences in the P, T, and dP/dt values obtained from simulation with those reported in literature for self-pressurization in the Aydelott and MHTB tanks
2. Demonstrate the ability of the model to predict the conditions the tank for different combinations of propellant fill level and heat transfer rate
3. Identify the predictive limitations of the model and provide extensions to the model assumptions if necessary

5.1.2 Setup and Procedure

The first step in the experiment involves recreating the test conditions for simulation. The initial tank pressure, gas and bulk liquid temperatures, propellant fill level, heat transfer rate, and test time for each self-pressurization test was collected, along with the dimensions of the Aydelott and MHTB tanks. Table 5.1 lists these initial conditions and the tank geometry, which serve as inputs for the simulation. The first five tests (Tests 2 - 7) correspond to the inputs gathered for the Aydelott tank, and the last four tests (Tests P263981D - P263981T) correspond to the inputs for the MHTB tank, where the test number listed in the table corresponds to the test number obtained from the original study in literature.

A detailed description of the model is available in Section 4.3. A high-level overview of the inputs and outputs for the self-pressurization component is shown in Figure 4.7, where self-pressurization is represented by the inner loop (denoted by ①). For standard simulations, the model assumes that the tank is initially saturated and in thermal equilibrium. Only two variables need to be provided in order to specify the initial conditions within the tank: the initial pressure or temperature, and the propellant fill level. However, for the self-pressurization tests selected for this experiment, the starting conditions were not consistent with thermal equilibrium. Not only did the ullage and bulk liquid temperatures differ at the beginning of each test, thermal stratification was also present within the ullage region.

Table 5.1: Model inputs for Experiment 1a.

Test No.	P (Pa)	T_g (K)	T_l (K)	FL (% by vol.)	$\dot{Q}$ (W)	t (s)
2	105,462	20.53	20.53	51.4	9.5	1,441
3	122,161	21.02	20.13	34.9	31.5	433
4	110,633	20.68	20.19	48.9	34.1	400
5	127,036	21.16	20.53	76.5	38.1	272
7	105,462	20.53	20.53	50.7	58.5	222
P263981D	111,500	20.71	20.66	90.0	54.1	19,591
P263968E	111,500	20.71	20.62	90.0	20.2	51,138
P263968K	122,000	21.01	20.97	25.0	18.8	66,446
P263981T	111,500	20.71	20.70	50.0	51.0	49,869

(a) Test conditions

Test Article	Tank Shape	Tank Diameter (m)	Tank Height (m)
Aydelott tank	Spherical	0.23	0.23
MHTB tank[a]	Cylindrical	3.05	3.05

[a]2:1 elliptical end caps

(b) Tank geometry

For tests conducted in the Aydelott tank, the temperature difference ranged between 30 K and 77 K. For the MHTB tank, the extent of thermal stratification is unknown, since the temperature data provided in literature is limited to propellant fill levels between 95% and 98%.

In order to account for the lack of thermal equilibrium between the ullage and bulk liquid regions, the single temperature input in the model (T_o in the Initial Conditions block in Figure 4.7) was adjusted to include the temperature of the ullage and bulk liquid, represented by T_g and T_l, respectively, in Table 5.1. Given that a single node cannot account for thermal stratification, the initial temperature of the ullage region is assumed to be at the saturation temperature corresponding to initial the tank pressure, $T_g = T_{sat}(P)$. For the bulk liquid region, each simulation utilizes the initial temperature that was reported in

literature.

Based on the values of P, T_g, T_l and FL listed in Table 5.1, the model determines the remaining initial conditions for the ullage and bulk liquid regions (i.e., the mass and volume). At $t = 0$, the self-pressurization process is initiated by the thermal load $\dot{Q}$ on the tank from the surrounding environment. In order for self-pressurization to continue uninterrupted, the maximum pressure limit for the venting capability is set to the critical pressure for LH_2. Each simulation is run with a time step of 1.0 seconds.

For the purposes of this experiment, the model outputs the time histories for the tank pressure, and the ullage and bulk liquid temperatures, with the model and literature values presented in the same plot. From the time histories, a table is generated listing a summary of the measured and predicted pressure values, where the predicted values correspond to the values obtained from simulation, and the measured values correspond to those obtained from literature. These include the initial and final tank pressures (P_i and P_f, respectively), the tank pressurization rate (dP/dt), and the ratio of the predicted-to-measured pressurization rate (dP/dt ratio). Another table is similarly generated for the ullage ($T_{g,i}$, $T_{g,f}$, ΔT_g) and bulk liquid temperatures ($T_{b,i}$, $T_{b,f}$, ΔT_b).

Validation of the self-pressurization capability is conducted by analyzing the P, T, and dP/dt values via the method described in Section 3.2. For the Aydelott tank, the ullage and bulk liquid temperature histories obtained from the model are compared with temperature measurements obtained at a location corresponding to the lower ullage region, near the interface, and the coolest portion of the bulk liquid[1]. For the MHTB tank, the thermal distribution for the tank has not been reported in literature. Therefore the comparison is limited to one of two locations in the ullage, and single location in the bulk liquid[2]. For Tests P263981D, P263968E, and P263968K, ullage temperature histories obtained from the

[1]The temperature distribution for each region within the tank, and the corresponding locations at which these measurements were obtained is available in Appendix F. Temperature histories for Tests 2 and 7 are not included as they were not published in the original study.

[2]For the locations of the temperature transducers relative to the propellant fill levels utilized in each test, see Appendix G.

model are compared with temperature measurements obtained at a location corresponding to a propellant fill level of 95.4%. For Test P263981T, the ullage temperature predicted by the model is compared with temperature values that correspond to the average of measurements obtained at a propellant fill level of 95.4% and a lower propellant fill level that was not identifiable in the literature. For the bulk liquid temperatures, model values are compared with temperatures measured at a propellant fill level of 11.5%.

For each tank, dP/dt values are compared with those from literature to determine if the model responds accordingly as the conditions change. It is expected that while the model will overestimate dP/dt at higher propellant fill levels ($\geq$ 75%), the heat transfer assumptions utilized by the model will still enable the primary affects to be captured, and dP/dt will follow a similar trend exhibited by the literature values. That is, everything else remaining constant, dP/dt should increase with the propellant fill level, and likewise with an increasing thermal load on the tank.

The T and ΔT values for the ullage and bulk liquid are used to analyze how the heat transfer assumptions imposed on the model affect the temperature response in each region. Given that the ullage is represented as a single node, the temperature response is directly related to the heat entering the system, where for the literature values the temperature change is a result of heating of the gas near the tank wall and convection currents that subsequently develop within the fluid, resulting in thermal stratification. Therefore, the T_g and ΔT_g values for the model are not necessarily expected to follow the same trend displayed by the literature values.

Considering that thermal stratification in the bulk liquid is not nearly as extensive, this allows for a more direct comparison of the T_b and ΔT_b values. It can generally be assumed that the tank wall in contact with the bulk liquid is at the same temperature as the liquid propellant. Since the model assumes that the only thermal contribution to the bulk liquid is that from the external environment, and does not include heat transfer from the bottom side of the interface, it is expected that T_b, and thus ΔT_b, will be less than the measured values.

5.1.3 Results from Self-Pressurization Simulations

5.1.3.1 Aydelott Tank

A summary of the pressure and temperature values obtained from the experiment is provided in Tables 5.2 and 5.3, respectively, where measured values correspond to values obtained from literature, and predicted values correspond to those obtained from simulation. In order to better identify trends as the conditions change, the values for FL and $\dot{Q}$ are also included. Table 5.2 lists the values for P_i, P_f, dP/dt, and the dP/dt ratio. Table 5.3 lists the $T_{g,i}, T_{g,f}$, and ΔT_g values for the ullage, and the $T_{b,i}, T_{b,f}$, and ΔT_b values for the bulk liquid. Figures 5.1, 5.2, and 5.3 depict the time histories for the tank pressure, and the ullage and bulk liquid temperatures, respectively. In each figure, the data obtained from literature is represented by the dashed lines, and the data obtained from simulation is represented by the red (pressure), green (ullage temperature), and blue (bulk liquid temperature) lines[3].

As shown in Figure 5.1, the pressure histories obtained from simulation are in excellent agreement with the pressure histories obtained from literature for Tests 2 and 4, good agreement for Tests 3 and 7, and relatively good agreement for Test 5. From examination of the measured and predicted dP/dt values in Table 5.2, the model is capable of reproducing the effect of varying FL and $\dot{Q}$ on dP/dt. For Tests 3, 4, and 5, which were carried out at approximately the same $\dot{Q}$, the predicted dP/dt values increase (from 1.27 kPa/s, to 1.46 kPa/s, to 2.23 kPa/s) as FL increases (from 34.9%, to 48.9 %, to 76.5 %, respectively). For Tests 2 and 7, which were carried out at approximately the same FL, the predicted dP/dt values increase (from 0.43 kPa/s to 2.52 kPa/s) as $\dot{Q}$ increases (from 9.5 W to 58.5 W, respectively).

From Table 5.2, the value of the dP/dt ratio ranges from 0.91 to 1.14. For Tests 2 and 3, with dP/dt ratios of 1.03 and 1.00, respectively, the value of the ratio indicates that for these two tests, which have FLs and $\dot{Q}$s in the low to intermediate range, the

[3]For comparison, the pressure histories obtained using real gas properties to calculate the heat transfer from the ullage gas to the interface are located in Appendix I.

model is capable of accurately predicting dP/dt. For Tests 4 and 7, with intermediate FLs and intermediate-to-high $\dot{Q}$s, the model underestimates dP/dt slightly, as indicated by the dP/dt ratios of 0.91 (Test 7) and 0.93 (Test 4). The highest value of 1.14 for the dP/dt ratio corresponds to Test 5, which of the five tests, has the highest FL and an intermediate value of $\dot{Q}$.

From examination of the test conditions, and the corresponding dP/dt ratios, the results show that for this tank, the assumption that the tank wall can be omitted from the analysis is valid. Otherwise, the model predictions would have resulted in dP/dt ratios that were greater than 1, regardless of the conditions. With respect to the assumption that heat transfer from the ullage to the interface contributes entirely towards evaporation, the results also show that as anticipated, the assumption is less valid at higher propellant fill levels where the temperature gradient takes longer to develop, and thus yields higher dP/dt values than observed in literature.

Moving on to the temperature evaluation, the measured and predicted ullage temperatures for Tests 3, 4, and 5, are depicted in Figure 5.2, where the test data corresponds to measurements obtained at a lower ullage location, near the interface. For each test, the model exhibits an initial transient, which represents the initial period of heat transfer within the region. The transient phase takes approximately the same amount of time in Tests 3 and 4 (approximately 50 seconds), and lasts around half as long in Test 7 (about 25 seconds). After the initial transient period, the temperatures in Tests 2 and 4 each reach steady state, at temperatures of approximately 34.6 K and 35.0 K, respectively, whereas the temperature in Test 5 continues to gradually increase. This can be attributed to the smaller ullage volume at higher FLs – given the smaller amount of gas, less heat is required to raise to the temperature of the ullage.

From comparison of the measured and predicted temperature histories, the model predicts values that are in good agreement in Test 3, and that are slightly higher in Test 4. For Test 7, the model predicts values that are much lower (by approximately 30 K) than the

measured values. Typically, due to thermal stratification, the temperature of the gas near the interface is cooler than the gas located at the top of the tank. However, for higher FLs the gas near the interface is in closer proximity to warmer gas at the top of the tank. This is especially true for smaller tanks, such as the one considered here. These results show that, as previously discussed, the single nodal representation used for the ullage space is unable to fully capture the temperature behavior in the region. This is supported by the ΔT_g values in Table 5.3, where for the measured values, ΔT_g is greatest for the highest FL of 76.5% (43.34 K), and lowest for the intermediate FL of 48.9% (10.98 K). For the ΔT_g values predicted by the model, the trend is the opposite – the greatest ΔT_g values occurs for the lowest FL of 34.9% (13.97 K), and the lowest ΔT_g occurs for the highest FL of 76.5% (12.88 K).

The bulk liquid temperatures histories for Tests 3, 4, and 5, are depicted in Figure 5.3, where the test data corresponds to measurements obtained for the coldest portion of the bulk liquid. In all cases, the model predicts temperatures that are lower than those observed in literature, with the exception of the first 200 seconds in Test 3. This behavior is expected, since the model excludes the heat transfer from the bottom side of the interface – any heat that enters the liquid is solely from the external environment. Based on the temperature histories from literature, the corresponding ΔT_b values are 4.86 K, 4.58 K, and 2.68 K for FLs of 34.9%, 48.9%, and 76.5%, respectively. The model yields ΔT_b values that are lower – at 3.34 K, 2.95 K, and 1.98 K for FLs of 34.9%, 48.9%, and 76.5%, respectively – but that follow same trend exhibited the measured values. That is, ΔT_b decreases as FL increases. This demonstrates that while the model excludes the heat transfer from the bottom side of the interface, it is capable of predicting the overall temperature behavior in the region, and predicts temperatures with sufficient accuracy.

Table 5.2: Summary of tank pressures and pressurization rates obtained from recreation of self-pressurization tests for the Aydelott tank. Measured values are taken from literature [5], predicted values are from simulation using the new model.

Test No.	Fill Level FL (% by vol.)	Heat Transfer Rate $\dot{Q}$ (W)	Pressure (kPa)		Pressurization Rate dP/dt (kPa/s)	Pred.-to-Meas. dP/dt Ratio
			P_i	P_f		
Measured[a]						
2	51.4	9.5	105.462	705.396	0.42	-
3	34.9	31.4	122.161	671.488	1.27	-
4	48.9	34.1	110.633	741.566	1.58	-
5	76.5	38.1	127.036	658.015	1.95	-
7	50.7	58.5	105.462	717.103	2.75	-
Predicted						
2	51.4	9.5	105.462	723.274	0.43	1.03
3	34.9	31.4	122.161	672.938	1.27	1.00
4	48.9	34.1	110.633	695.119	1.46	0.93
5	76.5	38.1	127.036	732.554	2.23	1.14
7	50.7	58.5	105.462	664.835	2.52	0.91

[a]Pressure values were extracted from P versus t plots for each self-pressurization test

Table 5.3: Summary of ullage and bulk liquid temperatures obtained from simulation of self-pressurization tests for the Aydelott tank. Measured values are from literature [5], predicted values are from simulation.

Test No.	Fill Level	Heat Transfer Rate	Temperature (K)					
	FL (% by vol.)	$\dot{Q}$ (W)	$T_{g,i}$	$T_{g,f}$	ΔT_g	$T_{b,i}$	$T_{b,f}$	ΔT_b
Measured[a]								
3	34.9	31.4	20.12	35.44	15.32	20.13	24.99	4.86
4	48.9	34.1	20.19	31.17	10.98	20.19	24.77	4.58
5	76.5	38.1	20.51	63.85	43.34	20.53	23.21	2.68
Predicted								
3	34.9	31.4	21.02	34.99	13.97	20.13	23.47	3.34
4	48.9	34.1	20.68	34.63	13.95	20.19	23.13	2.94
5	76.5	38.1	21.16	34.04	12.88	20.53	22.52	1.99

[a]Temperature values were extracted from T versus t plots for each self-pressurization test

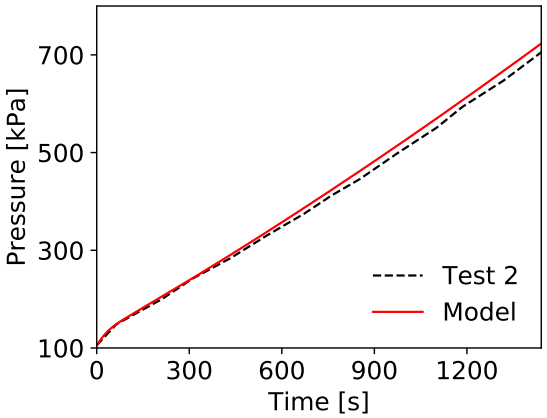

(a) FL = 51.4%, $\dot{Q}$ = 9.5 W

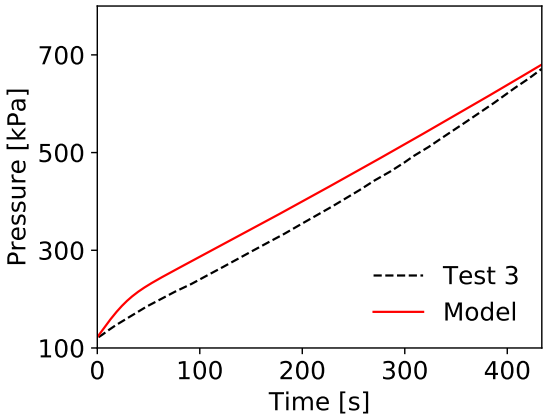

(b) FL = 34.9%, $\dot{Q}$ = 31.5 W

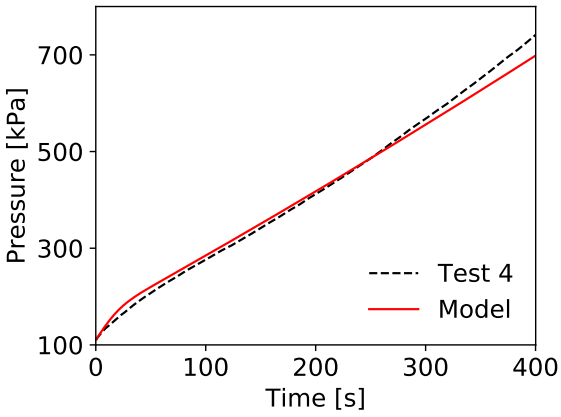

(c) FL = 48.9%, $\dot{Q}$ = 34.1 W

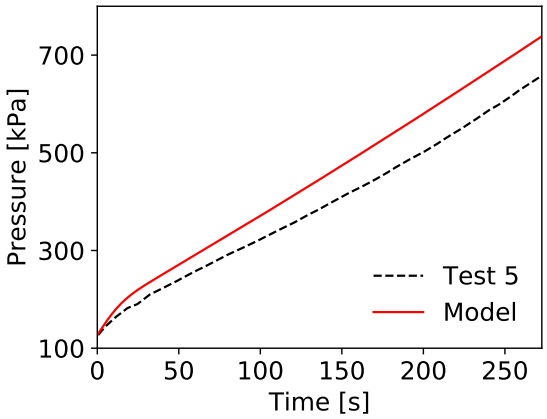

(d) FL = 76.5%, $\dot{Q}$ = 38.1 W

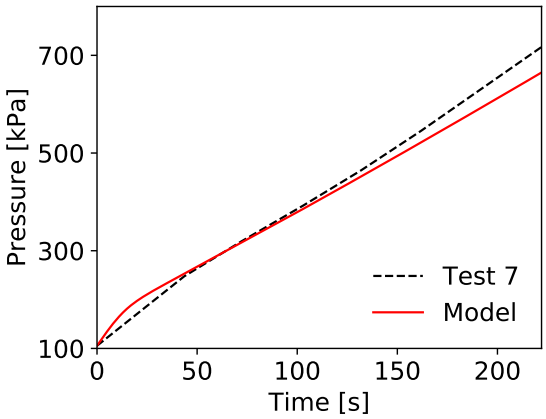

(e) FL = 50.7%, $\dot{Q}$ = 58.5 W

Figure 5.1: Pressure values obtained from simulation (red) versus values obtained from literature (black) for self-pressurization in a 23 cm diameter spherical tank.

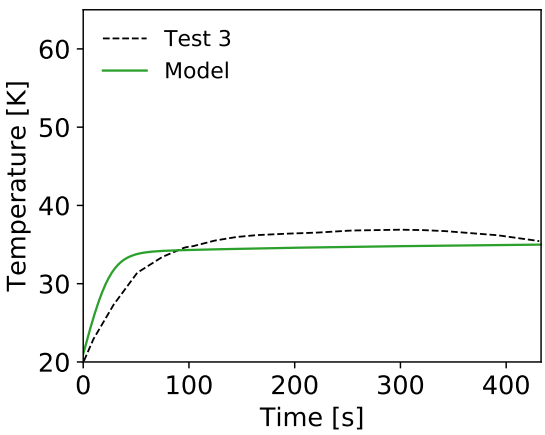

(a) FL = 34.9%, $\dot{Q}$ = 31.5 W

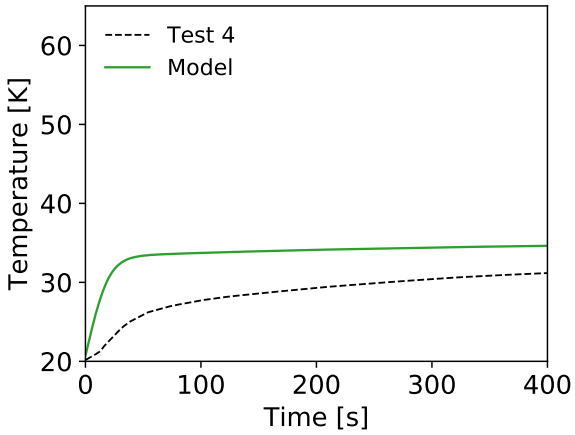

(b) FL = 48.9%, $\dot{Q}$ = 34.1 W

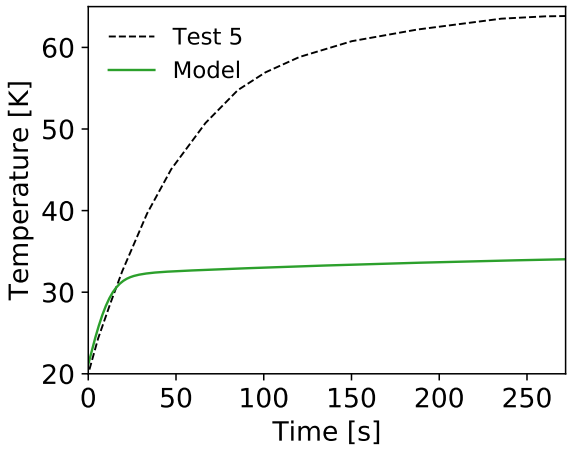

(c) FL = 76.5%, $\dot{Q}$ =38.1 W

Figure 5.2: Ullage temperature obtained from simulation (green) versus the temperature obtained from literature (black) for self-pressurization in a 23 cm diameter spherical tank.

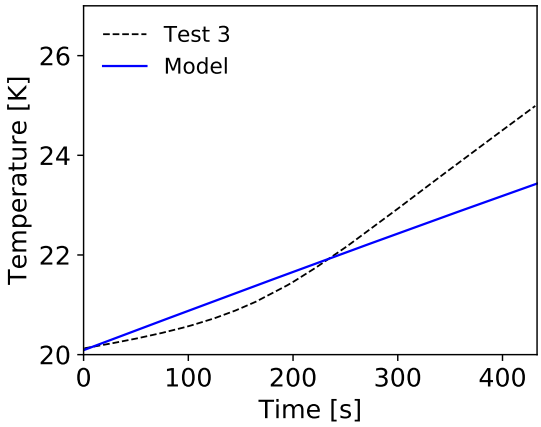

(a) FL = 34.9%, $\dot{Q}$ = 31.5 W

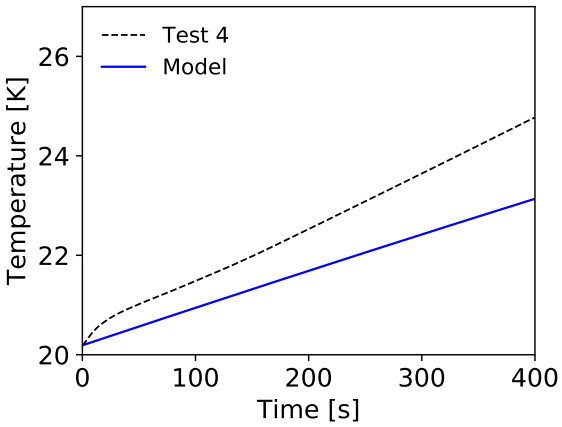

(b) FL = 48.9%, $\dot{Q}$ = 34.1 W

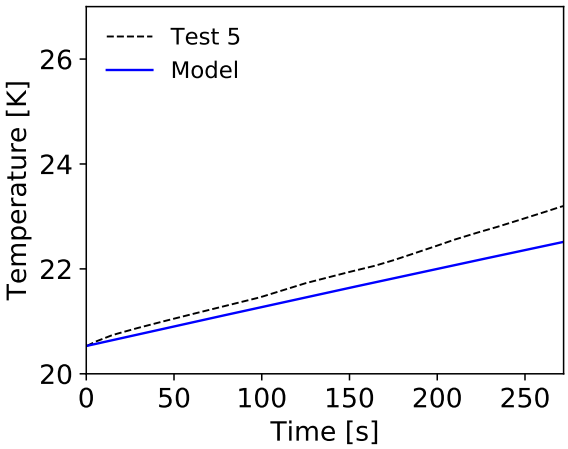

(c) FL = 76.5%, $\dot{Q}$ = 38.1 W

Figure 5.3: Bulk liquid temperature obtained from simulation (blue) versus the temperature obtained from literature (black) for self-pressurization in a 23 cm diameter spherical tank.

5.1.3.2 MHTB Tank

A summary of the pressure and temperature values obtained from the experiment are provided in Tables 5.4 and 5.5, respectively. As before, measured values correspond to those obtained from literature, and predicted values correspond to those obtained from simulation. The parameters listed in these tables are unchanged from those in the previous section. Figures 5.4, 5.5, and 5.6 depict the time histories for the tank pressure, and the ullage and bulk liquid temperatures, respectively, where the data obtained from literature is represented by the dashed lines, and the data obtained from simulation is represented by the red (pressure), green (ullage temperature), and blue (bulk liquid temperature) lines[4].

As shown in Figure 5.4, the model overestimates the tank pressure for Tests P263981D and P263968E, and predicts pressures that are in excellent agreement for Test P263968K, and that are in relatively good agreement for Test P263981T. From examination of the measured and predicted dP/dt values in Table 5.4, the model is capable of reproducing the effect of varying FL and $\dot{Q}$ on dP/dt. For Tests P263968E and P263968K, which were carried out at approximately the same $\dot{Q}$ of 19 W, the predicted dP/dt values increase (from 0.82 kPa/s to 8.27 kPa/s) as FL increases (from 25% to 90%). For Tests P263981D and P263981T, which were carried out at approximately 52.5 W, the predicted dP/dt values increase (from 2.24 kPa/s to 22.41 kPa/s) as FL increases (from 50% to 90%). For tests P263981D and P263968E, which were carried out at the same FL of 90%, the predicted dP/dt values increase (from 8.27 kPa/s to 22.41 kPa/s) as $\dot{Q}$ increases (from 20.2 W to 54.1 W).

From Table 5.4, the value of the dP/dt ratio ranges from 0.95 to 4.75. Examination of the dP/dt ratios show that, as FL increases, the ratio also increases, from 0.95 (Test P263968E, FL of 25%), to 1.17 (Test P263981T, FL of 50%), to 4.60 (Test P263981D, FL of 90%), and to 4.75 (Test P263968E, FL of 90%). For the last two tests, with FLs of

[4]Pressure histories obtained using real gas properties to calculate the heat transfer at the interface are located in Appendix I. The pressure histories obtained in Figure I.4 appear identical to those in Figure 5.4 as there is little difference between the saturated and real gas properties for the pressure and temperature range considered.

90%, the test with the lowest $\dot{Q}$ requires a greater amount of time for the thermal gradient to develop, and correspondingly exhibits the highest value for the dP/dt ratio. For the last two tests, with FLs of 90%, the test with the lowest $\dot{Q}$ requires a greater amount of time for the thermal gradient to develop, and correspondingly exhibits the highest value for the dP/dt ratio.

These results show that omitting the tank wall from the analysis continues to be a valid assumption. For this tank, and the correspondingly large propellant capacity, as FL increases the thermal gradient takes much longer to develop than for the smaller Aydelott tank. This is supported by the initial transient present in the pressure histories in Figures 5.4a and 5.4b. For this larger tank, the assumption regarding the heat transfer at the interface causes the model to predict tank pressures that grow further away from literature values as FL increases beyond 25%.

Moving on to the temperature evaluation, the measured and predicted ullage temperatures for Tests P263981D, P263968E, P263968K, and P263981T are depicted in Figure 5.5, where the test data in Tests P263981D, P263968E, and P263968K correspond to measurements taken at an upper ullage location (FL of 95.4%), and the test data for Test P263981T corresponds to the average of the temperatures measured at two locations within the ullage region (FL of 95.4% and an unknown location). After the initial transient, the model predicts temperatures that rise more rapidly for the higher FLs of 90%, moderately for the intermediate FL of 50%, and for the lowest FL of 25%, the temperature reaches steady state immediately after the transient period.

For Test P263981D, the model predicts a temperature that is higher initially, and that continues to rises for the duration of the test, whereas the measured values reach steady-state around the 3-hour mark. The measured and predicted temperatures at the end of the test are similar at 23.65 K and 24.48 K, respectively. For Test P263968E, the model response is identical to the previous test, with the exception of the rate at which the temperature increases due to the decrease in $\dot{Q}$ from 54.1 W to 20.2 W (note that it takes nearly

twice as long for the temperature in Test P263968E to reach approximately the same final temperature as in Test P263981D). The corresponding measured temperature rapidly increases then drops, though at a slower rate, before reaching a relatively steady value around the 6-hour mark. The cause for the initial rise in the ullage temperature is not addressed by the authors of the original study; the decrease is attributed to the addition of cold gas to the ullage region, due to evaporation of the cooler bulk liquid at the interface. The model is unable to capture this effect, however, other higher fidelity models in literature have had similar difficulties [72]. At the end of the test, the measured and predicted temperature values are similar, at 23.08 K and 23.91 K, respectively.

For Test P263968K, the model predicts temperatures that are approximately 4 K - 5 K lower than measured values. The model temperature reaches steady state relatively quickly after the initial transient, whereas the measured temperature increases at a slightly faster rate throughout the test. For Test P263981T, the model initially predicts a temperature that is approximately 4 K lower than the the measure temperature, with the gap between the predicted and measured values increasing for duration of the test, resulting in final temperature values that are approximately 6 K apart.

From Table 5.5, the measured ΔT_g values, in ascending order, are of 1.48 K, 2.37 K, 2.94 K, and 3.41 K for Tests P263968K (FL of 25%), P263968E (FL of 90% and $\dot{Q}$ of 20.2 W), P263981D (FL of 90% and $\dot{Q}$ of 54.1 W), and P263981T (FL of 50%), respectively, and do not appear to subscribe to any particular set of conditions. The predicted ΔT_g values follow a similar, though not identical trend; values increase from 0.83 K, to 1.52 K, to 3.20 K, and to 3.77 K for Tests P263968K, P263981T, P263968E, and P263981D.

The bulk liquid temperature histories are depicted in Figure 5.6, where the test data corresponds to measurements obtained at FL of 11.5%. For all tests, the model predicts temperatures that are lower than the temperatures observed in literature, as expected, but that are still in excellent agreement, with less than a 1 K difference between measured and predicted values. Examination of the measured ΔT_b values in Table 5.5 show that, everything

else remaining constant, ΔT_b increases as FL decreases (Tests P263981D and P263981T, and Tests P263968E and P263968K), and as $\dot{Q}$ increases (Tests P263981D and P263968E). Predicted ΔT_b values display a similar trend, with the exception of Tests P263981D and P263968E, where for FL of 90%, ΔT_b remains constant when $\dot{Q}$ is increased from 20.2 W to 54.1 W.

Table 5.4: Summary of tank pressures and pressurization rates obtained from recreation of self-pressurization tests for the MHTB tank. Measured values are taken from literature [72], predicted values are from simulation using the new model.

Test No.	Fill Level	Heat Transfer Rate	Pressure (kPa)		Pressurization Rate	Pred.-to-Meas.
	FL (% by vol.)	$\dot{Q}$ (W)	P_i	P_f	dP/dt (kPa/s)	dP/dt Ratio
Measured[a]						
P263981D	90.0	54.1	111.500	138.012	4.87	-
P263968E	90.0	20.2	111.500	136.202	1.74	-
P263968K	25.0	18.8	122.000	137.993	0.87	-
P263981T	50.0	51.0	111.500	138.013	1.91	-
Predicted						
P263981D	90.0	54.1	111.500	233.436	22.41	4.60
P263968E	90.0	20.2	111.500	228.931	8.27	4.75
P263968K	25.0	18.8	122.000	137.161	0.82	0.95
P263981T	50.0	51.0	111.500	142.480	2.24	1.17

[a] Pressure values for tests P263981D, P263968K, and P263981T were obtained from [22]

[b] Pressure values values for test P263968E were obtained from [72]

Table 5.5: Summary of system temperatures and temperature changes obtained from recreation of self-pressurization tests for the MHTB tank. Measured values are taken from literature [72], predicted values are from simulation using the new model.

Test No.	Fill Level	Heat Transfer Rate	Temperature (K)					
	FL (% by vol.)	$\dot{Q}$ (W)	$T_{g,i}$	$T_{g,f}$	ΔT_g	$T_{b,i}$	$T_{b,f}$	ΔT_b
Measured[a]								
P263981D	90.0	54.1	20.71	23.65	2.94	20.66	20.82	0.16
P263968E	90.0	20.2	20.71	23.08	2.37	20.62	20.71	0.09
P263968K	25.0	18.8	24.84	26.32	1.48	20.97	21.27	0.30
P263981T	50.0	51.0	24.37	27.78	3.41	20.70	21.10	0.40
Predicted								
P263981D	90.0	54.1	20.71	24.48	3.77	20.66	20.68	0.02
P263968E	90.0	20.2	20.71	23.91	3.20	20.62	20.64	0.02
P263968K	25.0	18.8	21.01	21.84	0.83	20.97	21.12	0.15
P263981T	50.0	51.0	20.71	22.23	1.52	20.70	20.93	0.23

[a] Temperature values for tests P263981D, P263968K, and P263981T were obtained from [22]

[b] Temperature values for test P263968E were obtained from [72]

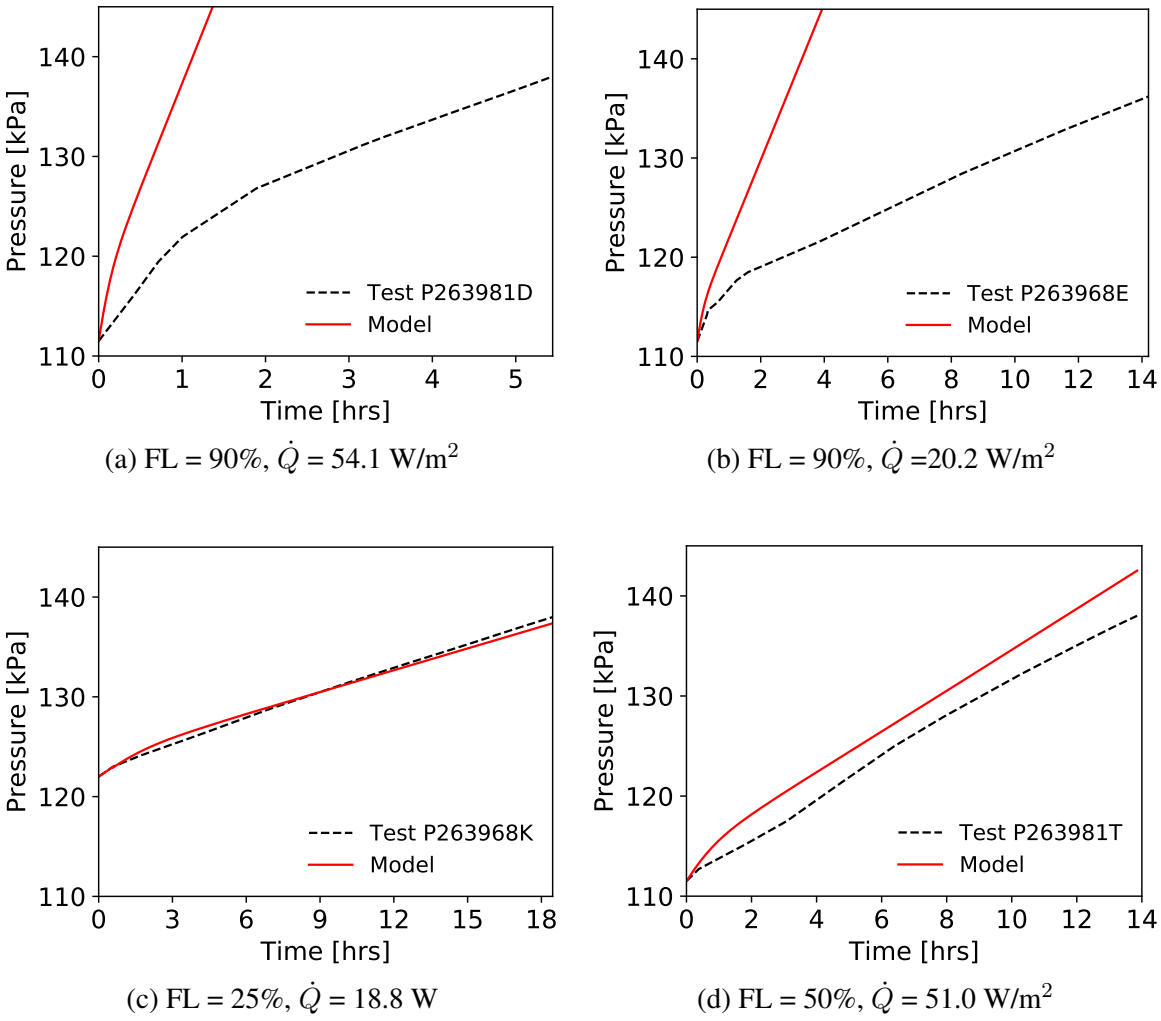

(a) FL = 90%, $\dot{Q}$ = 54.1 W/m^2

(b) FL = 90%, $\dot{Q}$ =20.2 W/m^2

(c) FL = 25%, $\dot{Q}$ = 18.8 W

(d) FL = 50%, $\dot{Q}$ = 51.0 W/m^2

Figure 5.4: Pressure values obtained from simulation (red) versus values obtained from literature (black) for self-pressurization in the MHT tank.

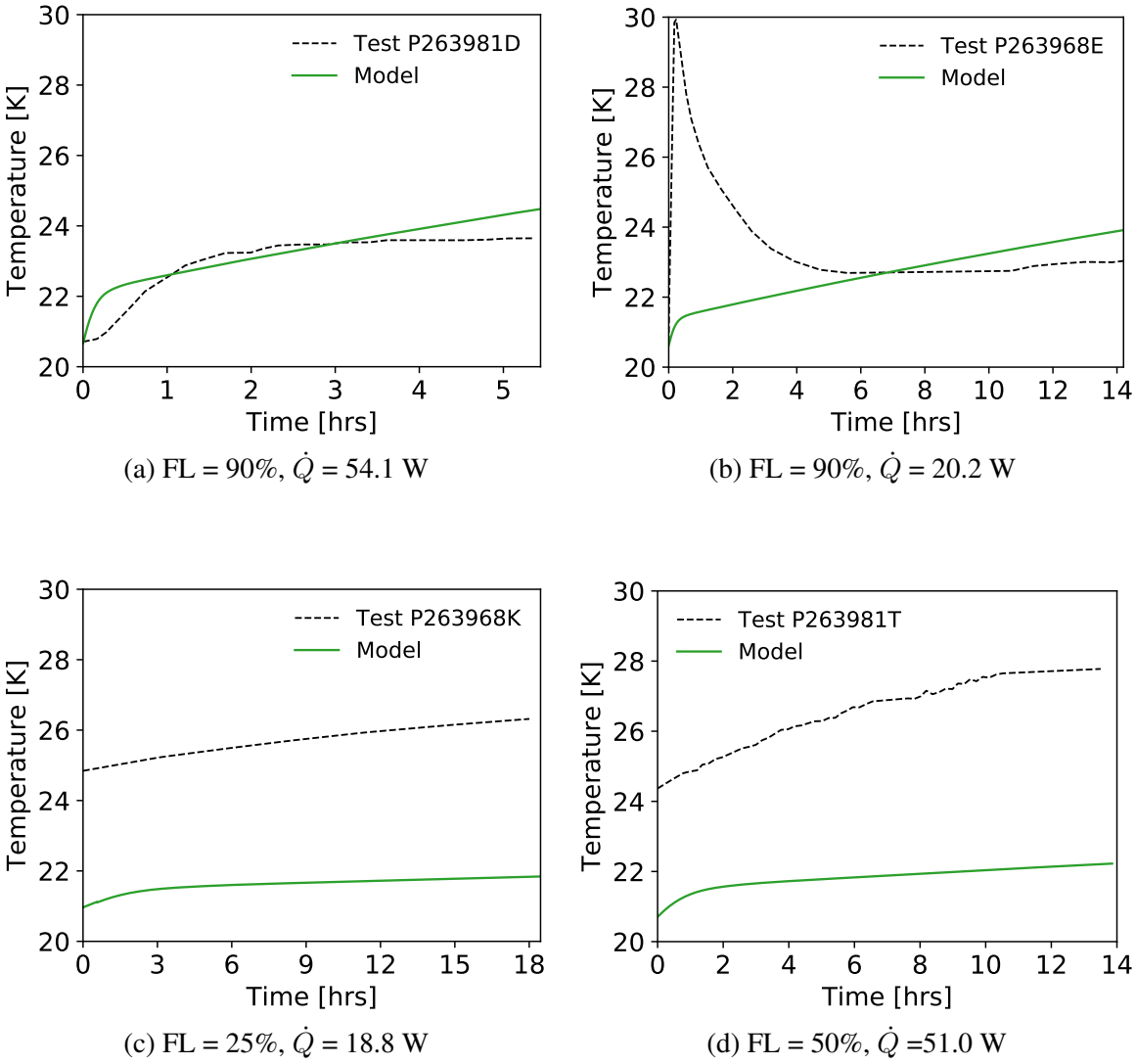

(a) FL = 90%, $\dot{Q}$ = 54.1 W

(b) FL = 90%, $\dot{Q}$ = 20.2 W

(c) FL = 25%, $\dot{Q}$ = 18.8 W

(d) FL = 50%, $\dot{Q}$ =51.0 W

Figure 5.5: Ullage temperature obtained from simulation (green) versus the temperature obtained from literature (black) for self-pressurization in the MHT tank.

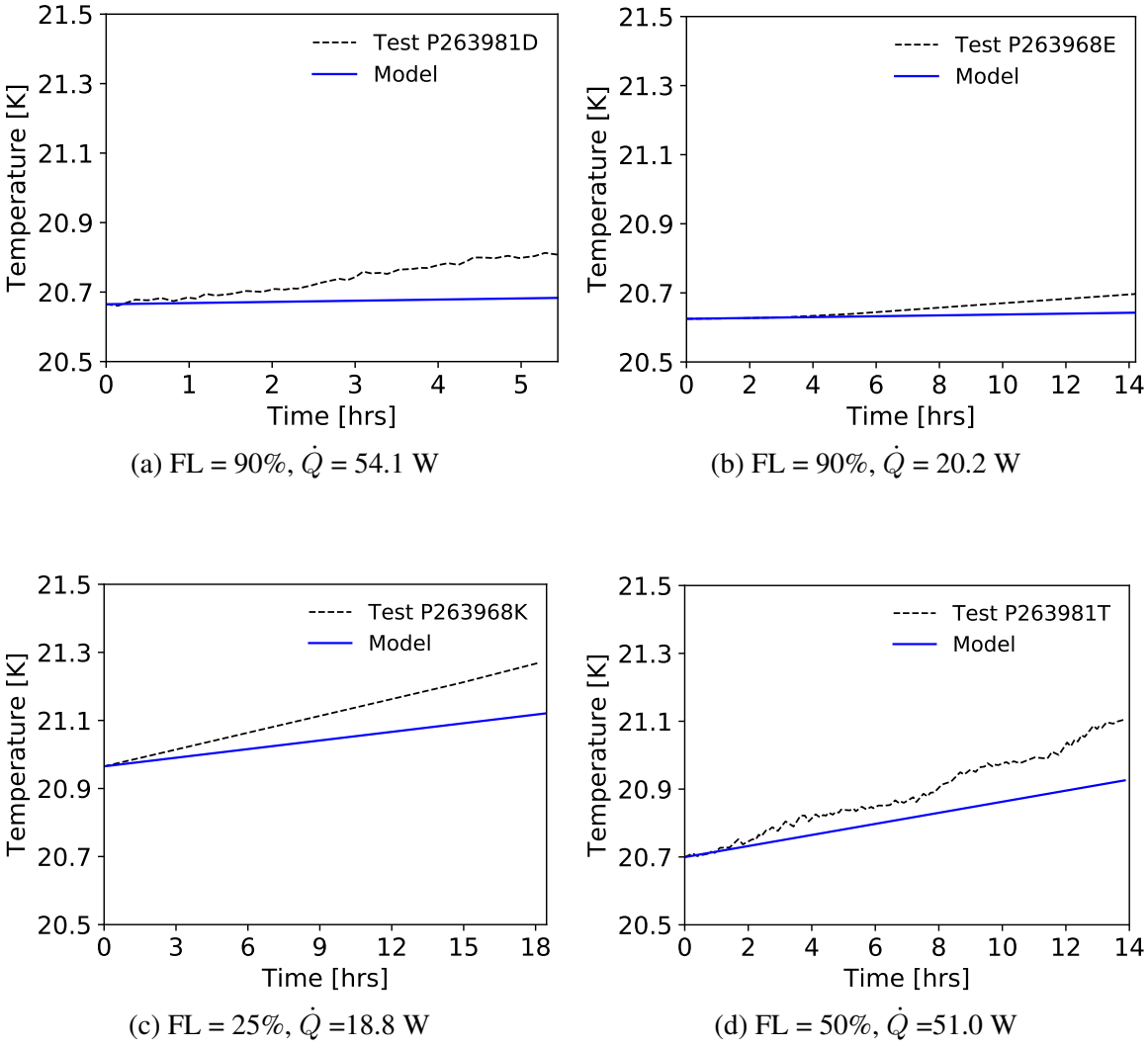

(a) FL = 90%, $\dot{Q}$ = 54.1 W

(b) FL = 90%, $\dot{Q}$ = 20.2 W

(c) FL = 25%, $\dot{Q}$ =18.8 W

(d) FL = 50%, $\dot{Q}$ =51.0 W

Figure 5.6: Bulk liquid temperature obtained from simulation (blue) versus the temperature obtained from literature (black) for self-pressurization in the MHT tank.

5.1.4 Summary

This numerical experiment sought to validate the self-pressurization capability of the model. Given that the model omits the tank wall from the analysis, the model ascribes a higher thermal input into the tank. In addition, the model assumes that the mass transfer at the interface is the result of the incoming heat from the ullage and does not consider the heat loss through the bottom side of the interface; this has the potential to overestimate the amount of evaporation that occurs. It was hypothesized that the combined effects of these two assumptions would result in higher dP/dt predictions when compared with values observed in literature, especially at higher propellant fill levels where thermal stratification takes longer to reach a quasi-steady state.

To test this hypothesis, several self-pressurization tests conducted in the Aydelott and MHTB tanks, for a range FLs and $\dot{Q}$s, were gathered from literature for simulation. For the Aydelott tank, the combination of small tank volume and high $\dot{Q}/A$ caused the temperature gradient to develop quickly within the tank. The model was capable of predicting both the tank pressure and dP/dt with sufficient accuracy, a quality that is difficult to achieve with simpler analytical models. For the MHTB tank, the combination of large tank volume and low $\dot{Q}/A$ increased the time for the temperature gradient to develop. The ability of the model to predict the tank pressure and dP/dt was maintained for lower and intermediate FLs; model predictions were conservative at higher FLs.

The results from the experiment show that the model is capable of sufficiently predicting the fluid behaviors, and thus dP/dt, for different tank geometries, subject to a variety of conditions. The hypothesis is partially substantiated – omitting the tank wall from the analysis does not negatively impact the predictive capability of the model; the heat transfer from the ullage to the interface leads to conservative predictions in scenarios where it takes longer for the temperature gradient to develop.

5.2 Experiment 1b - Fidelity in dP/dt Predictions

Recall that the primary objective of this research is to develop a simple cryogenic propellant tank model capable of predicting the tank pressurization rate, and hence boil-off, with a similar fidelity exhibited by higher-fidelity models in literature. If the research effort has been successful, the model will display a similar fidelity in the pressurization prediction capability. This will act as a verification that the boil-off provided by Equation 4.41 provides more accurate estimates than the boil-off provided by the theoretical model in Equation 1.1. Experiment 1b addresses the following research question:

Research Question 3.2: What is the dP/dt prediction capability of the model when compared to higher-fidelity propellant tank models in literature?

Several state-of-the-art propellant tank models were introduced as part of the literature review in Chapter 3. Of the handful of models that were presented, three utilized one or more of the self-pressurization tests carried out in the MHTB tank as a validation case. These include the model of Hastings et al., TankSIM, and GFSSP. These validation studies provide an opportunity to compare the predictive capability of several state-of-the-art models from two different categories (analytical and numerical), with that of the newly developed cryogenic propellant tank model (the extensible boil-off model, EBM). Given that the state-of-the-art models use greater detail in representing the heat and mass transfer processes, it is anticipated that they will provide more accurate dP/dt predictions when compared to predictions from the EBM. This idea is restated in the following hypothesis:

Hypothesis 3.2: *Due to the simplicity of the heat and mass transfer assumptions utilized in the formulation of the extensible boil-off model, the model will yield less accurate pressurization rates when compared with other higher-fidelity models in literature.*

A summary of the experimental objectives is provided in Section 5.2.1. The experimental procedure and the results from the experiment are presented in Sections 5.2.2 and 5.2.3, respectively. A summary of the experimental findings is provided in Section 5.2.4.

5.2.1 Purpose of Experiment

The primary objective of the numerical experiment is as follows:

1. For the initial self-pressurization period in the MHTB tank, compare the P and dP/dt values obtained from the EBM with those reported in literature for the following analytical and numerical models:

    - Hastings et al.
    - TankSIM
    - GFSSP

5.2.2 Setup and Procedure

The first step in the experiment involves gathering the pressure histories for each of the analytical and numerical models, the EBM, and the MHTB tank. The pressure data for the model of Hastings et al. (abbreviated Hastings et al. for the remainder of this section), TankSIM, and GFSSP were gathered from their corresponding validation studies that have been published in literature [22, 72, 102]. The data for the MHTB tank was previously collected in order to perform the validation of the EBM's self-pressurization capability in Experiment 1a, the results of which provide the necessary data for the EBM.

For the self-pressurization tests conducted in the MHTB tank, the tank was allowed to pressurize until the designated maximum pressure limit of 137.9 kPa was reached. The validation studies for the analytical and numerical models include this maximum pressure limit. However, the data collected for the EBM includes no such limit, since the objective of Experiment 1a was to examine how the tank pressure evolves over the course of the test period, rather than determine how long before the maximum pressure limit was reached. For the purposes of this experiment, the pressure history for the EBM is adjusted to reflect the appropriate pressure interval, that is, the initial tank pressure at the start of the simulation, up to the pressure limit of 137.9 kPa.

Once the pressure histories have been collected, the measured and predicted pressures are presented together in the same plot, where the predicted values correspond to the values obtained for each model, and the measured values correspond to those obtained for the MHTB tank. The plots are analyzed using the method described in Section 3.2. From the pressure histories, a table listing a summary of the measured and predicted dP/dt values and the dP/dt ratio is generated.

Recall from the literature review that although the model developed by Hastings et al. was created specifically to analyze self-pressurization and pressure control within the MHTB tank, TankSIM – a more detailed yet generalized model – proved more capable of predicting the fluid conditions in the tank, and thus provided more accurate values for dP/dt. The benefit provided by the additional accuracy however, was offset by the sheer amount of detail incorporated by the model, which utilizes 7 control volumes and includes approximately 40 heat and mass transfer processes. When compared to the prediction capability of GFSSP – which utilizes NFA – TankSIM provided similar, though less accurate results.

While it is anticipated that the EBM will not be capable of yielding predictions of similar accuracy to GFSSP or TankSIM, the author of this dissertation is optimistic that the EBM will be able to provide estimates similar to Hastings et al. – which if only the self-pressurization portion of that model is considered, is the most similar in complexity to the EBM. Note that while the primary objective of the experiment is to determine the fidelity in the EBM dP/dt predictions, the pressure histories will provide insight as to how the model assumptions affect the pressure behavior, and thus the dP/dt response, when compared with the analytical and numerical models from literature.

5.2.3 Results from dP/dt Comparison

The conditions for each of the self-pressurization tests conducted in the Aydelott tank are listed in Table 5.6; the corresponding measured and predicted dP/dt values, and the dP/dt ratios, are provided in Table 5.7. Figures 5.7a through 5.7d depict the time histories for the tank pressure, where the data corresponding to the MHTB tank is represented by the dashed lines, and the data corresponding to the various models is represented by the green (Hastings et al.), blue (TankSIM), orange (GFSSP), and red (EBM) lines.

From Figure 5.7a, the measured pressure increases linearly until approximately the 1-hour mark, where the tank pressure then begins to increase at a slower rate; around the 2-hour mark this behavior is repeated once more. Hastings et al. predict pressures that increase linearly with time; the model pressure is initially in excellent agreement with measured values, but begins to overestimate the tank pressure after the first hour. TankSIM underestimates the tank pressure for the majority of the test, but predicts a final pressure that is similar to the pressure value recorded in the tank. The EBM predicts elevated pressures for the duration of the test; the maximum pressure limit of 137.9 kPa is reached within the first hour of the test, while for Hastings et al., the pressure limit is reached after two hours, and for TankSIM, the limit is reached just under the 5-hour mark. From Table 5.7, the dP/dt values for the test period, in ascending order, are 4.87 kPa/s (MHTB tank), 5.23 kPa/s (TankSIM), 9.99 kPa/s (Hastings et al.), and 25.44 kP/s (EBM). Based on the dP/dt ratios of 1.07 (TankSIM), 2.05 (Hastings et al.), and 5.22 (EBM), the model predictions vary between values that are in excellent agreement (TankSIM) to conservative (Hastings et al. and the EBM).

For Test P263968E depicted in Figure 5.7b, the tank pressure rises quickly initially until around the 2-hour mark. The pressure then increases at a slower rate for the duration of the test period, resulting in a dP/dt value of 1.74 kPa/s. As before, Hastings et al. predicts pressures that are initially in agreement with measured values, but continues to increase linearly, resulting in a dP/dt value of 3.96 kPa/s. The EMB predicts pressures that are

higher initially, and continues to rise for the duration of the test, resulting in a dP/dt value of 8.57 kPa/s. Based on the dP/dt ratios of 2.27 (Hastings et al.) and 4.93 (EBM), both model predictions are conservative.

For Test P263968K, depicted in Figure 5.7c, TankSIM and the EBM predict final pressures, and therefore dP/dt values that are slightly lower than the measured value (0.81 kPa/s and 0.82 kPa/s, versus 0.87 kPa/s, respectively); but predict pressures that otherwise are in excellent agreement. Hastings et al. predict elevated pressures for the duration of the test, resulting in a dP/dt value of 4.14 kPa/s. From the corresponding dP/dt ratios of 0.94 (TankSIM), 0.95 (EBM), and 4.78 (Hastings et al.), the model predictions vary between values that are in excellent agreement (TankSIM and the EBM) to conservative (Hastings et al.).

For Test P263981T, depicted in Figure 5.7d, the models each exhibit pressures that increase almost linearly for the duration of the test, similar to the measured pressures, albeit at different rates – 1.91 kPa/s for the MHTB tank versus the predicted values of 2.05 kPa/s (GFSSP), 2.27 kPa/s (EBM), 2.79 kPa/s (TankSIM), and 9.81 kPa/s (Hastings et al.). Based on the dP/dt ratios of 1.07 (GFSSP), 1.19 (EBM), 1.46 (TankSIM), and 5.13 (Hastings et al.), model predictions vary between values that are in excellent agreement (GFSSP), to relatively good agreement (the EBM and TankSIM), to conservative (Hastings et al.).

Comparison of the measured and predicted values show that Hastings et al. predict tank pressures and dP/dt values that are conservative for all tests considered, with the gap between measured and predicted values increasing as FL decreases. TankSIM is not necessarily capable of predicting the tank pressure, but provides dP/dt predictions that are either in excellent agreement with, or that are in relatively good agreement with measured values. GFSSP, as expected, is capable of predicting both the tank pressure and dP/dt. The EBM provides the most conservative dP/dt predictions at higher FLs. However, for intermediate and lower FLs, the model is capable of predicting dP/dt with greater accuracy than Hastings et al., and with a similar fidelity to predictions provided by TankSIM and GFSSP.

Table 5.6: Test conditions for the MHTB tank.

Test No.	P (kPa)	FL (% by vol.)	$\dot{Q}$ (W)	t (s)
P263981D	111.5	90.0	54.1	19,591
P263968E	111.5	90.0	20.2	51,138
P263968K	122.0	25.0	18.8	49,869
P263981T	111.5	50.0	51.0	66,446

Table 5.7: Model dP/dt values and corresponding dP/dt ratios obtained for self-pressurization in the MHTB tank.

	dP/dt (kPa/hr)					Pred.-to-Meas. dP/dt Ratio			
Test No.	MHTB Tank	Hastings et al.	TankSIM	GFSSP	EBM	Hastings et al.	TankSIM	GFSSP	EBM
P263981D	4.87	9.99	5.23	-	25.44	2.05	1.07	-	5.22
P263968E	1.74	3.96	-	-	8.57	2.27	-	-	4.93
P263968K	0.87	4.14	0.81	-	0.82	4.78	0.94	-	0.95
P263981T	1.91	9.81	2.79	2.05	2.27	5.13	1.46	1.07	1.19

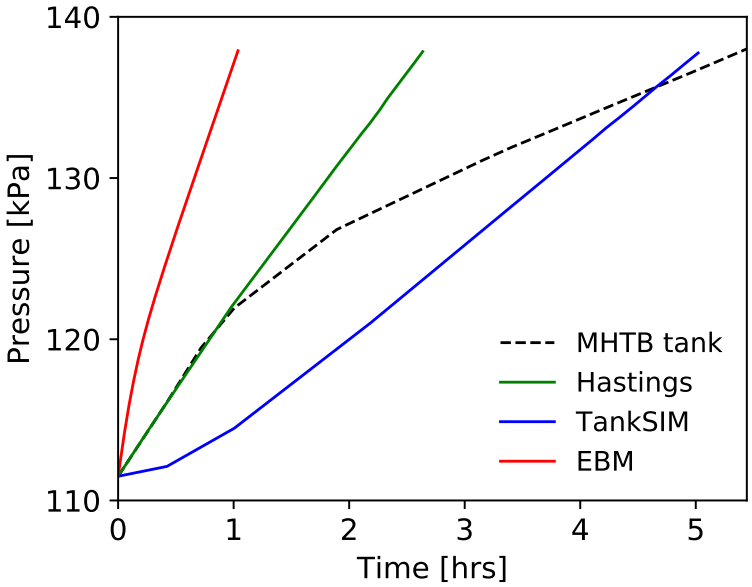

(a) Test P263981D

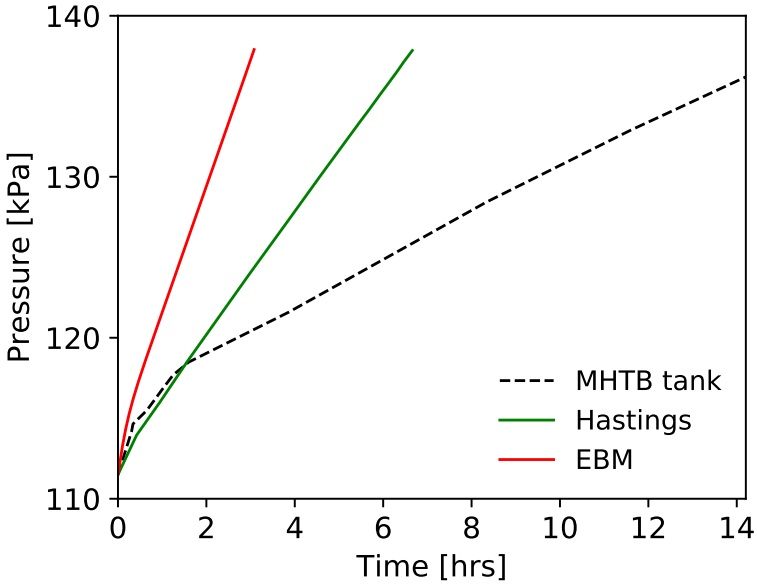

(b) Test P263968E

Figure 5.7: Measured (black) and predicted pressure histories for the initial self-pressurization period in the MHTB tank.

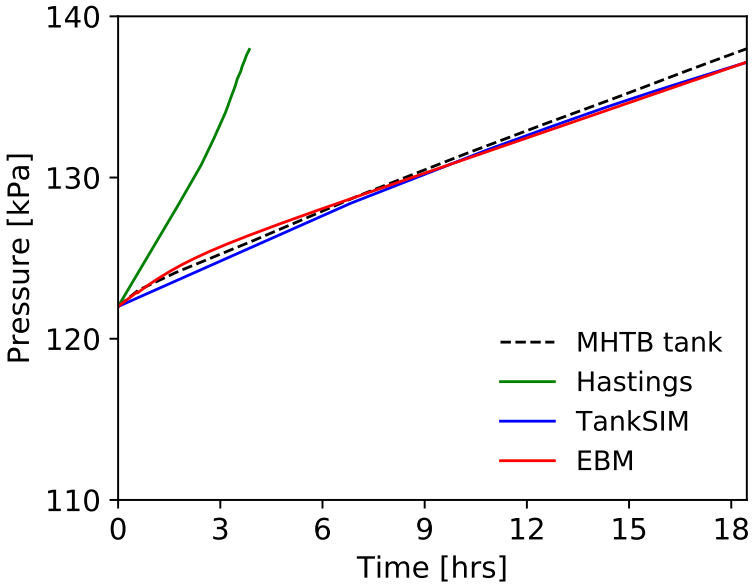

(c) Test P263968K

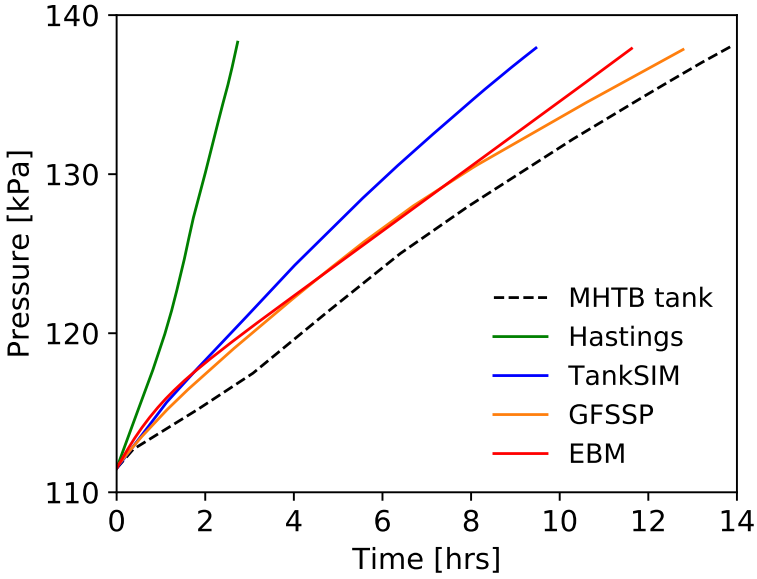

(d) Test P263981T

Figure 5.7: Measured (black) and predicted pressure histories for the initial self-pressurization period in the MHTB tank (continued).

5.2.4 Summary

The purpose of the experiment was to determine the fidelity in the EBM dP/dt prediction capability. Due the small number of heat and mass transfer processes utilized by the EBM, it was hypothesized that the model would predict less accurate dP/dt values when compared with those provided by other higher-fidelity analytical and numerical models in literature. Using the self-pressurization tests conducted in the MHTB tank as a baseline, EBM predictions were compared with those from several state-of-the-art models incorporating a pressure control capability: Hastings et al., TankSIM, and GFSSP.

For predictions obtained from the state of the art, Hastings et al. provided the lowest accuracy, especially at lower FLs. TankSIM performed well for all scenarios that were considered; the model provided dP/dt predictions with greater accuracy than Hastings et al., but with less accuracy than GFSSP, which was capable of predicting accurate values for both the tank pressure and dP/dt.

When compared to the above model predictions, the results showed that for lower and intermediate FLs, the EBM was capable of predicting the tank pressure and dP/dt with an accuracy very similar to that of TankSIM and GFSSP. These results bolster the approach used by the EBM to represent the physical processes in the tank; the model is capable of capturing the same fluid behavior, but with a significantly simpler model. However, for the highest FL of 90%, the EBM displayed the least accuracy in predictions for all models considered. As demonstrated in the previous experiment, the model assumptions used to capture the fluid behavior at the interface overestimate the amount of evaporation that occurs in the first few hours of the storage duration, resulting in high values for dP/dt. While model predictions are less accurate in larger tanks with higher FLs, in these scenarios predictions can be considered conservative[5].

Based on the results of the experiment, the hypothesis is invalidated. The EBM, while

[5]Note that this naturally brings to mind the following concern: if the EBM predicts conservative values, how does this compare to the theoretical model which also produces conservative values? This matter is addressed in Experiment 1c.

simple, provides dP/dt predictions with a fidelity similar to other higher-fidelity analytical and numerical models in literature. Now that confidence has been established in the dP/dt prediction capability, and thus boil-off, the model evaluation can now proceed to the venting component which relates the boil-off within the tank to the mass released during venting.

5.3 Experiment 1c - Verification of Venting Capability

The purpose of the venting component is to determine the amount of gas that should be released from the ullage in order to relieve the tank pressure from the maximum pressure limit P_{max}, to the desired pressure P_{min} specified for venting operations. In Chapter 4, Research Question 2 was posed regarding how to determine the mass released during venting, and the conditions in the tank once venting has concluded, as these quantities are not readily known. It was hypothesized that if the ullage is represented as a simple thermodynamic system, the mass released during venting can be determined without the need to examine the venting process itself. All that is required for the analysis is the thermodynamic state of the ullage, both immediately prior to and just after venting.

The conditions in the ullage at the start of the venting process, represented by P_1 = P_{max}, T_1, V_1, and m_1, are provided by the self-pressurization component of the model. The final state of the ullage is known if the ullage is assumed saturated, with a pressure P_{min} and a corresponding temperature of $T = T_{sat}(P_{min})$. The final state is then represented by $P_2 = P_{min}$, $T_2 = T_{sat}(P_{min})$, V_2 = V_1, and m_2, and the mass released during venting is simply the difference between the ullage mass before and after venting has occurred (Hypothesis 2).

All that now remains of this three-part model evaluation is to assess the venting capability of the model, which is addressed by the following research question:

Research Question 3.3: What is the ability of the model to simulate the venting process?

The effect on the ullage pressure and temperature during periods of pressure control

due to a spray bar TVS was presented as part of the literature review that was conducted in Chapter 3. While in this case, direct venting is the method of pressure control utilized, the overall behavior in the ullage pressure and temperature will be similar. Depressurization will occur at a much faster rate than repressurization; since venting is related to the tank pressurization rate, it is expected that the number of venting cycles will increase with FL, and time for repressurization from P_{min} to P_{max} will increase as FL decreases. Given that the tank pressure is directly related to ullage temperature, the temperature is expected to follow a similar oscillatory pattern.

Another aspect of the venting process that must be evaluated is the effect the saturated assumption has on the mass that is released during venting, which affects the propellant losses predicted by the model. The assumption that the tank is saturated for the entire storage duration, or a portion thereof, is used frequently in literature. However, it was found to be one of the primary causes that the traditional theoretical model (Equation 1.1, Figures 1.1a and 4.4) overestimates the propellant losses. In order to maintain saturation conditions, the heat entering the tank must be directed towards evaporation of the liquid propellant. In a actual tank, a portion of the entering heat goes towards heating of the ullage gas and the bulk liquid, thus reducing the amount of heat that contributes towards evaporation. Therefore, the theoretical model produces a higher rate of evaporation, and therefore higher propellant losses during venting than observed in literature.

For the model developed here, the heat entering the tank is distributed between the ullage and the bulk liquid. Experiment 1b demonstrated that the model is capable of predicting the tank pressurization rate, and therefore the propellant evaporation rate, with a degree of fidelity similar to other higher-fidelity models in literature. To determine the effect of the model assumption regarding the final saturated state of the ullage has on the venting process, consider the following: venting experiments conducted by Aydelott [7] showed that the temperature in the ullage after venting had concluded was higher than the saturation temperature, that is, $T_2 > T_{sat}$. For a pressure P_2 and volume V_2, in order for

the ullage to accommodate a higher temperature (that is, a temperature greater than T_{sat}), the ullage mass must correspondingly decrease. Therefore, if the final state of the ullage is assumed saturated, venting will release a greater amount of mass from the tank than if the ullage were superheated. Based on these observations, the following hypothesis can be formulated:

Hypothesis 3.3: *Given the assumption regarding the final saturated state of the ullage, the model will overestimate the mass that should be released during venting, and therefore the propellant losses due to boil-off, but to a lesser extent than the theoretical model in literature which assumes a saturated state for the entire storage period.*

Data with respect to direct venting of LH_2 tanks is not readily available in literature. One series of experiments performed by Aydelott in 1969 (mentioned above, and previously discussed in Section 4.2) investigated the propellant losses in a 56 cm diameter spherical tank due to venting. Experiments were conducted using heat flux rates of 74.1 W/m^2 and 275.7 W/m^2, at a propellant fill level of 65%. The pressure, temperature, and corresponding mass flow rate at the vent were measured over a duration of approximately 3 to 9 hours, while the tank was allowed pressurize and depressurize, from 345 kPa to 310 kPa, respectively.

Unfortunately, only approximately 20 - 80 minutes of the measured data is applicable, as beyond this time frame venting of the excess pressure took as long as 20 minutes, while repressurization required only seconds. This violates the principle of ideal operation, where venting is instantaneous compared to the time required for the tank to repressurize. In addition depending on the experiment, measurements for the mass flow rate at the vent either did not begin until after the 20 - 80 minute time frame or were too few. Therefore, these experiments are not suitable for model validation.

In absence of a suitable validation case, the next viable option is to verify the venting capability. To conduct this verification, and test the preceding hypothesis, Experiment 1c was developed which simulates a storage period of 2 days using 3.05 m spherical tank,

subject to a heat transfer rate of 54.1 W, at FLs of 90%, 50% and 25%. This combination of tank geometry and conditions was selected due to their combined effect on the ullage response during the period of pressure control. This provides an opportunity to investigate trends that are not present in other combinations, particularly those that include cylindrical tanks. Note that only a single $\dot{Q}$ need be examined, as varying $\dot{Q}$ only serves to change the speed at which the ullage responds (via the pressurization rate), rather than the nature of the response itself.

The verification entails an examination of the ullage pressure and temperature behavior during the period of pressure control, followed by an examination of the boil-off that accrues in the tank during pressurization, and the subsequent mass released during venting. With verification of the venting process complete, Hypothesis 3.3 is then tested by comparing the propellant losses predicted by the model for the 2-day storage period, to the losses predicted by theory. This last portion of the experiment provides the boil-off prediction capability of the model. That is, it answers Research Question 3, which is the objective of the evaluation effort conducted in this chapter.

A summary of the experimental objectives is provided in Section 5.3.1. Section 5.3.2 provides a brief review of the model, the input values used, the outputs that were gathered for the purposes of this experiment, and the procedure used for analyzing the results. Section 5.3.3.1 presents the results from verification of the ullage behavior predicted by the model. The results from examination of the boil-off and vented masses are presented in Section 5.3.3.2. The results from comparison of the model and theoretical propellant losses are presented in Section 5.3.3.3.

5.3.1 Purpose of Experiment

The primary objectives of the numerical experiment are as follows:

1. For the period of pressure control, verify the following behaviors:
    - The number of venting cycles increases with FL
    - The time for repressurization from P_{min} to P_{max} increases with decreasing FL
    - The ullage temperature exhibits an oscillatory behavior similar to the tank pressure, with a lower bound corresponding to $T = T_{sat}(P_{min})$
2. Examine the boil-off that accrues in the tank during pressurization and the mass released during venting
3. Compare the propellant losses predicted by the model with those predicted by theory

5.3.2 Setup and Procedure

A detailed description of the model was provided in Section 4.3. Here, a brief discussion is presented, with focus placed on the pressure control aspect of the model. Figure 4.7 illustrates a high-level overview of the model, where the self-pressurization process is represented by the inner loop (denoted ①), and the venting process is represented by the outer loop (denoted ②). The conditions, tank geometry, and pressure limits specified in Table 5.8 provide the necessary information in order to begin the simulation. Self-pressurization continues along the inner loop, until the tank pressure reaches P_{max} (details on this exit condition are discussed below). The conditions in the ullage (P_1, T_1, V_1, and m_1) are passed from the self-pressurization component to the venting component, where these conditions serve as the initial state for the venting process. Based on the value of P_{min} specified in Table 5.8, the model then determines the final state of the ullage ($P_2 = P_{min}$, $T_2 = T_{sat}(P_{min})$, $V_1 = V_2$, and m_2) at the end of the venting process, and the corresponding mass released during venting ($m_1 - m_2$). This final state is then passed from the venting component, back to the self-pressurization component, where it serves as the initial conditions for the next pressurization cycle. Pressurization and depressurization continues until the storage time

Table 5.8: Model inputs for Experiment 1c.

Variable	Description	Value	Units
$\dot{Q}$	Heat transfer rate	54.1	W
t	Time	2	days
P_o	Initial pressure	111.5	kPa
FL_o	Initial propellant fill level	95, 50, 25	% by vol.

(a) Conditions

Variable	Description	Value	Units
'sphere'	Tank shape	-	-
d	Tank diameter	3.05	m
l	Tank height	3.05	m

(b) Tank geometry

Variable	Description	Value	Units
P_{max}	Max. pressure	137.9	kPa
P_{min}	Min. pressure	131.0	kPa

(c) Venting operation

has elapsed. At the end of the simulation, the model outputs the total mass that was vented, which represents the total propellant losses for the storage period.

The 2-day simulation was conducted using the default time step of 10 seconds. The exit condition for the self-pressurization process is evaluated using an optional "events" argument in the solve_ivp module, which is utilized by the self-pressurization component to numerically integrate the system of ODEs representing the rate of change in the ullage and bulk liquid parameters, and solve for the conditions in the tank (P_g, T_g, T_l, etc.). The argument allows events to be tracked, where an event occurs at the zeroes of a continuous function of time and state. For each time step, the conditions in the tank are determined, and the continuous function defined by $P_{max} - P_g = 0$ is evaluated. When a sign change is detected, the event is triggered, and the integration is terminated. The variable values

corresponding to the time step immediately before the integration is terminated are the values that are used as the initial state in the venting component. For this reason, the tank pressure P_1 will vary slightly from P_{max}.

For the purposes of this experiment, additional outputs were collected. These included the time histories for the ullage pressure and temperature, the mass evaporated from the interface, and the total mass vented from the tank. For each instance that venting occurred, the initial and final conditions in the ullage were gathered, which are presented in the form of a "venting table" for each FL_o. Given that the volume is unchanged during the venting process, only the volume corresponding to initial state is provided. Also listed is the mass that was released during venting (m_{vent}), the boil-off (evaporated mass, m_{evap}) that accrued within the tank during the period of pressurization leading up to that particular venting cycle, and the percentage of the boil-off mass that was vented ($\mathcal{P}$).

The procedure for analyzing the outputs from the simulation is as follows: Verification of the ullage pressure and temperature behavior during the period of pressure control is rather straightforward. The pressure and temperature histories obtained from the model allow for visual confirmation as to whether or not the anticipated trends are present. The finer details regarding the ullage behavior as FL changes is achieved from comparison of the initial and final pressure (P_1, P_2) and temperature (T_1, T_2) values in the venting tables.

Examination of the boil-off and vented masses is carried out by plotting m_{evap} and m_{vent} values obtained from the venting tables with time. It is expected that m_{evap} for the first venting cycle will be greater than m_{evap} for subsequent cycles; the boil-off that accrues during the initial period of self-pressurization, from P_o to P_{max}, takes longer and thus provides more time for the propellant to evaporate than for subsequent periods of repressurization from P_{min} to P_{max}. Further, recall that as the ullage volume increases (FL decreases), the tank takes longer to pressurize. Therefore, it also expected that as FL decreases, m_{evap} will increase.

Regarding the vented mass, it is anticipated that m_{vent} will similarly increase as FL

decreases. Within the model, the vented mass is strictly a function of the conditions in the ullage, both immediately prior to and just after venting – where P_1, P_2, and T_2 are fixed by the values of P_{max} and P_{min} specified in Table 5.8 (as previously mentioned, the value of P_1 will vary slightly from P_{max}. For the purposes of this discussion P_1 can be considered constant, with a value equal to P_{max}). With these variables held constant, m_{vent} then becomes a function of V_1 and T_1, as shown by Equations 5.1 through 5.4 below:

$$m_{vent} = m_1 - m_2 \tag{5.1}$$

$$= \frac{P_1 V_1 M}{R_u T_1} - \frac{P_2 V_2 M}{R_u T_2} \tag{5.2}$$

$$= \frac{M V_1}{R_u}\left(\frac{P_1}{T_1} - \frac{P_2}{T_2}\right) \tag{5.3}$$

$$= f\left(V_1/T_1\right) \tag{5.4}$$

The expression for m_1 and m_2 in Equation 5.2 is obtained from rearrangement of the ideal gas equation of state, $PV = mR_uT/M$. Given that $V_1 = V_2$, Equation 5.2 can be simplified as shown in Equation 5.3. Per the above discussion, V_1 and T_1 are the only variables change that during the venting process. Therefore, m_{vent} is directly proportional to V_1, and inversely proportional T_1, as shown in Equation 5.4.

During the period of pressure control, the ullage temperature will fluctuate between T_1 and T_2. While T_1 is not strictly bounded – unlike T_2 – for the tank sizes and heat transfer rates anticipated in future missions, the ullage temperature and hence T_1 should not vary substantially. Since the ullage volume, regardless of the conditions, can reasonably take on values anywhere between 10% to 85% of the tank volume, m_{vent} is more affected by V_1. Therefore, it is expected that as FL decreases, m_{vent} will increase.

The final assessment of the boil-off and vented masses occurs through examination of the $\mathcal{P}$ values from the venting tables. At this point, while certain trends in m_{evap} and m_{vent} are anticipated, less is known regarding the relative amounts of the two masses. Inspection

of the $\mathcal{P}$ values will provide information as to how much of m_{evap} is vented, and how this changes over the course of the pressure control period.

Finally, the propellant losses predicted by the model are compared with those predicted by theory. Recall that the theoretical model assumes that the heat entering the tank contributes entirely towards evaporation of the liquid propellant, and the rate at which the propellant evaporates is equivalent to the mass flow rate of the escaping gas at the vent. The newly developed model assumes that only a portion of the entering heat contributes towards evaporation. Furthermore, the rate at which the propellant evaporates is affected by a variety of factors that change with time; the mass that is vented from the tank is not necessarily equivalent to the mass of the evaporated propellant. Therefore, it is expected that the theoretical losses will be greater than those predicted by the model (Hyp. 3.3).

The results predicted by the model are compared with those from theory by plotting the time histories for their respective propellant losses, m_{bo}. The time history for the theoretical losses is obtained by multiplying the boil-off rate in Equation 1.1 by the time array used in the simulation. The time history for the total mass vented from the tank serves as the propellant losses for the model. The plots are analyzed in a similar fashion as the tank pressure and the pressurization rate were evaluated in the literature review (Chapter 3, Section 3.2). That is, the propellant losses for both models are compared directly, while a visual inspection of the initial and final mass values provides information regarding the rate at which the losses are incurred, $\dot{m}_{bo}$. For the theoretical model, this is simply the boil-off rate, per Equation 1.1. However, for the model developed here, this is the rate at which losses are incurred due evaporation and subsequent venting, which is not necessarily equal to the rate of evaporation that occurs at the interface $\dot{m}_{evap}$.

Lastly, the ratio of the theoretical-to-model losses, or the "loss ratio" (analogous to the dP/dt ratio), serves as the final metric when comparing the results between the two models. The loss ratio quantifies the difference in the two m_{bo} predictions, which is a direct result of how the two models distribute the heat within the tank.

5.3.3 Results from Venting Simulations

5.3.3.1 Verification of Pressure and Temperature Behavior

The pressure and temperature histories obtained from simulation are depicted in Figures 5.8 and 5.9. For better visualization of trends, Figure 5.8 illustrates the pressure and temperature for the first 10 hours of the storage period, whereas Figure 5.9 illustrates the time histories for the full 2-day storage period. Tables 5.9 through 5.11 lists the results obtained for the initial FLs of 90%, 50% and 25%, respectively, where the initial and final states are denoted by State 1 and State 2, respectively. Also listed are the values of m_{evap}, m_{vent}, and $\mathcal{P}$. Of the variables listed, the ullage temperature is affected least during the simulation, so only one decimal place is used. In order to identify and confirm trends in the data, three decimal places are retained for the pressure and volume, and four decimal places are retained for mass values. Two decimal places are reported for the value of FL at the time that venting occurred, and one decimal place is used for $\mathcal{P}$.

As shown in the pressure plots in Figure 5.8, for the highest FL of 90%, the venting period is initiated at the 4-hour mark. As FL decreases, the venting period begins later, at around the 7-hour mark for FL of 50%, and around the 8-hour mark for FL of 25%, and the number of vent cycles decreases from 9, to 3, to 2. The greater number of venting cycles at the highest FL is due to the higher pressurization rate caused by the added mass from evaporation to a smaller ullage volume. As FL decreases, the effect lessens, which extends the time before the first vent is required. From Tables 5.9 through 5.11, the total number of venting cycles for the 2-day storage period totalled 60 for FL of 90%, and 34 for FLs of 50% and 25%. The number of venting cycles is the same for the intermediate and lower FLs since for this combination of tank geometry and FL, the repressurization rate, and therefore the time between successive venting cycles, remains relatively constant at approximately 5.7 kPa/hr and 73 minutes, respectively. This can be seen in Figure 5.9, where the pressure plots for FLs of 50% and 25% appear identical.

Referring now to the temperature plots in Figure 5.8, it can be seen that for each FL, the

ullage temperature follows a similar behavior as the tank pressure, depicted immediately to the left. It can also be observed that the final temperature T_1 attained in the ullage region at the end of the initial self-pressurization period, just before the first venting cycle is initiated, increases slightly as FL decreases. From Tables 5.9 through 5.11, the T_1 values for this first venting cycle correspond to temperatures 22.0 K, 22.2 K, and 22.5 for FLs of 90%, 50%, and 25%, respectively. This trend can be attributed to the length of the self-pressurization period – the greater the time before venting is initiated, the greater the heat input, and thus temperature increase in the region. For each FL, the T_1 values for subsequent venting cycles are constant but increase slightly, by 0.1 K and 0.2 K for FLs 50% and 25%, respectively, for the same reason previously discussed regarding ullage heating during the initial self-pressurization period. For all three FLs, T_2 remains constant, at 21.3 K, for the duration of the storage period. These trends in the ullage temperature are more easily observed in Figure 5.9.

These results demonstrate that the model is capable of simulating the appropriate pressure and temperature behavior during the period of pressure control. Once venting is initiated, the tank pressure is maintained within the pressure band specified by P_{max} and P_{min}. The number of venting cycles increases with FL, and is ultimately determined by the tank pressurization rate, which is a function of the tank geometry and FL. The time for repressurization from P_{min} to P_{max} increases as FL decreases, and is similarly affected by the governing factors that influence the tank pressurization rate. The ullage temperature displays a behavior similar to the tank pressure with a lower bound determined by $T = T_{sat}(P_{min})$, but does not subscribe to a strict maximum value on the temperature T_1 achieved in the ullage just before venting is initiated. For this 3.05 m diameter spherical tank, T_1 increases slightly as FL decreases. However, the strength of the response will vary with the tank geometry.

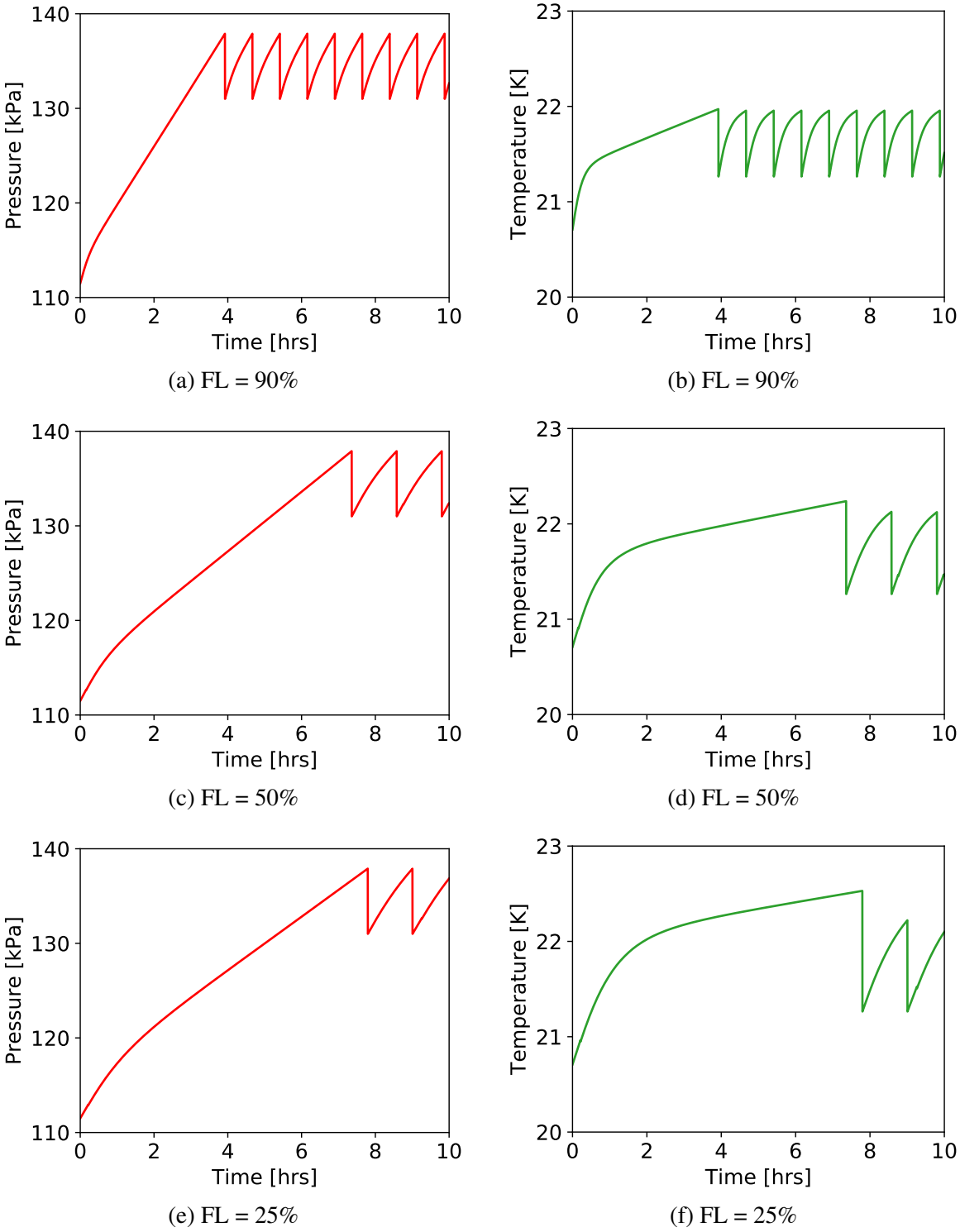

(a) FL = 90%

(b) FL = 90%

(c) FL = 50%

(d) FL = 50%

(e) FL = 25%

(f) FL = 25%

Figure 5.8: Ullage pressure (red) and temperature (green) histories obtained from simulation of the first 10 hours of the 2 day storage period.

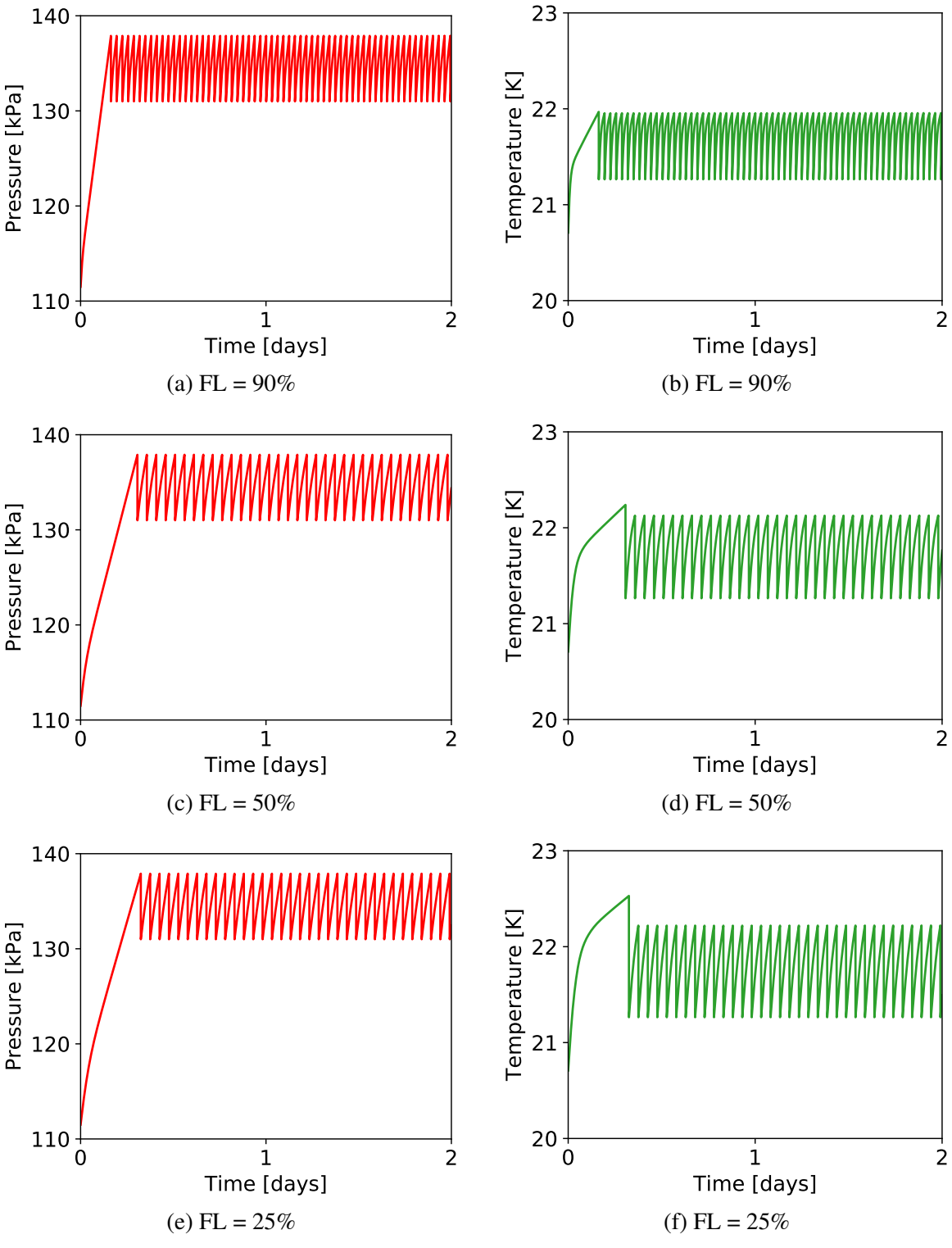

(a) FL = 90%

(b) FL = 90%

(c) FL = 50%

(d) FL = 50%

(e) FL = 25%

(f) FL = 25%

Figure 5.9: Ullage pressure (red) and temperature (green) histories obtained from simulation of a 2-day storage period in a 3.05 m diameter spherical tank, subject to a thermal load of 54.1 W, and FLs of 90%, 50%, and 25%.

Table 5.9: Venting table for the initial FL of 90%.

FL	Vent	State 1				State 2			m_{evap}	m_{vent}	$\mathcal{P}$
(% by vol.)	Cycle	P_1 (kPa)	T_1 (K)	V_1 (m^3)	m_1 (kg)	P_2 (kPa)	T_2 (K)	m_2 (kg)	(kg)	(kg)	(%)
89.97	1	137.890	22.0	1.490	2.2682	131.000	21.3	2.2262	0.3287	0.0420	12.8
89.96	2	137.887	22.0	1.491	2.2706	131.000	21.3	2.2271	0.0444	0.0434	97.7
89.96	3	137.887	22.0	1.492	2.2715	131.000	21.3	2.2281	0.0444	0.0435	98.0
89.96	4	137.887	22.0	1.492	2.2725	131.000	21.3	2.2290	0.0444	0.0435	98.0
89.95	5	137.887	22.0	1.493	2.2735	131.000	21.3	2.2300	0.0444	0.0435	98.0
89.95	6	137.887	22.0	1.493	2.2744	131.000	21.3	2.2309	0.0445	0.0435	97.8
89.94	7	137.887	22.0	1.494	2.2754	131.000	21.3	2.2319	0.0445	0.0435	97.8
89.94	8	137.888	22.0	1.495	2.2763	131.000	21.3	2.2328	0.0445	0.0435	97.8
89.93	9	137.888	22.0	1.495	2.2773	131.000	21.3	2.2337	0.0445	0.0436	98.0
89.93	10	137.888	22.0	1.496	2.2783	131.000	21.3	2.2347	0.0445	0.0436	98.0
89.93	11	137.888	22.0	1.497	2.2792	131.000	21.3	2.2356	0.0445	0.0436	98.0
89.92	12	137.888	22.0	1.497	2.2802	131.000	21.3	2.2366	0.0446	0.0436	97.8
89.92	13	137.888	22.0	1.498	2.2812	131.000	21.3	2.2375	0.0446	0.0436	97.8
89.91	14	137.888	22.0	1.498	2.2821	131.000	21.3	2.2385	0.0446	0.0436	97.8
89.91	15	137.888	22.0	1.499	2.2831	131.000	21.3	2.2394	0.0446	0.0437	98.0

Continued on next page

Table 5.9 – continued from previous page

FL (% by vol.)	Vent Cycle	State 1				State 2			m_{evap} (kg)	m_{vent} (kg)	$\mathcal{P}$ (%)
		P_1 (kPa)	T_1 (K)	V_1 (m^3)	m_1 (kg)	P_2 (kPa)	T_2 (K)	m_2 (kg)			
89.90	16	137.888	22.0	1.500	2.2841	131.000	21.3	2.2404	0.0446	0.0437	98.0
89.90	17	137.888	22.0	1.500	2.2850	131.000	21.3	2.2413	0.0446	0.0437	98.0
89.90	18	137.888	22.0	1.501	2.2860	131.000	21.3	2.2423	0.0447	0.0437	97.8
89.89	19	137.888	22.0	1.502	2.2870	131.000	21.3	2.2432	0.0447	0.0437	97.8
89.89	20	137.889	22.0	1.502	2.2879	131.000	21.3	2.2442	0.0447	0.0437	97.8
89.88	21	137.889	22.0	1.503	2.2889	131.000	21.3	2.2451	0.0447	0.0438	98.0
89.88	22	137.889	22.0	1.504	2.2899	131.000	21.3	2.2461	0.0447	0.0438	98.0
89.87	23	137.889	22.0	1.504	2.2908	131.000	21.3	2.2470	0.0447	0.0438	98.0
89.87	24	137.889	22.0	1.505	2.2918	131.000	21.3	2.2480	0.0448	0.0438	97.8
89.87	25	137.889	22.0	1.505	2.2928	131.000	21.3	2.2490	0.0448	0.0438	97.8
89.86	26	137.889	22.0	1.506	2.2938	131.000	21.3	2.2499	0.0448	0.0438	97.8
89.86	27	137.889	22.0	1.507	2.2947	131.000	21.3	2.2509	0.0448	0.0439	98.0
89.85	28	137.889	22.0	1.507	2.2957	131.000	21.3	2.2518	0.0448	0.0439	98.0
89.85	29	137.889	22.0	1.508	2.2967	131.000	21.3	2.2528	0.0449	0.0439	97.8
89.84	30	137.889	22.0	1.509	2.2976	131.000	21.3	2.2537	0.0449	0.0439	97.8
89.84	31	137.890	22.0	1.509	2.2986	131.000	21.3	2.2547	0.0449	0.0439	97.8

Continued on next page

Table 5.9 – continued from previous page

FL (% by vol.)	Vent Cycle	State 1				State 2			m_{evap} (kg)	m_{vent} (kg)	$\mathcal{P}$ (%)
		P_1 (kPa)	T_1 (K)	V_1 (m^3)	m_1 (kg)	P_2 (kPa)	T_2 (K)	m_2 (kg)			
89.84	32	137.890	22.0	1.510	2.2996	131.000	21.3	2.2556	0.0449	0.0439	97.8
89.83	33	137.890	22.0	1.511	2.3006	131.000	21.3	2.2566	0.0449	0.0440	98.0
89.83	34	137.890	22.0	1.511	2.3016	131.000	21.3	2.2576	0.0449	0.0440	98.0
89.82	35	137.890	22.0	1.512	2.3025	131.000	21.3	2.2585	0.0450	0.0440	97.8
89.82	36	137.890	22.0	1.513	2.3035	131.000	21.3	2.2595	0.0450	0.0440	97.8
89.81	37	137.890	22.0	1.513	2.3045	131.000	21.3	2.2605	0.0450	0.0440	97.8
89.81	38	137.890	22.0	1.514	2.3055	131.000	21.3	2.2614	0.0450	0.0441	98.0
89.81	39	137.890	22.0	1.514	2.3064	131.000	21.3	2.2624	0.0450	0.0441	98.0
89.80	40	137.890	22.0	1.515	2.3074	131.000	21.3	2.2633	0.0451	0.0441	97.8
89.80	41	137.891	22.0	1.516	2.3084	131.000	21.3	2.2643	0.0451	0.0441	97.8
89.79	42	137.891	22.0	1.516	2.3094	131.000	21.3	2.2653	0.0451	0.0441	97.8
89.79	43	137.891	22.0	1.517	2.3104	131.000	21.3	2.2662	0.0451	0.0441	97.8
89.78	44	137.891	22.0	1.518	2.3114	131.000	21.3	2.2672	0.0451	0.0442	98.0
89.78	45	137.897	22.0	1.518	2.3123	131.000	21.3	2.2682	0.0451	0.0441	97.8
89.78	46	137.890	22.0	1.519	2.3133	131.000	21.3	2.2691	0.0451	0.0442	98.0
89.77	47	137.889	22.0	1.520	2.3143	131.000	21.3	2.2701	0.0451	0.0442	98.0

Continued on next page

Table 5.9 – continued from previous page

FL (% by vol.)	Vent Cycle	State 1				State 2			m_{evap} (kg)	m_{vent} (kg)	$\mathcal{P}$ (%)
		P_1 (kPa)	T_1 (K)	V_1 (m^3)	m_1 (kg)	P_2 (kPa)	T_2 (K)	m_2 (kg)			
89.77	48	137.888	22.0	1.520	2.3152	131.000	21.3	2.2711	0.0452	0.0442	97.8
89.76	49	137.887	22.0	1.521	2.3162	131.000	21.3	2.2720	0.0452	0.0442	97.8
89.76	50	137.887	22.0	1.522	2.3172	131.000	21.3	2.2730	0.0452	0.0442	97.8
89.75	51	137.886	22.0	1.522	2.3182	131.000	21.3	2.2740	0.0452	0.0442	97.8
89.75	52	137.885	22.0	1.523	2.3191	131.000	21.3	2.2749	0.0452	0.0442	97.8
89.74	53	137.884	22.0	1.524	2.3201	131.000	21.3	2.2759	0.0452	0.0442	97.8
89.74	54	137.883	22.0	1.524	2.3211	131.000	21.3	2.2769	0.0452	0.0442	97.8
89.74	55	137.882	22.0	1.525	2.3220	131.000	21.3	2.2778	0.0452	0.0442	97.8
89.73	56	137.882	22.0	1.525	2.3230	131.000	21.3	2.2788	0.0452	0.0442	97.8
89.73	57	137.899	22.0	1.526	2.3242	131.000	21.3	2.2798	0.0454	0.0445	98.0
89.72	58	137.898	22.0	1.527	2.3252	131.000	21.3	2.2807	0.0454	0.0445	98.0
89.72	59	137.898	22.0	1.527	2.3262	131.000	21.3	2.2817	0.0455	0.0445	97.8
89.71	60	137.897	22.0	1.528	2.3272	131.000	21.3	2.2827	0.0455	0.0445	97.8

Table 5.10: Venting table for the initial FL of 50%.

FL	Vent	State 1				State 2			m_{evap}	m_{vent}	$\mathcal{P}$
(% by vol.)	Cycle	P_1 (kPa)	T_1 (K)	V_1 (m^3)	m_1 (kg)	P_2 (kPa)	T_2 (K)	m_2 (kg)	(kg)	(kg)	(%)
49.86	1	137.893	22.2	7.449	11.2003	131.000	21.3	11.1280	1.5026	0.0723	4.8
49.84	2	137.895	22.1	7.451	11.2601	131.000	21.3	11.1308	0.1321	0.1293	97.9
49.83	3	137.895	22.1	7.453	11.2630	131.000	21.3	11.1336	0.1322	0.1294	97.9
49.82	4	137.896	22.1	7.455	11.2659	131.000	21.3	11.1364	0.1323	0.1295	97.9
49.81	5	137.897	22.1	7.457	11.2688	131.000	21.3	11.1392	0.1324	0.1296	97.9
49.79	6	137.898	22.1	7.459	11.2717	131.000	21.3	11.1421	0.1324	0.1296	97.9
49.78	7	137.899	22.1	7.461	11.2746	131.000	21.3	11.1449	0.1325	0.1297	97.9
49.77	8	137.900	22.1	7.462	11.2775	131.000	21.3	11.1477	0.1326	0.1297	97.8
49.75	9	137.889	22.1	7.464	11.2798	131.000	21.3	11.1505	0.1321	0.1293	97.9
49.74	10	137.890	22.1	7.466	11.2827	131.000	21.3	11.1533	0.1322	0.1294	97.9
49.73	11	137.891	22.1	7.468	11.2856	131.000	21.3	11.1562	0.1323	0.1294	97.8
49.72	12	137.892	22.1	7.470	11.2885	131.000	21.3	11.1590	0.1323	0.1295	97.9
49.70	13	137.893	22.1	7.472	11.2914	131.000	21.3	11.1618	0.1324	0.1296	97.9
49.69	14	137.894	22.1	7.474	11.2943	131.000	21.3	11.1646	0.1325	0.1296	97.8
49.68	15	137.895	22.1	7.476	11.2972	131.000	21.3	11.1675	0.1325	0.1297	97.9

Continued on next page

Table 5.10 – continued from previous page

FL (% by vol.)	Vent Cycle	State 1				State 2			m_{evap} (kg)	m_{vent} (kg)	$\mathcal{P}$ (%)
		P_1 (kPa)	T_1 (K)	V_1 (m^3)	m_1 (kg)	P_2 (kPa)	T_2 (K)	m_2 (kg)			
49.67	16	137.896	22.1	7.478	11.3000	131.000	21.3	11.1703	0.1326	0.1298	97.9
49.65	17	137.897	22.1	7.479	11.3029	131.000	21.3	11.1731	0.1327	0.1298	97.8
49.64	18	137.897	22.1	7.481	11.3058	131.000	21.3	11.1760	0.1327	0.1299	97.9
49.63	19	137.898	22.1	7.483	11.3088	131.000	21.3	11.1788	0.1328	0.1300	97.9
49.61	20	137.899	22.1	7.485	11.3117	131.000	21.3	11.1816	0.1329	0.1300	97.8
49.60	21	137.889	22.1	7.487	11.3140	131.000	21.3	11.1845	0.1324	0.1296	97.9
49.59	22	137.889	22.1	7.489	11.3170	131.000	21.3	11.1873	0.1325	0.1297	97.9
49.58	23	137.889	22.1	7.491	11.3198	131.000	21.3	11.1901	0.1325	0.1296	97.8
49.56	24	137.889	22.1	7.493	11.3226	131.000	21.3	11.1930	0.1325	0.1296	97.8
49.55	25	137.889	22.1	7.495	11.3254	131.000	21.3	11.1958	0.1325	0.1296	97.8
49.54	26	137.889	22.1	7.497	11.3283	131.000	21.3	11.1986	0.1325	0.1296	97.8
49.53	27	137.889	22.1	7.498	11.3311	131.000	21.3	11.2015	0.1325	0.1296	97.8
49.51	28	137.900	22.1	7.500	11.3345	131.000	21.3	11.2043	0.1330	0.1302	97.9
49.50	29	137.900	22.1	7.502	11.3373	131.000	21.3	11.2072	0.1330	0.1302	97.9
49.49	30	137.900	22.1	7.504	11.3402	131.000	21.3	11.2100	0.1330	0.1302	97.9
49.47	31	137.899	22.1	7.506	11.3430	131.000	21.3	11.2129	0.1330	0.1302	97.9

Continued on next page

Table 5.10 – continued from previous page

FL (% by vol.)	Vent Cycle	State 1				State 2			m_{evap} (kg)	m_{vent} (kg)	$\mathcal{P}$ (%)
		P_1 (kPa)	T_1 (K)	V_1 (m^3)	m_1 (kg)	P_2 (kPa)	T_2 (K)	m_2 (kg)			
49.46	32	137.899	22.1	7.508	11.3459	131.000	21.3	11.2157	0.1330	0.1302	97.9
49.45	33	137.899	22.1	7.510	11.3487	131.000	21.3	11.2186	0.1330	0.1302	97.9
49.44	34	137.899	22.1	7.512	11.3516	131.000	21.3	11.2214	0.1330	0.1302	97.9

Table 5.11: Venting table for the initial FL of 25%.

FL	Vent	State 1				State 2			m_{evap}	m_{vent}	$\mathcal{P}$
(% by vol.)	Cycle	P_1 (kPa)	T_1 (K)	V_1 (m^3)	m_1 (kg)	P_2 (kPa)	T_2 (K)	m_2 (kg)	(kg)	(kg)	(%)
24.81	1	137.899	22.5	11.171	16.5794	131.000	21.3	16.6873	2.0330	-0.1079	-5.3
24.79	2	137.894	22.2	11.173	16.8128	131.000	21.3	16.6900	0.1255	0.1228	97.8
24.78	3	137.894	22.2	11.174	16.8156	131.000	21.3	16.6927	0.1256	0.1230	97.9
24.77	4	137.895	22.2	11.176	16.8184	131.000	21.3	16.6953	0.1257	0.1230	97.9
24.76	5	137.896	22.2	11.178	16.8211	131.000	21.3	16.6980	0.1258	0.1231	97.9
24.75	6	137.897	22.2	11.180	16.8239	131.000	21.3	16.7007	0.1258	0.1232	97.9
24.73	7	137.898	22.2	11.182	16.8266	131.000	21.3	16.7034	0.1259	0.1232	97.9
24.72	8	137.900	22.2	11.183	16.8294	131.000	21.3	16.7061	0.1260	0.1233	97.9
24.71	9	137.888	22.2	11.185	16.8316	131.000	21.3	16.7088	0.1255	0.1228	97.8
24.70	10	137.889	22.2	11.187	16.8343	131.000	21.3	16.7114	0.1256	0.1229	97.9
24.68	11	137.890	22.2	11.189	16.8371	131.000	21.3	16.7141	0.1257	0.1230	97.9
24.67	12	137.891	22.2	11.191	16.8398	131.000	21.3	16.7168	0.1257	0.1230	97.9
24.66	13	137.893	22.2	11.192	16.8426	131.000	21.3	16.7195	0.1258	0.1231	97.9
24.65	14	137.894	22.2	11.194	16.8454	131.000	21.3	16.7222	0.1259	0.1232	97.9
24.64	15	137.893	22.2	11.196	16.8482	131.000	21.3	16.7249	0.1260	0.1234	97.9

Continued on next page

Table 5.11 – continued from previous page

FL	Vent	State 1				State 2			m_{evap}	m_{vent}	$\mathcal{P}$
(% by vol.)	Cycle	P_1 (kPa)	T_1 (K)	V_1 (m^3)	m_1 (kg)	P_2 (kPa)	T_2 (K)	m_2 (kg)	(kg)	(kg)	(%)
24.62	16	137.895	22.2	11.198	16.8508	131.000	21.3	16.7276	0.1260	0.1233	97.9
24.61	17	137.895	22.2	11.200	16.8535	131.000	21.3	16.7303	0.1259	0.1232	97.9
24.60	18	137.896	22.2	11.201	16.8562	131.000	21.3	16.7330	0.1259	0.1232	97.9
24.59	19	137.896	22.2	11.203	16.8589	131.000	21.3	16.7357	0.1259	0.1232	97.9
24.58	20	137.896	22.2	11.205	16.8616	131.000	21.3	16.7384	0.1259	0.1232	97.9
24.56	21	137.896	22.2	11.207	16.8643	131.000	21.3	16.7410	0.1259	0.1232	97.9
24.55	22	137.896	22.2	11.209	16.8669	131.000	21.3	16.7437	0.1259	0.1232	97.9
24.54	23	137.896	22.2	11.210	16.8696	131.000	21.3	16.7464	0.1259	0.1232	97.9
24.53	24	137.897	22.2	11.212	16.8723	131.000	21.3	16.7491	0.1259	0.1232	97.9
24.51	25	137.897	22.2	11.214	16.8750	131.000	21.3	16.7518	0.1259	0.1232	97.9
24.50	26	137.897	22.2	11.216	16.8777	131.000	21.3	16.7545	0.1259	0.1232	97.9
24.49	27	137.897	22.2	11.218	16.8804	131.000	21.3	16.7572	0.1259	0.1232	97.9
24.48	28	137.897	22.2	11.219	16.8831	131.000	21.3	16.7599	0.1258	0.1232	97.9
24.47	29	137.898	22.2	11.221	16.8857	131.000	21.3	16.7626	0.1258	0.1231	97.9
24.45	30	137.898	22.2	11.223	16.8884	131.000	21.3	16.7653	0.1258	0.1231	97.9
24.44	31	137.898	22.2	11.225	16.8911	131.000	21.3	16.7680	0.1258	0.1231	97.9

Continued on next page

Table 5.11 – continued from previous page

FL (% by vol.)	Vent Cycle	State 1				State 2			m_{evap} (kg)	m_{vent} (kg)	$\mathcal{P}$ (%)
		P_1 (kPa)	T_1 (K)	V_1 (m^3)	m_1 (kg)	P_2 (kPa)	T_2 (K)	m_2 (kg)			
24.43	32	137.898	22.2	11.227	16.8938	131.000	21.3	16.7707	0.1258	0.1231	97.9
24.42	33	137.898	22.2	11.228	16.8965	131.000	21.3	16.7734	0.1258	0.1231	97.9
24.41	34	137.899	22.2	11.230	16.8992	131.000	21.3	16.7761	0.1258	0.1231	97.9

5.3.3.2 *Examination of Boil-Off and Vented Masses*

Figure 5.10 depicts the boil-off and vented masses corresponding to each venting cycle listed in Tables 5.9 through 5.11. The first peak in the boil-off plots corresponds to the boil-off that accrued in the tank during the initial self-pressurization period, from P_o to P_{max}. The smaller peaks that follow correspond to the mass accrued during each period of repressurization, from P_{min} to P_{max}. For each FL, m_{evap} corresponding to the first venting cycle increases as FL decreases as expected. m_{evap} corresponding to subsequent venting cycles appears relatively constant for the remainder of the pressure control period. As FL decreases from 90% to 50%, m_{vent} increases, as expected. However, as FL decreases further, from 50% to 25%, m_{vent} appears unchanged. From the venting tables, it can be seen that m_{evap} actually decreases slightly from approximately 0.13 kg to 0.12 kg.

This slight decrease in m_{vent} can be attributed to the effect of the spherical tank geometry on the tank pressurization rate, or the time required to reach P_{max}, at intermediate and lower FLs. Figure 5.11 illustrates the ullage and bulk volumes at the three different FLs. Figures 5.12a and 5.12b depict the ullage volume and the rate of change in the ullage volume, respectively, as a function of decreasing liquid height, where the vertical dotted lines at 2.46 m, 1.53 m, and 1.00 m represent the height of the liquid propellant at FLs of 90%, 50%, and 25%, respectively. For FLs greater than 50%, the ullage volume increases at a greater rate since the cross section of the tank continues to increase as the liquid height decreases. For FLs below 50%, while the ullage volume overall continues to increase, the cross section of the tank decreases as the propellant boils-off. As a result, the time for the tank pressure to reach P_{max} decreases, although only slightly by about 10 - 20 seconds, which decreases the time between pressurization cycles, and thus the time for boil-off to accrue.

Moving onto the vented masses in Figure 5.10, for each FL, m_{vent} is relatively constant throughout the period of pressure control, with the exception of the first venting cycle in FLs 50% and 25%. for FL of 50% m_{vent} for the first venting cycle is approximately half

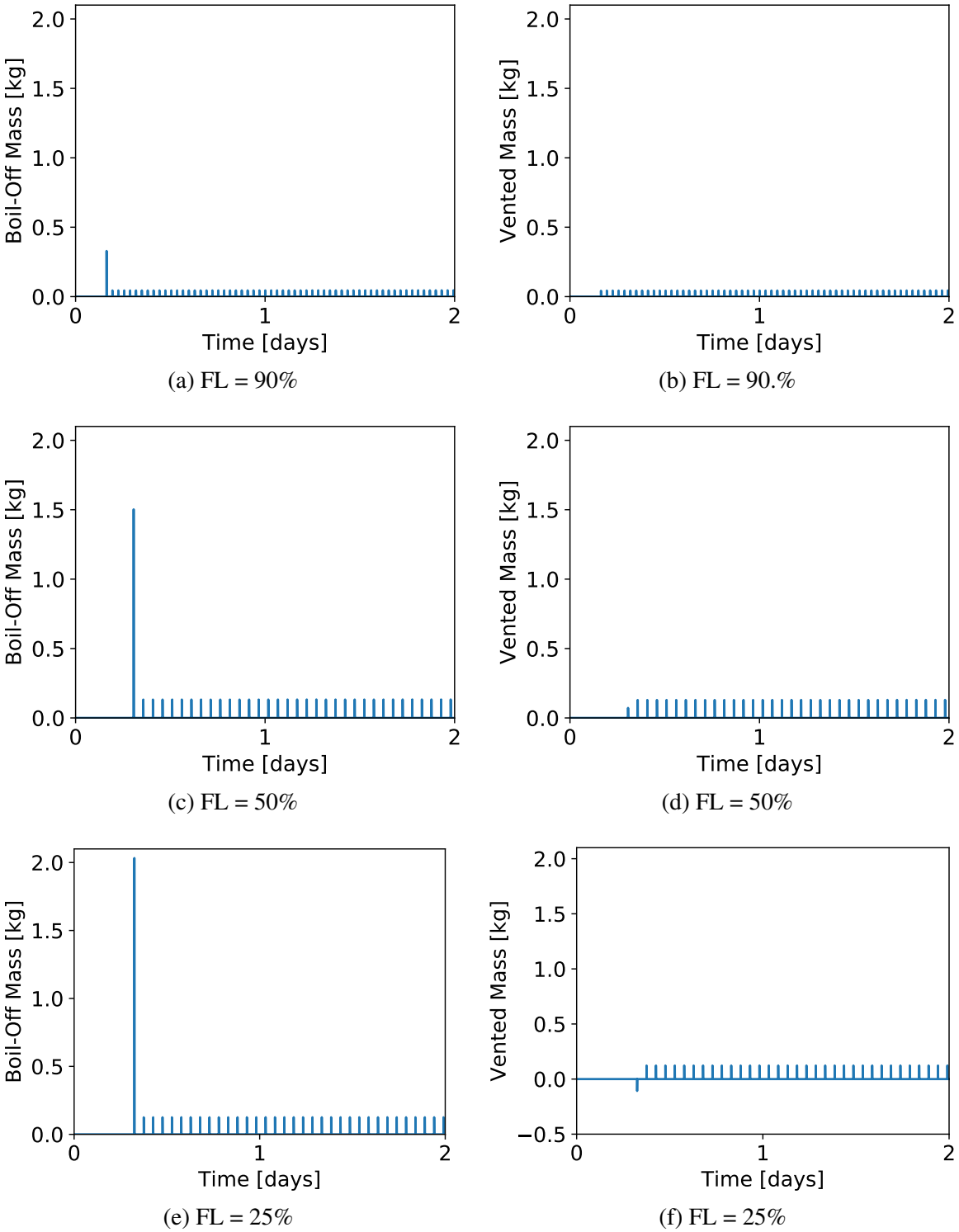

(a) FL = 90%

(b) FL = 90.%

(c) FL = 50%

(d) FL = 50%

(e) FL = 25%

(f) FL = 25%

Figure 5.10: Boil-off mass (left) and vented mass (right) obtained from simulation of a 2-day storage period in a 3.05 m diameter spherical tank, subject to a thermal load of 54.1 W, and FLs of 90%, 50%, and 25%.

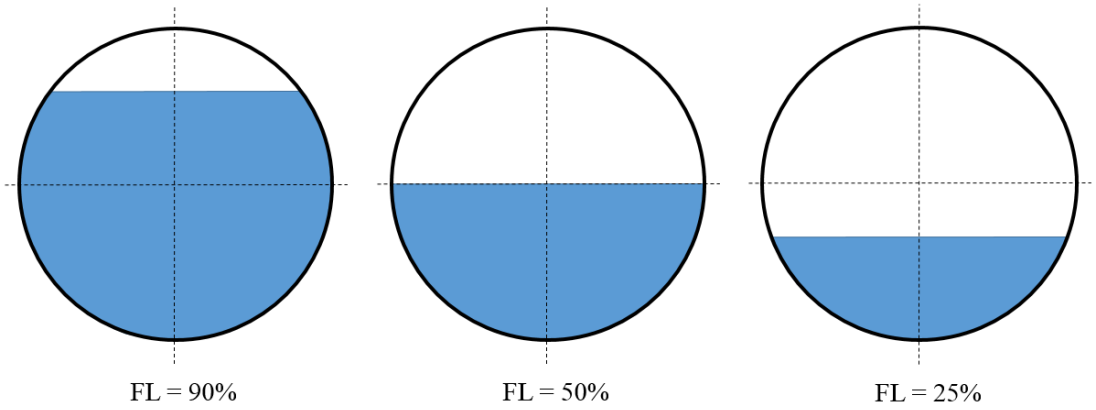

Figure 5.11: Ullage and bulk liquid volumes at FLs of 90%, 50%, and 25%.

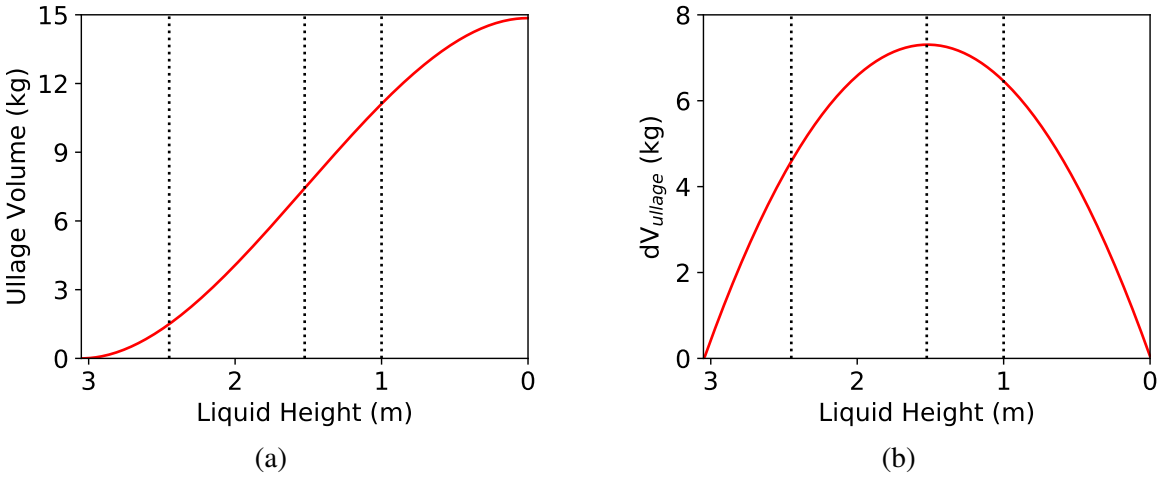

Figure 5.12: Ullage volume (left) and rate of change in the ullage volume (right) as a function of decreasing liquid height for a 3.05 m diameter spherical tank. The vertical lines (from left to right) represent the height of the liquid propellant at FLs of 90 %, 50%, and 25%.

the value for subsequent cycles. For FL of 25%, m_{vent} is negative. From the venting tables, it can be seen that for FLs of 50% and 25%, T_1 for the first venting cycle is greater, by 0.1 K and 0.3 K, respectively, than T_1 for subsequent cycles, whereas for FL of 90% T_1 remains constant. The increase in T_1 acts to decrease m_1 (per the ideal gas equation of state) relative to subsequent cycles. For FL of 50%, the 0.1 K increase in T_1 for the first

venting cycle causes the vented mass to decrease by approximately half. For FL of 25%, the 0.3 K increase in T_1 results in a value of m_1 that is less than m_2, which causes m_{vent} to become negative.

This behavior shows that the model is not necessarily sufficient at predicting the mass that should be vented immediately following the initial period of self-pressurization. With respect to predictions corresponding to the remainder of the pressure control period, it can be seen in Figure 5.10 and in the venting tables that m_{vent} is well behaved, and reacts in a similar fashion as m_{evap} as FL decreases, since m_{vent} is directly related to m_{evap} through m_1. Therefore, the model response with respect to the first venting cycle can be considered an initial start-up transient associated with the period of pressure control, whereas for venting cycles that occur thereafter, steady state is achieved. As the number of venting cycles increases, the impact from the initial transient becomes negligible.

After the initial transient has passed, the $\mathcal{P}$ values from the venting tables show that for each FL, the venting process releases between 97.7% and 98.0% of the boil-off that accrues in the tank. For each FL considered, the $\mathcal{P}$ values vary slightly over the course of the pressure control period due the variation of in m_{evap} that was described earlier, and which is similarly present in m_{vent}. While m_{evap} and m_{vent} both increase as FL decreases, the $\mathcal{P}$ values remain relatively constant, at around 98%.

These results demonstrate that the boil-off and vented masses predicted by the model respond appropriately during the period of pressure control. Boil-off is greatest for the initial period of self-pressurization, and smaller for subsequent pressurization cycles that occur thereafter. The vented masses are characterized by an initial transient, but reach steady state once the first venting cycle corresponding to the the initial period of self-pressurization has passed. Both the boil-off and vented masses in general decrease with FL, but are ultimately determined by the affect of the tank geometry on the time required for the tank to repressurize as FL decreases. The venting process releases approximately 98% of the boil-off that accrues in the tank, regardless of FL.

5.3.3.3 Comparison of Theoretical and Model Propellant Losses

Figure 5.13 illustrates the time histories for the theoretical and model propellant losses obtained for the 2-day storage period. For each of the initial FLs considered, Table 5.12 lists the the values for $\dot{m}_{bo}$, m_{bo}, and the loss ratio. Theory predicts that the propellant will boil-off at a rate of 10.00 kg/day, for a total of 20.00 kg for the 2-day storage period, based on the input $\dot{Q}$ of 54.1 W and h_{vap} of 444.29 kJ/kg, where the latter was determined from the initial pressure of 111.5 kPa and a corresponding saturated temperature of 20.7 K.

For each FL, the model similarly predicts that, once venting is initiated, propellant losses due to boil-off and subsequent venting occur at a constant, though much lower rate of 1.43 kg/day, 2.57 kg/day, and 2.36 kg/day for FLs 90%, 50%, and 25%, respectively, where the rates were calculated using the m_{bo} values from Table 5.12 and the time frame corresponding to the period of pressure control. This trend is consistent with other observations in the open literature, which state that $\dot{m}_{bo}$ is a function of the tank geometry and the amount of propellant in the tank; for an individual tank, $\dot{m}_{bo}$ increases as the amount of propellant decreases. Here, $\dot{m}_{bo}$ does not strictly increase as FL decreases due to the effect of the spherical tank geometry on the boil-off and venting processes, as discussed in the previous section. (If the tank were cylindrical, $\dot{m}_{bo}$ would strictly increase with decreasing FL, assuming that the propellant is settled and does not drop below the barrel section of the tank.) At the end of the 2-day storage period, the model predicts losses of 2.63 kg, 4.35 kg, and 3.96 kg for FLs of 90%, 50%, and 25%, respectively.

By assuming that the tank saturated, and that the heat entering the tank is directly responsible for evaporation of the liquid propellant, the theoretical model predicts losses that are between 4.60 and 7.60 times higher (per the loss ratio in Table 5.12) than the predictions obtained from the newly developed model, which ascribes a portion of the incoming heat to evaporation, and subsequently releases an amount of gas based on the assumption that the ullage is saturated at the end of the venting process. This supports Hypothesis 3.3, which states that due to the above assumptions, the model will overestimate

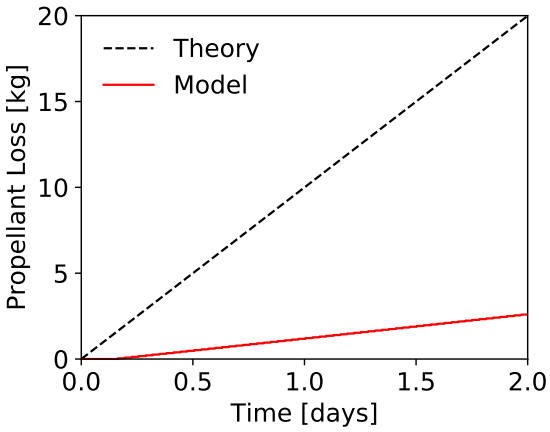

(a) FL = 90%

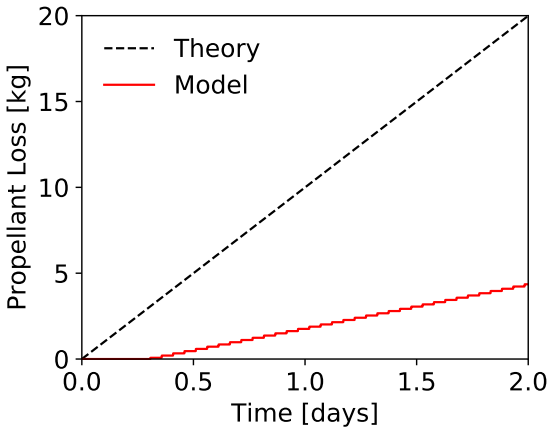

(b) FL = 50%

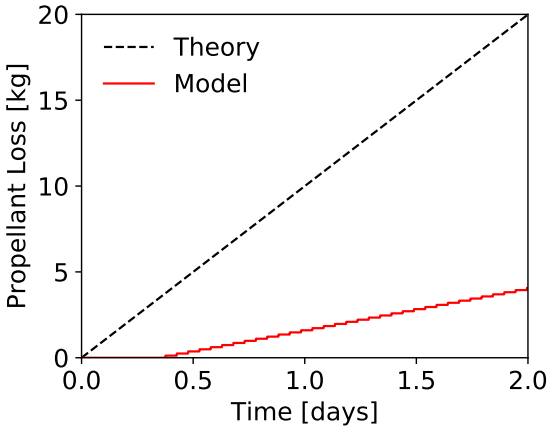

(c) FL = 25%

Figure 5.13: Theoretical (black) versus model (red) propellant loss predictions obtained for the 2-day storage period in a 3.05 m diameter spherical tank, subject to a thermal load of 54.1 W, and FLs of 90%, 50%, and 25%.

Table 5.12: Summary of boil-off rates and corresponding propellant losses predicted by theory and the newly developed model for the 2-day storage period.

FL (% by vol.)	Boil-Off Rate $\dot{m}_{bo}$ (kg/d)	Prop. Losses m_{bo} (kg)	Theoretical-to-Model Prop. Loss Ratio
Theoretical			
90	10.00	20.00	-
50	10.00	20.00	-
25	10.00	20.00	-
Model			
90	1.43	2.63	7.60
50	2.57	4.35	4.60
25	2.36	3.96	5.05

the mass that should be released during venting, and therefore the propellant losses due to boil-off, but to a lesser extent than the theoretical model in literature.

With the final portion of the experiment concluded, the boil-off prediction capability of the model is now established and the model evaluation is complete (i.e., Research Question 3 is resolved). Furthermore, these results also validate the founding hypotheses from which the model was formulated. That is, that a simplified cryogenic propellant tank model with pressure control capability can be developed if it is assumed that during operation the conditions in the tank are maintained such that there is no boiling of the liquid propellant or condensation of the propellant vapor. Then pressurization can be attributed strictly to evaporation of the liquid propellant at the interface, followed by an instantaneous reduction in the tank pressure due to venting of the ullage gas (Hypothesis 1). The mass released during venting, and the subsequent conditions in the tank after venting has concluded can be determined if (1) the ullage is modeled as a thermodynamic system consisting of an ideal gas in an insulated container in thermodynamic equilibrium just prior to, and immediately after venting, and (2) that immediately after venting the ullage is assumed to be saturated (Hypothesis 2).

5.3.4 Summary

This numerical experiment served as a verification exercise for the venting component. A 2-day storage period requiring pressure control was simulated using a 3.05 m diameter spherical tank, subject to a thermal load of 54.1 W, at propellant fill levels of 90%, 50%, and 25%. The approach used to represent the venting process was verified through an examination of the changes in the pressure, temperature, and mass within the ullage region.

The results demonstrate that the selected approach is a viable option for modeling pressure control due to direct venting. The tank pressure is maintained within the pressure band specified by P_{max} and P_{min}. The ullage temperature exhibits a similar behavior, with the lower limit bound by $T = T_{sat}(P_{min})$. The number of venting cycles, and the time between successive venting events is determined by the tank pressurization rate, which is a function of the propellant fill level and the tank geometry. Boil-off is least at higher propellant fill levels, in agreement with literature; the rate at which the propellant boils-off is influenced by the tank geometry as the amount of propellant in the tank decreases. Venting releases approximately 98% of the boil-off that is generated, and yields propellant losses that are much lower than those provided by the theoretical model, as predicted by Hypothesis 3.3.

The results also serve to validate the approach put forth by Hypotheses 1 and 2 regarding the model formulation. That is, that pressurization can be attributed strictly to evaporation of the liquid propellant at the interface, followed by an instantaneous reduction in the tank pressure due to venting, where the venting can be modeled as a simple thermodynamic process. With the boil-off prediction capability of the model capability now established, the next chapter explores how the new propellant loss estimates impact the vehicle when compared to those that are sized using estimates obtained from the theoretical model.

CHAPTER 6
APPLICATION & RESULTS

The previous chapter presented several experiments designed to test the model formulation and verify the boil-off prediction capability of the model. With this capability now established, the focus can now return to the original issue that was introduced at the beginning of this document. The purpose of this chapter is to demonstrate the impact to the vehicle design space when implementing two different boil-off models – one conservative and the other exhibiting more fidelity – in the vehicle sizing process.

6.1 Experiment 2 - Impact to the Vehicle Design Space

With the boil-off capability established, the opportunity now becomes available to investigate the advantages provided by the model. This leads to the final research question for this work:

Research Question 4: What are the benefits of implementing a higher-fidelity boil-off model in the vehicle sizing process?

Recall from Chapter 1 that the theoretical model has the tendency to significantly overestimate the boil-off rate, and thus the propellant losses. The uncertainty in the propellant losses is then propagated throughout the vehicle during the sizing process via the propellant mass requirements, resulting in oversized vehicles and artificial reduction of the design space. Increasing the fidelity of the boil-off rate will reduce the uncertainty in the propellant mass requirements, which will result in smaller vehicles and open up the design space. This is restated in the following hypothesis:

Hypothesis 4: *Utilizing a higher-fidelity model in the sizing process will result in smaller vehicles, and will therefore open up the vehicle design space.*

To test the above hypothesis, consider the following: At the system level, boil-off af-

fects the vehicle through the propellant mass requirements. The additional propellant required to offset boil-off affects the vehicle at the subsystem level through the mass growth in the propellant tanks, insulation, hardware, etc. As the mass of these components increases, the vehicle structure must correspondingly increase to compensate for the additional load. A true assessment of the impact to the vehicle requires that sufficient detail is captured at the subsystem level within the modeling and simulation environment (M&S). Otherwise, the benefits of the model cannot be realized. To test this hypothesis, a suitable testbed is required.

A summary of the experimental objectives is provided in Section 6.1.1. Sections 6.1.2 and 6.1.3 introduces the testbed and baseline vehicle, respectively, selected for use in the experiment. The experimental setup and procedure are discussed in Section 6.1.4, and the results are presented in Section 6.1.5.

6.1.1 Purpose of Experiment

The primary objectives of the numerical experiment are as follows:

1. Demonstrate the impact to the design space from the change in the following parameters when sizing the baseline vehicle with the theoretical model versus the higher-fidelity boil-off model:
    - LH_2 boil-off
    - Total vehicle mass
    - Loiter time
    - Vehicle payload capability

6.1.2 Testbed

Dynamic Rocket Equation Tool (DYREQT) is a Python-based multidisciplinary tool for sizing and analysis of space systems during the pre-conceptual and conceptual phases of design. The M&S environment was co-developed by the Aerospace Systems Design Lab-

oratory (ASDL) at Georgia Institute of Technology and the Advanced Concepts Office at NASA's Marshall Space Flight Center [109]. The framework is unique in its approach used to represent the vehicle subsystems. Each subsystem is represented by a user-defined model; the user can select the form of model to use (e.g., physics or empirical based) as well as the fidelity level (low, intermediate, high) to ascribe to it. During the sizing process, the M&S environment utilizes OpenMDAO, an open-source software developed by NASA's Glenn Research Center for multidisciplinary design and analysis, to automate the handling of inputs and outputs between the subsystem models [48, 64, 148]

The subsystems used to represent the vehicle include avionics, engines, power, structures, thermal, and tanks. Subsystem models for a generic spacecraft were developed by Trent in 2017 [149]. The objective of that dissertation research was to represent the vehicle with a sufficient level of detail so that the impact at the vehicle level from incorporating a technology in one or more of its subsystems, or a component within a subsystem, could be determined. The subsystems were modeled using a combination of physics- and empirical-based relationships, as well as historical data. Each model calculates the inert mass for the subsystem, the power requirement, and the heat load generated (if applicable).

Leveraging this previous work, ASDL developed a set of models to represent a lander system. Emphasis was placed on increasing the detail with which the CFM components were captured within the thermal subsystem. This included more detailed equations with respect to the insulation thickness, density, and configuration. As a result, the inert mass estimate of the CFM system was improved, as well as the estimate of the heat that penetrates the insulation and enters the propellant tank. The amount of boil-off that occurred over the course of the mission was determined using the standard method (Equation 1.1). This enabled a recent study on the impact of utilizing different propellant combinations (LOX/LH_2, LOX/LCH_4, and NTO/MMH) and thermal management approaches (passive versus active) on the payload capability of a reusable lunar lander [132].

The above capabilities makes this M&S environment uniquely suited for this final eval-

uation. The framework is capable of modeling a lander system and exhibits the necessary detail required at the subsystem level. This obviates the need to develop a sizing tool from the ground up. All that is required is that the vehicle and its corresponding mission be adequately defined within the environment (this is covered in more detail in Section 6.1.4.1). With minimal effort, the theoretical boil-off model can be exchanged for the higher-fidelity boil-off model.

Once mission and vehicle have been defined, the vehicle is sized using the form of the rocket equation shown in Equation 6.1. Based on a reasonable estimate for the final vehicle mass, the environment (using a built-in OpenMDAO optimizer) solves the multidisciplinary analysis problem via fixed point iteration to determine the propellant mass required. In the first iteration, the environment assumes that there is no propellant losses due to boil-off. For each iteration thereafter, the propellant losses determined by the thermal subsystem model are incorporated into the sizing process. Once the propellant mass has been determined, the initial mass of the vehicle is calculated as the sum of inert subsystem masses [149].

$$m_{prop} = m_{final}\Big[exp\Big(\frac{\Delta V}{g_o I_{sp}}\Big) - 1\Big] \tag{6.1}$$

6.1.3 Baseline Vehicle

The baseline vehicle utilized for this application problem is the descent stage of the Human Landing System (HLS), a human-rated three-element lander slated for use in the upcoming Artemis missions. A high-level CONOPS for the HLS portion of a crewed Artemis mission to the lunar surface is depicted in Figure 6.1, where the transfer stage (TS), descent stage (DS), and ascent stage (AS) represent the three elements that comprise the HLS. The elements are launched separately on a commercial launch vehicle, which places the element on a lunar trajectory. Each element is responsible for insertion into near-rectilinear halo orbit (NRHO) and subsequently rendezvous at Gateway (GW), a space station in orbit around the Moon that serves as a staging point for deep space exploration missions [116,

117].

Once the DS arrives at Gateway, Δt days elapse between the arrival of the ascent stage and crew, the aggregation of the elements to form the final "stack", or HLS vehicle, and the departure of the HLS from Gateway. The transfer stage performs the undocking maneuver, as well as the transfer from NRHO to low lunar orbit (LLO), where the vehicle is staged for LLO insertion. This process is assumed to take 0.5 days. The transfer stage is then dropped from the stack, and the descent from LLO to the lunar surface is performed by the DS. Upon touchdown, the role of the DS element is complete. The crew exit the vehicle, conduct science activities, and use the ascent stage – leaving the DS on the surface – to ascend and return to Gateway[1] [117].

The first demonstration mission of the HLS is planned for 2024. The requirements for the DS, as laid out in the Next Space Technologies for Exploration Partnerships - 2 (NextSTEP-2) document published by NASA's Advanced Explorations Systems Division, are that the DS be capable of delivering a minimum of 9 mt to the lunar surface, with the goal of increasing the payload capability to 12 mt. The DS is not to exceed a total mass of 16 mt (including propellant), and must fit within a dynamic envelope (stage diameter) of 6.3 m [117].

Development activities for the HLS are still in the initial design phase. Design contracts were awarded in early 2020 to Blue Origin, Space Exploration Technologies Corp. (SpaceX), and Dynetics. The HLS design by Dynetics utilizes LOX, though no information is yet available with respect to the fuel that will be used. The design makes use of a 14 to 20 day launch cadence between the various HLS elements, which is a much faster rate than is traditionally supported, in order to minimize boil-off [57]. The SpaceX design utilizes subcooled LOX and subcooled LCH_4 [38], which prolongs the time before boil-off occurs. Blue Origin's design utilizes LOX/LH_2, however there is no information as of yet as to the thermal management approach that will be implemented [56].

[1] Surface activities and ascent are not depicted in the CONOPS in Figure 6.1.

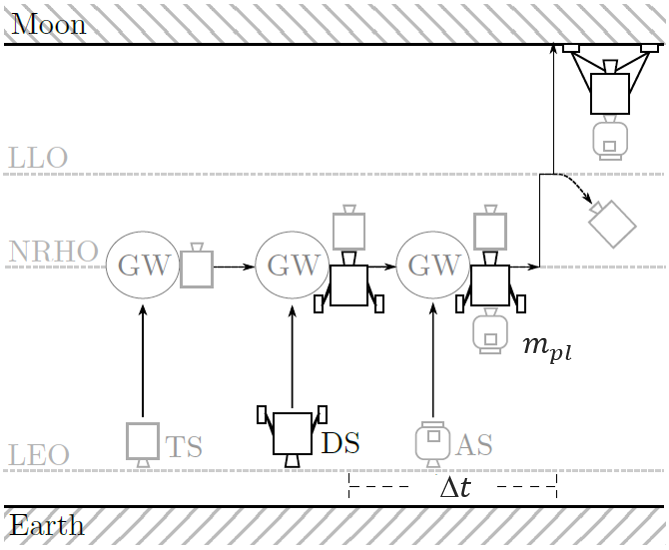

Figure 6.1: HLS CONOPS [132].

For cryogenic designs, such as those discussed above, the critical factor is the time spent at Gateway since each day that passes more of the propellant boils-off. This application problem will investigate the impact to the vehicle, in this case the DS, and its ability to loiter at Gateway when the vehicle is sized using two different boil-off models – the theoretical model and the higher-fidelity EBM.

6.1.4 Setup and Procedure

6.1.4.1 Mission and Vehicle Definitions

In order to size the vehicle, the mission and vehicle input definitions required by the M&S environment must first be specified. Within the environment, the mission is represented by a sequence of events defined by “burn”, “idle”, “mass delta”, “drop” and “connect”. The burn event represents changes in the vehicle velocity due to an MPS or reaction control system (RCS) burn. The effect on the vehicle is instantaneous and is modeled around impulsive burn assumptions based on the rocket equation. An idle event represents the passage of time, which is necessary for time-based effects such as propellant boil-off. The mass delta event represents a change in mass in the vehicle due to propellant refueling, the addition of a scientific payload, etc. The connect and drop events account for elements that

are added to (e.g., during aggregation) or removed from (e.g., during stage separation) the vehicle [149].

The CONOPS for the crewed Artemis mission was previously described in Section 6.1.3. Based on the CONOPS in Figure 6.1, Table 6.1a lists the mission events, the type of event, and the corresponding metric for the DS. The ΔV budget for Gateway insertion through LLO transfer was obtained from values published by NASA's Human Exploration Operations Committee [37]. A relation for the ΔV required for the descent to the lunar surface (Descent 2 in Table 6.1a) was obtained from regression of data that was derived from several Altair lunar lander design studies [89, 90]. The relationship, shown in Equation 6.2, is solely a function of the thrust-to-weight ratio T/W_o (based on Earth's gravity) at the beginning of the descent, where the first term in the equation represents the ideal ΔV needed to descend and the second term accounts for the losses due to gravity.

$$\Delta V_{descent} = 1911.67 + 1.92\left[\frac{T}{W_o}\right]^{-2.82} \tag{6.2}$$

The vehicle definition is listed in Table 6.1b, where the subsystems and variables included are those that are most relevant to the experiment. With the exception of the number of engines used, the engine thrust, the number of tanks, and ratio of the tank length to diameter (l/d ratio), the variable values listed in the table are the same as those used in the lunar lander study presented by Robertson et al. [132]. The variable values for the remaining subsystems (Avionics, Power, Structures) and the RCS can be found in the same study.

6.1.4.2 Vehicle Design Space

Table 6.2 represents the vehicle design space, which is defined by 5 degrees of freedom, each with a minimum and maximum value. The fuel and oxidizer tank l/d ratios trade the basic geometry of the tanks; the engine thrust, the payload mass, and the loiter time at Gateway represent the various trades on the vehicle performance.

To fully define the vehicle design space, a large number of candidate designs must be

Table 6.1: Mission and vehicle input definitions for the descent stage of the HLS.

Event	Type	Metric
Transit to Gateway	Idle	5 days
Gateway insertion	MPS burn	450 m/s
NRHO TCM*	RCS burn	20 m/s
In-space loiter	Idle	Δt
Aggregate HLS elements	Connect	m_{pl}
NRHO to LLO transfer	Idle	0.5 days
LLO to surface transfer		
Descent 1	RCS burn	15 m/s
Descent 2	MPS burn	Eqn. 6.2
Descent 3	RCS burn	10 m/s
Descent 4	MPS burn	50 m/s

*Trajectory Correction Maneuver

(a) Mission

Subsystem	Variable	Metric
Engines	Number of engines	1 MPS
	Propellants	LOX and LH_2
	Thrust	F
	I_{sp}	450 s
	Oxidizer-to-fuel ratio (OFR)	6.0
Tanks	Number of tanks	2 fuel, 2 ox
	Tank pressure	206.8 kPa, 275.8 kPa
	Ratio of the tank length to diameter	l/d
Thermal	Thermal control method	Passive
	Number of MLI layers	30
	SOFI density	36.8 kg/m^3
	SOFI thickness	0.025 m
	Thermal environment	Lunar surface
	Temperature	290 K
	Albedo	0.12
	Emissivity	1.0

(b) Vehicle

Table 6.2: Input variables for the DoE

Variable	Min.	Max.	Units
Thrust, F	35	160	kN
Fuel tank l/d ratio	1.0	5.0	–
Ox tank l/d ratio	1.0	5.0	–
Payload, m_{pl}	9,000	12,000	kg
Loiter time at Gateway, Δt	10	60,90	days

evaluated. In order to do so efficiently, the sampling technique of Design of Experiments (DoE) is utilized. The concept of a DoE is to design a set of experiments, physical or numerical, in order to maximize the information obtained while simultaneously minimizing the effort involved in retrieving that information [106]. The choice of the DoE depends on the problem at hand. For this application problem, is expected that the majority of the feasible designs lay within the ranges listed in Table 6.2 and that the designs formed from a combination of the minimum and maximum values on the variable ranges will result in designs that violate the constraints. Therefore, a combination of a Full Factorial (FF) and Latin Hypercube (LHC) designs was selected.

The LHC design provides a rich sampling of the interior of the design space, but is poor with respect to its ability to sample the edges of the space [106]. While feasible designs are not expected at the extremes of the design space, it is still desirable to capture information at these locations. For this reason a FF design was also included, which captures every combination of the minimum and maximum values for the variable ranges.

6.1.4.3 Model Operation within the M&S Environment

Model operation within the M&S environment occurs as described in Section 4.3, with the exception of three modifications. The first modification deals with the adjustment of the model inputs. As depicted in Figure 4.7, the model requires information on the initial tank conditions (P_o and/or T_o), the amount of propellant in the tank (via FL_o), the tank

geometry (via direct input of the tank shape and dimensions), the heat entering the tank ($\dot{Q}$), the parameters associated with venting operations (P_{max}, P_{min}), and the storage time (t). The inputs provided to the model from the M&S environment are listed in Table 6.3. The first three variables – P_o, P_{max}, P_{min} – correspond to the standard inputs related to the initial tank conditions and venting operations. T_{max} and FL_{min} correspond to limits placed on the liquid propellant, which will be addressed momentarily. $\dot{Q}_{mli}$ and t are also standard inputs which correspond to the heat entering the tank and the storage duration to be evaluated, respectively. m_{lh2} corresponds to the propellant mass in the tank at the start of the mission event and l/d is the ratio of the tank length to diameter.

These last two variables are not included in the standard set of inputs required by the model, but do provide the necessary information with simple manipulation. The value for FL_o required by the model is determined from P_o and m_{lh2} via $P=\rho R_u T$. The tank geometry is determined from the l/d ratio, where a value of less than or equal to 1.02 corresponds to a spherical tank, and any value greater than 1.02 corresponds to a cylindrical tank.

The second modification to the model is the introduction of a cutoff on the minimum allowable propellant in the tank. This is represented by the variable FL_{min}, which is set to a value of 10%. For previous experiments, there was no need for a cutoff since storage times were on the order of minutes or hours. Here, given that loiter times can be as long as 100 days, the cutoff is necessary. If during the loiter period, FL_{min} is reached, the model returns a value of m_{lh2} to the environment. This signifies that not enough propellant was available for the mission as the propellant mass that was received was entirely boiled-off.

The final modification accounts for heating of the bulk liquid. Given the length of the storage period, the thermal input to the liquid propellant can cause the temperature to reach the boiling point. In these cases a different pressure control device, such as a TVS, is implemented in order to ensure that the liquid temperature does not exceed a certain value. For the purposes of this experiment, a maximum temperature limit of $T_{max} = T_{sat}(P_{min})$ was placed on the the liquid propellant. If T_{max} is reached, the liquid temperature is held

Table 6.3: Inputs for the EBM.

Variable	Description	Value	Units
P_o	Initial tank pressure	206.8	kPa
P_{max}	Maximum pressure limit	285.0	kPa
P_{min}	Minimum pressure limit	250.0	kPa
T_{max}	Maximum bulk liquid temperature	23.9	K
FL_{min}	Minimum propellant fill level	0.5	% by vol.

(a) Inputs related to venting operations and initial tank conditions

Variable	Description	Units
$\dot{Q}_{MLI}$	Heat transfer rate through MLI	W
m_{lh2}	Propellant mass	kg
l/d	Ratio of tank length to diameter	–
t	Idle time	s

(b) Inputs received from DYREQT

constant for the remainder of the mission event; the heat entering the region from that point forward does not affect the liquid propellant. This in effect acts as a simplified version of a TVS which, once the temperature limit is reached, maintains the liquid propellant within a small temperature band near T_{max} while removing the heat from the bulk liquid.

6.1.4.4 Additional Ground Rules and Assumptions

This section summarizes the principal ground rules and assumptions (GR&As) utilized by the M&S environment when sizing the DS. For a more detailed discussion, the reader is referred to Ref. [132].

CFM ..... The LH_2 and LOX tanks utilize a combination of VDMLI and SOFI. The VDMLI consists of 30 layers, with 6, 9, and 15 layers in the inner, middle, and outer segments, and corresponding densities of 8, 12, and 16 layers/cm. The SOFI has a thickness of 25 mm and a density of 36.8 kg/m^3.

Thermal Environment ..... To be conservative with respect to the thermal load on the vehicle, the thermal environment of the lunar surface (rather than LLO or NRHO was used) was used when modeling the thermal control subsystem. This corresponds to a surface temperature 207 K, an albedo of 1.2, and an emissivity of 1.0.

Tank Configuration ..... Each propellant tank is composed of Al 2195. The tanks are pressurized at 206.8 kPa (30 psia) and 275.8 kPa (40 psia) for LH_2 and LOX, respectively. Tanks are sized to be a constant thickness as a function of the ullage pressure, and with a safety factor of 1.5.

Main Propulsion System ..... The MPS propellants are assumed to be powered by expander cycles, where the I_{sp} and OFR are assumed constant. LOX and LH_2 are pressurized by GHe which has negligible effect on the boil-off process. The time in which the engines are used is small compared to the overall mission duration. Therefore, the heat radiated from the engine onto the vehicle, as well as any other ΔV losses that are not listed in Table 6.1a, are considered negligible. Propellant and Isp penalties associated with engine start-up and shutdown are also assumed negligible.

Reaction Control System ..... The RCS is assumed to be a pressure-fed NTO/MMH system, with an I_{sp} of 300 s, and comprised of four pods, each with four 444.8 kN (100 lbf) thrusters. It is assumed that propellant settling maneuvers are performed by the RCS through ullage burns.

Vehicle Structure ..... The basic mass of the vehicle structure is assumed to be 30% of the total vehicle dry mass. In this 30%, all primary and secondary structures, including the landing gear, are accounted for.

Reserves and Margins ..... A 2.5% flight performance reserve is applied to each burn. An additional 1% is added to the MPS propellants for additional reserves. A mass growth allowance of 25% is applied in addition to the vehicle dry mass to determine the inert mass used for ΔV calculations.

6.1.5 Results

A total of approximately 23,000 cases were evaluated using the DoE discussed in Section 6.1.4.2. Of these cases, approximately 12,000 correspond to the theoretical boil-off model and the remaining 11,000 correspond to the EBM. For simulations run with the theoretical model, each case required on average 4.5 seconds to evaluate, for a total run time of around 12 hours using standard desktop computer. Simulations utilizing the EBM were run on a single modern workstation capable of running 35 parallel processes. Evaluation required an average of 840 seconds per case, for a total evaluation time of around 12 days.

To visualize the impact of using the different boil-off models in the sizing process for the DS, the results from the DoE are assessed with the aid of a scatterplot matrix. The matrix is composed of individual scatterplots which allows for a visual assessment of the relationship between a pair of variables. The scatterplot matrix for the designs sized using the theoretical model is depicted in Figure 6.2a, and the scatterplot corresponding to the EBM is depicted in Figure 6.2b. The model inputs used to create the DoE are located on the x-axis, and the outputs gathered from the M&S environment are located on the y-axis.

Immediately noticeable in Figure 6.2b, within the scatterplot formed by boil-off and the payload mass, is a gap. The designs located above the gap correspond to scenarios where the propellant fill level cutoff FL_{min} was reached during the loiter period. It is suspected that the gap, and the higher density in points along to top "shelf" of the gap, is a result of the model negatively interfering with the fixed point iteration within the M&S environment in these scenarios. (This will be addressed further momentarily.) Focusing now on the general trends, it can be seen in both figures that boil-off increases with the loiter time at Gateway. As expected, the total propellant mass required increases in order to satisfy the longer loiter times. From inspection of the scatterplots corresponding to the stage diameter and loiter time, as the loiter time increases the dynamic envelope required to contain the growing propellant tanks also increases. As a result of the growth in the above quantities, the total mass of the DS must correspondingly increase.

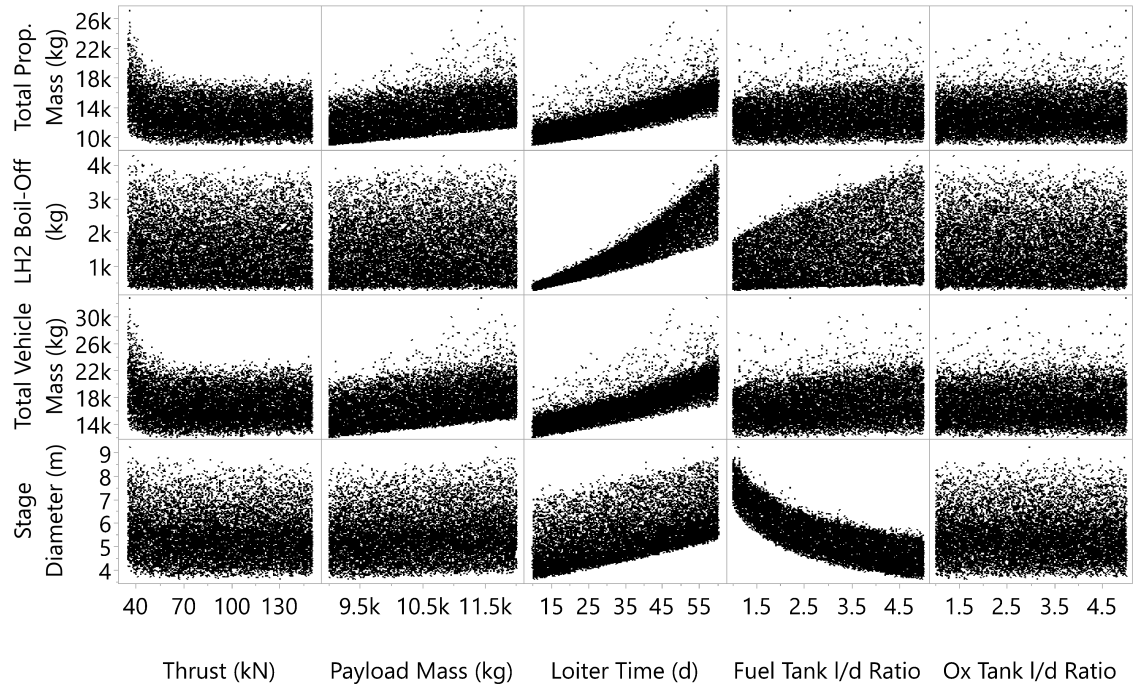

(a)

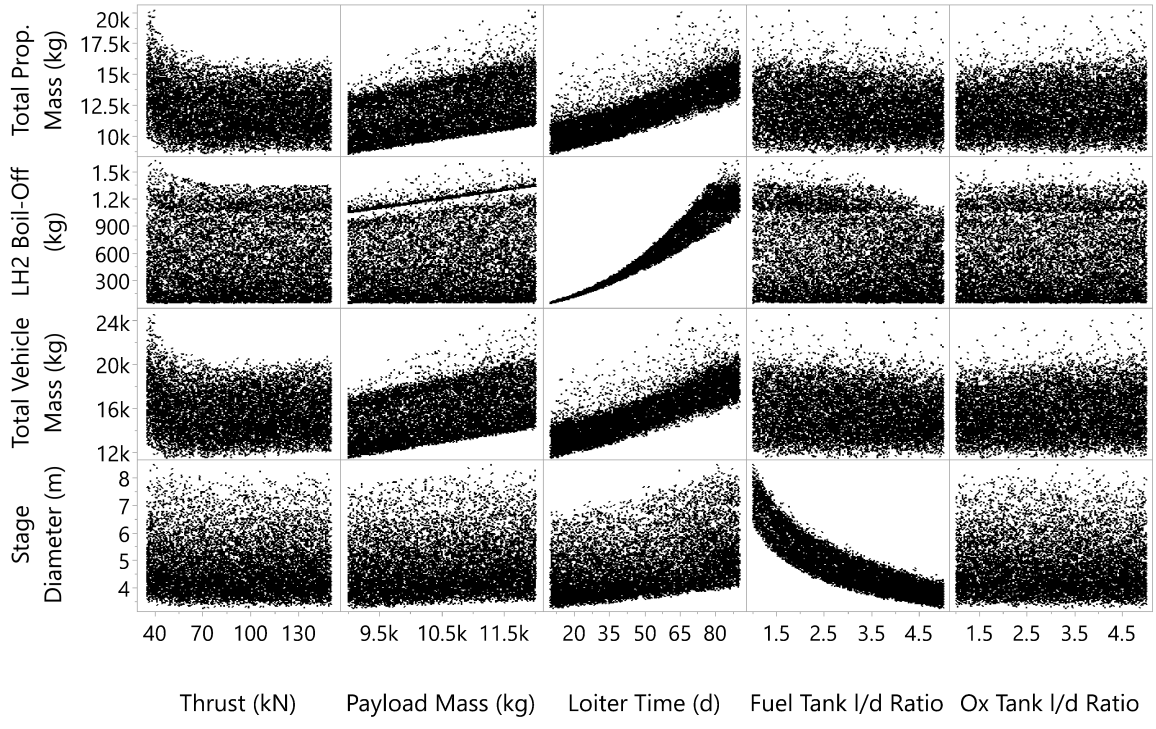

(b)

Figure 6.2: Scatterplot matrix for designs sized with the (a) theoretical and (b) higher-fidelity boil-off models.

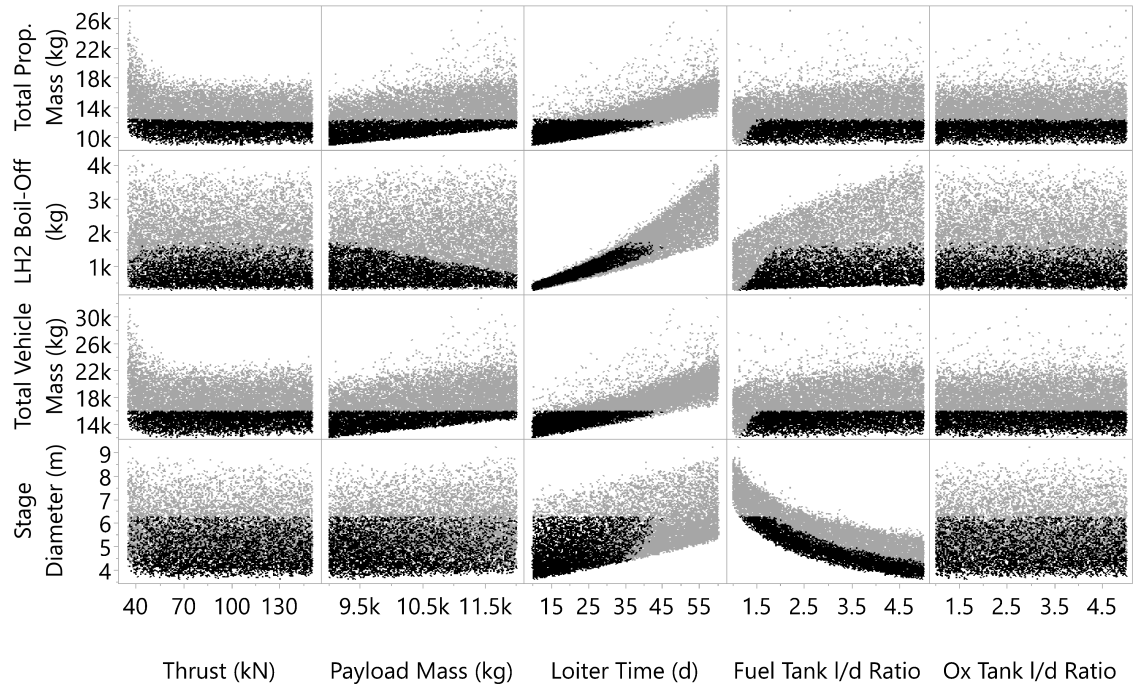

(a)

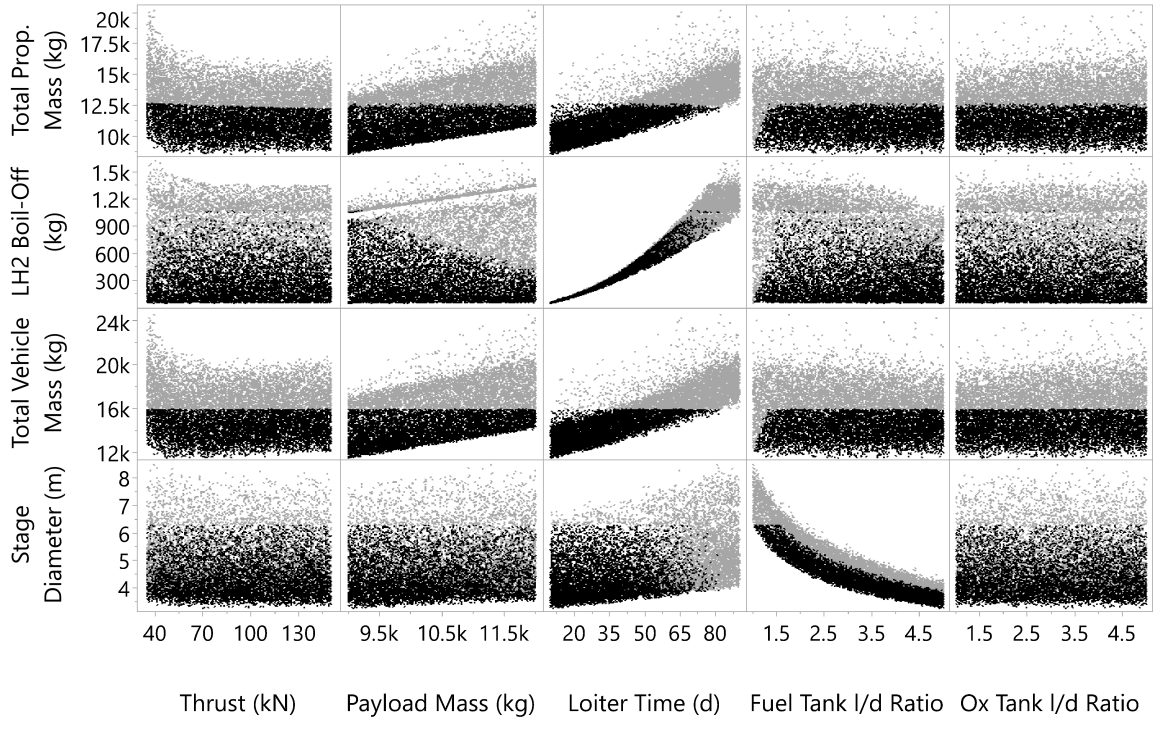

(b)

Figure 6.3: Scatterplot matrix displaying the feasible designs (black points) sized with the (a) theoretical and (b) higher-fidelity boil-off models.

The feasible designs can be obtained by applying the constraints on the total vehicle mass (16,000 kg) and the stage diameter (6.3 m). Within Figure 6.3, the feasible designs are denoted by the black points, and the designs that lay outside the constraints are denoted by the grey points. From comparison of the two scatterplots in the figure, the theoretical model yields boil-off masses of 300 kg to 4,300 kg whereas the EBM yields much lower masses of around 55 kg to 1600 kg. The resulting impact on the performance of the DS is profound. The propellant mass required for designs sized using the traditional boil-off model ranges from 9,100 kg to 27,000 kg; designs sized with EBM require approximately 8,600 kg to 21,000 kg. The additional propellant required to offset boil-off predicted by the theoretical model decreases the loiter capability of the DS. As shown in Figure 6.3a, the maximum loiter time for designs sized with the theoretical model is 45 days. The maximum loiter time for designs sized with the higher-fidelity model is nearly double, at around 80 days.

While the data obtained from the DoE is useful in visualizing the impact to the design space, to conduct a more thorough evaluation of the space surrogate modeling was employed. Due to the complexity of the design space, Neural Networks were selected over a more traditional response surface equation. Further, the Neural Network allows for the space to explored with the use of a single equation, rather than with a set of equations where each output would have to be fitted individually. The fitting parameters, the number of points used to train and validate the network, and the resulting error are available in Appendix H.

Once the Neural Networks were developed, they were run through a Non-Dominated Sorting Genetic Algorithm II (NSGA-II) [43] in order to identify designs with the maximum payload capability. The results are depicted in Figure 6.4, where the red and blue lines correspond to designs sized with the theoretical and higher-fidelity boil-off models, respectively. Note that the lines are formed by a collection of designs. That is, the line is composed of a series of points found on the Pareto Front by the NGSA-II. For the Pareto

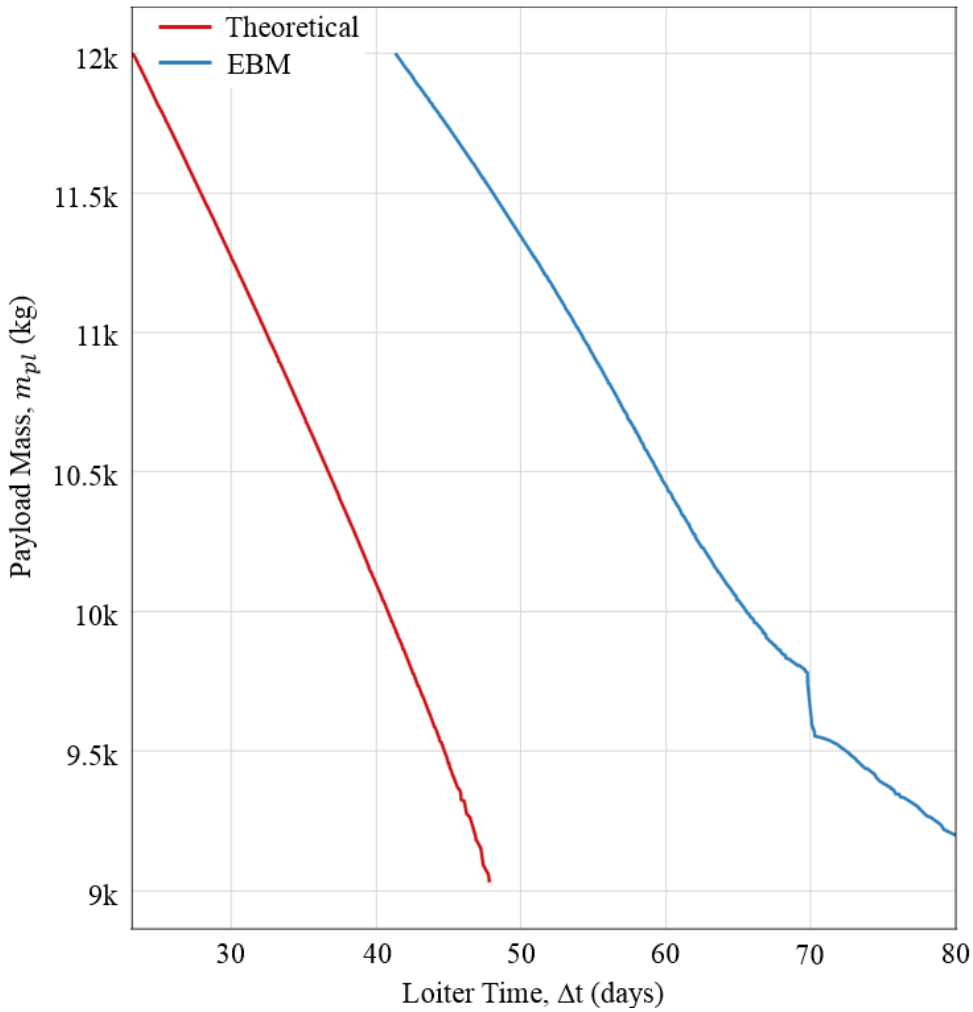

Figure 6.4: Constrained Pareto frontiers showing the maximum payload capability for the given loiter time.

Front corresponding to the EBM, the behavior around the 70 day mark corresponds to the gap in data that was discussed previously. For designs sized with the theoretical model, the maximum and minimum payload capabilities corresponds to loiter times of approximately 23 days and 48 days, respectively. For designs sized with the EBM, the maximum and minimum payload capability corresponds to loiter times of approximately 41 days and 80 days, respectively. Note also that this minimum payload capability is slightly higher (9,200 kg versus 9,030 kg). Based on the trend displayed by the Pareto Front, once the issue between the model and the fixed point iteration is addressed, the payload capability of the designs

with loiter times beyond 70 days will be greater than what they currently show in the figure, thus further extending the gap in the payload capabilities predicted by the two models.

6.2 Summary

The purpose of this experiment was to demonstrate the implications of utilizing two boil-off models, each with a different fidelity, in the vehicle sizing process. Given that the theoretical model assumes the worst-case scenario with respect to boil-off, it was hypothesized that incorporating a higher-fidelity boil-off model in the sizing process would result in smaller vehicles and open up the design space.

The descent stage of the HLS was selected as the baseline vehicle for use in this experiment as it provided an opportunity to investigate the impact on a relevant system. It was assumed that the descent stage utilizes a single engine and carries a total of 4 MPS propellant tanks, 2 of which are LH_2 and the other 2 LOX. The vehicle design space was defined by the engine thrust, the loiter time at Gateway, the payload mass, and the propellant tank geometry. A DoE was utilized to evaluate approximately 23,000 candidate vehicle designs between the two design spaces obtained from the different models. The constraints on the total vehicle mass and the stage diameter were applied to identify the feasible designs.

The results showed that incorporating the higher-fidelity model in the sizing process opened up the design space significantly. The boil-off predicted by the theoretical model was as much as two times the values predicted by the EBM. Therefore, the resulting designs were smaller and demonstrated greater loitering capabilities (up to 80 days). The vehicles sized with the theoretical model, on the other hand, were not capable loitering beyond 45 days.

Neural Networks were used to conduct a more thorough evaluation of each design space. Using NGSA-II, the vehicles with the maximum payload capability were identified for each day within the loiter period. For the designs sized with the theoretical model, the payload capability of the optimum vehicles decreases almost linearly as the loiter time

increases. The maximum payload capability corresponded to a loiter time of 23 days. For the EBM, the maximum payload capability occurred for a loiter time of 41 days, a significant increase from the theoretical model. The payload capability exhibited a linear trend that decreased at a slower rate than the payload capabilities corresponding to the theoretical model.

The above results validate the aforementioned hypothesis. Further, the results demonstrate that the objective of this research – to improve conceptual design and analysis of cryogenic in-space vehicles by providing more accurate propellant mass estimates through the development of a higher-fidelity boil-off model – has been achieved.

CHAPTER 7
CONCLUSIONS

7.1 Summary and Discussion of Results

The primary objective of this research was to improve conceptual design and analysis of cryogenic in-space vehicles by improving the fidelity with which the boil-off process is captured. During the conceptual design process, the standard approach for estimating propellant losses due to boil-off is to divide the heat transfer rate to the tank by the enthalpy of vaporization of the propellant. This provides a simple method for estimating the propellant losses that can easily be integrated into the vehicle sizing process. However, the majority of vehicle designers implement this method not knowing what the underlying assumptions are and how they impact the design.

The approach is based on a theoretical model that assumes that the heat entering the tank is directly responsible for evaporation of the liquid propellant at the interface. By ascribing all of the incoming heat to the evaporation process, the model assumes the worst-case scenario, since in an actual tank only a portion of the incoming heat contributes to boil-off. Due to the simplicity and corresponding low fidelity that is used when representing the boil-off process, the model has the potential to significantly overestimate boil-off, and thus the propellant losses. The uncertainty in the propellant losses is then propagated throughout the vehicle during the sizing process through the propellant mass requirements.

In order to increase the fidelity in boil-off predictions, more of the physical effects responsible for the boil-off processes must be captured. This necessitated modeling of heat and mass transfer processes that occur within the propellant tank. A wide variety of cryogenic propellant tank models exist in literature. Chapter 3 presented a review of notable models from three different categories – theoretical, analytical, and numerical – with the goal of identifying a candidate with a sufficient boil-off prediction capability, but

with enough simplicity so that it can easily be incorporated into the design process.

Unfortunately, the primary objective of propellant tank modeling and analysis is to predict the fluid conditions in the tank; boil-off is typically not addressed or is not published as part of the results. To circumvent this issue, the tank pressurization rate was used as the primary figure of merit when evaluating the boil-off prediction capability of each model. Based on the models surveyed in the literature review, it was found that theoretical models do not adequately capture the heat and mass transfer in the tank, resulting in poor estimates of the pressurization rate. Numerical models provide the most accurate values of the pressurization rate, but are not practical during the conceptual design phase where multiple vehicle alternatives must be evaluated. While analytical models provided the desired fidelity, they either did not provide enough information on the implementation, or were too detailed in their implementation which made the computational time prohibitive.

Of the notable models surveyed in the literature review, none were viable candidates. This necessitated the development of a cryogenic propellant tank model capable of predicting the tank pressurization rate, and thus boil-off, with a similar fidelity provided by analytical models but with a simpler approach for modeling the heat and mass transfer in the tank. To guide model development, three requirements were formulated based on observations made during the literature review. The first requirement was that the model have a quick evaluation time. This was absolutely necessary if the model was going to be utilized for design space exploration, trade studies, etc. This second of these requirements was that any model that was developed needed to be extensible. That is, it needed to be capable of analyzing tanks of various geometries. The last requirement was that model incorporate a pressure control capability in order to simulate long-term missions. Given the complexity of incorporating a TVS, direct venting was selected as the form of pressure control to be implemented within the model.

As demonstrated by the literature review, the chief difficulty in developing any model is in capturing the primary fluid behaviors in the tank without incurring the penalty of the ad-

ditional complexity. This motivated the first research question (RQ1): How can a simplified cryogenic propellant tank model with pressure control capability be developed? Leveraging observations from several pressurization experiments in literature, it was hypothesized (H1) that the number of physical processes used to analyze to tank can be greatly reduced if it is assumed that the tank is subjected to low thermal loads during storage; then pressurization of the tank can then be attributed strictly to evaporation of the liquid propellant at the interface. The number of physical processes can be further reduced if it is assumed that depressurization is instantaneous. This hypothesis formed the technical approach from which the model was formulated.

The proposed model was divided into two separate components – self-pressurization and venting – which were formally developed in Chapter 4. The self-pressurization component forms the crux of the model, as it comprises all the thermodynamics that occur within the tank. The principal physical processes were modeled using the method presented by E. Ring. Since the analysis does not conform to a particular tank geometry, it enforces the necessary extensibility. The final form of the model was developed by implementing several modifications based on observations from self-pressurization experiments in literature. The first modification served to further simplify the heat and mass transfer within the tank by omitting the tank wall from the analysis. The next two modifications accounted for the effects of thermal stratification on the heat and mass transfer at the interface, an aspect that is difficult to capture when using a single node. The second modification utilized the saturated properties, rather than the real gas properties, when evaluating the heat transfer at the interface. The third modification assumed that a warm thermal layer exists just beneath the interface. Due to the presence of the warm thermal layer, the heat transfer from the ullage to the interface – rather than the net heat transfer through the interface – results in evaporation.

Hypothesis 1 simplified venting operations by assuming that venting is instantaneous. In order to complete the venting model, the mass released during venting and the condi-

tions in the tank once venting has concluded must still be determined. Given the lack of information available in literature, the second research question was posed regarding how to obtain the above information. This necessitated the development of a suitable approach for capturing the above parameters. The venting component uses a simple thermodynamic process to model the pressure reduction in the tank and to determine the mass released during venting. The basic premise was that if the ullage was represented as an ideal gas in an insulated container, and if the conditions before and after the venting process were known, then mass released during venting could be determined without the need to model the venting process itself (H2). This obviated the need for details with respect to the venting process that are not readily available in literature. The initial state in the ullage is known and is provided by the self-pressurization component. The final state is assumed saturated, which is a common assumption utilized in literature. Together, the self-pressurization and venting components provide the propellant losses incurred over the storage duration. The self-pressurization component provides the amount of boil-off that occurs during pressurization. Once the tank pressure reaches the pressure limit, the venting component releases that excess pressure due to boil-off. The total mass released over the course of the storage duration represents the propellant losses due to boil-off.

Chapter 5 centers around the third research question: What is the boil-off prediction capability of the new model? Several experiments were developed in order to test the capability of the individual model components. This piece-wise evaluation was necessary since the boil-off prediction capability could not be validated directly. Experiment 1a sought to validate the self-pressurization capability of the model (RQ3.1). Two series of LH_2 self-pressurization tests carried out in literature in a small spherical tank and the larger MHTB tank were used as validation cases. The tests were performed using a range of thermal loads and propellant fill levels. If the heat and mass transfer assumptions used to formulate the self-pressurization component were sound, then the model would predict pressurization rates similar to those observed in literature. However, it was anticipated that based on

the assumptions, the model would predict higher pressurization rates at higher propellant fill levels (H3.1). The results showed that the model predicts conservative values for the pressurization rate in cases where it takes longer for the thermal gradients within the bulk liquid to become established. This typically occurs in larger tanks at higher propellant fill levels. Even so, the model was capable of sufficiently predicting the pressurization rate for the two different tank geometries and the range of conditions considered.

Experiment 1b sought to determine the fidelity of the pressurization prediction capability of the model (RQ3.2). Though the capability was validated by the previous experiment, the objective here was to determine how the predictive capability compared with other higher-fidelity analytical and numerical models in literature, since the original goal was to develop a model with a similar fidelity. Recall that the fidelity in the pressurization rate is representative of the fidelity in the rate at which the propellant boils-off. Using the self-pressurization tests performed in the MHTB tank as a baseline, the pressurization rate predicted by the model was compared with the pressurization rates predicted by Hastings et al., TankSIM, and GFSSP. It was hypothesized that due to the simplicity of the heat and mass transfer assumptions utilized by the model, it would yield less accurate predictions when compared to the higher-fidelity models of Hastings et al., TankSIM, and GFSSP (H3.2). The results showed that for lower propellant fill levels, the model was capable of predicting pressurization rates with an accuracy similar to TankSIM and GFSSP, which of the three models are the most detailed. At higher propellant fill levels, the model predicted values that were more conservative. This established confidence in the model's ability to predict the boil-off that occurs at the interface.

Experiment 1c served as a verification of the approach used to represent the venting process (RQ3.3). It was anticipated that the approach used to model the venting process would overestimate the mass released during venting, but to a lesser extent than the theoretical model in literature (H3.3). A 2-day storage period in which pressure control was required was simulated using a 3.05 m diameter spherical tank, subject to a thermal load of 54.1 W,

at propellant fill levels of 90%, 50%, and 25%. The verification involved an examination of the changes in the ullage pressure and temperature during venting, as well as certain behaviors such as the number and time between venting cycles at different propellant fill levels. The results showed that during the period of pressure control, the ullage responded as expected. The venting component was capable of maintaining the pressure between the specified limits; the number and time between venting cycles is determined by the tank pressurization, which is a function of the tank geometry and propellant fill level. Based on the assumption that the ullage is saturated at the end of the venting process, the venting releases approximately 98% of the boil-off that is generated in the tank. When compared to the propellant losses predicted by the theoretical model, which assumes that the heat entering the tank contributes directly to boil-off of the liquid propellant, the newly developed model predicted losses that were as much as 7.6 times lower than the theoretical model. These results demonstrated that the selected approach was a viable option for modeling pressure control due to venting. Further, the results confirmed observations from literature that the theoretical model has the potential to significantly overestimate propellant losses.

With the boil-off prediction capability of the model now established, the final experiment focused on demonstrating the benefits of utilizing a higher-fidelity boil-off model in the sizing process (RQ4). Due to the conservative nature of the theoretical model, it was hypothesized that incorporating a higher-fidelity boil-off model in the vehicle sizing process would predict lower boil-off rates, and therefore propellant losses, resulting in smaller vehicles and a larger design space (H4). The descent stage of the Human Landing System was selected a baseline vehicle. It was assumed that the descent stage carried a total of 4 MPS tanks – 2 fuel and 2 oxidizer – and utilized a single engine. The vehicle design space was defined by engine thrust, loiter time, payload mass, and tank geometry. In order to determine the impact to the vehicle, the descent stage was sized using the two different boil-off models and the resulting changes in the design space were investigated.

The results showed that incorporating the higher-fidelity boil-off model in the sizing

process resulted in smaller vehicle masses. Further, the lower boil-off predicted by the model allowed the designs to loiter up to the maximum value of 60 days placed on the loiter time, whereas vehicles sized with the theoretical model could not loiter beyond 47 days. Vehicle designs with the maximum payload capability were identified for each day in the loiter window. Comparison of these optimal designs showed that for designs sized with the theoretical model, the maximum payload capability was achieved for a loiter time of 27 days. For the designs sized with the EBM, the maximum payload capability was achieved for a loiter time of 51 days, a significant increase from the theoretical model. The payload capabilities in the optimal designs corresponding to each boil-off model both decreased as the loiter time increased. However, the payload capability of the vehicles associated with EBM were not as sensitive to changes in the loiter time.

This final experiment demonstrated that the primary research objective – to improve conceptual design and analysis of cryogenic in-space vehicles by providing more accurate propellant mass estimates through the development of a higher fidelity boil-off model – has been achieved. Per the guiding model requirements, the model is extensible, enables rapid evaluation of the design space, and incorporates a pressure control capability which allows simulation of extended mission durations.

7.2 Contributions

One of the principle goals, in addition to the research objective put forth by this dissertation, was to develop a model that could easily be interpreted and recreated by others in the space community without the need or involvement of a cryogenic subject matter expert. It is the hope of the author that this work was successful in that endeavor. Below is a list of the contributions this research has provided in support of the above efforts.

- Improved understanding of the theoretical model that is commonly used by the space community to estimate propellant losses and size in-space vehicles.
- Development of a simplified cryogenic propellant tank model capable of capturing

the evaporation process that occurs at the gas-liquid interface.

- Identification of an acceptable approach for implementing the pressure control capability required for simulating periods of extended storage.
- Improved understanding of the physical effects that influence the boil-off phenomenon, and how it changes throughout the mission in comparison to the constant losses predicted by the theoretical model.
- Quantification of the benefits of implementing higher-fidelity boil-off estimates in the sizing process when compared to the traditional model from literature.

7.3 Future Work

The majority of the research effort was dedicated to the formulation of the cryogenic propellant tank model. It was essential that the model predict the fluid conditions in the tank with a sufficient amount of fidelity, and yet retain a certain degree of simplicity in order to maintain computational efficiency. During the model development, several opportunities for expanding upon the current capabilities was identified as potential avenues for future research. While there are certainly aspects of the model that can be improved through the adjustment or the inclusion of more physical effects, the following were identified as providing the greatest benefit to the designer in terms of the investigations that become available.

One extension that would perhaps have the greatest impact on the model capability would be to include a TVS as a method of pressure control. Given the durations anticipated for future missions, propellant tanks will most likely utilize a combination of mixing and venting in order to delay and reduce the amount of boil-off that occurs within the tank. At a minimum, the range of operations within the tank will have to be expanded to include condensation due to mixing, along with the appropriate heat transfer processes. The inclusion of a noncondensable gas to the ullage space is not strictly required, as data for

TVS experiments conducted on GH_2/LH_2 systems is readily available in literature. Once the TVS capability has been integrated, the model can be used not just for vehicle sizing, but also to support trade studies on the different pressure control methods, since the TVS, while it provides much lower propellant losses, comes at the cost of additional mass and complexity which may not be desirable for shorter missions.

Another critical extension to the model capability would be to incorporate additional cryogenic propellants, such LOX and LCH_4, into the model. This is the simplest of the proposed extensions since the heat and mass transfer assumptions made for GH_2/LH_2 apply equally well to LOX and LCH_4 systems. However, unlike LH_2, LOX and LCH_4 require an additional pressurant since the propellants are not as prone to boil-off. Therefore, the effects due to the presence of a noncondensable gas will also need to be included in the model. Once the propellants and the pressurant have been incorporated, the model can be used to conduct trades studies on the different cryogenic propellant combinations, as well against other traditional propellants.

Appendices

APPENDIX A
RESEARCH QUESTIONS AND HYPOTHESES

Research Question 1	How can a simplified cryogenic propellant tank model with pressure control capability be developed?
Hypothesis 1	If ideal operation within the tank is assumed, then pressurization can be attributed strictly to evaporation of the liquid propellant at the interface, followed by an instantaneous reduction in the tank pressure due to venting of the ullage gas. This will greatly reduce the number of physical processes necessary to analyze the tank.
Research Question 2	How can the mass released during venting, and the subsequent conditions in the tank be determined?
Hypothesis 2	If the ullage is modeled as a thermodynamic system consisting of an ideal gas in an insulated container in thermodynamic equilibrium just prior to, and immediately after venting, and further, if the state of the gas after venting is assumed saturated, then the final conditions in the tank and the mass released during venting can be determined.
Research Question 3	What is the boil-off prediction capability of the model?
Research Question 3.1	What is the ability of the model to simulate the self-pressurization process?

Hypothesis 3.1	Due to the assumptions regarding heat transfer at the tank wall and at the interface, the model will predict higher pressurization rates than observed in literature, especially at higher propellant fill levels.
Research Question 3.2	What is the dP/dt prediction capability of the model when compared to higher-fidelity propellant tank models in literature?
Hypothesis 3.2	Due to the simplicity of the heat and mass transfer assumptions utilized in the formulation of the extensible boil-off model, the model will yield less accurate pressurization rates when compared with other higher-fidelity models in literature.
Research Question 3.3	What is the ability of the model to simulate the venting process?
Hypothesis 3.3	Given the assumption regarding the final saturated state of the ullage, the model will overestimate the mass that should be released during venting, and therefore the propellant losses due to boil-off, but to a lesser extent than the theoretical model in literature which assumes a saturated state for the entire storage period.
Research Question 4	What are the benefits of implementing a higher-fidelity boil-off model in the vehicle sizing process?

Hypothesis 4	Utilizing a higher-fidelity model in the sizing process will result in smaller vehicles, and will therefore open up the vehicle design space.

APPENDIX B

PROPELLANT TANK MODEL SCHEMATICS

B.1 Model by Hastings et al.

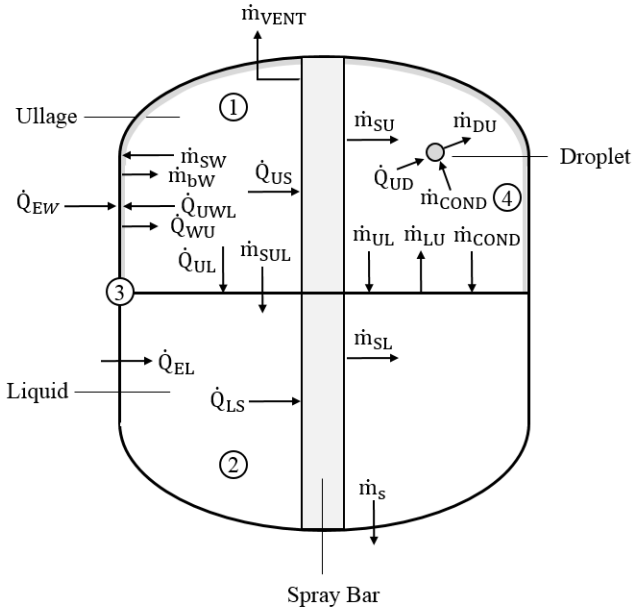

Figure B.1: Propellant tank model developed by Hastings et al. for modeling and analysis of a spray bar TVS. Control volumes consist of (1) the ullage, (2) bulk liquid, (3) tank wall, and (4) liquid on the tank wall.

Heat transfer rates:

- $\dot{Q}_{EL}$ Heat added to the liquid on tank wall by the environment
- $\dot{Q}_{EW}$ Environment and wall
- $\dot{Q}_{LS}$ Liquid and submerged spray bar
- $\dot{Q}_{UD}$ Ullage and liquid droplet
- $\dot{Q}_{UL}$ Ullage and bulk liquid
- $\dot{Q}_{US}$ Ullage and unsubmerged spray bar
- $\dot{Q}_{UWL}$ Ullage and wall liquid

$\dot{Q}_{WU}$ Tank wall and ullage

Mass flow rates:

$\dot{m}_{bW}$ Boiling of liquid on the tank wall

$\dot{m}_{COND}$ Liquid surface condensation

$\dot{m}_{DU}$ Liquid droplet evaporation in the ullage

$\dot{m}_{LU}$ Bulk liquid boiling

$\dot{m}_{S}$ Pump flow rate

$\dot{m}_{SL}$ Liquid spray flow rate into the bulk liquid

$\dot{m}_{SU}$ Spray flow rate into the ullage from orifice

$\dot{m}_{SUL}$ Liquid spray falling into the bulk liquid

$\dot{m}_{SW}$ Liquid spray accumulating on tank wall

$\dot{m}_{UL}$ Ullage condensation

$\dot{m}_{VENT}$ Overboard vent flow rate

B.2 TankSIM

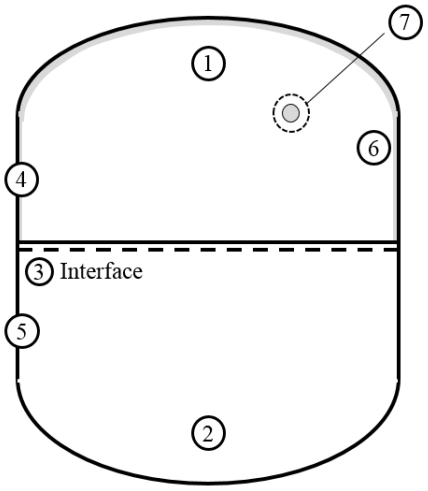

Figure B.2: TankSIM propellant tank model consisting of seven control volumes: (1) ullage, (2) bulk liquid, (3) interface, (4) tank wall adjacent to the ullage, (5) tank wall adjacent to the bulk liquid, (6) the liquid on the tank wall adjacent to the ullage, and (7) droplets in the ullage [22].

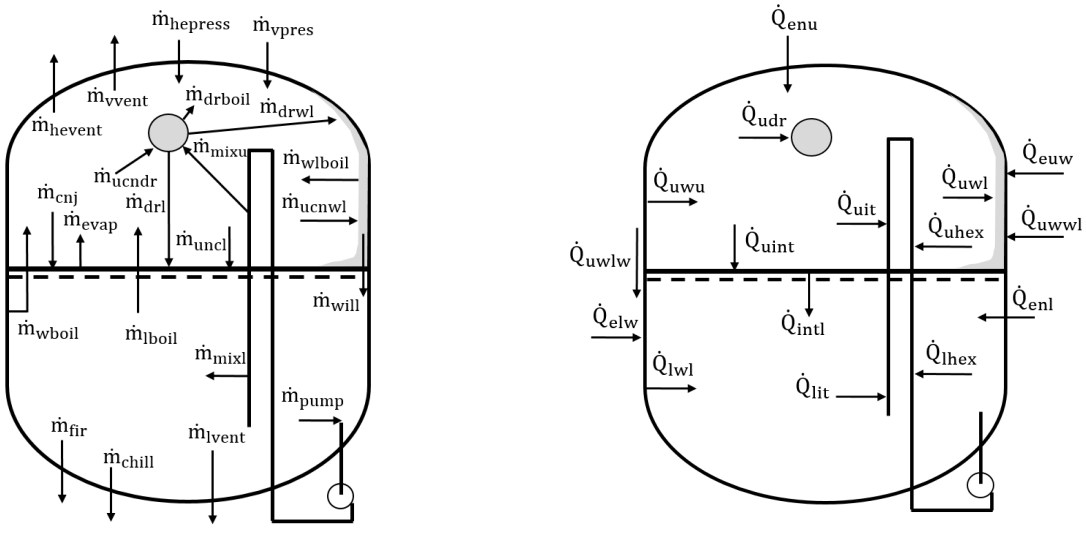

(a) Mass flow rates

(b) Heat transfer rates

Figure B.3: Predominant heat and mass flow rates included in the TankSIM propellant tank model [22].

Heat transfer rates:

$\dot{Q}_{elw}$	From environment to the liquid wall
$\dot{Q}_{enl}$	From environment to the liquid
$\dot{Q}_{enu}$	From environment to the ullage
$\dot{Q}_{euw}$	From environment to the ullage wall
$\dot{Q}_{intl}$	From ullage-liquid interface to bulk liquid
$\dot{Q}_{lhex}$	From liquid to the heat exchanger
$\dot{Q}_{lwl}$	From liquid wall to bulk liquid
$\dot{Q}_{udr}$	From ullage to droplets
$\dot{Q}_{uhex}$	From ullage to the heat exchanger
$\dot{Q}_{uint}$	From the ullage to the ullage-liquid interface
$\dot{Q}_{uit}$	From ullage to the injection pipe
$\dot{Q}_{uwl}$	Ullage to wall liquid
$\dot{Q}_{uwu}$	From ullage wall to ullage
$\dot{Q}_{uwlw}$	Conduction from the ullage wall to the liquid wall
$\dot{Q}_{uwwl}$	From the ullage wall to the wall liquid
$\dot{Q}\prime_{unif}$	Heat flux from the environment, uniformly distributed on the tank surface, W/m^2

Mass flow rates:

$\dot{m}_{chill}$	Liquid taking from the tank for pipe system chilldown
$\dot{m}_{cnj}$	Condensation initiated by axial jet
$\dot{m}_{drboil}$	Droplets boil-off to ullage
$\dot{m}_{drl}$	Unevaporated droplets falling to liquid
$\dot{m}_{drwl}$	Unevaporated droplets move to wall liquid
$\dot{m}_{evap}$	Evaporation from liquid interface to ullage
$\dot{m}_{fir}$	Liquid taken from the tank for engine firing

$\dot{m}_{hepress}$	Noncondensable pressurant to the ullage
$\dot{m}_{hevent}$	Noncondensable gas vented from the ullage
$\dot{m}_{lboil}$	Bulk liquid boil-off
$\dot{m}_{lvent}$	Vented liquid
$\dot{m}_{mixl}$	Total from injection pipe to bulk liquid
$\dot{m}_{mixu}$	Total from injection pipe to ullage (droplets)
$\dot{m}_{pump}$	Liquid pumped from tank to thermodynamic venting system
$\dot{m}_{ucndr}$	Bulk vapor condensation on the droplet
$\dot{m}_{ucnl}$	Vapor condensation on the ullage bulk liquid interface
$\dot{m}_{ucnwl}$	Vapor condensation on the wall liquid interface
$\dot{m}_{vpress}$	Autogenous pressurant mass flow rate
$\dot{m}_{vvent}$	Vapor vented from the ullage
$\dot{m}_{wboil}$	Bulk liquid boiling on the wall boil-off
$\dot{m}_{wlboil}$	Wall liquid boil-off
$\dot{m}_{wll}$	From wall liquid to bulk liquid

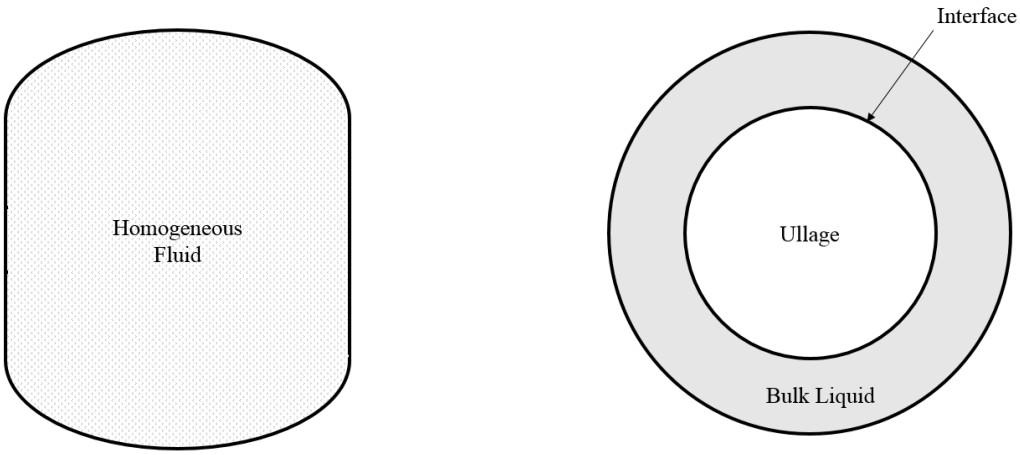

(a) Mixing

(b) Without mixing

Figure B.4: Ullage and bulk liquid propellant configurations utilized by TankSIM for modeling the heat and mass transfer in an unsettled tank [22].

B.3 CPPPO

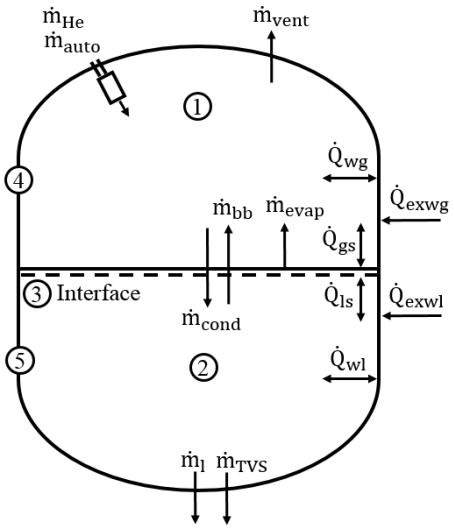

Figure B.5: CPPPO propellant tank model consisting of five control volumes: (1) ullage, (2) bulk liquid, (3) interface, (4) tank wall adjacent to the ullage, and (5) tank wall adjacent to the bulk liquid [36].

Heat transfer rates:

$\dot{Q}_{exwg}$	From external environment to tank wall exposed to ullage gas
$\dot{Q}_{exwl}$	From external environment to tank wall exposed to liquid
$\dot{Q}_{wg}$	Ullage gas and tank wall exposed to ullage gas
$\dot{Q}_{wl}$	Liquid and tank wall exposed to liquid
$\dot{Q}_{gs}$	Ullage gas and saturated surface layer (interface)
$\dot{Q}_{ls}$	Liquid and saturated surface layer (interface)

Mass flow rates:

$\dot{m}_{auto}$	Autogenous GH_2 or GO_2
$\dot{m}_{He}$	Helium pressurant gas
$\dot{m}_{vent}$	Vent relief
$\dot{m}_{evap}$	Propellant evaporation
$\dot{m}_{bb}$	Propellant bulk boiling

$\dot{m}_{cond}$	Propellant vapor condensation
$\dot{m}_{l}$	Propellant liquid
$\dot{m}_{TVS}$	Propellant Thermodynamic Vent System (TVS)

B.4 General Liquid Propellant Tank Model by Ring

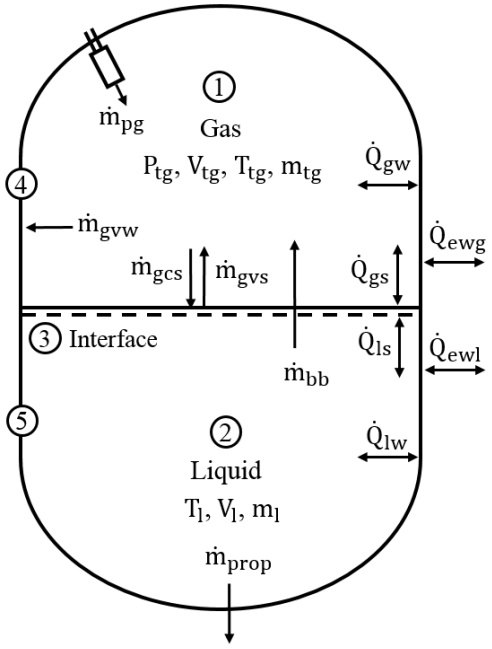

Figure B.6: Liquid propellant tank model developed by Ring for preliminary sizing and analysis of liquid rocket propellant pressurization systems. Control volumes include: (1) ullage, (2) bulk liquid, (3) interface, (4) tank wall adjacent to the ullage, and (5) tank wall adjacent to the bulk liquid [131].

Heat transfer rates:

- $\dot{Q}_{lw}$ Liquid and wall adjacent to liquid
- $\dot{Q}_{ls}$ Liquid and liquid surface layer
- $\dot{Q}_{gs}$ Ullage gas and liquid surface layer
- $\dot{Q}_{gw}$ Ullage gas and wall adjacent to gas
- $\dot{Q}_{awl}$ External surroundings and wall adjacent to liquid
- $\dot{Q}_{awg}$ External surroundings and wall adjacent to gas

Mass transfer rates:

- $\dot{m}_{pg}$ Pressurant gas entering the ullage space
- $\dot{m}_{bb}$ Bulk liquid boiling
- $\dot{m}_{gvw}$ Propellant vapor condensation at the tank wall
- $\dot{m}_{gvs}$ Propellant evaporation at the liquid surface
- $\dot{m}_{gcs}$ Propellant vapor condensation at the liquid surface
- $\dot{m}_{prop}$ Propellant leaving the tank

APPENDIX C

TANK EQUATIONS

Tank parameters:

A_{wet}	Tank surface area in contact with the bulk liquid
d	Tank diameter
r	Tank radius
V	Liquid volume
V_{top}	Volume in top cap
V_{bottom}	Volume of liquid in bottom cap
y	Liquid height in tank or section of tank
z	Dome height on elliptical end cap
ε	Eccentricity

Interface parameters:

A_s	Area of the interface
w	Width (or diameter) of the interface

C.1 Spherical Tank

$$A_{wet} = 2\pi ry \tag{C.1}$$

$$V = \pi ry^2 - \frac{1}{3}\pi y^3 \tag{C.2}$$

$$w = 2\sqrt{(2r - y)y} \tag{C.3}$$

$$A_s = \pi(2r - y)y \tag{C.4}$$

C.2 Cylindrical Tank

Cylindrical tanks are analyzed in sections – top, middle, and bottom – where the top and bottom sections can be either hemispherical or elliptical. For cylindrical tanks with elliptical end caps, width of the interface w, is assumed to be the same as the tank diameter d. Given this assumption, the area of the interface is circular for all sections of the tank, and is determined using the following equation:

$$A_s = \pi(2r - y)y \tag{C.5}$$

C.2.1 Cylindrical Section

$$A_{wet} = \pi dy \tag{C.6}$$

$$V = \frac{\pi}{4}d^2y \tag{C.7}$$

$$w = 2r \tag{C.8}$$

C.2.2 Hemispherical Heads

$$A_{wet} = 2\pi ry \tag{C.9}$$

$$V = \frac{\pi y^2}{3}(3r - y) \tag{C.10}$$

$$V = \frac{\pi}{3}\left[2r^3 - y^2(3r - y)\right] \tag{C.11}$$

$$w = 2\sqrt{(2r - y)y} \tag{C.12}$$

C.2.3 Elliptical Heads

For 2:1 elliptical heads, C = 1/2 and ε = 0.866.

$$A_{wet} = \frac{\pi d^2}{8}\left[2 + \frac{1}{4\varepsilon} ln\Big(\frac{2\varepsilon + 2}{2 - \sqrt{3}}\Big)\right] \tag{C.13}$$

$$\varepsilon = \sqrt{1 - \frac{4z^2}{d^2}} \tag{C.14}$$

$$V = d^3 C \frac{\pi}{24}\left[3\Big(\frac{y}{z}^2\Big) - \Big(\frac{y}{z}^3\Big)\right] \tag{C.15}$$

$$V = d^3 C \frac{\pi}{24}\left[3\Big(\frac{y}{z}\Big) - \Big(\frac{y}{z}^3\Big)\right] \tag{C.16}$$

$$w = 2r \tag{C.17}$$

APPENDIX D

ERROR IN REAL GAS PROPERTIES

D.1 Specific Heat at Constant Volume

Training	
Cv (J/g*K)	
Measures	**Value**
RSquare	0.9999892
RMSE	0.0021154
Mean Abs Dev	0.0014632
-LogLikelihood	-46803.08
SSE	0.0441916
Sum Freq	9875

Validation	
Cv (J/g*K)	
Measures	**Value**
RSquare	0.9999888
RMSE	0.0021504
Mean Abs Dev	0.0014589
-LogLikelihood	-11656.71
SSE	0.011413
Sum Freq	2468

(a) R^2 and Root Mean Square Error

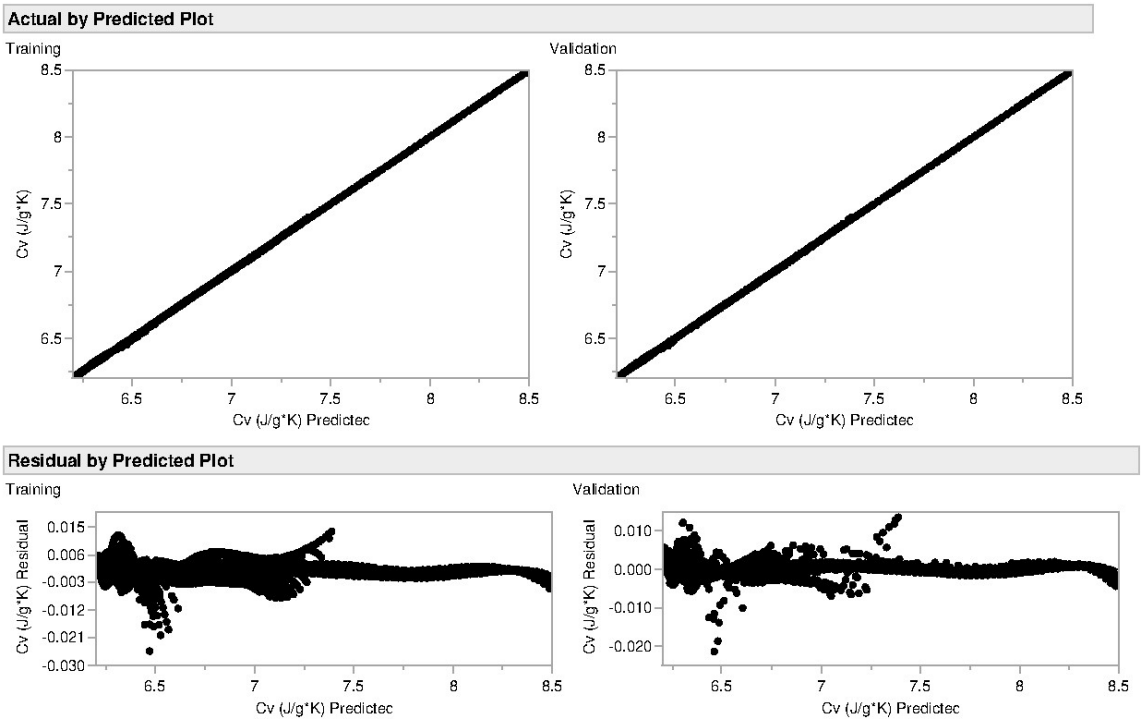

(b) Actual by Predicted (top) and Residual by Predicted (bottom) plots

Figure D.1: (a) Predictive accuracy associated with the Neural Network fit obtained for c_v, and (b) plots of the actual values versus those predicted by the model and the corresponding residual error.

D.2 Internal Energy

Training	
Internal Energy (kJ/kg)	
Measures	**Value**
RSquare	1
RMSE	0.016012
Mean Abs Dev	0.0107486
-LogLikelihood	-26815.34
SSE	2.5317984
Sum Freq	9875

Validation	
Internal Energy (kJ/kg)	
Measures	**Value**
RSquare	1
RMSE	0.0167386
Mean Abs Dev	0.0111253
-LogLikelihood	-6592.272
SSE	0.6914868
Sum Freq	2468

(a) R^2 and Root Mean Square Error

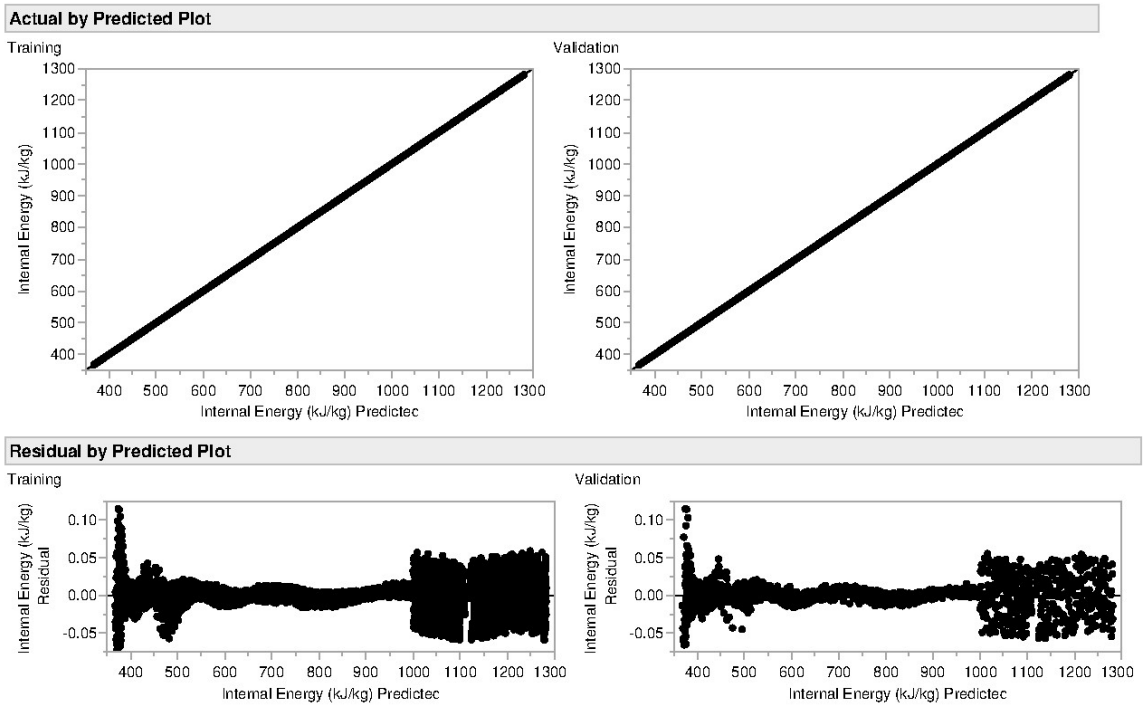

(b) Actual by Predicted (top) and Residual by Predicted (bottom) plots

Figure D.2: (a) Predictive accuracy associated with the Neural Network fit obtained for u, and (b) plots of the actual values versus those predicted by the model and the corresponding residual error.

D.3 Enthalpy

Training	
Enthalpy (kJ/kg)	
Measures	**Value**
RSquare	1
RMSE	0.0655873
Mean Abs Dev	0.0478893
-LogLikelihood	-12889.86
SSE	42.474903
Sum Freq	9874

Validation	
Enthalpy (kJ/kg)	
Measures	**Value**
RSquare	1
RMSE	0.0642948
Mean Abs Dev	0.0472686
-LogLikelihood	-3272.26
SSE	10.206402
Sum Freq	2469

(a) R^2 and Root Mean Square Error

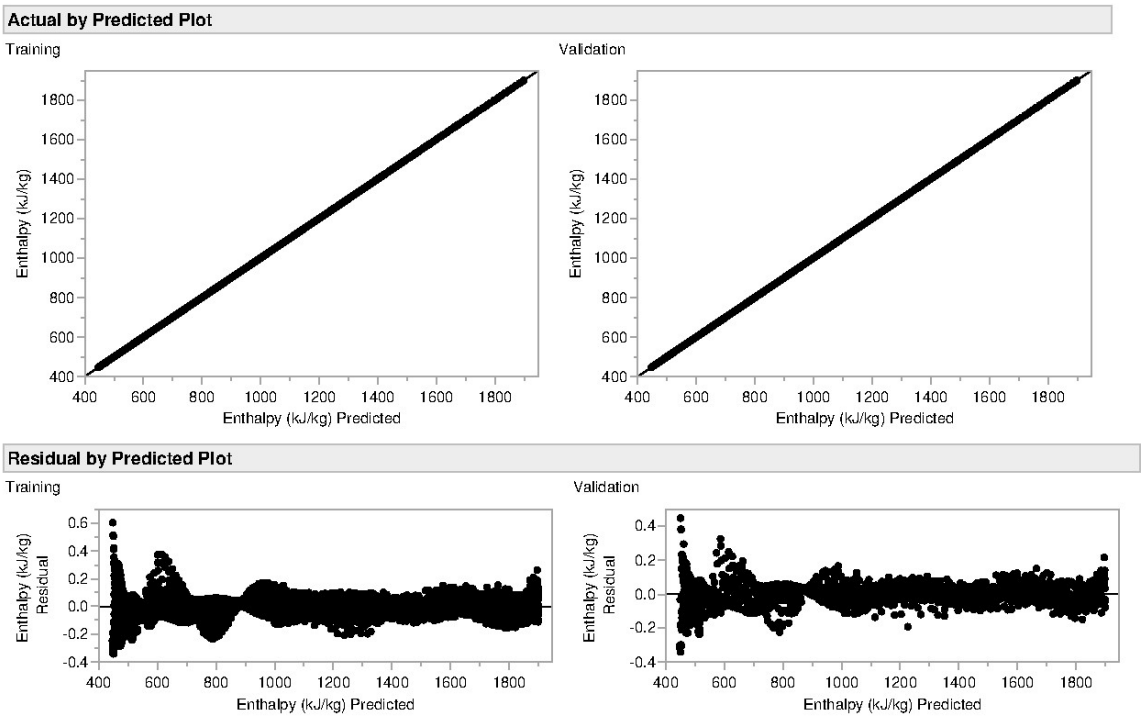

(b) Actual by Predicted (top) and Residual by Predicted (bottom) plots

Figure D.3: (a) Predictive accuracy associated with the Neural Network fit obtained for h, and (b) plots of the actual values versus those predicted by the model and the corresponding residual error.

APPENDIX E

SOURCE CODE FOR LIQUID HYDROGEN BOIL-OFF MODEL

E.1 Boil-Off Model

```
import numpy as np
from auxiliary_functions import tank_parameters, initial_conditions, vent
from self_pressurization import run_self_pressurization

def run_model(P_o, P_max, P_min, shape, diameter, length, FL_o,
                                    q_dot_env, duration, tank):

    # max allowable bulk liquid, T_max = Tsat(P_min)
    T_max = 22.509518 + 9.5791e-6*P_min - 5.85e-12*(P_min-598825)**2
            + 3.292e-18*(P_min-598825)**3 - 1.246e-24*(P_min-598825)**4
            + 2.053e-29*(P_min-598825)**5 - 3.463e-35*(P_min-598825)**6

    # model params
    t = int(86400*duration)  # convert days to seconds
    pts = t//10+1            # num pts required for a time step of 10s
    x = np.linspace(0,t,pts) # time array for model
    z = 0

    m_vented = []   # mass vented at each time step

    # fully define the tank
    tank_data = tank_parameters(shape, diameter, length)

    # determine heat leak rate into tank
    q_dot_SA = q_dot_env/tank_data[3]  # [W/m^2]

    # Step 3: gather remaining initial conditions
    mo_gh2, Vo_gh2, To_gh2, To_lh2
                    = initial_conditions(P_o, FL_o, tank_data[2])


    # --- initial self-pressurization segment --- #
    P_g, T_g, V_g, m_g, T_l, FL_l, t
                = run_self_pressurization(t, pts, To_gh2, mo_gh2,
                                          Vo_gh2, To_lh2,
                                          FLo, q_dot_SA,
                                          tank_data, P_max,T_max)

    # --- collect data for conditions in the tank --- #
    j = 0
    while j <= pts:

        for i in list(range(0,len(t))):
            m_vented.append(0)
```

```
            j +=1

        # time remaining in storage duration
        z = int(x[-1]-t[-1])
        if z == 0:
            break

        # --- venting --- #
        m_new, T_new, m_vent, m_pr, T_pr = vent(P_g[-1], P_min, T_g[-1],
                                                m_g[-1],V_g[-1])
        m_vented[-1] = m_vent

        # --- repressurization --- #
        P_g, T_g, V_g, m_g, T_l, FL_l, t
                = run_self_pressurization(z,z//10+1, T_new, m_new,
                                          V_g[-1], T_l[-1],
                                          FL_l[-1], q_dot_SA,
                                          tank_data, P_max, T_max)

    # grab data for j[0] through j[pts]
    m_vented = np.array(m_vented[0:len(x)])

    # propellant losses due to boil-off
    total_vented_mass = np.sum(m_vented)

    return(total_vented_mass)
```

E.2 Self-Pressurization Model

```
# constants
R = 8.314           # [J/mol-K], universal gas constant
g = 9.806           # [m/s^2], gravity
MW_lh2 = 2.016e-3   # [kg/mol], molecular weight gh2
MW_gh2 = MW_lh2     # [kg/mol], molecular weight lh2


# solve the system dy/dt = f(y, t)
def f(t,y, tank_data, heat_rate_SA,Tmax):
    # This def solves the system of first order ODEs
    # args:
    #   y: vector of initial conditions
    #   tank_data: list of tank geometry
    #   heat_rate_SA: heat leak rate per tank SA [W/m^2]


    q_SA = heat_rate_SA   # [W/m^2]

    m_g = y[0]  # mass in ullage space
    V_g = y[1]  # ullage volume
    T_g = y[2]  # ullage temp
    T_l = y[3]  # bulk liquid temp

    # ullage pressure at time t based on ullage parameters
    P_g = m_g * T_g * R / (V_g * MW_gh2)

    # ullage properties
    c_vg, u_g, h_g = gh2_properties(P_g, T_g)

    # bulk properties
    P_l, rho_l, u_l, h_l, c_vl, c_pl, visc_l, k_l, beta_l
                                        = lh2_properties(T_l)

    # interface properties
    T_s, h_s = sh2_properties(P_g)

    # gh2 properties at mean film temp
    T_m = (T_g + T_s)/2
    rho_gsf, h_gsf, c_pgsf, k_gsf, visc_gsf, beta_gsf
                                    = gh2_properties_gsf(T_m)

    # enthalpies
    h_gsat = sat_gh2_enthalpy(P_g)
    h_fg = h_g - h_s

    # bulk liquid vol.
    V_l = tank_data[2] - V_g

    # interface geometry
    h, A, L = interface_params(tank_data, V_l)

    # dry and wet tank wall areas
```

```
    wet_SA, dry_SA = tank_surface_areas(tank_data, h)

    # heat transfer coefficient
    h_gs = heat_transfer_coef(c_pgsf, visc_gsf, k_gsf, beta_gsf,
                                            rho_gsf, T_g, T_s, L)

    # heat transfer rates
    q_dot_ge = dry_SA*q_SA            # environment to gas
    q_dot_le = wet_SA*q_SA            # environment to liquid
    q_dot_gs = h_gs * A * (T_g - T_s) # gas --> interface

    # --- system of equations (ODEs) --- #
    # roc m_g
    f0 = q_dot_gs/(h_fg + c_pl*(T_s - T_l) + (h_g - h_gsat))
    # roc V_g
    f1 = f0*(1/rho_l)
    # roc T_g
    f2 = (q_dot_ge - q_dot_gs + f0*h_g - P_g*f1 - f0*u_g) / (m_g*c_vg)
    # roc T_l
    f3 = (q_dot_le - f0*h_l - P_l*(-f1) - (-f0)*u_l )/ (rho_l *V_l*c_pl)

    # once the max bulk liquid temp is reached, hold the temp constant
    if Tmax - y[3] <= 0:
        f3 = 0.
    else:
        pass

    return[f0,f1,f2,f3]


def limit(t,y):
    global Pmax
    P_gas = y[0]*y[2]*R / (y[1]*MW_gh2)
    test = np.array(Pmax - P_gas)
    return(test)


def run_self_pressurization(duration, num_pts, T0_gh2, m0_gh2, V0_gh2,
                                                    T0_lh2, FL_0, q_dot_A,
                                            tank_geom, P_high, T_high):

    global Pmax
    Pmax = P_high

    t_span = np.linspace(0,duration,num_pts)

    # attributes for event
    limit.terminal = True
    limit.direction=-1

    # initial condition vector
    y0 = [m0_gh2,V0_gh2,T0_gh2,T0_lh2]

    # solve system of equations
```

```
soln = solve_ivp(lambda t,y: f(t,y,tank_geom, q_dot_A, T_high),
                    [t_span[0],t_span[-1]], y0, method='LSODA',
                                        t_eval=t_span, events=limit)

# save results
m_tg = soln.y[0]        # ullage mass
V_tg = soln.y[1]        # ullage volume
T_tg = soln.y[2]        # ullage temp
T_lh2 = soln.y[3]       # bulk temp
t = soln.t

# calculate FL
FL_lh2 = (tank_geom[2] - V_tg)/tank_geom[2]

return(P_tg, T_tg, V_tg, m_tg, T_lh2, FL_lh2, t)
```

E.3 Venting Model

```
"""
Calculates the mass in the ullage after venting.
The ideal gas law is applied to the tank just before
and after venting.
p1, T1, m1: pressure, temp, and mass of the ullage
            just before venting
p2, T2, m2: ullage properties after venting
Knowns: p1, T1, m1, V1, p2, T2, V2,
        where V1 = V2, and T2 = T(Psat).
m2 = p2*m1*T1 / p1*T2
"""
def vent(p1,p2,T1,m1):
    # determine T2 at saturation conditions
    T2 = 22.509518 + 9.5791e-6*p2 - 5.85e-12*(p2-598825)**2
            + 3.292e-18*(p2-598825)**3 - 1.246e-24*(p2-598825)**4
            + 2.053e-29*(p2-598825)**5 - 3.463e-35*(p2-598825)**6

    # mass in ullage after venting
    m2 = p2*m1*T1 / (p1*T2)

    return(m2,T2,m1-m2)
```

E.4 Auxiliary Functions

```
from numpy import pi
import numpy as np

# constants
R = 8.314               # [J/mol-K]
g = 9.806               # [m/s^2]
MW_g = MW_l = 2.016e-3 # [kg/mol]; molecular weight of h2

def tank_parameters(tank_shape, tank_diameter, tank_height):
    # calculates geometry of the tank

    d = tank_diameter    # diameter
    H = tank_height      # total tank height
    r = 0.5*d            # radius

    h_b = 0.             # height of barrel section
    h_d = 0.             # dome height
    V = 0.               # volume
    SA = 0.              # surface area
    if tank_shape == 'sphere':
        h_d = r
        V = (4/3)*pi*r**3
        SA = 4*pi*r**2
    elif tank_shape == 'cylinder_h': # hemispherical head
        h_d = r
        h_b = H - 2*h_d
        V = pi*r**2*h_b + (4/3)*pi*h_d**3
        SA = 2*pi*r*h_b + 4*pi*h_d**2
    elif tank_shape == 'cylinder_e': # 2:1 elliptical head
        h_d = 0.25*d # dome hieght
        h_b = H - 2*h_d
        V = pi*r**2*h_b + (4/3)*pi*r**2*h_d
        a = r
        b = r
        c = h_d
        SA = 2*pi*r*h_b + 4*pi*(((a*b)**1.6
                + (a*c)**1.6 + (b*c)**1.6)/3)**(1/1.6)

    tank_info = [tank_shape, tank_diameter, V, SA, h_b, h_d]
    return(tank_info)

def initial_conditions(P_gas, FL, V_tank):

    T_liq = 22.509518 + 9.5791e-6*P_gas - 5.85e-12*(P_gas-598825)**2
            + 3.292e-18*(P_gas-598825)**3 - 1.246e-24*(P_gas-598825)**4
            + 2.053e-29*(P_gas-598825)**5 - 3.463e-35*(P_gas-598825)**6

    # initial ullage conditions for system of ODEs
    T_gas = T_liq                          # [K]
    V_gas = (1-FL) * V_tank                # [kg]
    m_gas = P_gas*V_gas*MW_g / (T_gas*R) # [kg]
```

```
    return(m_gas, V_gas, T_gas, T_liq)


def interface_params(tank_params, vol_liquid):
    """ Calculates the height of the liquid in the tank (h), and the
    corresponding interface area (A_int),  diameter (w), and length
    dimension (L_int)."""

    # tank array
    # tank_params[0]  # tank shape
    # tank_params[1]  # diameter
    # tank_params[2]  # volume
    # tank_params[3]  # surface area
    # tank_params[4]  # barrel height
    # tank_params[5]  # dome height

    V_l = vol_liquid

    d = tank_params[1]
    r = 0.5*d
    V_t = tank_params[2]    # tank volume
    h_b = tank_params[4]    # barrel height
    a = tank_params[5]      # dome height

    # volumes for full cap and barrel
    V_cap = (2/3)*pi*a**3    # fluid vol for end cap
    V_barrel = pi*r**2*h_b   # fluid vol for full barrel

    h = 0. # height of the liquid
    w = 0. # width of the interface

    if tank_params[0] == 'sphere':
        c1 = -(1/3)*pi
        c2 = pi*r
        c3 = 0
        c4 = -V_l
        coef = [c1,c2, c3, c4]
        h_array = np.roots(coef)
        h = h_array[1]           # height of liquid
        w = 2*((2*r-h)*h)**0.5   # width (or diameter) of the interface

    elif tank_params[0] == 'cylinder_h':
        """ 'height' corresponds to the volume in the tank. The
        tank is separated into three regions - bottom cap, middle
        barrel section, and the top cap. The liquid height
        corresponding to the volume is found for each section and
        then summed to find the final liquid height."""
        # if liquid is contained in the bottom cap
        if V_l <= V_cap:
            c1 = -(1/3)*pi
            c2 = pi*r
            c3 = 0
            c4 = -V_l
            coef = [c1,c2, c3, c4]
```

```
            h_array = np.roots(coef)
            h = h_array[1]
            w = 2*((2*r-h)*h)**0.5
        # if liquid contained to the barrel section
        elif V_l > V_cap and V_l <= V_cap + V_barrel:
            V_middle = V_l - V_cap
            h = V_middle/(pi*r**2) + r
            w = 2*r
        # if liquid is somewhere in the top cap
        elif V_l > V_cap + V_barrel:
            """In order to find the height of liquid in the top cap,
            analyze the top and bottom cap together as a single
            sphere of radius r, and apply the standard equations for
            finding the liquid height and width of the interface.
            Here, the liquid height in the sphere is y, and the height
            of the interface in the tank is represented by h."""
            # liquid volume sphere of radius r, formed by the two end caps
            V_c = V_l - V_barrel
            c1 = -(1/3)*pi
            c2 = pi*r
            c3 = 0
            # volume of liquid in top AND bottom cap
            c4 = -V_c
            coef = [c1,c2, c3, c4]
            y_array = np.roots(coef)
            y = y_array[1]
            w = 2*((2*r-y)*y)**0.5
            h = y + h_b
    # if liquid vol > vol bottom cap + barrel
    elif tank_params[0] == 'cylinder_e':
        w = 2*r
        # if liquid is contained in the bottom cap
        if V_l <= V_cap:
            c1 = (pi/48)*(d**3/a**3)
            c2 = -(pi/16)*(d**3/a**2)
            c3 = 0
            c4 = V_l
            coef = [c1,c2, c3, c4]
            h_array = np.roots(coef)
            h = h_array[1]
        # if liquid contained to the barrel section
        elif V_l > V_cap and V_l <= V_cap + V_barrel:
            V_middle = V_l - V_cap # vol liquid inside the barrel
            h = V_middle/(pi*r**2) + a
        # if liquid is somewhere in the top cap
        elif V_l > V_cap + V_barrel:
            # vol of the "free space" in the top cap
            V_f = V_t - V_l
            c1 = (pi/48)*(d**3/a**3)
            c2 = -(pi/16)*(d**3/a**2)
            c3 = 0
            c4 = V_f
            coef = [c1,c2, c3, c4]
            f_array = np.roots(coef)
```

```
            h = (a - f_array[1]) + h_b + a

    # calculate interface area and characteristic length
    h_int = h
    A_int = pi*(0.5*w)**2  # area of circular interface
    L_int = A_int / (pi*w) # length dimension

    return(h_int, A_int, L_int)

def tank_surface_areas(tank_params, height_liq):
    """ Calculates the wet and dry tank surface areas corresponding
    to the liquid level in the tank."""

    d = tank_params[1]       # tank diameter
    r = 0.5*d                # tank radius
    a = tank_params[5]       # dome height
    h_b = tank_params[4]     # barrel height
    tank_SA = tank_params[3]

    # surface areas full cap and barrel
    SA_cap = 2*pi*r**2       # wet SA for full end cap
    SA_barrel = 2*pi*r*h_b   # wet SA for full barrel

    h = height_liq

    SA_wet = 0.
    if tank_params[0] == 'sphere':
        SA_wet = 2*pi*r*h # verified

    # for cylindrical tank w/ hemispherical head
    elif tank_params[0] == 'cylinder_h':

        # interface located in bottom cap
        if h <= r:
            SA_wet = 2*pi*r*h
        # interface located in barrel
        elif h > r and h <= (r + h_b):
            # a = r in this case
            SA_wet = 2*pi*r**2 + 2*pi*r*(h-r)
        # interface in top cap
        elif h > r + h_b:
            SA_wet = 2*pi*r*(h-h_b) + 2*pi*r*h_b # verified
    # cylindrical tank w/ ellipsoidal head
    elif tank_params[0] == 'cylinder_e':
        # surface located in the bottom cap
        if h <= a:
            num = a*( (r**2 - a**2)**0.5 + r)
            den = (a-h)*(r**2-a**2)**0.5 + (a**4
                    + (a-h)**2 * (r**2-a**2))**0.5
            SA_wet = pi*r**2 - (pi/a**2)*(a-h)*r*(a**4+(a-h)**2
                    * (r**2-a**2) )**0.5 + (pi*a**2*r/(r**2-a**2)**0.5)
                    * np.log(num/den) # cap
        # surface somewhere in the barrel section
        elif h > a and h <= a + h_b:
```

```
            num = r + (r**2-a**2)**0.5
            den = r - (r**2-a**2)**0.5
            SA_wet = pi*r**2 + pi*a**2*r/(2*(r**2-a**2)**0.5)
                    * np.log(num/den) + 2*pi*r*(h-a) # cap + barrel
        # surface in top cap
        elif h > a + h_b:
            H = h_b + 2*a # total tank height
            f = H - h     # height of empty space in top cap
            num = a*((r**2-a**2)**0.5 + r)
            den = (a-f)*(r**2-a**2)**0.5 + (a**4 + (a-f)**2
                    * (r**2-a**2))**0.5
            SA_dry = pi*r**2 - (pi/a**2)*(a-f)*r*(a**4+(a-f)**2
                    * (r**2-a**2) )**0.5
                    + (pi*a**2*r/(r**2-a**2)**0.5) * np.log(num/den)
            SA_wet = SA_cap - SA_dry
    SA_dry = tank_SA - SA_wet

    return(SA_wet, SA_dry)

def heat_transfer_coef(c_p, visc, k, beta, rho, T_high, T_low, char_L):
    # calculates the heat transfer coefficient for natural convection
    # over flat horizontal plate

    # constants for top of cold horizontal surface
    C = 0.27
    n = 0.25

    # fluid properties
    Pr = c_p * visc/k
    Gr = g * beta * rho**2 * abs(T_high - T_low) * char_L**3 /(visc**2)
    X = Pr * Gr
    Nu = C * X**n
    # heat transfer coef.
    h_c = (k/char_L) * Nu # [W/m^2-K]

    return(h_c)
```

E.5 Fluid Properties File

```
import numpy as np

def gh2_properties(pressure, temperature):
    # pressure: float [Pa]
    # temperature: float [K]

    indata = {"Pressure (MPa)":pressure/1e6,
              "Temperature (K)": temperature}
    outdata = {}

    c_v(indata, outdata)
    u(indata, outdata)
    h(indata, outdata)
    specific_heat_vol = outdata["Predicted Cv (J/g*K)"]*1000
    internal_energy = outdata["Predicted Internal Energy (kJ/kg)"]*1000
    enthalpy = outdata["Predicted Enthalpy (kJ/kg)"]*1000

    return(specific_heat_vol, internal_energy, enthalpy)

def lh2_properties(T):
    P = (0.0138 * T**5.2644)
    rho = 115.53291 - 2.0067591*T - 0.1067411*(T-27.6691)**2
          - 0.0085915*(T-27.6691)**3 - 0.0019879*(T-27.6691)**4
          - 0.0003988*(T-27.6691)**5 - 2.7179e-5*(T-27.6691)**6
    u = -334268 + 15183.043*T + 614.10133*(T-27.6691)**2
        + 40.845478*(T-27.6691)**3 + 9.1394916*(T-27.6691)**4
        + 1.8297788*(T-27.6691)**5 + 0.1246228*(T-27.6691)**6
    h = -371985.2 + 16864.749*T + 893.59208*(T-27.6691)**2
        + 103.63758*(T-27.6691)**3 + 7.756004*(T-27.6691)**4
    c_v = 4138.1395 + 72.04929*T + 3.6470929*(T-27.6691)**2
          + 1.5258739*(T-27.6691)**3 + 0.3466932*(T-27.6691)**4
          + 0.026033*(T-27.6691)**5
    c_p = 1/(0.0002684 - 7.6143e-6*T - 2.5759e-7*(T-27.6691)**2)
    visc = 2.367e-5 - 5.7263e-7*T + 6.9609e-9*(T-27.6691)**2
          - 2.4303e-9*(T-27.6691)**3
    k = 0.1575097 - 0.0020718*T - 0.0002477*(T-27.6691)**2
        - 1.762e-5*(T-27.6691)**3 - 1.8652e-6*(T-27.6691)**4
    beta = np.e**(-6.185192 + 0.1016509*T
          + 0.0068955*(T-23.0338)**2 + 0.0006315*(T-23.0338)**3)
    return(P, rho, u, h, c_v, c_p, visc, k, beta)

def sh2_properties(P):
    T = 22.509518 + 9.5791e-6*P - 5.85e-12*(P-598825)**2
        + 3.292e-18*(P-598825)**3 - 1.246e-24*(P-598825)**4
        + 2.053e-29*(P-598825)**5 - 3.463e-35*(P-598825)**6
    h = -371985.2 + 16864.749*T + 893.59208*(T-27.6691)**2
        + 103.63758*(T-27.6691)**3 + 7.756004*(T-27.6691)**4
    return(T, h)

def gh2_properties_gsf(T):
    rho = -28.97599 + 1.2864736*T + 0.1140157*(T-27.6691)**2
          + 0.0086723*(T-27.6691)**3 + 0.0019006*(T-27.6691)**4
```

```
          + 0.0003805*(T-27.6691)**5 + 2.5918e-5*(T-27.6691)**6
    h = 577302.07 - 4284.432*T - 1084.1238*(T-27.6691)**2
        - 73.011186*(T-27.6691)**3 - 15.407809*(T-27.6691)**4
        - 2.9987887*(T-27.6691)**5 - 0.2022147*(T-27.6691)**6
    c_p = np.e**(6.445199 + 0.1249361*T + 0.0125811*(T-27.6691)**2
          + 0.0027137*(T-27.6691)**3 + 0.0006249*(T-27.6691)**4
          + 4.8352e-5*(T-27.6691)**5)
    k = 1/(110.21937 - 2.6596443*T - 0.0153377*(T-27.6691)**2
        - 0.0088632*(T-27.6691)**3)
    visc = 1/(1582670.2 - 34545.242*T - 211.73722*(T-27.6691)**2
          - 283.70972*(T-27.6691)**3 - 18.848797*(T-27.6691)**4)
    beta = 1 / T
    return(rho, h, c_p, k, visc, beta)

def sat_gh2_enthalpy(P):
    T = 22.509518 + 9.5791e-6*P - 5.85e-12*(P-598825)**2
        + 3.292e-18*(P-598825)**3 - 1.246e-24*(P-598825)**4
        + 2.053e-29*(P-598825)**5 - 3.463e-35*(P-598825)**6
    h = 577302.07 - 4284.432*T - 1084.1238*(T-27.6691)**2
        - 73.011186*(T-27.6691)**3 - 15.407809*(T-27.6691)**4
        - 2.9987887*(T-27.6691)**5 - 0.2022147*(T-27.6691)**6
    return(h)


\newpage
\section{Saturated Fluid Property Equations} \label{app:sat_fluid_properties}
\begin{minted}[baselinestretch = 1,fontsize=\footnotesize]{python}
"""
Equations of saturated gh2 and lh2 properties.
Units:
    mass [kg]
    vol [m^3]
    density [kg/m^3]
    pressure [Pa]
    temp [K]
    energy [J]
    specific heats [J/kg]
    viscosity [Pa-s]
    themal conductivity [W/m-K]
"""
import numpy as np

# Pressure as a function of temp
P = 0.0138 * T**5.2644

# Temperature based on pressure increments
T = 22.509518 + 9.5791e-6*P - 5.85e-12*(P-598825)**2
    + 3.292e-18*(P-598825)**3 - 1.246e-24*(P-598825)**4
    + 2.053e-29*(P-598825)**5 - 3.463e-35*(P-598825)**6

# lh2 properties as a function of T
rho_l = 115.53291 - 2.0067591*T - 0.1067411*(T-27.6691)**2
        - 0.0085915*(T-27.6691)**3 - 0.0019879*(T-27.6691)**4
        - 0.0003988*(T-27.6691)**5 - 2.7179e-5*(T-27.6691)**6
```

```
u_l = -334268 + 15183.043*T + 614.10133*(T-27.6691)**2
        + 40.845478*(T-27.6691)**3 + 9.1394916*(T-27.6691)**4
        + 1.8297788*(T-27.6691)**5 + 0.1246228*(T-27.6691)**6
h_l = -371985.2 + 16864.749*T + 893.59208*(T-27.6691)**2
        + 103.63758*(T-27.6691)**3 + 7.756004*(T-27.6691)**4
c_vl = 4138.1395 + 72.04929*T + 3.6470929*(T-27.6691)**2
        + 1.5258739*(T-27.6691)**3 + 0.3466932*(T-27.6691)**4
        + 0.026033*(T-27.6691)**5
c_pl = 1/(0.0002684 - 7.6143e-6*T - 2.5759e-7*(T-27.6691)**2)
visc_l = 2.367e-5 - 5.7263e-7*T + 6.9609e-9*(T-27.6691)**2
        - 2.4303e-9*(T-27.6691)**3
k_l = 0.1575097 - 0.0020718*T - 0.0002477*(T-27.6691)**2
        - 1.762e-5*(T-27.6691)**3 - 1.8652e-6*(T-27.6691)**4
beta_l = np.e**(-6.185192 + 0.1016509*T + 0.0068955*(T-23.0338)**2
        + 0.0006315*(T-23.0338)**3)
h_vapl = 643518.5 - 9414.2796*T - 864.42293*(T-23.0338)**2
        - 42.793416*(T-23.0338)**3 - 4.8186135*(T-23.0338)**4
        - 0.0982576*(T-23.0338)**5

# gh2 properties as a function of T
rho_g = -28.97599 + 1.2864736*T + 0.1140157*(T-27.6691)**2
        + 0.0086723*(T-27.6691)**3 + 0.0019006*(T-27.6691)**4
        + 0.0003805*(T-27.6691)**5 + 2.5918e-5*(T-27.6691)**6
u_g = 466116.69 - 3220.3735*T - 748.772*(T-27.6691)**2
        - 53.773598*(T-27.6691)**3 - 11.581018*(T-27.6691)**4
        - 2.2673071*(T-27.6691)**5 - 0.1532033*(T-27.6691)**6
h_g = 577302.07 - 4284.432*T - 1084.1238*(T-27.6691)**2
        - 73.011186*(T-27.6691)**3 - 15.407809*(T-27.6691)**4
        - 2.9987887*(T-27.6691)**5 - 0.2022147*(T-27.6691)**6
c_vg = 1/(0.0002214 - 2.8943e-6*T - 1.7113e-7*(T-27.6691)**2
        - 1.1894e-8*(T-27.6691)**3 - 1.9205e-9*(T-27.6691)**4
        - 1.244e-10*(T-27.6691)**5)
c_pg = np.e**(6.445199 + 0.1249361*T + 0.0125811*(T-27.6691)**2
        + 0.0027137*(T-27.6691)**3 + 0.0006249*(T-27.6691)**4
        + 4.8352e-5*(T-27.6691)**5)
visc_g = 1/(1582670.2 - 34545.242*T - 211.73722*(T-27.6691)**2
        - 283.70972*(T-27.6691)**3 - 18.848797*(T-27.6691)**4)
k_g = 1/(110.21937 - 2.6596443*T - 0.0153377*(T-27.6691)**2
        - 0.0088632*(T-27.6691)**3)
```

E.6 Saturated Fluid Property Equations

```
"""
Equations of saturated gh2 and lh2 properties.
Equations are based on data obtained from NIST chemistry webbook for
saturated thermophysical properties of hydrogen.
Fits were made in JMP software for the range of T = 20.369 K - 32 K.
A note on units:
mass [kg]
vol [m^3]
density [kg/m^3]
pressure [Pa]
temp [K]
energy [J]
specific heats [J/kg]
viscosity [Pa-s]
themal conductivity [W/m-K]
"""
import numpy as np

# Pressure as a function of temp
P = 0.0138 * T**5.2644

# Temperature based on pressure increments
T = 22.509518 + 9.5791e-6*P - 5.85e-12*(P-598825)**2
    + 3.292e-18*(P-598825)**3 - 1.246e-24*(P-598825)**4
    + 2.053e-29*(P-598825)**5 - 3.463e-35*(P-598825)**6

# lh2 properties as a function of T
rho_l = 115.53291 - 2.0067591*T - 0.1067411*(T-27.6691)**2
        - 0.0085915*(T-27.6691)**3 - 0.0019879*(T-27.6691)**4
        - 0.0003988*(T-27.6691)**5 - 2.7179e-5*(T-27.6691)**6
u_l = -334268 + 15183.043*T + 614.10133*(T-27.6691)**2
        + 40.845478*(T-27.6691)**3 + 9.1394916*(T-27.6691)**4
        + 1.8297788*(T-27.6691)**5 + 0.1246228*(T-27.6691)**6
h_l = -371985.2 + 16864.749*T + 893.59208*(T-27.6691)**2
        + 103.63758*(T-27.6691)**3 + 7.756004*(T-27.6691)**4
c_vl = 4138.1395 + 72.04929*T + 3.6470929*(T-27.6691)**2
        + 1.5258739*(T-27.6691)**3 + 0.3466932*(T-27.6691)**4
        + 0.026033*(T-27.6691)**5
c_pl = 1/(0.0002684 - 7.6143e-6*T - 2.5759e-7*(T-27.6691)**2)
visc_l = 2.367e-5 - 5.7263e-7*T + 6.9609e-9*(T-27.6691)**2
        - 2.4303e-9*(T-27.6691)**3
k_l = 0.1575097 - 0.0020718*T - 0.0002477*(T-27.6691)**2
        - 1.762e-5*(T-27.6691)**3 - 1.8652e-6*(T-27.6691)**4
beta_l = np.e**(-6.185192 + 0.1016509*T + 0.0068955*(T-23.0338)**2
        + 0.0006315*(T-23.0338)**3)
h_vapl = 643518.5 - 9414.2796*T - 864.42293*(T-23.0338)**2
        - 42.793416*(T-23.0338)**3 - 4.8186135*(T-23.0338)**4
        - 0.0982576*(T-23.0338)**5

# gh2 properties as a function of T
rho_g = -28.97599 + 1.2864736*T + 0.1140157*(T-27.6691)**2
        + 0.0086723*(T-27.6691)**3 + 0.0019006*(T-27.6691)**4
```

```
        + 0.0003805*(T-27.6691)**5 + 2.5918e-5*(T-27.6691)**6
u_g = 466116.69 - 3220.3735*T - 748.772*(T-27.6691)**2
        - 53.773598*(T-27.6691)**3 - 11.581018*(T-27.6691)**4
        - 2.2673071*(T-27.6691)**5 - 0.1532033*(T-27.6691)**6
h_g = 577302.07 - 4284.432*T - 1084.1238*(T-27.6691)**2
        - 73.011186*(T-27.6691)**3 - 15.407809*(T-27.6691)**4
        - 2.9987887*(T-27.6691)**5 - 0.2022147*(T-27.6691)**6
c_vg = 1/(0.0002214 - 2.8943e-6*T - 1.7113e-7*(T-27.6691)**2
        - 1.1894e-8*(T-27.6691)**3 - 1.9205e-9*(T-27.6691)**4
        - 1.244e-10*(T-27.6691)**5)
c_pg = np.e**(6.445199 + 0.1249361*T + 0.0125811*(T-27.6691)**2
        + 0.0027137*(T-27.6691)**3 + 0.0006249*(T-27.6691)**4
        + 4.8352e-5*(T-27.6691)**5)
visc_g = 1/(1582670.2 - 34545.242*T - 211.73722*(T-27.6691)**2
        - 283.70972*(T-27.6691)**3 - 18.848797*(T-27.6691)**4)
k_g = 1/(110.21937 - 2.6596443*T - 0.0153377*(T-27.6691)**2
        - 0.0088632*(T-27.6691)**3)
```

E.7 Real Gas Property Equations

```
from numpy import tanh
import numpy as np

def c_v(indata, outdata):
    # specific heat @ constant vol. [J/g-K]

    _temp_0 = 56.0992565764207

    H1_1 = tanh((0.3990654435825 + 0.275976950953691
            * indata[u"Pressure (MPa)"]
            + -0.0364541001467881 * indata[u"Temperature (K)"]))
    H1_2 = tanh((-4.86826687998567 + -2.62940079620686
            * indata[u"Pressure (MPa)"]
            + 0.216404289884235 * indata[u"Temperature (K)"]))
    H1_3 = tanh((1.12548975067467 + 0.269571399186571
            * indata[u"Pressure (MPa)"]
            + -0.0349250996335972 * indata[u"Temperature (K)"]))
    H1_4 = tanh((-5.57528770123298 + -3.1347851189393
            * indata[u"Pressure (MPa)"]
            + 0.276378205247149 * indata[u"Temperature (K)"]))
    H1_5 = tanh((-0.768555052808218 + -0.415187001771689
            * indata[u"Pressure (MPa)"]
            + 0.0303660811195935 * indata[u"Temperature (K)"]))
    H1_6 = tanh((0.271020942398391 + -1.67288064390926
            * indata[u"Pressure (MPa)"]
            + 0.0673489649704582 * indata[u"Temperature (K)"]))
    H1_7 = tanh((-1.10142968268782 + 0.0083174017874869
            * indata[u"Pressure (MPa)"]
            + 0.0108662672630239 * indata[u"Temperature (K)"]))
    H1_8 = tanh((1.90064900956529 + 1.17456681024276
            * indata[u"Pressure (MPa)"]
            + -0.0902336799991085 * indata[u"Temperature (K)"]))
    H1_9 = tanh((-0.673064219823259 + -0.943525497821755
            * indata[u"Pressure (MPa)"]
            + 0.0734160926798799 * indata[u"Temperature (K)"]))
    H1_10 = tanh((-1.6061497898911 + -1.99739736255923
            * indata[u"Pressure (MPa)"]
            + 0.108199114343877 * indata[u"Temperature (K)"]))
    H1_11 = tanh((1.73534543350612 + 0.388202467775416
            * indata[u"Pressure (MPa)"]
            + -0.0616088045146524 * indata[u"Temperature (K)"]))
    H1_12 = tanh((2.70166390032434 + 1.3326759135354
            * indata[u"Pressure (MPa)"]
            + -0.118211564739528 * indata[u"Temperature (K)"]))
    H1_13 = tanh((-9.32984593347698 + 9.42488755971789
            * indata[u"Pressure (MPa)"]
            + 0.0784916020511085 * indata[u"Temperature (K)"]))
    H1_14 = tanh((1.2207418073194 + 1.13189377766378
            * indata[u"Pressure (MPa)"]
            + -0.0841043542652104 * indata[u"Temperature (K)"]))
    H1_15 = tanh((2.58665026763982 + 1.84291010959674
            * indata[u"Pressure (MPa)"]
```

```
            + -0.13970364770731 * indata[u"Temperature (K)"]))

    _temp_0 += -70.3037835837473 * H1_1
    _temp_0 += -12.804152874995 * H1_10
    _temp_0 += 8.56885046215908 * H1_11
    _temp_0 += 16.8828056394326 * H1_12
    _temp_0 += 0.000773883721821057 * H1_13
    _temp_0 += -11.6665802642623 * H1_14
    _temp_0 += -43.8044401310621 * H1_15
    _temp_0 += -3.65980723192549 * H1_2
    _temp_0 += 16.4087880702894 * H1_3
    _temp_0 += -3.5451526649205 * H1_4
    _temp_0 += 1.59237668513045 * H1_5
    _temp_0 += 16.3356631788945 * H1_6
    _temp_0 += 2.87332235554376 * H1_7
    _temp_0 += -32.0695317395356 * H1_8
    _temp_0 += -162.92972771138 * H1_9
    outdata[u"Predicted Cv (J/g*K)"] = _temp_0

    return outdata[u"Predicted Cv (J/g*K)"]


def c_p(indata, outdata):
    # specific heat @ constant pressure [J/g-K]

    _temp_0 = -163.178217071559

    H1_1 = tanh((0.614735260887242 + 1.13159708689763
            * indata[u"Pressure (MPa)"] + -0.0551837204578247
            * indata[u"Temperature (K)"]))
    H1_2 = tanh((-0.400739830511314 + -0.0140493655427582
            * indata[u"Pressure (MPa)"] + -0.000581742517018706
            * indata[u"Temperature (K)"]))
    H1_3 = tanh((-1.25439265281633 + -0.584213145968296
            * indata[u"Pressure (MPa)"] + 0.100382842687856
            * indata[u"Temperature (K)"]))
    H1_4 = tanh((0.613718515601412 + 1.1389617257106
            * indata[u"Pressure (MPa)"] + -0.0766902288518594
            * indata[u"Temperature (K)"]))
    H1_5 = tanh((0.783863063691068 + 1.12786935775064
            * indata[u"Pressure (MPa)"] + -0.0580710892849312
            * indata[u"Temperature (K)"]))
    H1_6 = tanh((3.0862845706326 + 6.11836677910538
            * indata[u"Pressure (MPa)"] + -0.28171194186548
            * indata[u"Temperature (K)"]))
    H1_7 = tanh((-4.01267608558022 + -1.74531315193444
            * indata[u"Pressure (MPa)"] + 0.13245397217098
            * indata[u"Temperature (K)"]))
    H1_8 = tanh((-4.73597371609159 + -2.69493649415449
            * indata[u"Pressure (MPa)"] + 0.241924487447467
            * indata[u"Temperature (K)"]))
    H1_9 = tanh((-3.13544345816356 + -2.55750416599446
            * indata[u"Pressure (MPa)"] + 0.149566251986045
            * indata[u"Temperature (K)"]))
```

```
    H1_10 = tanh((-3.57473472514032 + -4.95468689159338
            * indata[u"Pressure (MPa)"] + 0.281591654527403
            * indata[u"Temperature (K)"]))
    H1_11 = tanh((4.41722437760112 + 3.38001091079686
            * indata[u"Pressure (MPa)"] + -0.242556425504075
            * indata[u"Temperature (K)"]))
    H1_12 = tanh((-0.398001325855848 + 0.0072937040171696
            * indata[u"Pressure (MPa)"] + 0.000277104672759379
            * indata[u"Temperature (K)"]))
    H1_13 = tanh((-0.31379942783082 + 0.576128323850331
            * indata[u"Pressure (MPa)"] + 0.0347928080405698
            * indata[u"Temperature (K)"]))
    H1_14 = tanh((7.34692537702712 + 1.16723768888899
            * indata[u"Pressure (MPa)"] + -0.317917699002537
            * indata[u"Temperature (K)"]))
    H1_15 = tanh((-0.816554474050802 + 0.784988883943678
            * indata[u"Pressure (MPa)"] + 0.0377876586456731
            * indata[u"Temperature (K)"]))

    _temp_0 += 346.455492384544 * H1_1
    _temp_0 += -131.305889878852 * H1_10
    _temp_0 += -87.5906286526561 * H1_11
    _temp_0 += -881.40560167543 * H1_12
    _temp_0 += -87.1001293092837 * H1_13
    _temp_0 += -2.24612605221145 * H1_14
    _temp_0 += 40.3225563600741 * H1_15
    _temp_0 += -521.915978427339 * H1_2
    _temp_0 += 137.870380603119 * H1_3
    _temp_0 += 452.163820434345 * H1_4
    _temp_0 += -374.519768532003 * H1_5
    _temp_0 += -41.7239727718235 * H1_6
    _temp_0 += 2.51241979089427 * H1_7
    _temp_0 += -55.4472053157707 * H1_8
    _temp_0 += 23.7176680036494 * H1_9
    outdata[u"Predicted Cp (J/g*K)"] = _temp_0

    return outdata[u"Predicted Cp (J/g*K)"]


def u(indata, outdata):
    # internal energy [kJ/kg]

    _temp_0 = 673.611983193655

    H1_1 = tanh((0.233539747755315 + 0.948951297504785
            * indata[u"Pressure (MPa)"] + -0.0499745330828293
            * indata[u"Temperature (K)"]))
    H1_2 = tanh((2.05471470504367 + 2.13093505892378
            * indata[u"Pressure (MPa)"] + -0.119572061260962
            * indata[u"Temperature (K)"]))
    H1_3 = tanh((0.398892133197 + 0.587703772663913
            * indata[u"Pressure (MPa)"] + -0.00336363426965824
            * indata[u"Temperature (K)"]))
    H1_4 = tanh((0.143237719165029 + 0.992347038797521
```

```
        * indata[u"Pressure (MPa)"] + -0.0143964824374372
        * indata[u"Temperature (K)"]))
H1_5 = tanh((-3.96616131435837 + -2.74657042229242
        * indata[u"Pressure (MPa)"] + 0.186453818992668
        * indata[u"Temperature (K)"]))
H1_6 = tanh((1.44405264544866 + -0.645489048931109
        * indata[u"Pressure (MPa)"] + -0.0104476083443945
        * indata[u"Temperature (K)"]))
H1_7 = tanh((2.02006732389655 + 3.10126879273836
        * indata[u"Pressure (MPa)"] + -0.132381179154892
        * indata[u"Temperature (K)"]))
H1_8 = tanh((0.455915191247191 + -0.295895155010423
        * indata[u"Pressure (MPa)"] + -0.00270733720731719
        * indata[u"Temperature (K)"]))
H1_9 = tanh((-1.42121486333193 + 0.135982980631872
        * indata[u"Pressure (MPa)"] + 0.0473542542463267
        * indata[u"Temperature (K)"]))
H1_10 = tanh((-0.662630708916202 + -0.206113999100671
        * indata[u"Pressure (MPa)"] + 0.00414455453741901
        * indata[u"Temperature (K)"]))
H1_11 = tanh((0.56740916395517 + 1.67371525829477
        * indata[u"Pressure (MPa)"] + -0.0218895513528701
        * indata[u"Temperature (K)"]))
H1_12 = tanh((0.237517777100042 + 0.1589500143037
        * indata[u"Pressure (MPa)"] + -0.0106519272801902
        * indata[u"Temperature (K)"]))
H1_13 = tanh((1.54182270996619 + 0.754447306182754
        * indata[u"Pressure (MPa)"] + -0.0541064232047049
        * indata[u"Temperature (K)"]))
H1_14 = tanh((2.62921984539398 + 1.72079624611917
        * indata[u"Pressure (MPa)"] + -0.0971068814297633
        * indata[u"Temperature (K)"]))
H1_15 = tanh((-1.04212680836281 + -0.484939056845666
        * indata[u"Pressure (MPa)"] + 0.0116518536560464
        * indata[u"Temperature (K)"]))

_temp_0 += -1446.64509367172 * H1_1
_temp_0 += 1174.42287038803 * H1_10
_temp_0 += 26.0663709626282 * H1_11
_temp_0 += 478.510727358678 * H1_12
_temp_0 += 213.76235040309 * H1_13
_temp_0 += 47.1707429768787 * H1_14
_temp_0 += -14.8049823561287 * H1_15
_temp_0 += 399.518468943879 * H1_2
_temp_0 += -333.71693491459 * H1_3
_temp_0 += -228.44619912214 * H1_4
_temp_0 += 30.515033222315 * H1_5
_temp_0 += 74.6722187603707 * H1_6
_temp_0 += -58.2024392498572 * H1_7
_temp_0 += -1594.44683837146 * H1_8
_temp_0 += 69.542870910495 * H1_9
outdata[u"Predicted Internal Energy (kJ/kg)"] = _temp_0

return outdata[u"Predicted Internal Energy (kJ/kg)"]
```

```
def h(indata, outdata):
    # enthalpy [kJ/kg]

    _temp_0 = 1281.75444728572

    H1_1 = tanh((1.73579390297524 + -0.511704824190866
            * indata[u"Pressure (MPa)"] + -0.00328063298246929
            * indata[u"Temperature (K)"]))
    H1_2 = tanh((-0.17506458742044 + -0.0787067450602815
            * indata[u"Pressure (MPa)"] + 0.0043943295092826
            * indata[u"Temperature (K)"]))
    H1_3 = tanh((-1.49793344088779 + -2.75869130445277
            * indata[u"Pressure (MPa)"] + 0.110698824574587
            * indata[u"Temperature (K)"]))
    H1_4 = tanh((-1.37669485784553 + 0.133730746273731
            * indata[u"Pressure (MPa)"] + 0.00649135107315252
            * indata[u"Temperature (K)"]))
    H1_5 = tanh((-1.1405914153055 + -1.88672855275111
            * indata[u"Pressure (MPa)"] + 0.0981301522587858
            * indata[u"Temperature (K)"]))
    H1_6 = tanh((0.446124093572671 + 0.429585607469454
            * indata[u"Pressure (MPa)"] + -0.0285787427235227
            * indata[u"Temperature (K)"]))
    H1_7 = tanh((-2.49683893292792 + 0.398927054757526
            * indata[u"Pressure (MPa)"] + 0.0128111795517157
            * indata[u"Temperature (K)"]))
    H1_8 = tanh((-1.34037612046496 + -1.82172820931808
        * indata[u"Pressure (MPa)"] + 0.0975510622080853
        * indata[u"Temperature (K)"]))
    H1_9 = tanh((-0.00454329936396595 + -0.0840846337708169
        * indata[u"Pressure (MPa)"] + 0.00192700682148055
        * indata[u"Temperature (K)"]))
    H1_10 = tanh((3.25989647210865 + -0.817575328835318
        * indata[u"Pressure (MPa)"] + -0.00790145526484188
        * indata[u"Temperature (K)"]))
    H1_11 = tanh((1.2138688950769 + -5.5187467484401
        * indata[u"Pressure (MPa)"] + 0.115937604475061
        * indata[u"Temperature (K)"]))
    H1_12 = tanh((-4.2841473959043 + -3.44784008416792
        * indata[u"Pressure (MPa)"] + 0.225314720754115
        * indata[u"Temperature (K)"]))
    H1_13 = tanh((-0.749714454876193 + 0.59904718534549
        * indata[u"Pressure (MPa)"] + 0.015852118328226
        * indata[u"Temperature (K)"]))
    H1_14 = tanh((-3.56659915773571 + -3.26552973737454
        * indata[u"Pressure (MPa)"] + 0.201884080139387
        * indata[u"Temperature (K)"]))
    H1_15 = tanh((-0.368559368031245 + -4.14838409559996
        * indata[u"Pressure (MPa)"] + 0.1417710518596
        * indata[u"Temperature (K)"]))

    _temp_0 += -245.023690422356 * H1_1
```

```
_temp_0 += 143.039857861931 * H1_10
_temp_0 += 57.936905487342 * H1_11
_temp_0 += 141.765833322109 * H1_12
_temp_0 += 91.6603988756128 * H1_13
_temp_0 += -354.856864121115 * H1_14
_temp_0 += -407.462486717321 * H1_15
_temp_0 += -762.587308746834 * H1_2
_temp_0 += -117.086388339974 * H1_3
_temp_0 += 2084.0234411658 * H1_4
_temp_0 += 3494.85395981366 * H1_5
_temp_0 += -79.8462693619194 * H1_6
_temp_0 += -257.346057454727 * H1_7
_temp_0 += -2180.32225879755 * H1_8
_temp_0 += 3232.88193434466 * H1_9
outdata[u"Predicted Enthalpy (kJ/kg)"] = _temp_0

return outdata[u"Predicted Enthalpy (kJ/kg)"]
```

APPENDIX F

TEMPERATURE DISTRIBUTION AND TRANSDUCER LOCATIONS FOR THE 23 CM DIAMETER SPHERICAL TANK

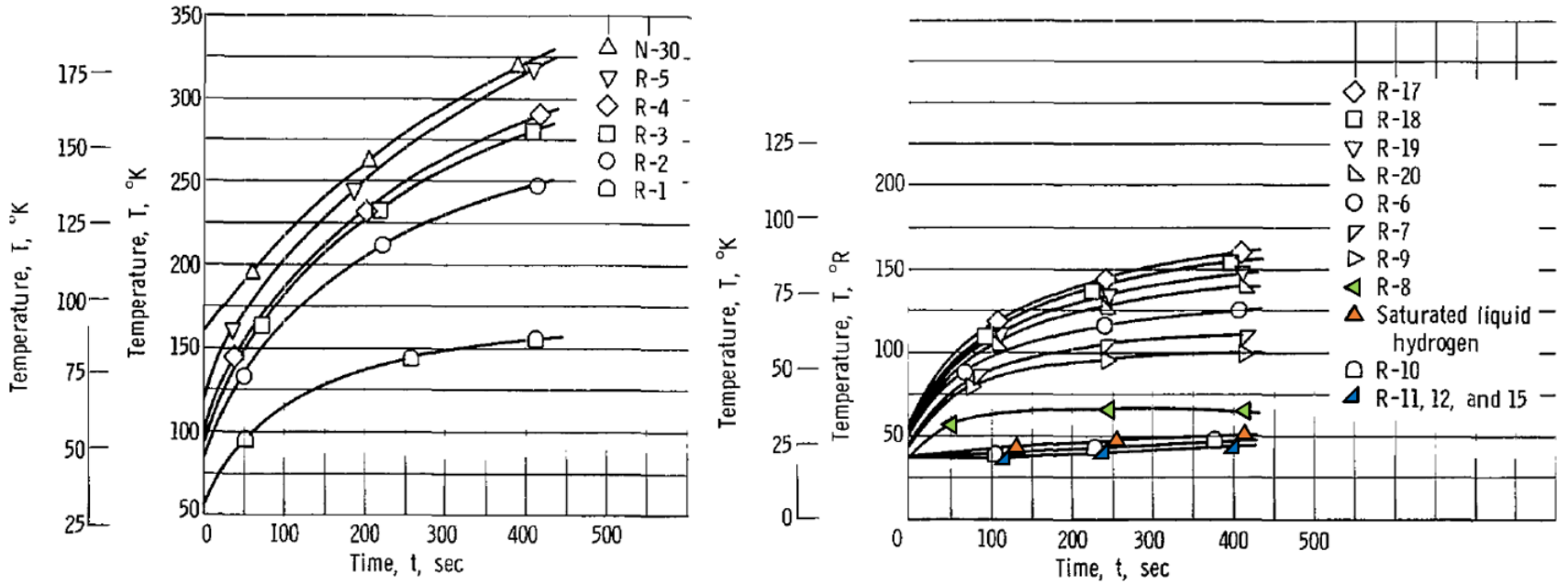

Figure F.1: Test 3 temperature distribution in the upper (left) and lower (right) halves of the tank [5]. Temperature measurements corresponding to the ullage gas near the interface, the interface, and the coldest portion of the bulk liquid are indicated by the green, orange, and blue markers, respectively.

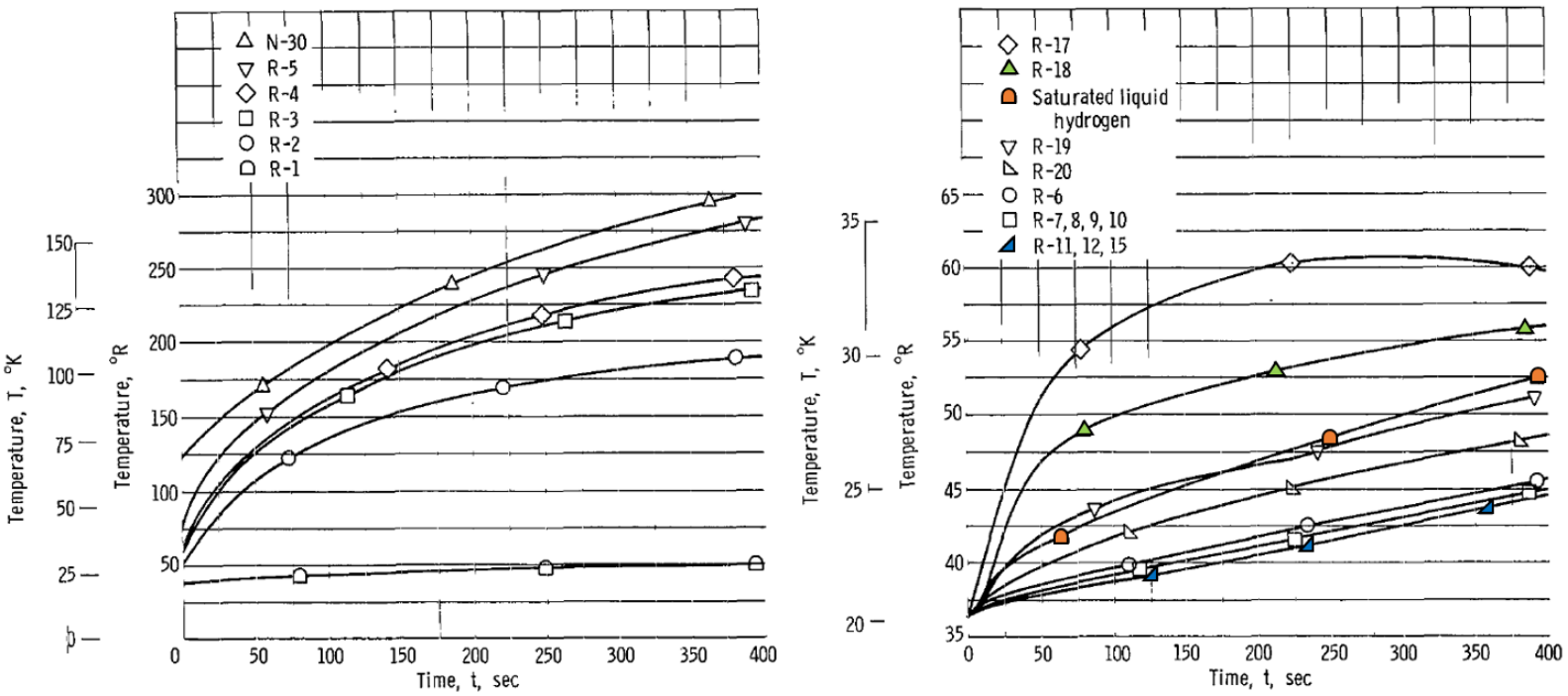

Figure F.2: Test 4 temperature distribution in the upper (left) and lower (right) halves of the tank [5]. Temperature measurements corresponding to the ullage gas near the interface, the interface, and the coldest portion of the bulk liquid are indicated by the green, orange, and blue markers, respectively.

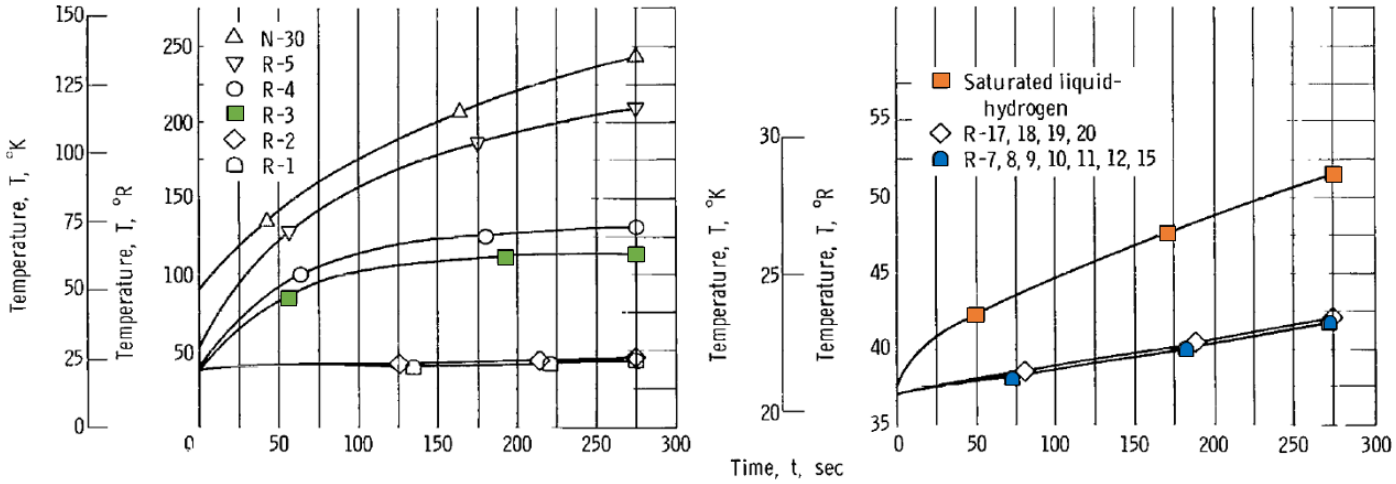

Figure F.3: Test 5 temperature distribution in the upper (left) and lower (right) halves of the tank [5]. Temperature measurements corresponding to the ullage gas near the interface, the interface, and the coldest portion of the bulk liquid are indicated by the green, orange, and blue markers, respectively.

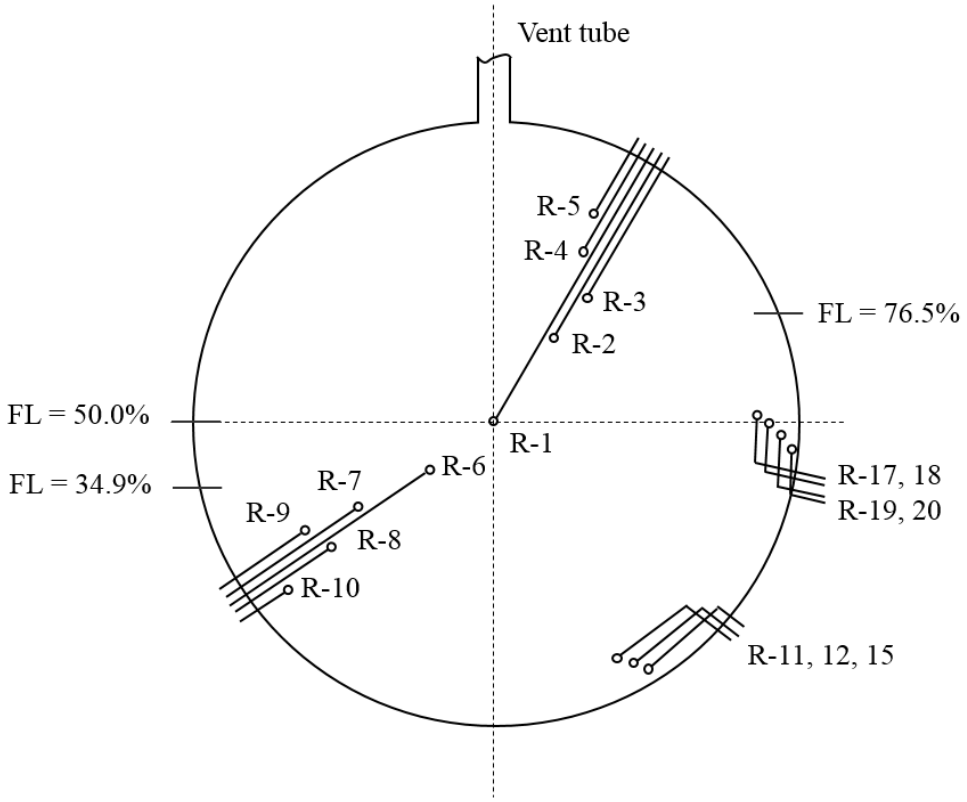

Figure F.4: Temperature transducer locations for the Aydelott tank [5].

APPENDIX G

TEMPERATURE TRANSDUCER LOCATIONS FOR THE MHTB TANK

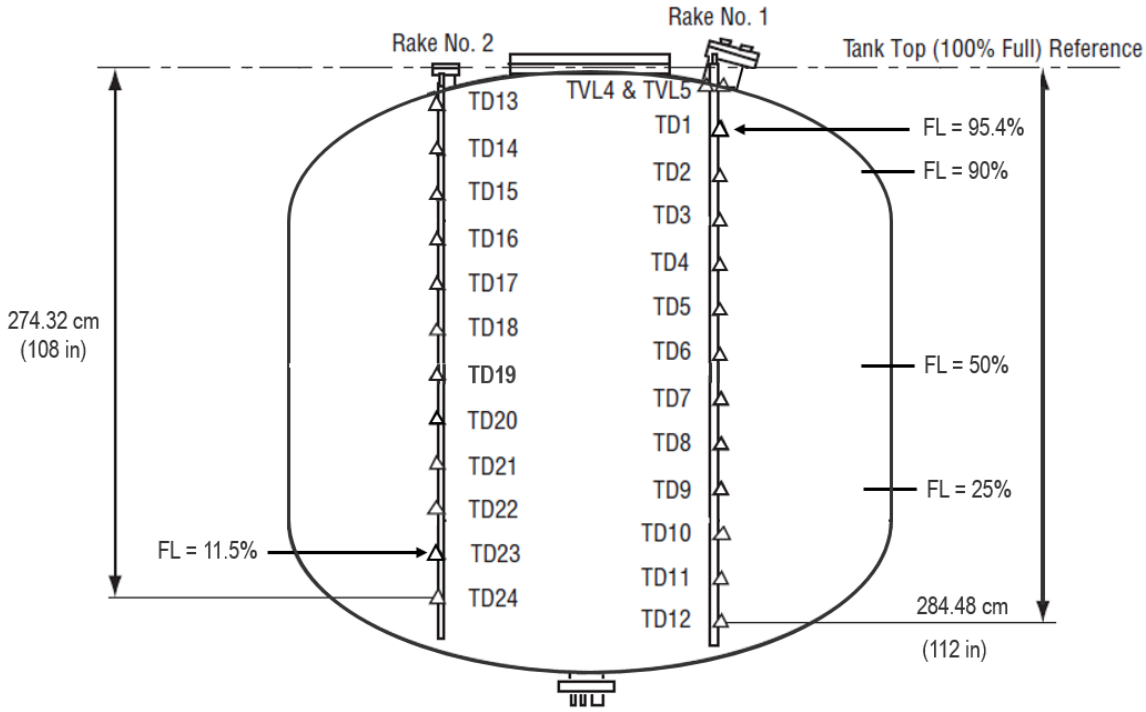

Figure G.1: Temperature transducer locations for the MHTB tank [72]. Transducers in each rake are spaced at intervals of 22.86cm (9 in) apart.

APPENDIX H

NEURAL NETWORK FITS

H.1 Theoretical Model

Training	
Total Propellant Mass (kg)	
Measures	**Value**
RSquare	0.9999402
RMSE	16.260959
Mean Abs Dev	9.8362902
-LogLikelihood	47917.352
SSE	3011201.3
Sum Freq	11388
LH2 Boil-Off (kg)	
Measures	**Value**
RSquare	0.9999982
RMSE	1.0787163
Mean Abs Dev	0.6064652
-LogLikelihood	17021.76
SSE	13251.405
Sum Freq	11388
Total Vehicle Mass (kg)	
Measures	**Value**
RSquare	0.9998768
RMSE	27.684784
Mean Abs Dev	15.948441
-LogLikelihood	53977.087
SSE	8728301.6
Sum Freq	11388
Stage Diameter (m)	
Measures	**Value**
RSquare	0.999996
RMSE	0.0019447
Mean Abs Dev	0.0011047
-LogLikelihood	-54932.37
SSE	0.0430681
Sum Freq	11388
LH2 Mass (kg)	
Measures	**Value**
RSquare	0.9999912
RMSE	2.6536942
Mean Abs Dev	1.5777513
-LogLikelihood	27273.021
SSE	80195.354
Sum Freq	11388
Tank Height (m)	
Measures	**Value**
RSquare	0.9999991
RMSE	0.0017639
Mean Abs Dev	0.001091
-LogLikelihood	-56043.41
SSE	0.0354335
Sum Freq	11388

Validation	
Total Propellant Mass (kg)	
Measures	**Value**
RSquare	0.9999367
RMSE	16.576798
Mean Abs Dev	10.229521
-LogLikelihood	2531.9386
SSE	164599.35
Sum Freq	599
LH2 Boil-Off (kg)	
Measures	**Value**
RSquare	0.9999986
RMSE	0.9646998
Mean Abs Dev	0.6296175
-LogLikelihood	828.41713
SSE	557.45677
Sum Freq	599
Total Vehicle Mass (kg)	
Measures	**Value**
RSquare	0.9998261
RMSE	32.569853
Mean Abs Dev	17.609218
-LogLikelihood	2936.4931
SSE	635416.4
Sum Freq	599
Stage Diameter (m)	
Measures	**Value**
RSquare	0.9999955
RMSE	0.0020536
Mean Abs Dev	0.0011833
-LogLikelihood	-2856.757
SSE	0.0025262
Sum Freq	599
LH2 Mass (kg)	
Measures	**Value**
RSquare	0.9999898
RMSE	2.8689055
Mean Abs Dev	1.7421339
-LogLikelihood	1481.2486
SSE	4930.1406
Sum Freq	599
Tank Height (m)	
Measures	**Value**
RSquare	0.9999991
RMSE	0.0018415
Mean Abs Dev	0.0011118
-LogLikelihood	-2922.078
SSE	0.0020312
Sum Freq	599

	Generalized RSquare	-LogLikelihood
Training	1.0000	35213.449
Validation	1.0000	1999.2617

Figure H.1: Predictive accuracy associated with the NN fit obtained for the descent stage of the HLS when sized using boil-off estimates from the theoretical model.

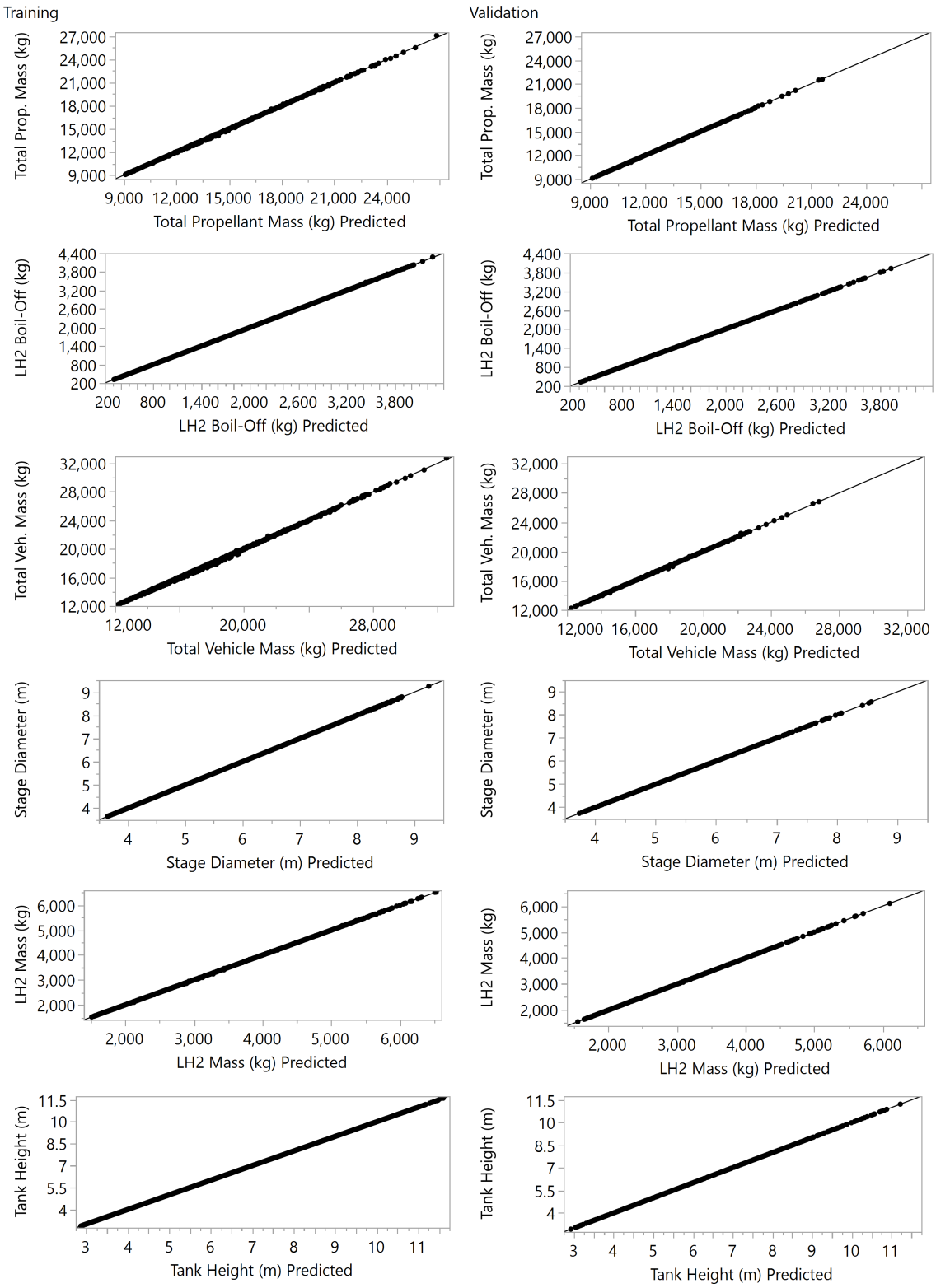

Figure H.2: Plot of actual versus predicted values predicted by the NN fit corresponding to the theoretical boil-off model.

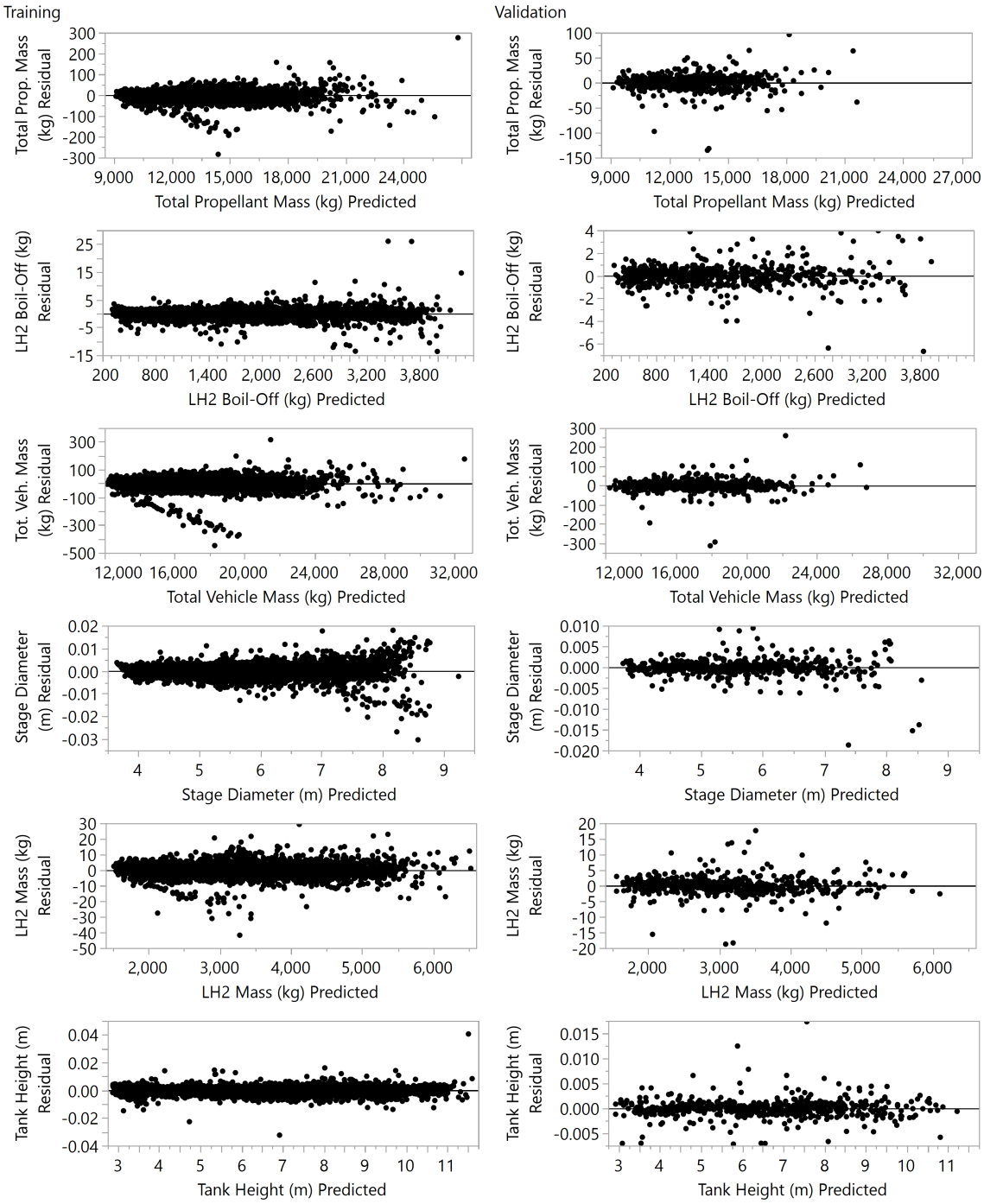

Figure H.3: Residual error associated with the predicted values from the NN fit corresponding to the theoretical boil-off model.

H.2 Extensible Boil-off Model

Training	
Total Propellant Mass (kg)	
Measures	**Value**
RSquare	0.999823
RMSE	24.060218
Mean Abs Dev	13.481071
-LogLikelihood	49761.972
SSE	6263055.3
Sum Freq	10819
LH2 Boil-Off (kg)	
Measures	**Value**
RSquare	0.9998255
RMSE	5.1749965
Mean Abs Dev	2.8270467
-LogLikelihood	33136.187
SSE	289739.19
Sum Freq	10819
Total Vehicle Mass (kg)	
Measures	**Value**
RSquare	0.9997539
RMSE	32.214973
Mean Abs Dev	18.656985
-LogLikelihood	52919.731
SSE	11228007
Sum Freq	10819
Stage Diameter (m)	
Measures	**Value**
RSquare	0.9999783
RMSE	0.004524
Mean Abs Dev	0.0025682
-LogLikelihood	-43053.27
SSE	0.2214309
Sum Freq	10819
LH2 Mass (kg)	
Measures	**Value**
RSquare	0.9998272
RMSE	6.0713616
Mean Abs Dev	3.3314455
-LogLikelihood	34864.459
SSE	398803.83
Sum Freq	10819
Tank Height (m)	
Measures	**Value**
RSquare	0.9999871
RMSE	0.0049415
Mean Abs Dev	0.0029034
-LogLikelihood	-42098.31
SSE	0.2641839
Sum Freq	10819

Validation	
Total Propellant Mass (kg)	
Measures	**Value**
RSquare	0.9998258
RMSE	23.72098
Mean Abs Dev	14.20729
-LogLikelihood	2609.0348
SSE	320167.71
Sum Freq	569
LH2 Boil-Off (kg)	
Measures	**Value**
RSquare	0.9998541
RMSE	4.8374615
Mean Abs Dev	2.7282175
-LogLikelihood	1704.342
SSE	13315.188
Sum Freq	569
Total Vehicle Mass (kg)	
Measures	**Value**
RSquare	0.9997758
RMSE	30.564721
Mean Abs Dev	18.279433
-LogLikelihood	2753.2686
SSE	531561.04
Sum Freq	569
Stage Diameter (m)	
Measures	**Value**
RSquare	0.999979
RMSE	0.0043574
Mean Abs Dev	0.002495
-LogLikelihood	-2285.637
SSE	0.0108036
Sum Freq	569
LH2 Mass (kg)	
Measures	**Value**
RSquare	0.9998366
RMSE	5.9804897
Mean Abs Dev	3.2843754
-LogLikelihood	1825.0339
SSE	20351
Sum Freq	569
Tank Height (m)	
Measures	**Value**
RSquare	0.9999884
RMSE	0.004727
Mean Abs Dev	0.0027633
-LogLikelihood	-2239.318
SSE	0.0127139
Sum Freq	569

	Generalized RSquare	-LogLikelihood
Training	1.0000	85530.767
Validation	1.0000	4366.7235

Figure H.4: Predictive accuracy associated with the NN fit obtained for the descent stage of the HLS when sized using boil-off estimates from the extensible boil-off model.

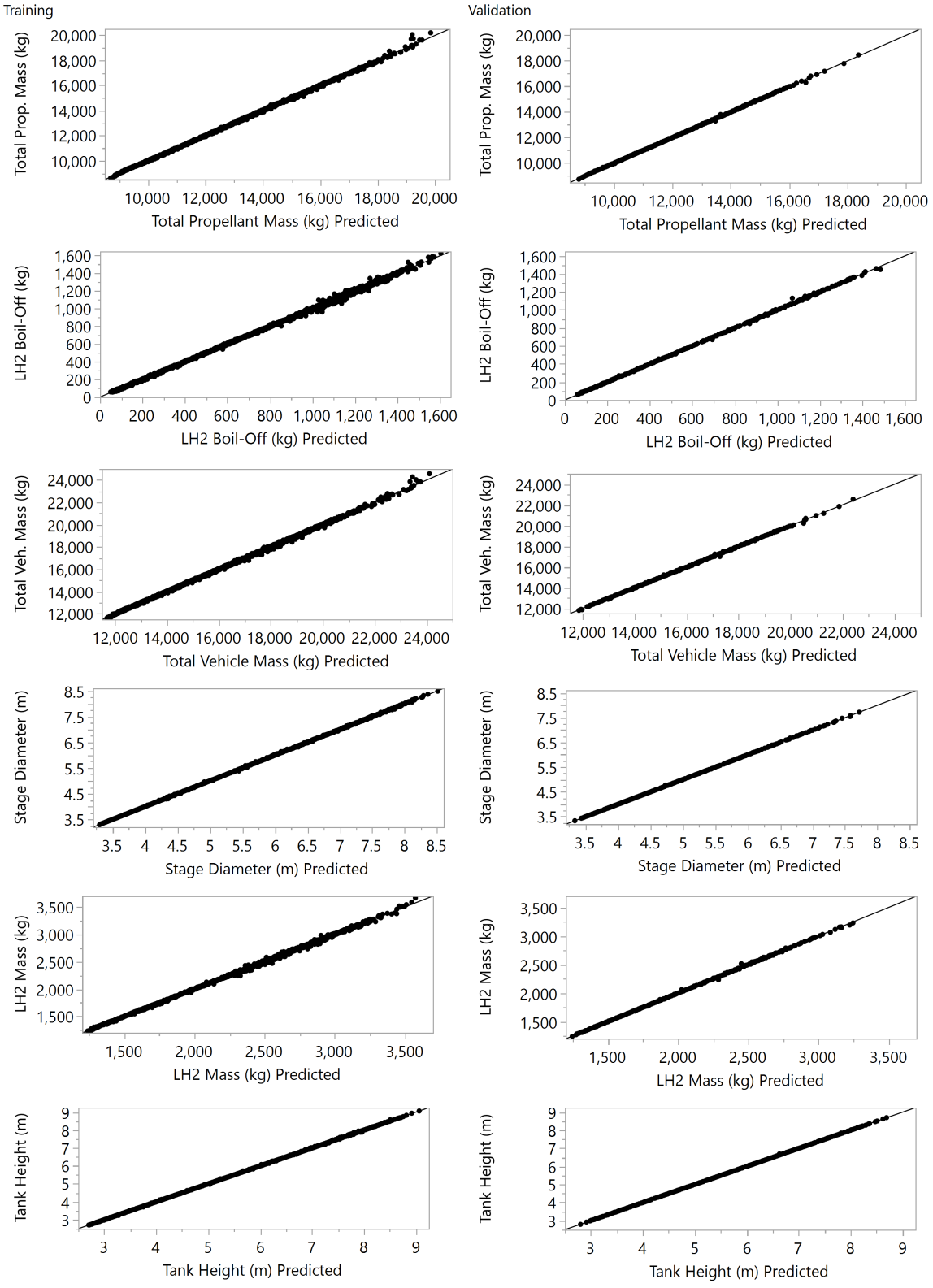

Figure H.5: Plot of actual versus predicted values predicted by the NN fit corresponding to the extensible boil-off model.

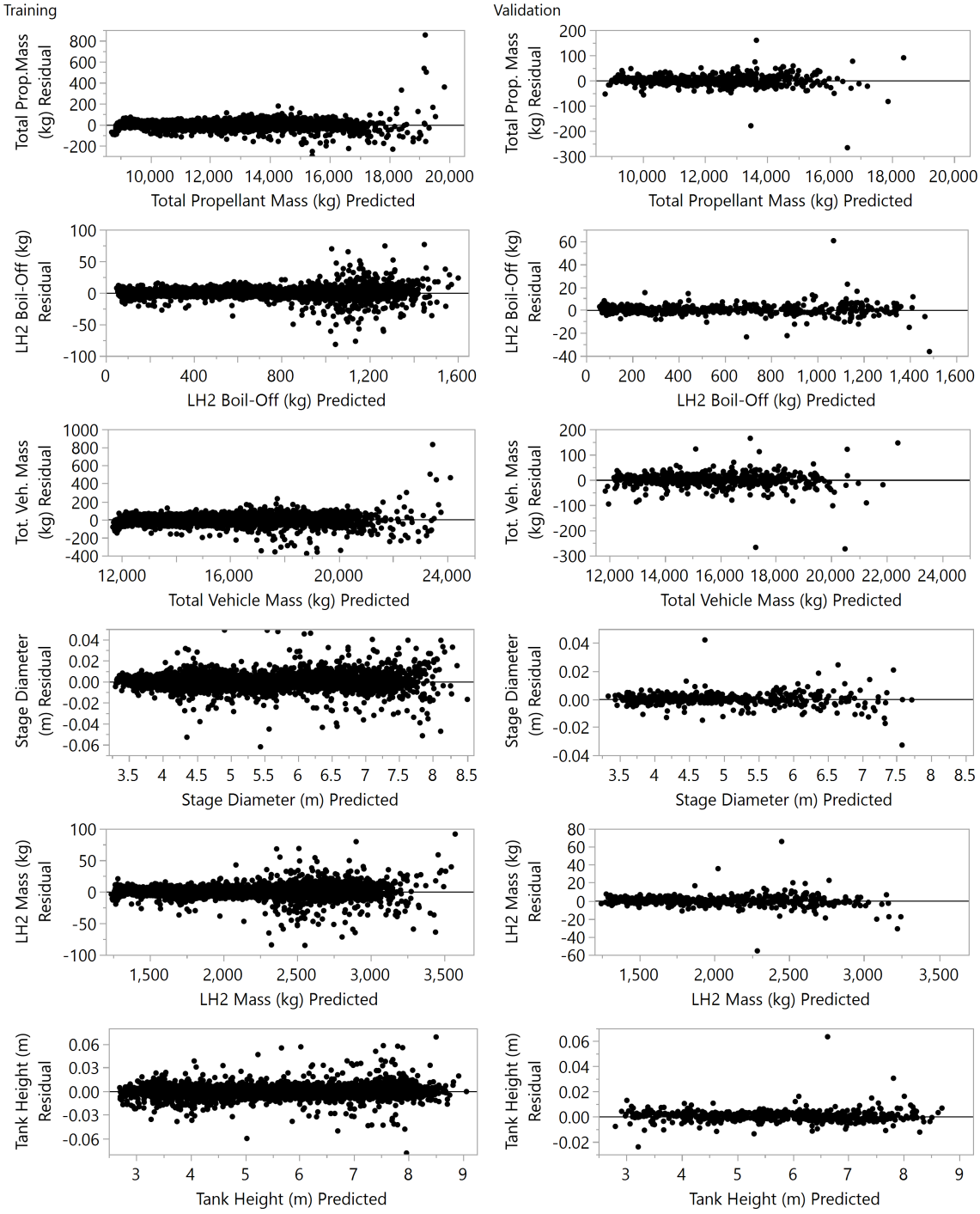

Figure H.6: Residual error associated with the predicted values from the NN fit corresponding to the extensible boil-off model.

APPENDIX I

VALIDATION CASES USING REAL GAS PROPERTIES WHEN CALCULATING THE HEAT TRANSFER COEFFICIENT

Aydelott Tank: Net Heat Transfer at the Interface

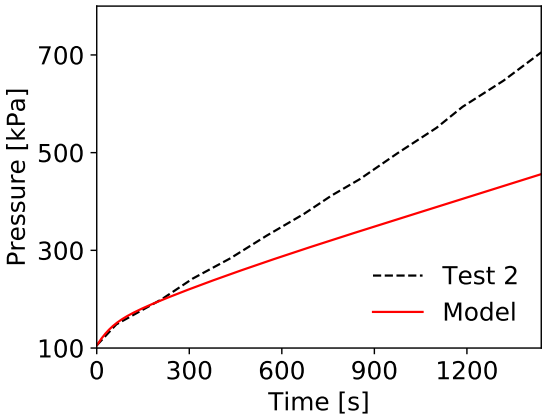

(a) FL = 51.4%, $\dot{Q}$ = 9.5 W

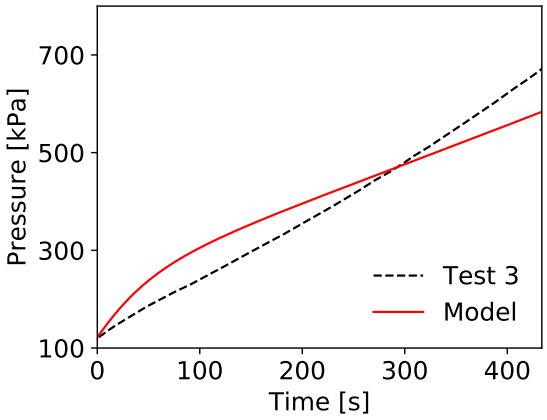

(b) FL = 34.9%, $\dot{Q}$ = 31.5 W

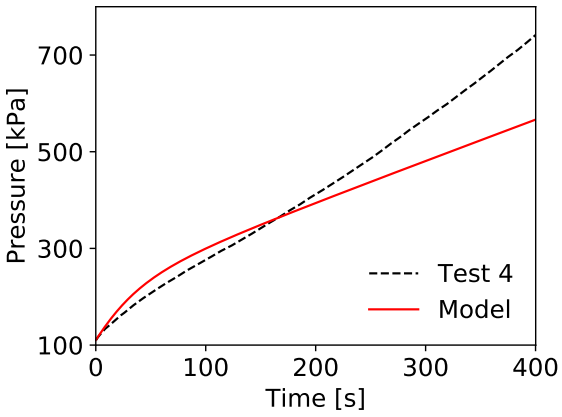

(c) FL = 48.9%, $\dot{Q}$ = 34.1 W

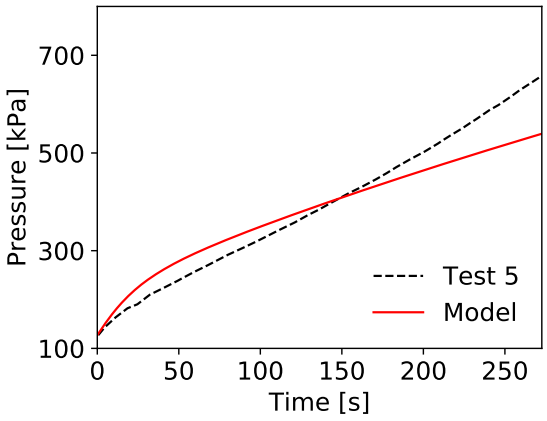

(d) FL = 76.5%, $\dot{Q}$ = 38.1 W

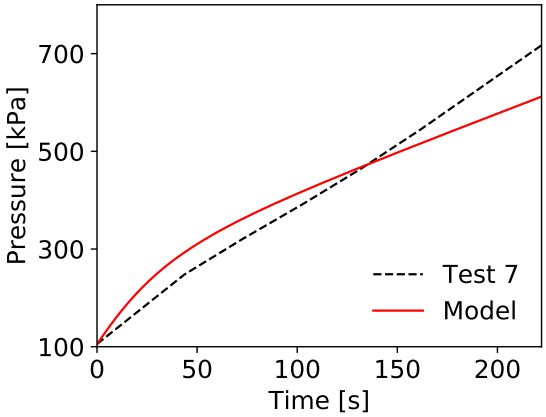

(e) FL = 50.7%, $\dot{Q}$ = 58.5 W

Figure I.1: Pressure values obtained from simulation (red) versus values obtained from literature (black) for self-pressurization in a 23 cm diameter spherical tank.

Aydelott Tank: Heat Transfer from Ullage to Interface

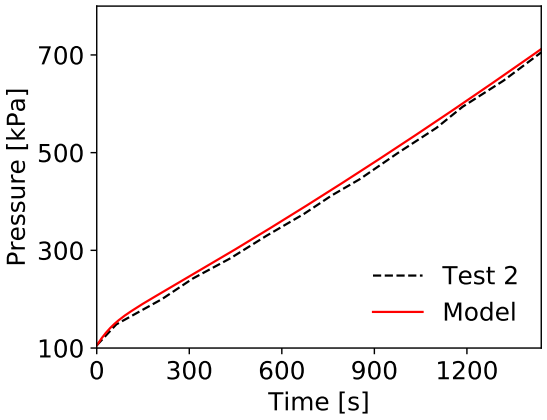

(a) FL = 51.4%, $\dot{Q}$ = 9.5 W

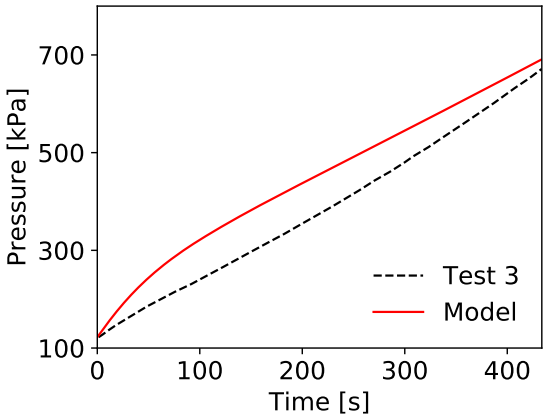

(b) FL = 34.9%, $\dot{Q}$ = 31.5 W

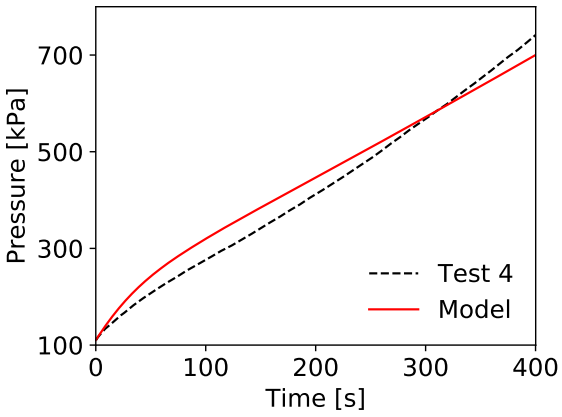

(c) FL = 48.9%, $\dot{Q}$ = 34.1 W

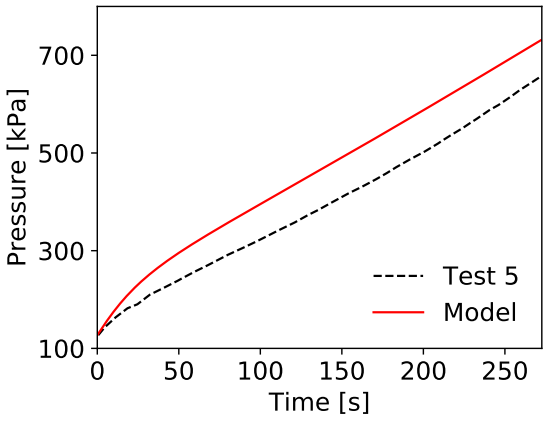

(d) FL = 76.5%, $\dot{Q}$ = 38.1 W

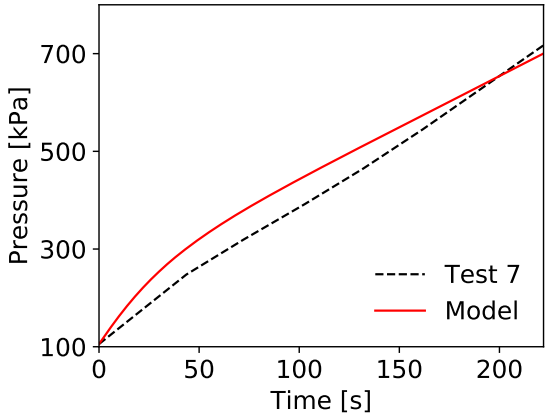

(e) FL = 50.7%, $\dot{Q}$ = 58.5 W

Figure I.2: Pressure values obtained from simulation (red) versus values obtained from literature (black) for self-pressurization in a 23 cm diameter spherical tank.

MHTB Tank: Net Heat Transfer at the Interface

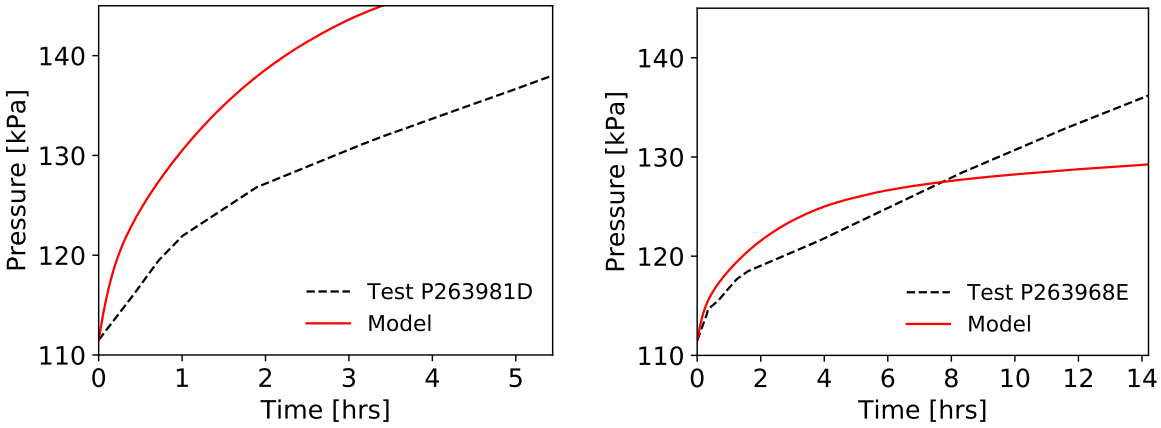

(a) FL = 90%, $\dot{Q}$ = 54.1 W/m^2

(b) FL = 90%, $\dot{Q}$ =20.2 W/m^2

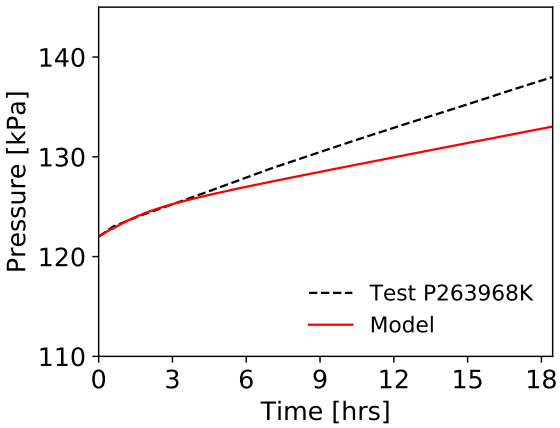

(c) FL = 25%, $\dot{Q}$ = 18.8 W

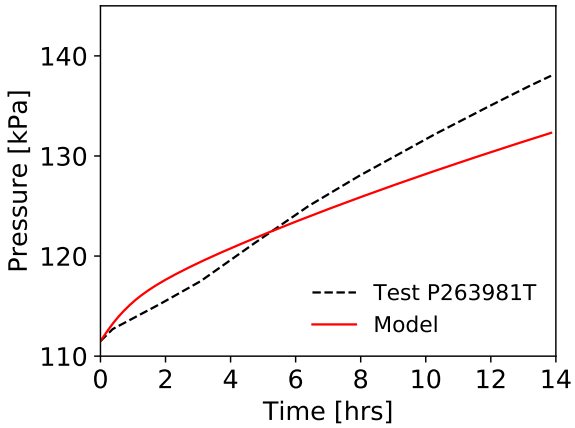

(d) FL = 50%, $\dot{Q}$ = 51.0 W/m^2

Figure I.3: Pressure values obtained from simulation (red) versus values obtained from literature (black) for self-pressurization in the MHT tank.

MHTB Tank: Heat Transfer from Ullage to Interface

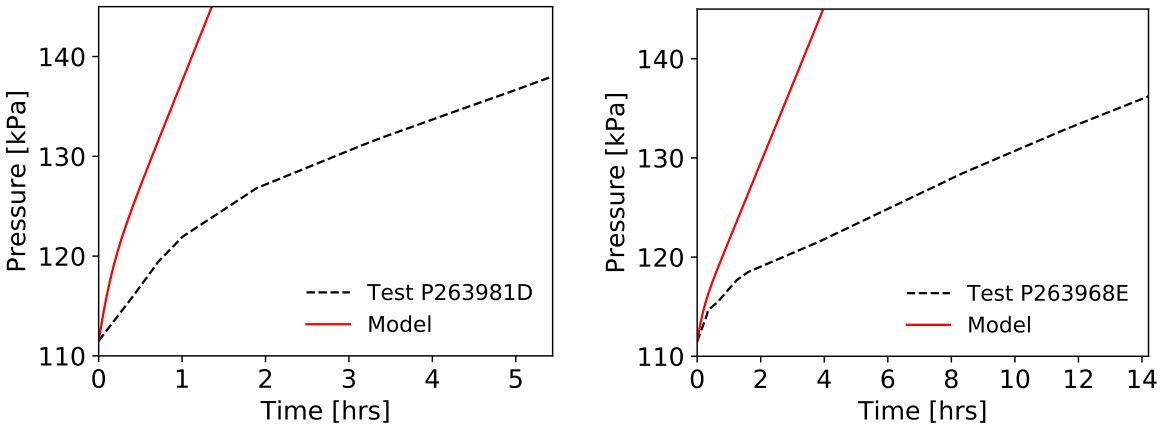

(a) FL = 90%, $\dot{Q}$ = 54.1 W/m^2

(b) FL = 90%, $\dot{Q}$ =20.2 W/m^2

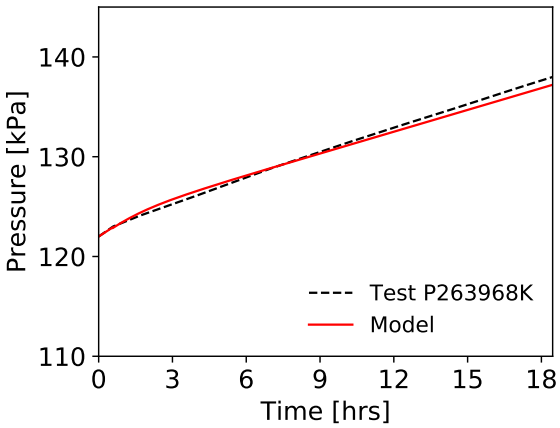

(c) FL = 25%, $\dot{Q}$ = 18.8 W

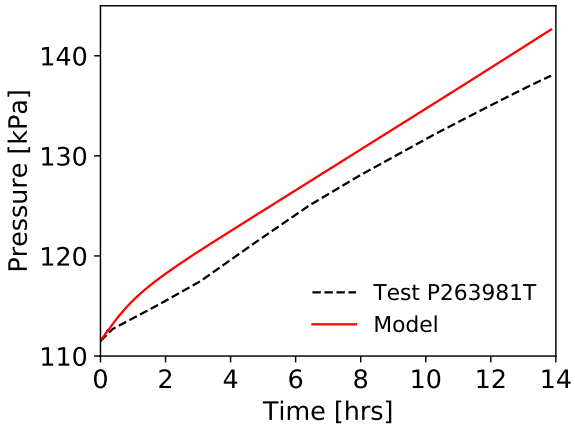

(d) FL = 50%, $\dot{Q}$ = 51.0 W/m^2

Figure I.4: Pressure values obtained from simulation (red) versus values obtained from literature (black) for self-pressurization in the MHT tank.

REFERENCES

[1] Adams, K. A., "Titan/Centaur D-1T TC-5 Helios B Flight Data Report," National Aeronautics and Space Administration, Tech. Rep., 1976.

[2] Ahuja, V. *et al.*, "Computational Analyses of Pressurization in Cryogenic Tanks," in *44th AIAA/ASME/SAE/ASEE Joint Propulsion Conference & Exhibit*, NASA Stennis Space Center; Combustion Research and Flow Technology, Hartford, CT, 2008.

[3] Apriyanti, V., Adriansyah, W., Abdurrachim, and Pasek, A. D., "A Review of Direct Contact Condensation of Steam on Water Droplets," in *AIP Conference Proceedings*, vol. 1984, 2018.

[4] Arnett, R. W. and Voth, R. O., "A Computer Program for the Calculation of Thermal Stratification and Self-Pressurization in a Liquid Hydrogen Tank," Tech. Rep., 1972.

[5] Aydelott, J. C., "Normal Gravity Self-Pressurization of 9-inch- (23 CM) Diameter Spherical Liquid Hydrogen Tankage," National Aeronautics and Space Administration, Tech. Rep., Oct. 1967.

[6] Aydelott, J. C. and Spuckler, C. M., "Effect of Size on Normal-Gravity Self-Pressurization of Spherical Liquid Hydrogen Tankage," Natonal Aeronautics and Space Administration, Tech. Rep., 1969.

[7] ——, "Venting of Liquid Hydrogen Tankage," National Aeronautics and Space Administration, Tech. Rep., Jun. 1969.

[8] Bailey, L. J., et al., Folta, D., Barbee, B. W., Vaughn, F., Campbell, B., Thronson, H. A., Englander, J., and Lin, T. Y., "A Lean, Fast Mars Round-trip Mission Architecture: Using Current Technologies for a Human Mission in the 2030s," *AIAA SPACE Conference and Exposition, San Diego, CA.*, pp. 1–38, 2013.

[9] Bandyopadhyay, A., Majumdar, A. K., Leclair, A. C., and Valenzuela, J. G., "Multi-Node Modeling of Cryogenic Tank Pressurization System using Generalized Fluid System Simulation Program," in *AIAA Propulsion and Energy*, 2019.

[10] Barron, R. F., *Cryogenic Heat Transfer*, CRC Press, Ed. CRC Press, 1999, ch. 2: pp. 117–120.

[11] Barsi, S. and Kassemi, M., "Numerical and Experimental Comparisons of the Self-Pressurization Behavior of an LH2 Tank in Normal Gravity," *Cryogenics*, vol. 48, no. 3-4, pp. 122–129, Mar. 2008.

[12] Barsi, S., Moder, J., and Kassemi, M., "Numerical Investigation of LO2 and LCH4 Storage Tanks on the Lunar Surface," in *AIAA 45th Aerospace Sciences Meeting and Exhibit*, American Institute of Aeronautics and Astronautics, 2008.

[13] Barsi, S. *et al.*, "A Tank Self-Pressurization Experiment Using a Model Fluid in Normal Gravity," in *43rd AIAA Aerospace Sciences Meeting*, American Institution of Aeronautics and Astronautics, 2005, pp. 10–13.

[14] Barsi, S., "Ventless Pressure Control of Cryogenic Storage Tanks," PhD thesis, Case Western Reserve, 2011.

[15] Barsi, S. and Kassemi, M., "Validation of Tank Self-Pressurization Models in Normal Gravity," in *45th AIAA Aerospace Sciences Meeting and Exhibit*, 2007.

[16] ——, "Investigation of Tank Pressurization and Pressure Control-Part I: Experimental Study," vol. 5, no. 4, 2013.

[17] Beduz, C., Rebiai, R., and Scurlock, R. G., "Thermal Overfill and the Surface Evaporasation of Cryogenic Liquids Under Storage Conditions," *Advances in Cryogenic Engineering*, pp. 795–803, 1984.

[18] Benton, M. G., "A Conceptual Mars Exploration Vehicle Architecture with Chemical Propulsion, Near-Term Technology, and High Modularity to Enable Near-Term Human Missions to Mars," in *AIAA SPACE 2015 Conference and Exposition*, 2015, pp. 1–60.

[19] Bentz, M. D., Wilkinson, C. L., Hentz, M. D., and Wilkinson, C. L., "Experimental Study of Flasu Boiling in Liquid Nitrogen," in *19th Joint Propulsion Conference*, 1975.

[20] Bilstein, R. E., "Stages to Saturn: A Technological History of the Apollo/Saturn Launch Vehicle," National Aeronautics and Space Administration, Tech. Rep., 1999.

[21] Bolshinskiy, L. G., Hedayat, A., Hastings, L. J., Moder, J. P., Schnell, A. R., Sutherlin Presenter, S. G., and Bolshinskiy, L., "TankSIM: A Cryogenic Tank Performance Prediction Program," Tech. Rep., 2015.

[22] Bolshinskiy, L. G., Hedayat, A., and Moder, J. P., "Tank System Integrated model: A Cryogenic Tank Performance Prediction Program," National Aeronautics and Space Administration, Tech. Rep., 2017.

[23] Bostock, T. D. and Scurlock, R. G., "Evaporation of Cryogenic Liquids," in *Low Loss Storage and Handling of Cryogenic Liquids*, 2019, ch. 2.

[24] Bradshaw, R. D., "Evaluation and Application of Data from Low-Gravity Orbital Experiment Phase I - Final Report," Convair Division of General Dynamics, Tech. Rep., Apr. 1970.

[25] Braun, R. D., "Investments in the Future: NASA's Technology Programs," in *Presentation at TEDxNASA*, Virginia: Newport News, 2010.

[26] Brentari, E. G., Giarratano, P. J., and Smith, R. V., "Boiling Heat Transfer for Oxygen, Nitrogen, Hydrogen, and Helium," U.S. Department of Commerce National Bureau of Standards, Tech. Rep., 1965.

[27] Campbell, N. S., "Analysis Methods for Reusable Spacecraft Undergoing Aeroassist Maneuvers," PhD thesis, 2019.

[28] Campbell, N. S. and Argrow, B. M., "Earth Aerobraking Architectures for a Reusable Upper Stage," in *70th International Astronautical Congress*, 2019.

[29] Cengel, Y. A. and Boles, M. A., *Thermodynamics: An Engineering Approach*, 5th ed. 2006.

[30] Chai, P. R. and Wilhite, A. W., "Cryogenic Thermal System Analysis for Orbital Propellant Depot," *Acta Astronautica*, vol. 102, pp. 35–46, 2014.

[31] Chato, D. J., "Flight Development for Cryogenic Fluid Management in Support of Exploration Missions," Tech. Rep., 2006.

[32] Chato, D. J. and Doherty, M. P., *NASA Perspectives on Cryo LH2 Storage*, Feb. 2011.

[33] Churchill, S. W. and Usagi, R., "A General Expression for the Correlation of Rates of Transfer and Other Phenomena," *AIChE Journal*, vol. 18, no. 6, pp. 1121–1128, Nov. 1972.

[34] Clark, J. A., *Cryogenic Heat Transfer*. 1969, vol. 5, pp. 325–517.

[35] Condon, G. L., Clark Esty, C., Berry, C. F., Downs, S. P., Ocampo, C., Mahajan, B., and Burke, L. M., "Mission and Trajectory Design Considerations for a Human Lunar Mission Originating from a Near Rectilinear Halo Orbit," in *AIAA SciTech Forum*, Jan. 2020.

[36] Corpening, J. H., "Analytical Modeling of Pressurization and Cryogenic Propellant Conditions for Liquid Rocket Based Vehicle Designs," Teledyne Brown Engineering, Tech. Rep., 2010.

[37] Crusan, J., *Gateway Update: Human Explorations Committee*, 2018.

[38] Cummings, N., *Human Landing System: Putting Boots Back on the Moon*, 2020.

[39] Davis, M. L., Allgeier, R. K. J., Rogers, T. G., and Rysavy, G., "The Development of Cryogenic Storage Systems for Space Flight," National Aeronautics and Space Administration, Tech. Rep., 1970.

[40] De Kruif, J. S. and Kutter, B. F., "Cenatur Upper Stage Applicability for Several-Day Mission Durations with Minor Insulation and Modifications," in *Joint Propulsion Conference & Exhibit*, American Institute of Aeronautics and Astronautics, 2007.

[41] De Quay, L., "Validation Prediction of Pressure Gas Requirements in Cryogenic Run Tanks at Subcritical and Supercritical Pressures," PhD thesis, Mississippi State University, 2009.

[42] De Quay, L. and Hodge, B. K., "A History of Collapse Factor Modeling and Empirical Data for Cryogenic Propellant Tanks," in *46th AIAA/ASME/SAE/ASEE Joint Propulsion Conference and Exhibit*, 2010.

[43] Deb, K., Pratap, A., Agarwal, S., and Meyarivan, T., "A Fast and Elitist Multiobjective Genetic Algorithm: NSGA-II," *IEEE Transactions on Evolutionary Computation*, vol. 6, no. 2, pp. 182–197, 2002.

[44] Doherty, M. P., Meyer, M. L., Motil, S. M., and Ginty, C. A., "Cryogenic Propellant Storage and Transfer (CPST) Technology Maturation: Establishing a Foundation for a Technology Demonstration Mission (TDM)," National Aeronautics and Space Administration, Tech. Rep., 2014.

[45] Donabedian, M., *Spacecraft Thermal Control Handbook Volume II – Cryogenics*. Aerospace Press, 2003, vol. I.

[46] Drake, B. G., "Human Exploration of Mars Design Reference Architecture 5.0 Addendum," National Aeronautics and Space Administration, Tech. Rep., Jul. 2009.

[47] Ebbing, D. D. and Gammon, S. D., "States of Matter and Solutions," in *General Chemistry*, 7th, Houghton Milton Company, 2002, ch. 3, p. 448.

[48] Edwards, S. J., Trent, D., Diaz, M. J., and Mavris, D. N., "A Model-Based Framework for Synthesis of Space Transportation Architectures," in *AIAA SPACE and Astronautics Forum and Exposition*, 2018.

[49] Estey, P. N., Lewis, D. H., and Connor, M., "Prediction of a Propellant Tank Pressure History Using State Space Methods," *Journal of Spacecraft and Rockets*, vol. 20, no. 1, p. 54, 1983.

[50] Evans, M. E. and Graham, L. D., "A Flexible Lunar Architecture for Exploration (FLARE) supporting NASA's Artemis Program," *Acta Astronautica*, vol. 177, pp. 351–372, Dec. 2020.

[51] Fan, S. C., Chu, J. C., and Scott, L. E., "Thermal Stratification in Closed Cryogenic Containers," in *Advances in Cryogenic Engineering*, K. D. Timmerhaus, Ed., Springer US, 1969, pp. 249–257.

[52] Flachbart, R. H., Hastings, L. J., Hedayat, A., Nelson, S. L., and Tucker, S., "Testing the Effects of Helium Pressurant on Thermodynamic Performance with Liquid Hydrogen," *AIP Conference Proceedings*, vol. 985, no. 1, pp. 1483–1490, 2008.

[53] Flachbart, R. H., Hastings, L. J., Hedayat, A., Nelson, S. L., and Tucker, S. P., "Testing of a Spray-Bar Thermodynamic Vent System in Liquid Nitrogen," *AIP Conference Proceedings*, vol. 823, no. 1, pp. 240–247, 2006.

[54] Flachbart, R. H., Hastings, L. J., Martin, J. J., Flachbart, R. H., Hastings, L. J., and Martin, J. J., "Testing of a Spray Bar Zero Gravity Cryogenic Vent System for Upper Stages," in *35th AIAAI/ASME/SAEIASEE Joint Propulsion Conference and ExhibitSAEIASEE Joint Propulsion Conference and Exhibit*, 1999.

[55] Flynn, T., *Cryogenic Engineering*. CRC Press, 2004, pp. 698–700.

[56] Froust, J., *SPACENEWS: Blue Origin Team Delivers Lunar Lander Mockup to NASA*, 2020.

[57] ——, *SPACENEWS: Dynetics to Use In-Space Refueling for NASA Lunar Lander*, Sep. 2020.

[58] Fuller, P. D. and McLagan, J. N., "Storage and Transfer of Cryogenic Fluids," in *Applied Cryogenic Engineering*, 1962, ch. 9.

[59] Gilmore, D. G. and Donabedian, M., *Spacecraft Thermal Control Handbook Volume I – Fundamental Technologies*. American Institute of Aeronautics and Astronautics, 2002.

[60] Glaister, D. and Mills, G., "Cryogenic Systems Analysis," in *Spacecraft Thermal Control Handbook*, ser. Spacecraft Thermal Control Handbook, M. Donabedian, Ed., vol. 2, The Aerospace Press, American Institute of Aeronautics, and Astronautics, Inc., 2003, ch. 20, pp. 483–531.

[61] Glaister, D., Schmidt, J., McLean, C., and Mills, G., "Long Term Cryogenic Storage Technologies Overview for NASA Exploration Applications," in *42nd AIAA Thermophysics Conference*, American Institute of Aeronautics and Astronautics, 2011.

[62] Glover, D., "NASA Cryogenic Fluid Management Space Experiment Efforts," in *Conference on Advanced Space Exploration Initiative Technologies*, 1991.

[63] Gluck, D. F. and Kline, J. F., "Gas Requirements in Pressurized Transfer of Liquid Hydrogen," *Advances in Cryogenic Engineering*, pp. 219–233, 1962.

[64] Gray, J. S., Moore, K. T., Hearn, T. A., and Naylor, B. A., "A Standard Platform for Testing and Comparison of MDAO Architectures," in *AIAA/ASME/ASCE/AHS/ASC Structures, Structural Dynamics and Materials Conference*, Honolulu, Hawaii: AIAA, 2012.

[65] Grayson, G. D., "Engineering Notes Coupled Thermodynamic-Fluid-Dynamic Solution for a Liquid-Hydrogen Tank," *Journal of Spacecraft and Rockets*, vol. 32, no. 5, 1995.

[66] Grayson, G., Lopez, A., Chandler, F., Hastings, L., Hedayat, A., and Brethour, J., "CFD Modeling of Helium Pressurant Effects on Cryogenic Tank Pressure Rise Rates in Normal Gravity," in *43rd AIAA/ASME/SAE/ASEE Joint Propulsion Conference and Exhibit*, 2007.

[67] Griffin, M. D. and French, J. R., *Space Vehicle Design*, 2nd ed. American Institute of Aeronautics and Astronautics, 2004, p. 665.

[68] Gursu, S., Lordgooei, M., Sherif, S. A., and Veziroglu, T. N., "An Optimization Study of Liquid Hydrogen Boil-Off Losses," *International Journal of Hydrogen Energy*, vol. 17, no. 3, pp. 227–236, 1992.

[69] Gursu, S., Sherif, S. A., Veziroglu, T. N., and Sheffield, J. W., "Analysis and Optimization of Thermal Stratification and Self-Pressurization Effects in Liquid Hydrogen Storage Systems-Part 1: Model Development," *Journal of Energy Resources Technology*, vol. 115, pp. 221–227, 1993.

[70] Hansen, H. C., Johnson, W. L., Meyer, M. L., Werkheiser, A. H., and Stephens, J. R., "Cryogenic Fluid Management Technologies Enabling for the Artemis Program and Beyond," in *ASCEND 2020*, Nov. 2020.

[71] Hasan, M. M., Lin, C. S., and Van Dresar, N. T., "Self-Pressurization of a Flightweight Liquid Hydrogen Storage Tank Subjected to Low Heat Flux," in *ASME/AIChE National Heat Transfer Conference*, National Aeronautics and Space Administration, 1991.

[72] Hastings, L. J., "Spray Bar Zero-Gravity Vent System for On-Orbit Liquid Hydrogen Storage," National Aeronautics and Space Administration, Tech. Rep., 2003.

[73] Hastings, L. J., Hedayat, A., Brown, T. M., and Marshall, G. C., "Analytical Modeling and Test Correlation of Variable Density Multilayer Insulation for Cryogenic Storage," National Aeronautics and Space Administration, Hastings2004, Tech. Rep., 2004.

[74] Hastings, L. J., Tucker, S. P., Flachbart, R. H., Hedayat, A., and Nelson, S. L., "Marshall Space Flight Center In-Space Cryogenic Fluid Management Program Overview," in *41st AIAA/ASME/SAE/ASEE Joint Propulsion Conference & Exhibit*, 2005.

[75] Hedayat, A., Bailey, J. W., Hastings, L. J., and Flachbart, R. H., "Test Data Analysis of a Spray Bar Zero-Gravity Liquid Hydrogen Vent System for Upper Stages," *Proceedings*, vol. 710, p. 232, 2004.

[76] Hedayat, A., Hastings, L. J., Bryant, C., and Plachta, D. W., "Large scale demonstration of liquid hydrogen storage with zero boiloff," in *AIP Conference Proceedings*, vol. 613, 2002, pp. 1276–1283.

[77] Hochstein, J. I., Ji, H.-C., and Aydelott, J. C., "Prediction of Self-Pressurization Rate of Cryogenic Propellant Tankage," *Journal of Propulsion and Power*, vol. 6, no. 1, pp. 11–17, Jan. 1990.

[78] Holman, J. P., *Heat Transfer*, 10th. McGraw-Hill, 2008.

[79] Holt, K., Majumdar, A., Steadman, T., and Hedayat, A., "Numerical Modeling and Test Data Comparison of Propulsion Test Article Helium Pressurization System," in *36th AIAA/ASME/SAE/ASEE Joint Propulsion Conference and Exhibit*, 2000.

[80] Honour, R., Kwas, R., O'Niel, G., and Kutter, B., "Thermal Optimization of an On-Orbit Long Duration Cryogenic Propellant Depot," National Aeronautics Space Administration and United Launch Alliance, Tech. Rep., 2012.

[81] Hosangadi, A., Ahuja, V., and Ungewitter, R. J., "Simulations of Cavitating Flows in Turbopumps," *Journal of Propulsion and Power*, vol. 20, no. 4, 2004.

[82] Hosangadi, A. and Ahuja, V., "Numerical Study of Cavitation in Cryogenic Fluids," *Journal of Fluids Engineering*, vol. 127, 2005.

[83] Jacobs, R. B., "Theory of Boil-Off Calorimetry," *Review of Scientific Instruments*, vol. 35, no. 7, p. 946, 1964.

[84] Johnson, L., Meyer, M., Palaszewski, B., Coote, D., Goebel, D., and White, H., "Development Priorities for In-Space Propulsion Technologies," *Acta Astronautica*, vol. 82, no. 2, pp. 148–152, Aug. 2013.

[85] Johnson, W., Tomsik, T., and Moder, J., *Fundamentals of Cryogenics*, Aug. 2014.

[86] Joyner, C., "Nuclear Propulsion Technology for Exploration and a Sustainable Presence on the Moon, Mars, and Beyond," in *70th International Astronautical Congress*, 2019.

[87] Kartuzova, O., Kassemi, M., Agui, J., and Moder, J., "Self-Pressurization and Spray Cooling Simulations of the Multipurpose Hydrogen Test Bed (MHTB) Ground-Based Experiment," in *50th AIAA/ASME/SAE/ASEE Joint Propulsion Conference*, 2014.

[88] Klell, M., "Storage of Hydrogen in the Pure Form," in *Handbook of Hydrogen Storage: New Materials for Future Energy Storage*, WILEY-VCH Verlag GmbH & Co. KGaA Weinheim, 2010, ch. 1, pp. 17–24.

[89] Kos, L., *Personal Communication*, 2018.

[90] Kos, L. D., Polsgrove, T. P., Sostaric, R. R., Braden, E. M., Sullivan, J. J., and Le, T. T., "Altair descent and ascent reference trajectory design and initial dispersion analyses," in *AIAA Guidance, Navigation, and Control Conference*, 2010.

[91] Lemmon, E. W., Huber, M. L., and McLinden, M. O., *NIST Standard Reference Database 23: Reference Fluid Thermodynamic and Transport Properties-REFPROP*, 2010.

[92] Lemmon, E. W., McLinden, M. O., and Friend, D. G., "NIST Chemistry WebBook, SRD69 Thermophysical Properties of Fluid Systems," in *NIST Chemistry WebBook, NIST Standard Reference Database Number 69*, P. L. Mallard and W.G., Eds., National Institute of Standards and Technology, 2018.

[93] Liebenberg, D. and Edeskuty, F., "Pressurization Analysis of a Large-Scale Liquid-Hydrogen Dewar," *International Advances in Cryogenic Engineering*, vol. 10, no. 142, pp. 284–289, 1965.

[94] Lienhard, J. H., *A Heat Transfer Textbook*. Prentice Hall, Inc., 2011.

[95] Lin, C. and Hasan, M., "Self-Pressurization of a Spherical Liquid Hydrogen Storage Tank in a Microgravity Environment," in *30th Aerospace Sciences Meeting*, American Institute of Aeronautics and Astronautics, 1992.

[96] Lin, C. S., Van Dresar, N. T., and Hasan, M. M., "Pressure Control Analysis of Cryogenic Storage Systems," *Journal of Propulsion and Power*, vol. 20, no. 3, pp. 480–485, May 2004.

[97] Liu, Z., Li, Y., and Jin, Y., "Pressurization Performance and Temperature Stratification in Cryogenic Final Stage Propellant Tank," *Applied Thermal Engineering*, vol. 106, pp. 211–220, Aug. 2016.

[98] Ludwig, C. and Dreyer, M. E., "Investigations on Thermodynamic Phenomena of the Active-Pressurization Process of a Cryogenic Propellant Tank," *Cryogenics*, vol. 63, pp. 1–16, 2014.

[99] Majumdar, A. K., Steadman, T. E., and Maroney, J. L., "Numerical Modeling of Propellant Boiloff in Cryogenic Storage Tank," Tech. Rep., 2007.

[100] Majumdar, A., LeClair, A., Moore, R., and Schallhorn, P., "Generalized Fluid System Simulation Program (GFSSP)-Version 6," in *AIAA/SAE/ASEE Joint Propulsion Conference*, 2015.

[101] Majumdar, A. and Steadman, T., "Numerical Modeling of Pressurization of a Propellant Tank," *Journal of Propulsion and Power*, vol. 17, no. 2, pp. 385–390, 2001.

[102] Majumdar, A., Valenzuela, J., LeClair, A., and Moder, J., "Numerical Modeling of Self-Pressurization and Pressure Control by a Thermodynamic Vent System in a Cryogenic Tank," *Cryogenics*, vol. 74, pp. 113–122, 2016.

[103] Martin Marietta Aerospace, "Titan IIIE/Centaur D-1T Systems Summary," Tech. Rep., 1973.

[104] Martin, J. J. and Marshall, L. H., "Large-Scale Liquid Hydrogen Testing of a Variable Density Multilayer Insulation With a Foam Substrate," National Aeronautics and Space Administration, Tech. Rep., 2001.

[105] Mattick, S. and al., et, "Progress in Modeling Pressurization in Propellant Tanks," in *46th AIAA/ASME/SEA/ASEE Joint Propulsion Conference*, American Institute of Aeronautics and Astronautics, 2010.

[106] Mavris, D. N., *Design of Experiments for Practical Applications in Modeling, Simulation, and Analysis*, 2011.

[107] Mavris, D. N., Delaurentis, D. A., Bandte, O., and Hale, M. A., "A stochastic approach to multi-disciplinary aircraft analysis and design," in *36th AIAA Aerospace Sciences Meeting and Exhibit*, Reno, Jan. 1998.

[108] McAdams, W. H., *Heat transmission*. McGraw-Hill, 1954.

[109] Mcbrayer, K. T., Edwards, S. J., and Birbasov, N., "Keplerian Analysis for Versatile Evaluation of Arbitrary Trajectories," in *ASCEND*, 2020.

[110] McLean, C., Mustafi, S., Walls, L., Pitchford, B., Wollen, M., and Schmidt, J., "Simple, Robust Cryogenic Propellant Depot for Near Term Applications," *IEEE Aerospace Conference Proceedings*, IEEE, 2011.

[111] Motil, S. M., Meyer, M. L., and Tucker, S. P., "Cryogenic Fluid Management Technologies for Advanced Green Propulsion Systems," in *45th AIAA Aerospace Sciences Meeting and Exhibit*, vol. 35812, 2007.

[112] Mukhopadhyay, M., *Fundamentals of Cryogenic Engineering*, PHI Learning, Ed. PHI Learning Pvt. Ltd., 2010, ch. 7, pp. 242–261.

[113] Muratov, C. B., Osipov, V. V., and Vadim, N., "Issues of Long-Term Cryogenic Propellant Storage in Microgravity," National Aeronautics and Space Administration, Tech. Rep., 2011.

[114] National Aeronautics and Space Administration, *Power Reactant Storage and Distribution*, 2002.

[115] ——, *Space Shuttle - Extended Duration Missions*, J. Ryba, Ed., 2008.

[116] ——, *NASA's Lunar Outpost will Extend Human Presence in Deep Space*, 2018.

[117] ——, "Appendix E: Human Landing System Studies, Risk Reduction, Development, and Demonstration," in *Next Space Technologies for Exploration Partnerships -2 (NextSTEP-2)*, 2019.

[118] Navickas, J. and Madsen, R. A., "Propellant Behavior during Venting in an Orbiting Saturn S-IVB Stage," *Advances in Cryogenic Engineering*, vol. 13, pp. 188–198, 1968.

[119] Norquist, L., "External Tank for the Space Shuttle Main Propulsion Systems," in *Journal of Spacecraft and Rockets*, 6, vol. 14, 1977, pp. 358–364.

[120] Orloff, R. W., "Apollo by the Numbers: A Statistical Reference," National Aeronautics and Space Administration, Tech. Rep. NASA/SP-2000-4029, 2000.

[121] Panzarella, C. H. and Kassemi, M., "On the validity of purely thermodynamic descriptions of two-phase cryogenic fluid storage," *Journal of Fluid Mechanics*, vol. 484, pp. 41–68, 2003.

[122] Partridge, J. K., "Fractional Consumption of Liquid Hydrogen and Liquid Oxygen During the Space Shuttle Program," *AIP Conference Proceedings*, vol. 1434, no. 1, 2010.

[123] Perrin, T. M. and Casler, J. G., "Architecture Study for a Fuel Depot Supplied from Lunar Resources," PhD thesis, University of North Dakota, 2016.

[124] Perrin, T. M. and Casler, J. G., "Compensating for Cryogenic Propellant Boiloff for a Cargo Mission to Mars," in *AIAA SPACE and Astronautics Forum and Exposition*, American Institute of Aeronautics and Astronautics, 2017, pp. 1–10.

[125] Plachta, D. W., Johnson, W. L., and Feller, J. R., "Cryogenic Boil-Off Reduction System Testing," in *50th AIAA/ASME/SAE/ASEE Joint Propulsion Conference*, 2014, p. 3579.

[126] Plachta, D., Stephens, J., Johnson, W., and Zagarola, M., "NASA cryocooler technology developments and goals to achieve zero boil-off and to liquefy cryogenic propellants for space exploration," *Cryogenics*, vol. 94, pp. 95–102, 2018.

[127] Plachta, D., "Results of an Advanced Development Zero Boil-Off Cryogenic Propellant Storage Test," in *AIAA/ASME/SAE/ASEE Joint Propulsion Conference and Exhibit*, 2004.

[128] Plachta, D. W., "Hybrid Thermal Control Testing of a Cryogenic Propellant Tank," National Aeronautics and Space Administration, Tech. Rep., 1999.

[129] Plachta, D. and Kittel, P., "An Updated Zero Boil-Off Cryogenic Propellant Storage Analysis Applied to Upper Stages or Depots in an LEO Environment," in *38th AIAA/ASME/SAE/ASEE Joint Propulsion Conference and Exhibit*, 2002.

[130] Riemer, D. H., "Cryogenic Tank Stratification A Simpler Approach," *Advances in Cryogenic Engineering*, R. W. Fast, Ed., pp. 957–962, 1986.

[131] Ring, E., "Pressurizing Gas Thermodynamics," in *Rocket Propellant and Pressurization Systems*, 1964, ch. 18.

[132] Robertson, B., Mendez Ramos, E. D., and Diaz, M. J., "A Conceptual Design Study for an Unmanned Reusable Cargo Lunar Lander," in *International Astronautical Congress*, International Astronautical Federation, 2019.

[133] Robinson, J. S., "An Overview of NASA's Integrated Design and Engineering Analysis (IDEA) Environment," in *17th AIAA International Space Planes and Hypersonic Systems and Technologies Conference*, 2014.

[134] Rohsenow, W. M., Harnett, J. P., and Cho, Y. I., *Handbook of Heat Transfer*, 3, Ed. McGraw-Hill, 1998, ISBN: 0070535558.

[135] Roudebush, W. H., "An Analysis of the Problem of Tank Pressurization During Outflow," National Aeronautics and Space Administration, Tech. Rep., 1965.

[136] Ryan, R. S. and Townsend, J. S., "Fundamentals and Issues in Launch Vehicle Design," *JOURNAL OF SPACECRAFT AND ROCKETS*, vol. 34, no. 2, 1997.

[137] Salerno, L. J. and Kittel, P., "Cryogenics and the Human Exploration of Mars," *Cryogenics*, vol. 39, no. 4, pp. 381–388, Apr. 1999.

[138] Schaffer, M., Germain, B. S., and Bradford, J. E., "Cryogenic Propulsive Stage (CPS) Mission Sensitivity Studies Low Earth Orbit Departure Results," United Launch Alliance, Tech. Rep. Revision D, Oct. 2012.

[139] Schaffer, M., St Germain, B., and Bradford, J. E., "Cryogenic Propulsive Stage (CPS) Mission Sensitivity Studies Earth-Moon L1 Departure Results," United Launch Alliance, Tech. Rep., 2012.

[140] Schaffer, M. and Wenner, C., "A Study of Cryogenic Propulsive Stages for Human Exploration Beyond Low Earth Orbit," SpaceWorks Enterprises, Inc., and United Launch Alliance, LLC, Tech. Rep. GLEX-2012.05.1.4x12564, Oct. 2012.

[141] Scott, R. B., *Cryogenic Engineering*. Von Nostrand, 1959.

[142] Seo, M. and Jeong, S., "Analysis of Self-Pressurization Phenomenon of Cryogenic Fluid Storage Tank with Thermal Diffusion Model," *Cryogenics*, vol. 50, no. 9, pp. 549–555, Sep. 2010.

[143] *Starship*, 2020.

[144] Stewart, M. E. M., "Pressurization of a Flightweight, Liquid Hydrogen Tank: Evaporation & Condensation at the Liquid/Vapor Interface," in *53rd AIAA/SAE/ASEE Joint Propulsion Conference*, 2017.

[145] Stewart, M. E. M. and Moder, J. P., "Self-Pressurization of a Flightweight, Liquid Hydrogen Tank: Simulation and Comparison with Experiments," in *52nd AIAA/SAE/ASEE Joint Propulsion and Energy Conference*, Salt Lake City, UT: American Institute of Aeronautics and Astronautics, 2016.

[146] Sutton, G. P., *Rocket Propulsion Elements*, 7th. John Wiley & Sons, 2001, ISBN: 0471326429.

[147] Tatom, J. W., Brown, W. H., Knight, L. H., and Coxe, E. F., "Analysis of Thermal Stratification of Liquid Hydrogen in Rocket Propellant Tanks," *Advances in Cryogenic Engineering*, pp. 265–272, 1964.

[148] Trent, D. J. and Edwards, S. J., "Analysis of Alternative Architectures for a 2024 Lunar Sortie," in *ASCEND*, Nov. 2020.

[149] Trent, D. J., "Integrated Architecture Analysis and Technology Evaluation for Systems of Systems Modeled at the Subsystem Level," PhD thesis, Georgia Institute of Technology, 2017.

[150] Van Dresar, N. T., Lin, C. S., and Hasan, M. M., "Self-Pressurization of a Flightweight Liquid Hydrogen Tank: Effects of Fill Level at Low Wall Heat Flux," in *30th Aerospace Sciences Meeting and Exhibit*, American Institute of Aeronautics and Astronautics, 1992.

[151] Van Dresar, N. T., "Liquid Oxygen Thermodynamic Vent System Testing With Helium Pressurization," Tech. Rep., 2014.

[152] Van Dresar, N. T. and Stochl, R. J., "Pressurization and Expulsion of Cryogenic Liquids: Generic Requirements for a Low-Gravity Experiment," in *29th Joint Propulsion Conference and Exhibit*, National Aeronautics and Space Administration, 1993.

[153] Vance, R. W., *Applied Cryogenic Engineering*, R. W. Vance, Ed. Wiley, 1962, pp. 221–222, ISBN: 0 419 18780 4.

[154] Wang, L., Li, Y., Li, C., and Zhao, Z., "CFD investigation of thermal and pressurization performance in LH 2 tank during discharge," *Cryogenics*, vol. 57, pp. 63–73, Oct. 2013.

[155] Ward, W. D. *et al.*, "Evaluation of AS-203 Low Gravity Orbital Experiment," National Aeronautics and Space Administration, Tech. Rep., 1967.

[156] Wertz, J. R. and Larson, W. J., *Space Mission Analysis and Design*, Third, Wiley J. Larson and James R. Wertz, Ed. Microcosm Press, 2010.

[157] Zakar, D. R. and Baldauff, R. W., "Zero-Boil-Off Cryogen Storage Cryogenic Loop Heat Pipe for use in Unmanned Air Vehicles," in *15th International Energy Conversion Engineering Conference*, 2017.

[158] Zilliac, G. and Karabeyoglu, M., "Modeling of Propellant Tank Pressurization," in *41st AIAA/ASME/SAE/ASEE Joint Propulsion Conference and Exhibit*, Reston, Virginia: American Institute of Aeronautics and Astronautics, Jul. 2005.

[159] Zimmerman, D., Wagner, S., and Wie, B., "The First Human Asteroid Mission: Target Selection and Conceptual Mission Design," in *AIAA/AAS Astrodynamics Specialist Conference*, American Institute of Aeronautics and Astronautics, 2010, pp. 1–21.

VITA

Eugina D. Mendez Ramos graduated in June 2009 from the University of California Riverside with Bachelor of Science degrees in Chemistry and Physics. Eugina then attended the graduate program within the Daniel Guggenheim School of Aerospace Engineering at the Georgia Institute of Technology in 2011, where she was awarded her Master of Science degree in Fall 2013. As a Graduate Research Assistant at the Aerospace Systems Design Laboratory (ASDL), she worked on a number of collaborative research projects with the Advanced Concepts Office of NASA's Marshall Space Flight Center. These projects focused on modeling and simulation of a variety of in-space vehicle propulsion concepts, including solar electric, nuclear thermal, cryogenic, and traditional storable options.